International Committee for Future Accelerators

Sponsored by the Particles and Fields Commission of IUPAP

Beam Dynamics Newsletter

No. 71

Issue Editor:
J. Gao

Editor in Chief:
Y. H. Chin

August 2017

Contents

14

1   Foreword

1.1   From the Chair

Yong Ho Chin, KEK

Mail to: yongho.chin@kek.jp

We have an announcement. Geroge Neil has stepped down from the ICFA Beam Dynamics Panel (BDP) members, leaving his long standing achievements on beam dynamics studies. We have now a new ICFA BDP member who succeded him, Eliana Gianfelice-Wendt of FNAL, an excellent beam dynamics physisit. Her membership was officially approved by ICFA.

You can find information on forthcoming events (workshops, conferences, etc.) on the the ICFA BDP website:

http://icfa-bd.kek.jp

We have approved a new ICFA mini-workshop since the last Newsletter:

1. ICFA Mini-Workshop on Dynamic Apertures of Circular Accelerators, on November 1-3, 2017, at IHEP, China.

The date of ICFA Mini-Workshop on Beam-Beam Effects in Circular Colliders in Berkeley, CA, USA was moved to 5-7 February 2018. These information and workshop URLs can be found on the above ICFA BDP webpage.

The editor of this issue is Dr. Jie Gao, a panel member and a senior scientist at IHEP, Beijing. The theme is the lattice design of various kinds of rings including circular colliders (electron-position, muons, proton-proton) and light sources. He collected 19 well-written review articles, and they provide very good and comprehensive reviews of the lattice design of circular colliders and light source facilities.

The theme part of this edition starts with a letter from Prof. Evgeni Levitchev of BINP, Russia. He addresses the historical development of the lattic design and the importance of its continuous development for future circular colliders and light sources.

1.2   From the Editor

Jie Gao, Institute of High Energy Physics, CAS, China

Mail to: gaoj@ihep.ac.cn

Since the discovery of the Higgs boson particle in July 2012 on LHC at CERN, an

electron-positron circular collider serving as a Higgs factory becomes possible again, which makes circular accelerator family revive covering from electron-positron collider, proton-proton collider and light sources. For accelerator physicists, the most common tasks in all these accelerators are the lattice designs, and as editor of this issue, I am very pleased to focus on them with the first obvious goal to provide the reader a useful reference on lattice designs of circular accelerators of all kinds. The second goal is to unite accelerator physicists spreading in different accelerator application domains through their common interests, lattice designs, which I have experienced vividly during inviting respectful authors.

Finally, I hope that this issue could be used regularly both by accelerator designers and students who enter this field to learn corresponding accelerator physics.

2 Letters to the Editor

Evgeni Levitchev

BINP, Russia

Mail to: e.b.levichev@inp.nsk.su

The particle accelerator is a scientific tool providing high energy beams for research, industrial, medical or other applications. Performance of circular accelerator or storage ring depends heavily on the magnetic lattice design. I would dare compare the lattice with a skeleton shaping the whole accelerator body and supporting all other important systems and functions, like injection, extraction, and generation of bright photon flux in synchrotron light sources or providing high luminosity in colliders.

The first strong focusing lattices for circular accelerators were simple, compact, and robust and used identical FODO cells. The main function of such lattices was providing the betatron motion stability. With development and differentiation of circular machines, and optimization of their performance, the magnetic lattice has become increasingly sophisticated and complex. Luminosity improvement required low-beta insertion. High-brightness light sources inspired invention of low-emittance lattice family, which started with the Chasmann-Green lattice and through the double- and triple-bend achromat came to the multi-bend achromat structure, providing an emittance close to the diffraction limit for the X-ray source. To accommodate a strong field insertion device, a dispersion-free straight section was developed together with matching cells connecting the straight to the rest of the accelerator.

The lattice evolution reminds the biological anamorphosis, the accelerator "organism" changing over successive generations (for instance, DBA, TBA, and MBA) due to selection by accelerator experts for better satisfaction of experimentalists' requirements. Following the analogy of biological evolution, I believe that composing

an atlas collecting the diversity of accelerator magnetic cells, insertions, structures and lattices would be of great importance for both young and experienced accelerator physicists.

In spite of more than fifty years of progress, there is still space for new ideas in the area of accelerator lattice development and improvement. One example is given by light sources of extremely low emittance. Only ten years ago it was commonly accepted that the development of low-emittance light sources came to the end with their third generation and the fourth generation was announced to be free electron lasers. However due to multi-bend achromat cells, bending magnets with longitudinal gradient, and damping wigglers with short period and strong peak field, the circular machines cheered up with a new classification of circular synchrotron radiation sources of the fourth generation. One of the essential challenges of extremely low-emittance storage ring is the dynamic aperture dramatically reduced, and lattice modifications (such as Hybrid MBA at ESRF or low emittance cell with the minus-unity optical transform) were proposed to overcome the problem. It is worth mentioning that the new light-source generation has appeared without any new accelerator physics behind but with better understanding of the old principles, development of new powerful lattice optimization software and careful study of already known lattice solutions.

Another example of the power of magnet lattice adaptation is the novel collision technology Crab Waist, which promises significant enhancement of luminosity in e+e- colliders. The new method requires a rather complicated final focus structure placed close to the IP (even inside the detector) and a sophisticated interaction region with local chromaticity correction sections and Crab sextupoles phased properly with respect to the interaction point. The Crab Waist colliders require a low emittance to gain the luminosity and in this issue their lattices converge to synchrotron light sources, inheriting the relevant low-emittance solutions.

With the growing demands and challenges of the modern and future circular lepton and hadron accelerators, the lattice design and optimization are still rather art than craft. Specialized workshops for generation of ideas and approaches on lattice detailed development, discussions of simulation algorithm, and comparison and cross-check of computer codes would be topical.

3   Electron Positron and Muon Circular Colliders

3.1   Ground-Up Circular e+e- Higgs Factory Design and Cell Length Optimization

Richard Talman

Laboratory for Elementary-Particle Physics

Cornell University, Ithaca, NY, 14853

United States of America

(richard.talman@cornell.edu)

3.1.1   Introduction

A ``ground-up'' CEPC Higgs Factory design methodology is described. The goals are to find: (i) optimal parameters, (ii) improved understanding (iii) a tentative lattice design. As illustration of the method, six chromaticity-corrected lattices, with cell lengths ranging from 45 m to 280 m, all with identical βy=2 mm or βy=10 mm intersection region optics, are designed and their properties compared. For simplicity only a single ``toy ring'', circumference (76 km), with one interaction point, and a single beam energy (120 GeV) is considered. For the cell-length optimization a figure of merit FOM (essentially integrated luminosity) is maximized consistent with a dimensionless fine tuning penalty function'' or figure of demerit FOD, not being allowed to exceed a conservatively chosen upper limit. The tentative recommendation from this investigation is that the optimal route is (except for obvious changes) to simply copy LEP: 80 m cell length and two-in-one single-ring operation.

A new circular e+e- Higgs factory can have significant luminosity advantages relative to LEP. One LEP parameter that CEPC must not copy is the luminosity of 1032/cm2/s. Some guaranteed improvements (with their improvement factors) are: increased ring-radius x RF power product (3x5≈15); non-interleaved sextupoles (2); full-energy, top-off injection (5); more bunches (110/6≈15); improved intersection region optics (2). It would be double counting to simply multiply these factors. But, barring unforced errors, more than two orders of magnitude improvement is conservatively available. So, with these changes, luminosity in excess of 1034/cm2/s is assured, with little uncertainty or risk.

Possible unforced errors'' that could jeopardize these luminosity improvement factors include too-short cell length, which causes excessively large fine tuning penalty, and local chromatic compensation, which requires strong bends adjacent to the intersection regions (IR). At the high Higgs factory energy the synchrotron radiation from these bends contains hundreds of kilowatts of hard x-rays.

3.1.1.1 *Two results from my 2015 IAS Higgs factory white paper*

For my 2015 IAS Higgs Factory white paper [1] I determined a universal scaling relation for radiation dominated colliding storage rings shown in Figure 1. This graph was introduced primarily in reference to the choice of ring circumference. As such it is not very important for the present paper, which concentrates on optimizing the cell length for constant circumference. In fact, the present paper investigates moving away from this nominal (constant dispersion) behavior (primarily by reducing cell length) to optimize the luminosity.
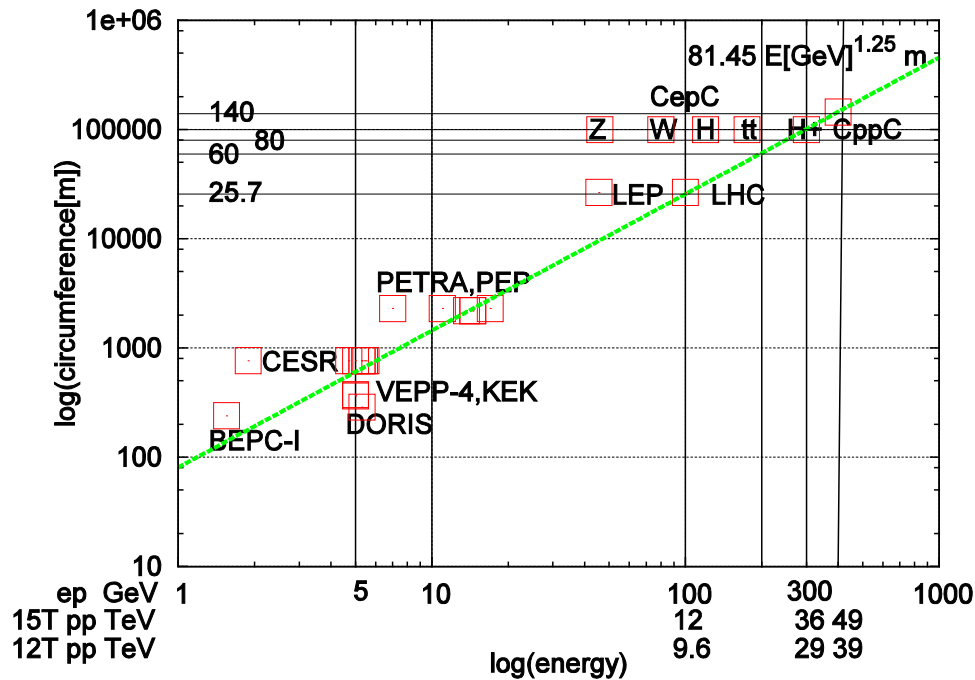
Figure 1. Dependence of circumference on beam energy for radiation-dominated colliders. i.e. GeV-scale electron colliders, and TeV-scale proton colliders of magnetic field 12 T or 15 T.

Of much greater importance for the present paper, also copied from my 2015 white paper, is Table 1, which compares past and future colliding beam rings on the basis of FOD=βy[max]/(l_c<D>) a ``figure of demerit'' introduced in that paper; here βy[max] is the maximum vertical beta function anywhere in the ring, l_c is the arc cell length, and <D> is the average dispersion. This formula is justified more fully later in this paper. Though having physical dimension 1/m, this FOD becomes dimensionless after multiplication by an (unknown) positioning length uncertainty, that reflects state-of-the-art construction, positioning, and stabilization precision. The FOD figure of demerit is based on the assumption that construction, positioning, and stabilization uncertainties are comparable in all rings---though possibly improving due to improved technology over time. To the extent this is valid, the degree of conservatism of diverse storage rings can be compared just on the basis of dimensional analysis. The vindication for applying dimensional analysis comes from the degree of constancy exhibited by the entries in the last column of Table 1. The actually-measured values in the upper six rows vary from 5.1 to 49, which can hardly be said to represent constancy. But both electron and proton

rings are represented, and the particle energies range over a much greater three orders of magnitude range.

In preparing the present paper I came to realize that an appropriate name for this measure of ring sensitivity is ``fine tuning penalty''. Having heard theorists emphasizing their disapproval of theories that required ``fine tuning'' for many years, it came to me that accelerator physicists have been facing up to fine tuning difficulties during the same era. Surely there are few instruments more finely tuned than a colliding beam. My ``fine tuning'' epiphany reminded me of a line in the Moliere play, ``Le Bourgeois Gentilhomme''. Monsieur Jourdain, during a discussion of poetry and prose announces, ``Good heavens, you mean that for more than forty years I have been speaking prose without knowing it.'' So, as already stated, for parameter optimization, the fine tuning penalty provides a quantitative constraint on the storage ring sensitivity. Tentatively, based on measured values in the table, I have adopted FOD<50 as the maximum allowable fine tuning penalty. It will be easy, later, to haggle about the validity of the fine tuning penalty, for example replacing it by some other ring sensitivity measure.

Table 1. Sampling of collider FOD's ("Fine Tuning Penalties") for previous and planned colliding rings, both p,p and e+e-, low and high energy.

β_y^*	Ring		$\langle D \rangle$	l_c	β_y^{max}	$\frac{\beta_y^{max}}{\langle D \rangle l_c}$ FOD
m			m	m	m	1/m
0.015	CESR	measured	1.1	17	95	5.1
0.08	PETRA	measured	0.32	14.4	225	49
	HERA	measured	1.5	48	2025	28
0.05	LEP	measured	0.8	79	441	7.0
0.007	KEKB	measured	0.5	20	290	29
	LHC	measured	1.6	79	4500	36
0.001	CEPC	design	0.31	47	6000	410
0.001	FCC-ee	design	0.10	50	9025	1805

In describing the ``ground up'' optimization methodology, the ``fine tuning penalty'' will also be referred to as a ``figure of demerit'' (FOD) where, numerically, FOD is given by $\beta_y[max]/(l\_c \langle D \rangle)$. Hands-on experience with any particular ring suggests that increased $\beta_y[max]$ correlates well with increased tuning sensitivity. (A positional uncertainty at a $\beta_y = \beta_y[max]$ quadrupole location produces a positional uncertainty proportional $\sqrt{(\beta_y[max])}$ elsewhere in the ring, and proportional to $\beta_y[max]$ at all high β_y locations.) The previously introduced transverse position uncertainty introduces another length.

With the unknown position uncertainty being a length, the FOD itself has to have inverse length dimensionality. To cancel length-squared, a natural further factor, with

dimensions of inverse-length-squared, is the typical sextupole strength S needed to cancel the ring chromaticities. (This is why sextupoles are present in the ring, with their undesirable nonlinear aperture-limiting effects). Since sextupole strengths are not routinely available, it is convenient to replace S by the 1/(l_c<D>) factor, which scales proportionally. (This is because quadrupole q induced chromaticity q δ is cancelled by sextupole induced chromatic compensation -S<D>δ, where δ is fractional momentum offset, and q scales as 1/l_c. The ground-up methodology I recommend includes the following design principles for CEPC and FCC-ee:

- Luminosity is a dependent variable, not an input parameter.
- The ``ground-up'' methodology is incompatible with ``defined parameter'' colliding beam ring design. For example, luminosity is treated as output, not input.
  - Circular colliders and linear colliders are not the same. This is not inconsequential; currently, by adopting linear-collider-like intersection region optics, neither CEPC nor FCC-ee intersection region designs have adequately appreciated this.
- Transverse sensitivity, upper limit on fine tuning penalty; FOD< 50/m. (This may be too conservative. If so, it can be relaxed later.)
- The Higgs Factory design problem is *not* chromatic mismatch of IR and arcs; it is the loss of off-momentum particles, for example due to the Telnov[2] effect.

Though not exactly a ``design principle'' my preliminary ground-up design calculations suggest that local chromatic correction (with its strong bends, large dispersion, and hard x-rays aimed toward the detectors) are unnecessary. (Another quotation from a different Moliere play, ``Nearly all men die of their remedies, and not of their maladies.'') To understand this analogy it is necessary to think of chromaticity as the malady, and sextupoles as remedy. In this case the potentially lethal side effects of the sextupole medicine include both reduced dynamic aperture and hard x-rays incident on the IP detector.

3.1.1.2 *Optimization variables*

It is important to distinguish between independent and dependent variables. The main independent variables are:

- $l^* =$ (1/2) free length for detector [m]

- $l\_c =$ lattice cell length [m]

- $^*_y =$ vertical beta function at IP [m]

- $δ =$ fractional momentum offset [%]

- The main dependent variables are:

- L = actual luminosity [in units of 10^{34}/cm^2/s]

- L'_0 = luminosity per momentum acceptance

- $\Delta\delta[max] = \delta[max] - \delta[min]$

- figure of merit,

  FOM = l^* x $\Delta\delta[max]$/$\sqrt{(\backslash\varepsilon\_x\ \varepsilon\_y)}$

Rationale for this figure of merit: FOM encapsulates the most important lattice-dependent ``useful'' (i.e. including l^* factor) luminosity factors (other than β^*_y).
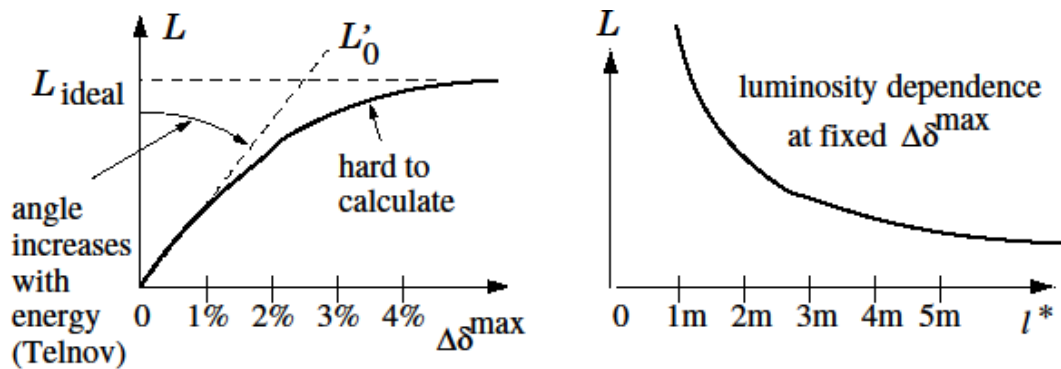
L'_0 is a scale factor to be determined after "best so far" values of cell length l_c and detector half–length l* have been determined.

The ultimate value of l* needs to be negotiated with detector designers

Figure 2. Qualitative luminosity dependencies. Luminosity vs momentum acceptance of the left, luminosity vs IR half-length l^* on the right.

Qualitative luminosity dependencies are sketched in Table 2. Standard luminosity formulas (which ignore momentum acceptance) yield the luminosity labeled L_ideal in the figure on the left. It has always been known that actual luminosity also depends on momentum acceptance. As the figure indicates, the actual luminosity initially increases linearly with momentum acceptance, with slope L'_0. As noted in the figure, it was Telnov[2] who first emphasized that the increasing importance of beamstrahlung with increasing beam energy places increasing demands on the momentum acceptance.

The target for the optimization is to maximize FOM, consistent with limiting FOD. The strategy is to perform multiple scans varying one input parameters while holding constant the other input parameters, including β^*_y. Successive scans establish ``best so far'' values of detector half-length l^* and cell length l_c, without exceeding FOD=50/m.

Major variables held constant for this preliminary study have been:

- Ring circumference C ≈ 75 km (midway between CEPC and FCC-ee).

- Beam energy E_0=120 GeV.

- All lattices investigated are ``toy" lattices consisting of *just one intersection region*, inert straight-section opposite, and two dispersion-suppressed arcs.

- *Just two* sextupole families, tuned to cancel both horizontal and vertical chromaticities. Since there are no other nonlinear elements there are no sextupole strengths to be optimized.

- Any benefit from more sophisticated optics, such as more sextupole families or local chromaticity compensation, will necessarily increase the luminosity. Parameter scan policies include:

- When scanning input variables, hold β^*_y constant, but not necessarily small (to avoid lattice tune-up difficulties). β^*_y can be optimized later. This is opposite to the ``defined parameter" approach, which obstinately fixes β^*_y to a very small value, such as 1 mm, thought to be necessary to produce a specified luminosity.

- When scanning cell length l_c, the intersection region optics are held constant. The number of arc cells is adjusted to hold circumference C (more or less) constant.

- When scanning free length l^* the arcs are held constant, except for tweaking phase advance per cell to adjust β^*_y and sextupole strengths to cancel chromaticities.

One aspect of ground-up design is probing to find favorable and unfavorable dependencies. Inferences gleaned so far include:

- One may as well have *the game as the name*; high beta points in every arc cell can be exploited without doing more harm than one, or a few, points with the same high beta values; e.g. in local chromaticity-correction sectors.

- It is not necessary to ``match" the arc beta functions. Systematic $\beta_y$ ``beats" are found to be harmless. This is the only *radical* deviation from orthodoxy suggested in this paper.

- Also suggested, though not proved in general, is the observation, with best-so-far parameters, that β^*_y can be changed over a substantial range without much change in momentum acceptance.

3.1.2   **Six storage ring designs with varied cell length**

3.1.2.1   *Chromatic correction in the arcs.*

Non-interleaved sextupole, arc-only chromatic compensation has been based entirely on arcs consisting of repetition of enough identical five-cell sectors having the following fivecell pattern to make two arcs of the proper length**:**

```
fivecell:line=(

    .0   quadhf,sext1,bend,quadvf,

    .125 quadvf,    bend,quadhf,

    ------------------------------------

    .25  quadhf,    bend,quadvf,

    .375 quadvf,    bend,quadhf,

    ------------------------------------

    .50  quadhf,sext1,bend,quadvf,

    .625 quadvf,sext2,bend,quadhf,

    ------------------------------------

    .75  quadhf,    bend,quadvf,

    .875 quadvf,    bend,quadhf,

    ------------------------------------

    1.00 quadhf,    bend,quadvf,

    1.125 quadvf,sext2,bend,quadhf ) 1.25
```

The numbers listed in the margins are tune advances to that location, from the beginning of fivecell. All phase advances per cell are very close to $\pi/2$, but tweaked to control beta functions at the IP. There are just two sextupole families, with strengths sext1 and sext2. Phase advances between matched sextupoles are very close to π, as required to cancel on-momentum sextupole kicks.

Zooming of ring sectors for tuning the six ``toy lattices'' for this study has been possible using the following simple ring design.

```
    arc : line = ( dsin, 35*fivecell, dsout )
```

irtoarc : line = (dr01p,qir1p,dr12p,qir2p,dr23p,qir3p,

       qir1, dr12, qir2, dr23, qir3)

arctoir : line = (-irtoarc)

ring : line = (irtoarc, arc, farstraight, arc, arctoir)

The ``35'' entry in arc is appropriate for lattice CEPC4.0. The corresponding entries for other lattices are given in a later table. Here dsin and dsout are dispersion suppression, while other elements starting with ``d'', such as dr01p, dr12p etc. are drifts. Elements qir1p, qir2p, etc. are quadrupoles. To change cell-length (for this investigation) all arc element lengths (including dispersion suppression and far straight) are scaled proportionally, with all quads varying inversely (to hold phase advance per cell almost constant). Optically this resembles zooming a telephoto lens. But (also like the final stage of a zooming telephoto lens) the intersection region optics are held fixed.

3.1.2.2 *Scans leading to best performance (so far)*

My preliminary parameter scans have been organized as illustrated in

Figure 3, and described in the following list. Qualitative observations made during these runs are indicated by circled numbers.

- Scan I, is made ``easy to tune'' in spite of the low value β^*_y =2 mm, by the small free length l^*=0.8 m (circled 1). Even so, with lattice tune-up routines not yet developed, the tunes were not carefully controlled.

- Scan II becomes ``hard to tune'' for large l^*. To relieve this β^*_y is increased to 10 mm. (circled 2). A surprise during this scan was that momentum acceptance increased (or, at least, did not decrease) with increasing l^*.

- Scan III is to find best case so far; l_c=85 m, l^*=2.0 m. (circled 3). To make tuning easier β^*_y was increased to 10 mm.

- Scan IV is to adjust β^*_y (circled 4) surprisingly, momentum acceptance is nearly independent of β^*_y. But (obviously) FOD increases strongly above its maximum allowable value, as β^*_y is reduced towards 1 mm.
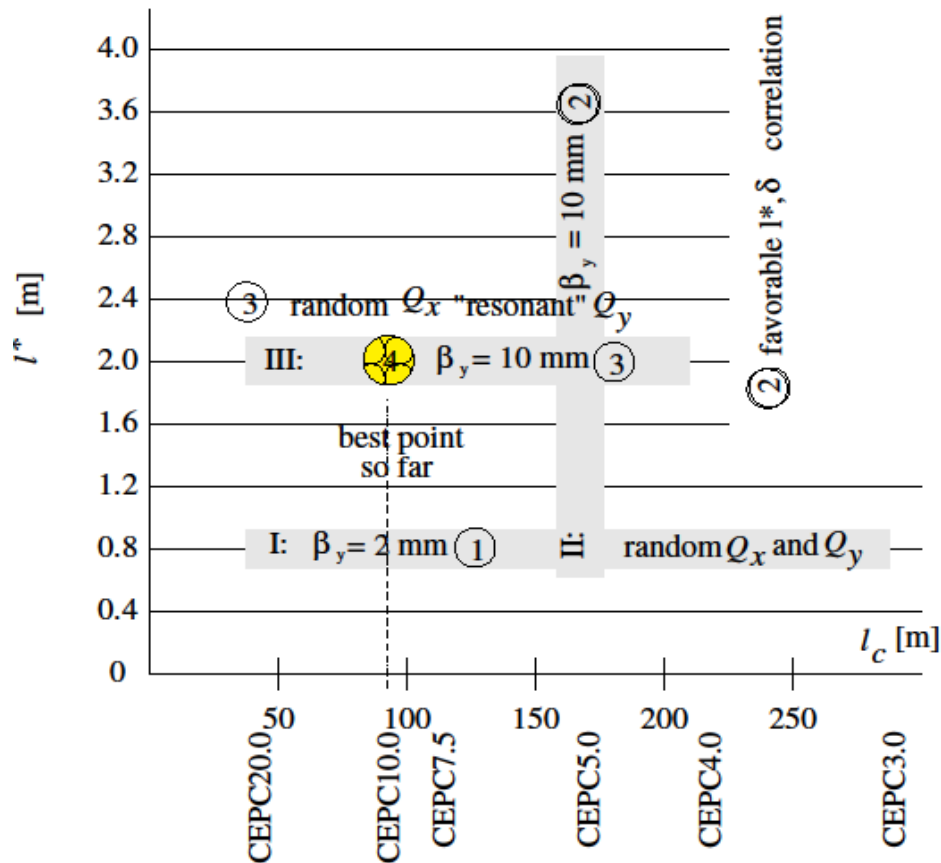
Figure 3. Parameter scans performed so far. Qualitative comment points mentioned in the text are tagged by circled numbers.

3.1.2.3 *Parameters of the six test lattices*

Parameters for lattices used in Scan I are given, above the double line, in Table 2. The shaded row represents nominal ``constant dispersion'' radiation-dominated extrapolation from LEP. Fixed Scan I parameters are β^*_y =2 mm, l^*=0.8 m. Parameters for Scan IV, varying β^*_y with l^*=2.0 m fixed, are given below the double line in Table 2.

In column 4, num5 is the total number of five-cell chromatic modules in each of the two main ring arcs; values of num5 were adjusted to keep the total ring circumference (more or less) constant for all lattices. Vertical β^*_y, ring and (nominally 90 degree) phase advance per cell, were held constant by tweaking the phase advance per cell, as the cell length was changed. Both integer and fractional parts of the Q_x and Q_y tunes were established in the process. *Ideally, for this study, the fractional parts would have been held fixed, but there was no fine tuning provision for this.*

In all cases the two sextupole currents, for the sext1 and sext2 families were adjusted for zero chromaticity in both planes.

Table 2. Parameters for Scan I and, below the double line, for scan IV. The shading in the CEPC5.0 row, in this and some subsequent tables, indicates that this row is the result of "nominal", constant dispersion, extrapolation from LEP.

Lattice name	circum	cell length	num5	l^*	Q_x	Q_y	β_x^*	β_y^*
unit	m	m		m			m	m
CEPC3.0	76061	281.7	26	0.8	69.14	68.51	0.489	0.0020
CEPC4.0	76131	211.3	35	0.8	92.08	91.52	0.333	0.0020
CEPC5.0	74483	169.0	43	0.8	112.54	111.02	0.208	0.0020
CEPC7.5	74540	112.7	65	0.8	169.06	166.02	0.137	0.0020
CEPC10.0	74568	84.5	87	0.8	223.83	227.02	0.172	0.0020
CEPC20.0	80949	42.3	190	0.8	494.10	496.03	0.046	0.0020
CEPC10.0 (best so far)	74618.6	84.5	87	2.0	223.841	221.504	0.961	0.010
CEPC10.0 (better?)	74618.6	84.5	87	2.0	223.848	226.501	0.958	0.0014

3.1.2.4 *Nonlinear ring optics*

Sextupole strength dependent parameters for Scan I, with β^*_y =2 mm are plotted in Figure 4.
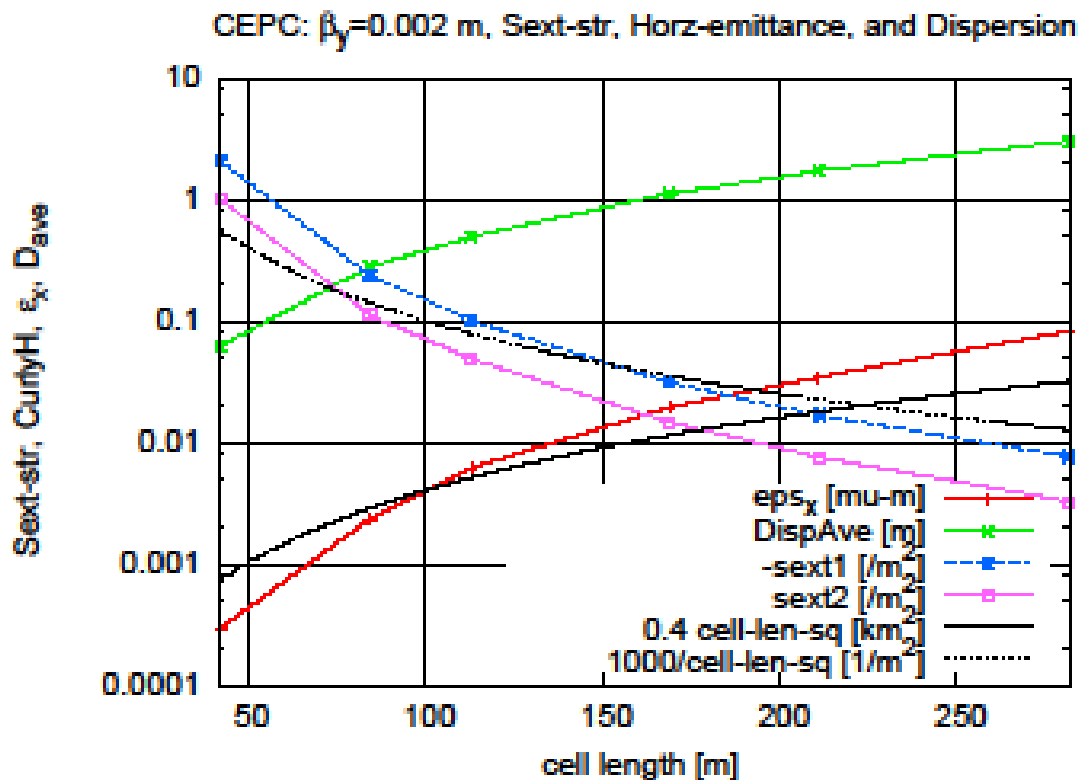
Figure 4. Parameter depemdencies imposed by chromatic correction for β^*_y =2 mm.

The ring vertical beta function could not be reduced below 0.004 m for 4**2** m cell length. Note that the achromatic sextupole strengths are independent of β^*_y. This means the chromaticity due to IR optics is relatively unimportant. This permits β^*_y to be made

``arbitrarily'' small, without much detuning the ring optics**.** (It can be observed that) sextupole strengths vary inversely with horizontal emittance. As a result the dynamic aperture tends to ``track'' the emittance. This dependence limits the ability to increase luminosity by decreasing the cell length---increasing the luminosity necessarily decreases the dynamic aperture.

3.1.3   Ring emittance and acceptance performance

Acceptance and emittance are directly commensurate. *Emittance must be less than acceptance for an injected beam to be stored without loss*. Raw acceptance plots (irrespective of beam emittances) for the six test lattices are shown in Figure 5.
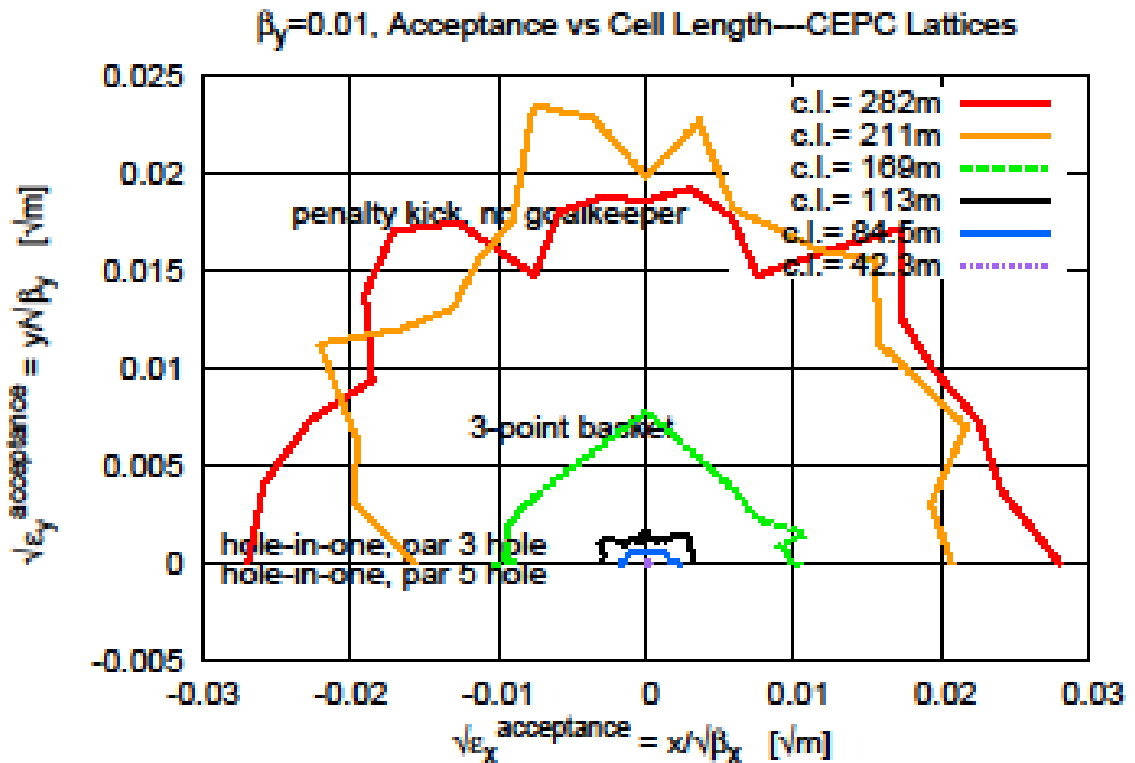
Figure 5. Raw acceptance plots (irrespective of beam emittances) for the six toy lattices. ``Cartoon'' annotations are mnemonics indicating the challenges of ``putting things'' in small containers.

The dynamic *x, y* product aperture is many orders of magnitude greater with 282 m cell length than 42 m cell length. For a large $\varepsilon^{\wedge}$(emittance) beam, for example for a muon collider, the cell length would be chosen as large as possible. This plot shows, however, and it is born out by tuning experience, that decreasing l_c causes the lattice to be harder to tune. This is reflected in the fine tuning penalty FOD increasing strongly as *l_c* is reduced. This is easily understandible in terms of lattice dispersion, which

scales as *l_c^2*. Since the sextupole strengths needed for chromatic correction scale inversely with dispersion, the dynamic aperture decreases strongly with decreasing *l_c*.

But radiation damping shrinks our electron beams to micron scale transverse size at the IP, mm scale elsewhere, allowing our acceptance to be much smaller. To account for this it is conventional to plot the acceptances in units of the equilibrium beam sigmas, which is done in Figure 6. (This is made risky, especially as regards vertical aperture, by the fact that the vertical emittance itself is the least reliably known beam parameter.)

It can be seen that large cell length is still strongly favored. But the values of σ_x and σ_y are different for the six test lattices. To maximize the luminosity we need to minimize σ_x and σ_y (by reducing the cell-length) consistent with maintaining

acceptably small fine tuning penalty FOD. Acceptances are plotted in units of beam sigmas for the six toy lattices in Figure 6.
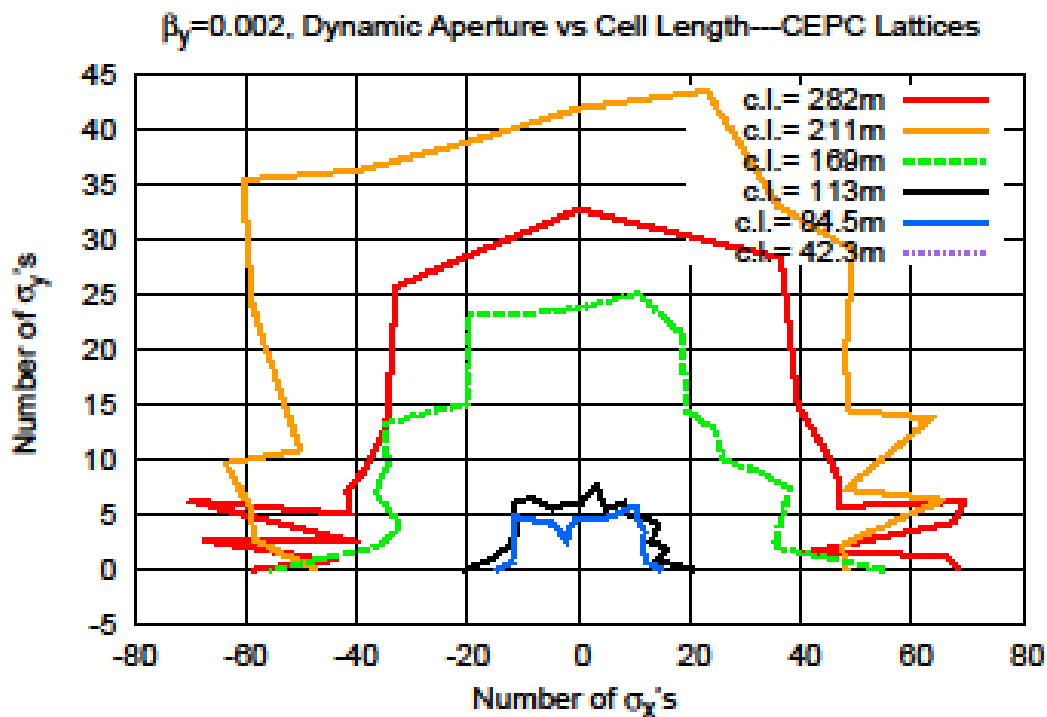
Figure 6. Acceptances plotted in units of beam sigmas for the six toy lattices.

Emittance and acceptance parameters for the six lattices are tabulated in Table 3. CEPC20.0 approximates the August 2015 CEPC design. (As indicated by the shaded row). CEPC5.0 approximates to constant dispersion scaling from LEP and the linear fit in Figure 1. The emittance ratio in these tables, ε_y/ε_x=0.068 is determined from the beam-beam saturated-tuneshift model. (Not by *ad hoc* assignment of a numerical value,

such as *m*=0.003, to a ``coupling coefficient'' which, in theory, scales as $1/\gamma$, and should be completely negligible.)

As explained previously (and in greater detail in my earlier CEPC white paper[1], for conservative transverse insensitivity, the fine tuning penalty FOD should be less than 50. Values of FOD for the six test lattices are evaluated in Table 4.

Table 3. Emittance and acceptance parameters for the six test lattices; above the double line for Scan I, below for Scan IV.

Lattice name	cell length	l^*	ϵ_x	$\epsilon_x^{accept.}$	ϵ_y	$\epsilon_y^{accept.}$
unit	m	m	nm	nm	nm	nm
CEPC3.0	281.7	0.8	82.3	3.4e+06	5.61	1.184E+07
CEPC4.0	211.3	0.8	34.8	1.7e+07	2.38	4.504E+07
CEPC5.0	169.0	0.8	19.4	1.088e+07	1.32	1.917E+07
CEPC7.5	112.7	0.8	9.27	1.52e+08	0.630	4.348E+06
CEPC10.0	84.5	0.8	2.33	6.19e+05	0.158	1.714E+06
CEPC20.0	42.3	0.8	0.293	1.3E+05	0.0199	9.82E+04
CEPC10.0 (best so far)	84.5	2.0	2.25		0.153	@β_y = 0.01 m
CEPC10.0 (better?)	84.5	2.0	2.26		0.154	@β_y = 0.0014 m

Table 4. Factors entering the fine tuning penalty function FOD for the six test lattices; above the double line for Scan I, below for Scan IV.

Lattice name	cell-length	l^*	β_x^{max}	β_y^{max}	$\langle D \rangle$	transverse FOD $\beta_y^{max}/(\langle D \rangle\, x\, c.l.)$
unit	m		m	m	m	1/m
CEPC3.0	281.7	0.8	500	3510	3.044	4.1
CEPC4.0	211.3	0.8	412	3080	1.703	8.6
CEPC5.0	169.0	0.8	420	3220	1.108	17.7
CEPC7.5	112.7	0.8	615	3005	0.488	33.8
CEPC10.0	84.5	0.8	190	3100	0.278	132
CEPC20.0	42.3	0.8	170	2780	0.0618	1060
CEPC10.0 (best so far)	84.5	2.0	310	1850	0.277	79 @β_y = 0.01 m
CEPC10.0 (better?)	84.5	2.0	312	9900	0.278	421 @β_y = 0.0014 m

3.1.3.1 *Scan I cell length optimization*

Scan I results are plotted in Figure 7. This plot is shown more as an example than as a definitive result. It shows how maximizing the luminosity while limiting FOD is supposed to work. Superficially the maximum luminosity is for the CEPC10.0 case. But the maximum fine tuning penalty is badly exceeded in this case. The nominal optimum is where the green dashed FOD curve crosses the black dotted FOD=50/m constant line.

Table 5. FOMs, FODs, luminosities and other parameters for the six test lattices, six test lattices; above the double line for Scan I, below for Scan IV.

Lattice name	cell-length	l^*	ϵ_x	ϵ_y	$\Delta\delta$	$\frac{\Delta\delta}{\sqrt{\epsilon_x \epsilon_y}}$ FOM/l^*	$\mathcal{L}$
unit	m	m	nm	nm		10^9	$10^{34}\,m^{-2}s^{-1}$
CEPC3.0	281.7	0.8	82.3	5.61	0.022	1.023E-3	
CEPC4.0	211.3	0.8	34.8	2.36	0.020	2.21E-3	
CEPC5.0	169.0	0.8	19.4	1.32	0.020	3.95E-3	
CEPC7.5	112.7	0.8	9.27	0.630	0.015	6.21E-3	
CEPC10.0	84.5	0.8	2.33	0.158	0.006	9.89E-3	
CEPC20.0	42.3	0.8	0.293	0.0199	0.0005	6.55E-3	
CEPC10.0 (best so far)	84.5	2.0	2.25	0.146	0.031	0.0540	1.5 @$\beta_y = 0.005$ m
CEPC10.0 (better?)	84.5	2.0	2.25	0.146	0.031	0.0540	2.5 @$\beta_y = 0.003$ m
CEPC10.0 (better?)	84.5	2.0	2.26	0.147	0.033	0.0572	4.9 @$\beta_y = 0.0015$ m
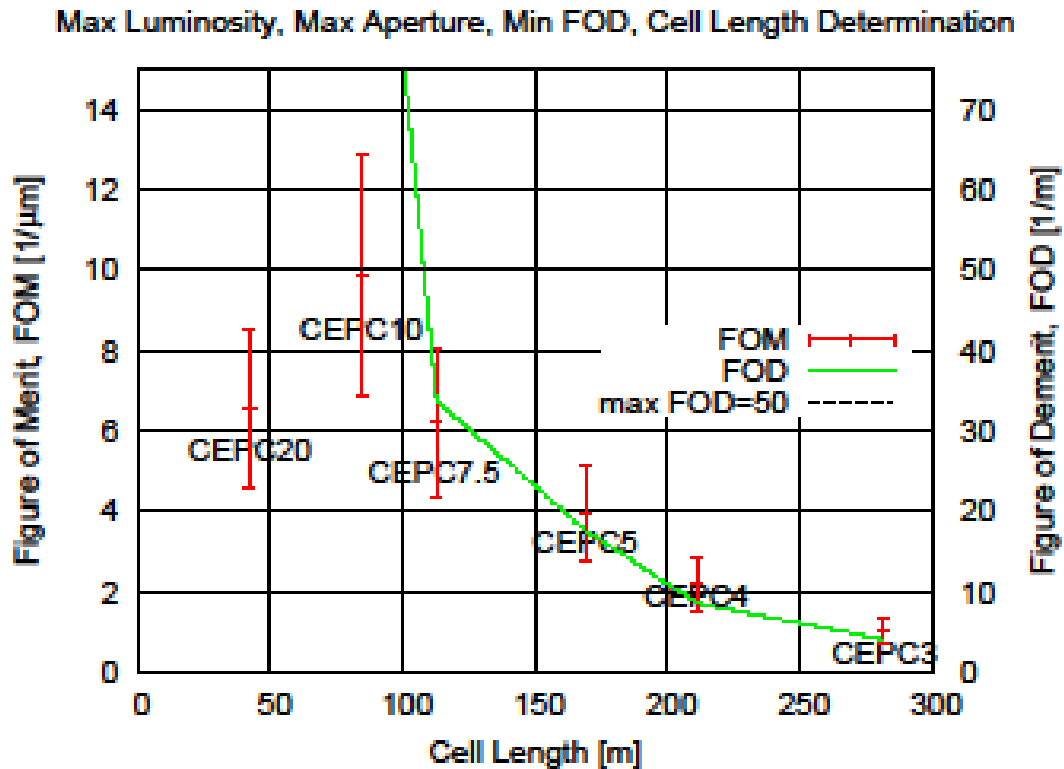
Figure 7. Plot of luminosity (data points) and fine tuning penalty function FOD (smooth dashed green curve) for Scan I. The maximum value of luminosity, consistent with keeping FOD below its limiting value is given by the point where the dashed green curve crosses the black dotted line.

3.1.3.2 *Scan IV dependence of momentum acceptance on β^*_y.*

Figure 8 shows, as expected, comfortably large acceptances for $\beta_y^* = 10$ mm. This is promising for ``top-off'' injection. More surprising is Figure 9, which shows

acceptances for the same lattice, but with β^*_y =2 mm. The jagged contours are indicative of nearby nonlinear resonances. But the range of momenta for which the aperture is acceptably large is as great as the β^*_y =10 mm range shown in the previous figure. This means one can reduce β^*_y almost arbitrarily without seriously harming the momentum acceptance. Of course $\beta_y{}^\wedge(max) \propto 1/\beta_y{}^*$, which ``blows''  the ``fine tuning penalty'' budget for small β^*_y.
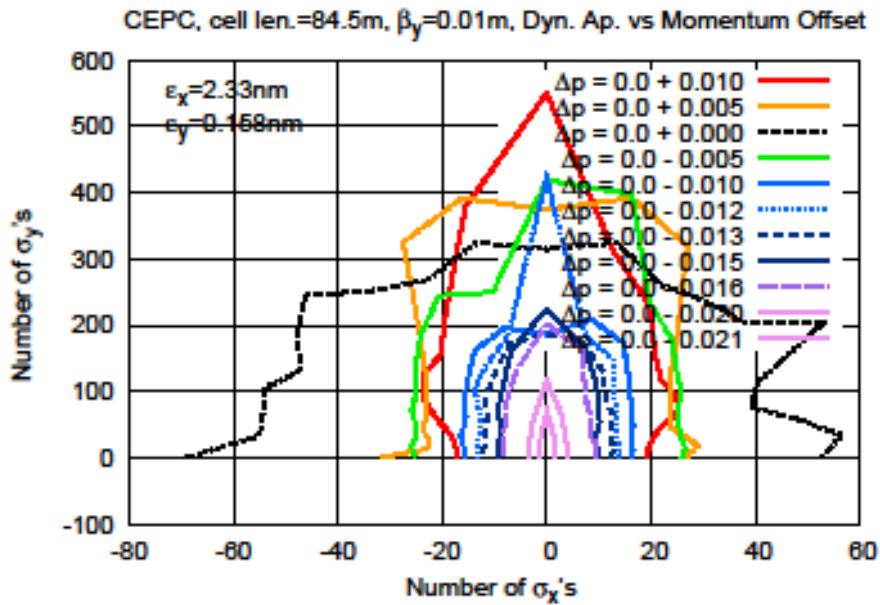
Figure 8. Dynamic aperture plots for lattice CEPC10.0 with β^*_y =10 mm for a range of beam momentum offsets.
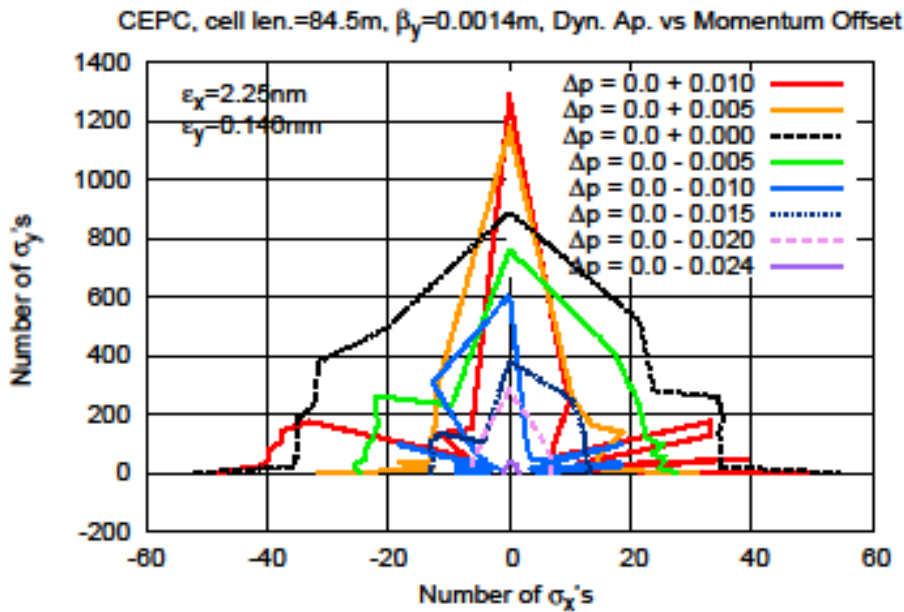
Figure 9. Dynamic aperture plots for lattice CEPC10.0 with β^*_y =2 mm for a range of beam momentum offsets. Though jagged, indicating nearby nonlinear resonances, the momentum acceptance is as good as in the previous β^*_y =10 mm case.

3.1.3.3 *Best so far lattice functions; l_c = 85 m, l*=2.0 m*

Lattice functions for the CEPC10.0 lattice with β^*_y=10 mm are shown in Figure 10.For increased luminosity β^*_y would need to be decreased from this value. But the FOD value is 1800/(85 x 0.278)=76 m which already exceeds the nominal 50/m maximum. If the FOD=50/m limit is too conservative, then the luminosity can be increased by reducing β^*_y.

The left column of graphs in Figure 10 show a short lattice section starting at the IP. The graphs on the right show the entire ring. The middle figure on the right indicates the beta function mismatch mentioned earlier. This mismatch has seemed to be harmless in tracking studies. This has been the basis for my phrase ``we may as well have the game as the name'', meaning that having large beta functions at locations in every cell is not essentially worse than having large beta functions at just a few locations (for example in a local chromatic correction section).

3.1.4 **Predicted CEPC10.0 Luminosities: Single Ring Optics**

Luminosity predictions for the CEPC10.0 lattice are shown in Table 6. The entries in this (and following) tables ignore the FOD fine tuning penalty by assuming that β^*_y can be reduced arbitrarily. As such they are appropriate for comparisons with

luminosity predictions that assume the FOM<50/m fine tuning penalty limit is too conservative (perhaps simply replacing this FOM by β_y(max)). Seemingly favorable choices (e.g. because the number of bunches is not too large) are indicated by shaded rows. Two beams in one ring is assumed. Also the possibility of bunch separation tricks, such as bunch trains with crossing angle, is not exploited. Pretzel beam separation requires the number of bunches N_b not to exceed half of the horizontal tune, which is 223/2=110 for CEPC10.0. For the Higgs energy (120 GeV) and above, this excludes entries with β^{*}_{y} <2 mm (at the top of the table). Since the fine tuning penalty function FOD limit is not respected for many entries in this table, some luminosities are overly optimistic.

Table 7 is a less busy table, showing only luminosities with the number of bunches required to not exceed 110. Where appropriate the luminosities are de-rated to account for the reduced number of bunches.

3.1.4.1 *Low energy luminosities*

Luminosity at energies below the Higgs energy are given in Table 8. Contrary to common lore, two-beams-in-one-ring operation at the Z_0 pole, can yield very large luminosity, such as L=4.3 x 10^{35}/cm^2/s.
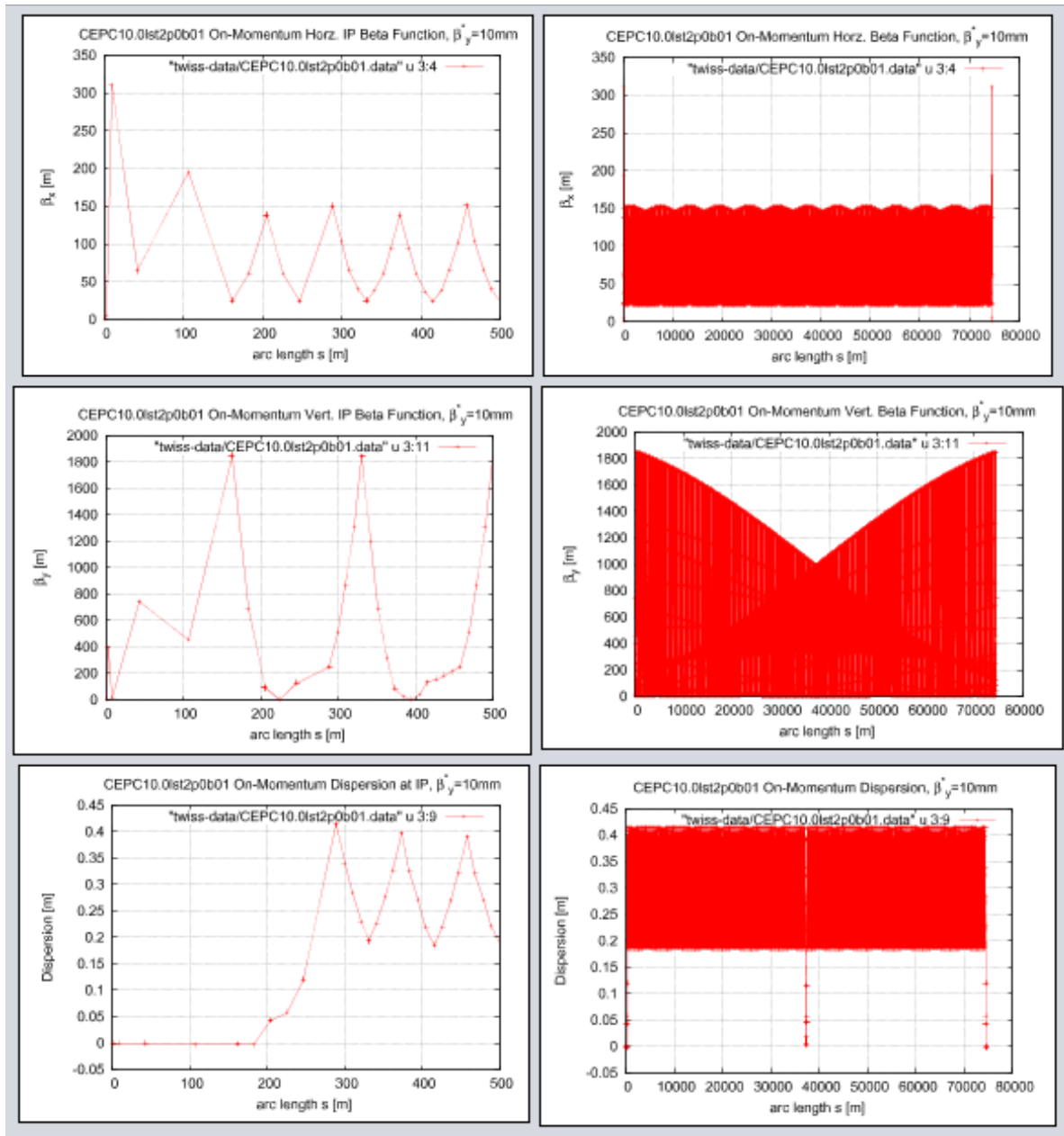
Figure 10. Lattice functions β_x, β_y, and dispersion D plots for the CEPC10.0 lattice. Short ranges starting at the IP are on the left, full ring plots are on the right. For these plots β^*_y =10 mm, which is undesirably large for maximizing luminosity, but comfortably small for limiting the fine tuning penalty function.

Table 6. Luminosity predictions for the CEPC10.0 lattice. Beam energy increases from row to row between the horizontal lines, between which the IP beta function β^*_y is held fixed. Ideally tuned, the entries in the three luminosity columns (corresponding to RF power (L^{RF}) beam-beam tune shift (L^{bb}), and beamstrahlung (L^{bs}_(trans) limits) would be equal. When unequal, the lowest of the three values has to be accepted as the actual luminosity.

E GeV	ϵ_x μm	β^*_y m	ϵ_y μm	ξ_{ml}	N_{tot}	σ_y μm	σ_z μm	$\mathcal{L}^{RF}$ 10^{34}	$\mathcal{L}^{bs}_{trans}$ 10^{34}	$\mathcal{L}^{bb}$ 10^{34}	N_b	β^*_z m	P_{RF} MW
120	2.40e-09	0.0015	1.09e-11	0.101	4.9e+13	0.128	28.12	4.9	6.94	4.903	333	0.33	50.0
150	1.02e-09	0.0015	4.63e-12	0.110	2.0e+13	0.0833	18.33	2.51	3.52	2.510	257	0.33	50.0
175	5.64e-10	0.0015	2.56e-12	0.115	1.1e+13	0.062	13.65	1.58	2.2	1.581	215	0.33	50.0
200	3.38e-10	0.0015	1.54e-12	0.120	6.4e+12	0.048	10.57	1.06	1.46	1.059	184	0.33	50.0
225	2.16e-10	0.0015	9.80e-13	0.129	4.0e+12	0.0383	8.43	0.744	1.02	0.744	160	0.33	50.0
120	5.96e-09	0.0020	2.71e-11	0.101	4.9e+13	0.233	51.20	3.68	4.94	3.677	134	0.44	50.0
150	2.53e-09	0.0020	1.15e-11	0.110	2.0e+13	0.152	33.40	1.88	2.5	1.883	103	0.44	50.0
175	1.41e-09	0.0020	6.39e-12	0.115	1.1e+13	0.113	24.87	1.19	1.56	1.186	86	0.44	50.0
200	8.43e-10	0.0020	3.83e-12	0.120	6.4e+12	0.0876	19.26	0.794	1.04	0.794	74	0.44	50.0
225	5.38e-10	0.0020	2.44e-12	0.129	4.0e+12	0.0699	15.38	0.558	0.726	0.558	64	0.44	50.0
120	2.16e-08	0.0030	9.80e-11	0.101	4.9e+13	0.542	119.28	2.45	3.06	2.451	37	0.66	50.0
150	9.18e-09	0.0030	4.17e-11	0.110	2.0e+13	0.354	77.86	1.26	1.55	1.255	29	0.66	50.0
175	5.10e-09	0.0030	2.32e-11	0.115	1.1e+13	0.264	58.00	0.79	0.966	0.790	24	0.66	50.0
200	3.06e-09	0.0030	1.39e-11	0.120	6.4e+12	0.204	44.94	0.529	0.642	0.529	20	0.66	50.0
225	1.95e-09	0.0030	8.88e-12	0.129	4.0e+12	0.163	35.90	0.372	0.447	0.372	18	0.66	50.0
120	1.09e-07	0.0050	4.97e-10	0.101	4.9e+13	1.58	346.79	1.47	1.67	1.471	7	1.1	50.0
150	4.67e-08	0.0050	2.12e-10	0.110	2.0e+13	1.03	226.57	0.753	0.841	0.753	6	1.1	50.0
175	2.59e-08	0.0050	1.18e-10	0.115	1.1e+13	0.768	168.88	0.474	0.524	0.474	5	1.1	50.0
200	1.56e-08	0.0050	7.09e-11	0.120	6.4e+12	0.595	130.96	0.318	0.348	0.318	4	1.1	50.0
225	9.96e-09	0.0050	4.53e-11	0.129	4.0e+12	0.476	104.65	0.223	0.242	0.223	3	1.1	50.0
120	9.97e-07	0.0100	4.53e-09	0.101	4.9e+13	6.73	1480.93	0.589	0.905	0.735	1	2.2	50.0
150	4.27e-07	0.0100	1.94e-09	0.110	2.0e+13	4.4	968.88	0.231	0.594	0.377	1	2.2	50.0
175	2.38e-07	0.0100	1.08e-09	0.115	1.1e+13	3.29	722.94	0.121	0.445	0.237	1	2.2	50.0
200	1.43e-07	0.0100	6.50e-10	0.120	6.4e+12	2.55	561.09	0.069	0.346	0.159	1	2.2	50.0
225	9.15e-08	0.0100	4.16e-10	0.129	4.0e+12	2.04	448.75	0.042	0.277	0.112	1	2.2	50.0

Table 7. Stripped down version of Table 6, with bunch number limit imposed.

E GeV	β^*_y m	ξ_{ml}	$\mathcal{L}^{bb}$ $10^{34} cm^{-2} s^{-1}$	N_b	P_{RF} MW
120	0.0015	0.1	1.62	110	50.0
150	0.0015	0.11	1.07	110	50.0
175	0.0015	0.12	0.81	110	50.0
200	0.0015	0.12	0.63	110	50.0
225	0.0015	0.13	0.51	110	50.0
120	0.0020	0.1	3.02	110	50.0
150	0.0020	0.11	1.88	103	50.0
175	0.0020	0.12	1.19	86	50.0
200	0.0020	0.12	0.79	74	50.0
225	0.0020	0.13	0.56	64	50.0
120	0.0030	0.1	2.45	37	50.0
150	0.0030	0.11	1.26	29	50.0
175	0.0030	0.12	0.79	24	50.0
200	0.0030	0.12	0.53	20	50.0
225	0.0030	0.13	0.37	18	50.0
120	0.0050	0.1	1.47	7	50.0
150	0.0050	0.11	0.75	6	50.0
175	0.0050	0.12	0.47	5	50.0
200	0.0050	0.12	0.32	4	50.0
225	0.0050	0.13	0.22	3	50.0
120	0.0100	0.1	0.74	1	50.0
150	0.0100	0.11	0.38	1	50.0
175	0.0100	0.12	0.24	1	50.0
200	0.0100	0.12	0.16	1	50.0
225	0.0100	0.13	0.11	1	50.0

Table 8. Luminosities at low energies.

E GeV	β_y^* m	ξ_{sat}	$\mathcal{L}^{bb}$ 10^{34}cm^{-2}s^{-1}	N_b	P_{RF} MW
48	0.0015	0.038	9.65	110	50.0
60	0.0015	0.05	5.79	110	50.0
80	0.0015	0.067	3.41	110	50.0
100	0.0015	0.084	2.26	110	50.0
120	0.0015	0.1	1.62	110	50.0
48	0.0020	0.038	17.93	110	50.0
60	0.0020	0.05	10.77	110	50.0
80	0.0020	0.067	6.35	110	50.0
100	0.0020	0.084	4.21	110	50.0
120	0.0020	0.1	3.02	110	50.0
48	0.0030	0.038	43.02	110	50.0
60	0.0030	0.05	19.61	83	50.0
80	0.0030	0.067	8.27	60	50.0
100	0.0030	0.084	4.24	46	50.0
120	0.0030	0.1	2.45	37	50.0
48	0.0050	0.038	26.98	23	50.0
60	0.0050	0.05	11.77	17	50.0
80	0.0050	0.067	4.96	12	50.0
100	0.0050	0.084	2.54	9	50.0
120	0.0050	0.1	1.47	7	50.0
48	0.0100	0.038	13.49	3	50.0
60	0.0100	0.05	5.88	2	50.0
80	0.0100	0.067	2.48	1	50.0
100	0.0100	0.084	1.27	1	50.0
120	0.0100	0.1	0.74	1	50.0

3.1.5 Recapitulation

3.1.5.1 *Qualifications*

- A ring with only one IR has been investigated (to make tuning easier). Luminosities per IP are likely to be about twenty percent smaller with two IP's. Also tuning will be more difficult with two IP's.

- Only zero length quadrupoles have been used. This is an issue only for l^*=0.8, which is too small for a practical detector in any case.

- A major uncertainty concerns the fine tuning penalty FOD figure of demerit. The FOD<50/m used in this study has been very conservative. If it were valid to simply use an 10,000 m upper limit on β_y^(max) as FOD (which is what existing CEPC and FCC-ee designs seem to assume) then luminosity approaching 10^{35}/cm^2/s would be predicted.

- The parameters in this study are not entirely self-consistent. The worst discrepancy is a factor of 3 difference between β^*_x used in calculating the luminosity and the value actually provided by the lattice optimization procedure.

- Though pretzel separation of the two beams in one ring has been assumed, the simulations have not, in fact, had pretzel orbits.

3.1.6 Conclusions

The original intent of this white paper was to develop a ``ground up'' design methodology. The mere testing of this methodology has led to significantly improved understanding and the following tentative conclusions:

- *Local chromaticity compensation is unnecessary.* Two families of non-interleaved sextupoles in the arcs are sufficient to correct both IR and arc chromaticity while keeping acceptably large momentum acceptance.

- With proper choice of vertical tune, momentum acceptances in excess of 3 percent are achievable.

- Optimal values of vertical tune Q_y are close to half integers. Improved momentum acceptance there seems to be due to the detuning of off-momentum particles of pulling $Q\_y(\delta)$ away from (rather than accross) the necessarily-nearby $|\cos(\mu\_y)|>1$ precipice, as δ deviates from zero with either sign.

- With no need for local chromaticity compensation there is no need for finite dispersion nor bends near the IP, vastly reducing synchrotron radiation incident on the detector.

- The optimal cell length so far is 82\,m.

3.1.7 References

1. R. Talman, *Scaling Behavior of Circular Colliders Dominated by Synchrotron Radiation*, International Journal of Modern Physics A, Vol. 30 (2015) 1544003 (91 pages) World Scientific Publishing Company.

2. V.I. Telnov, *Restriction on the energy and luminosity of e+e- storage rings due to beamstrahlung*, arXiv:1203.6563v1 [physics.acc-ph] 29 Mar 2012.

3.2 CEPC lattice design and Dynamic Aperture study

Yiwei Wang, Dou Wang, Yuan Zhang, Huiping Geng,

Sha Bai, Tianjian Bian, Feng Su, Jie Gao

Mail to: wangyw@ihep.ac.cn

Institute for High Energy Physics,

P.O. Box 918, Beijing 100049, China

3.2.1 Introduction

CEPC is a Circular Electron and Positron Collider proposed by China to mainly study the Higgs boson. In order to achieve factory luminosity, a strong focusing system and low emittance are required. A momentum acceptance as large as 2% is also required to get a reasonable beam lifetime. This is one of the key issues of the CEPC accelerator physics. In this paper, the optics design of the interaction and arc region and the optimization of dynamic aperture for the whole ring will be presented [1].

3.2.2 Single Ring Scheme

The parameters for single ring scheme of CEPC are shown in Tab.1.

3.2.2.1 *Interaction Region*

The CEPC interaction region (IR) was designed with modular sections [2–4] including the final transformer (FT), chromaticity correction for vertical plane (CCY), chromaticity correction for horizontal plane (CCX) and matching transformer (MT). To achieve a momentum acceptance as large as 2%, local correction of the large chromaticity from final doublet (FD) is necessary. Two pairs of sextupoles separated with -I transportation are used to make the 1st order chromaticity correction. The optics of the IR starting from the interaction point (IP) is shown in Fig.1.

To correct the tune shift due to finite length of main sextupoles, two pairs of weak sextupoles are installed next to the main ones [5]. The 1st order tune shift terms are shown in Fig.2.

To reduce the 2nd order chromaticity, the phases of sextupoles are carefully tuned. To reduce the 3rd order chromaticity, only 2 quadrupoles are used in the final transformer [6,7] and one additional sextupole are installed at 1st image point [16]. Chromatic functions for the IR are shown in Fig.3. The change of the vertical tune is small than 0.03 when energy deviation dp/p=±2%. The horizontal plane can be optimized further with more additional sextupoles.

Table 1: Main parameters of CEPC single ring scheme [2]

Parameters	Unit	Value
Beam energy [E]	GeV	120
Circumference [C]	m	5,4374
Luminosity [L]	cm^{-2}s^{-1}	2.04×10^{34}
SR power/beam [P]	MW	51.7
Bending radius [ρ]	m	6094
Number of IP [N$_{IP}$]		2
Bunch number [n$_B$]		50
filling factor [κ]		0.7
Revolution period [T$_0$]	s	1.83×10^{-4}
momentum compaction factor [α_p]		3.36×10^{-5}
Energy acceptance Ring [h]		±0.02
lifetime due to radiative Bhabha scattering [τ_L]	min	50.61
Beam current [I]	mA	16.6
Bunch population [N$_e$]		3.79E+11
emittance-horizontal [$\varepsilon_x, \varepsilon_y$]	m· rad	6.12E-9, 1.84E-11
coupling factor [k]		0.003
Beam length SR [$\sigma_{s.SR}$]	mm	2.14
Beam length total [$\sigma_{s.tot}$]	mm	2.65
Betatron function at IP [β_x, β_y]	m	0.8, 0.0012
Transverse size [σ_x, σ_y]	μm	69.97, 0.15
Beam-beam parameter [ξ_x, ξ_y]		0.118, 0.083
Hourglass factor [Fh]		0.68
Lifetime due to Beamstrahlung-Telnov [τ_{BS}]	min	1005
Lifetime due to Beamstrahlung [simulation]	min	47
RF voltage [V$_{rf}$]	GV	6.87
RF frequency [f$_{rf}$]	GHz	0.65
Harmonic number [h]		118800

Synchrotron oscillation tune [ν_s]		0.18
Energy acceptance RF [h]	%	5.99
SR loss/turn [U_0]	GeV	3.11
Energy spread SR [$\sigma_{\delta.SR}$]	%	0.13
Energy spread BS [$\sigma_{\delta.BS}$]	%	0.09
Energy spread total [$\sigma_{\delta.tot}$]	%	0.16
Average number of photons emitted per electron during the collision [n_γ]		0.22
Transverse and Longitudinal damping time [n_x]	turns	78, 39
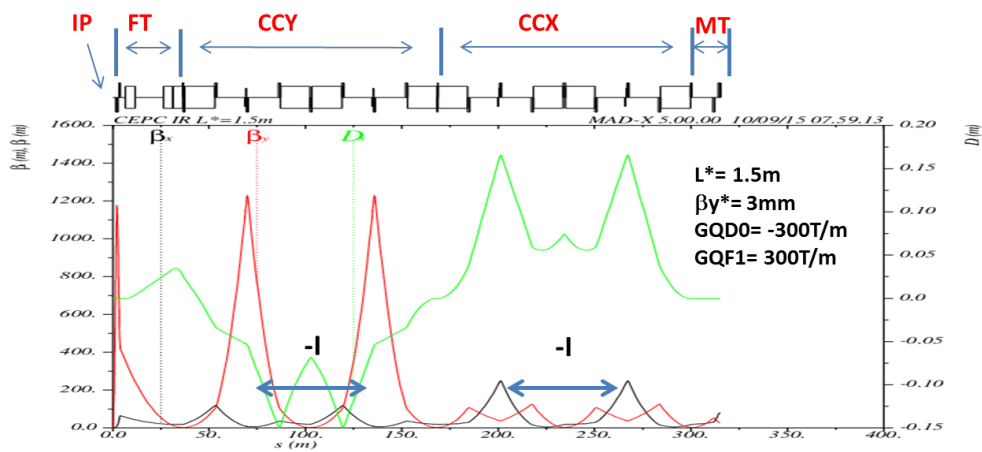
Figure 1: Optics of the interaction region (one side).
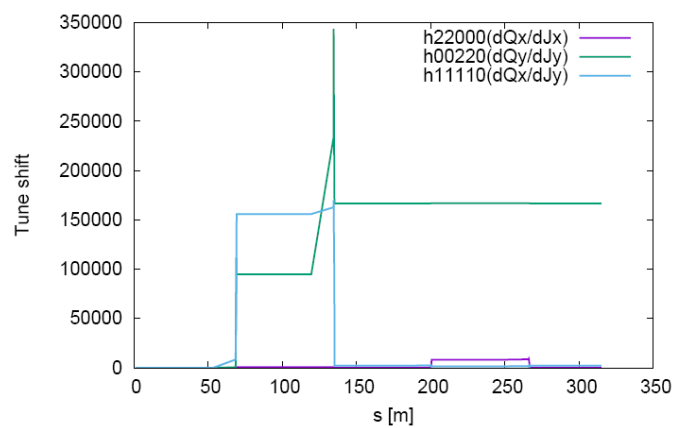
Figure 2: Tune shift correction in IR.
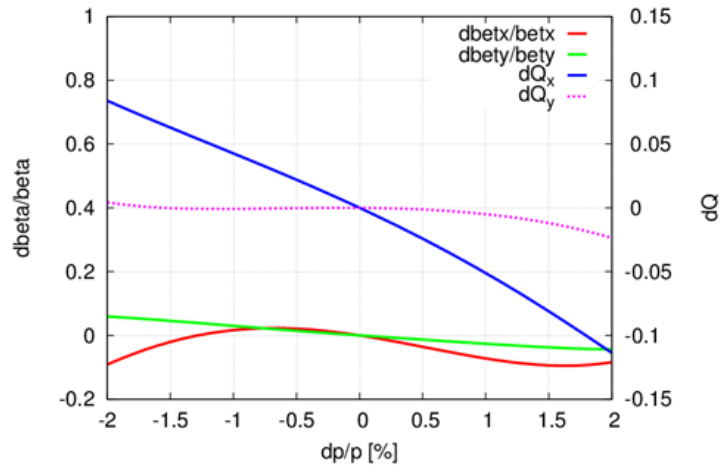
Figure 3: Chromatic functions at IP with the IR only (one side).

3.2.2.2   *Arc Region*

For the Arc region, the FODO cell structure is chosen to provide a large filling factor. The 60/60 degrees phase advances is selected due to its property of resonance cancellation [8, 9]. The 3rd and 4th order resonance driving terms (RDT) due to sextupoles in 24 cells is computed with Bengtsson's formular [11]. With only two families of sextupoles, all the 3rd and 4th order RDT except $2Q_x - 2Q_y$ are cancelled out within one betatron unit, i.e. 6 cells. However, as Yunhai Cai pointed out that the tune shift accumulate along the arc cells and reach a very large number with the ring [8], see Fig.6. The negative tune shift make the tune of CEPC (0.08/0.22) go to the integer resonance line thus limit the on-momentum dynamic aperture (Fig. 4 and 5).
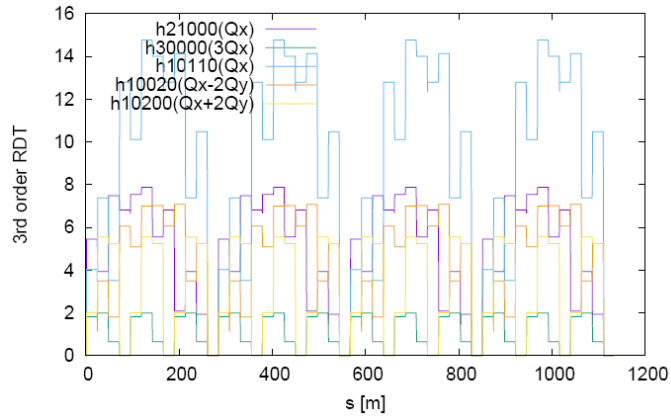
Figure 4: 3rd order resonance driving terms due to sextupoles in ARC (24cells).
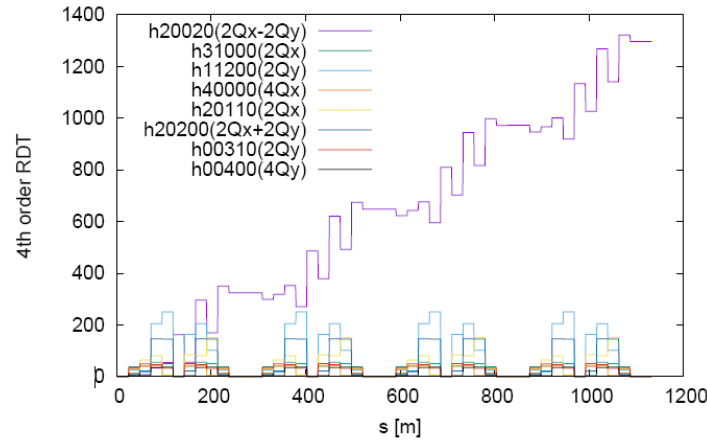
Figure 5: 4rd order resonance driving terms due to sextupoles in ARC (24cells).
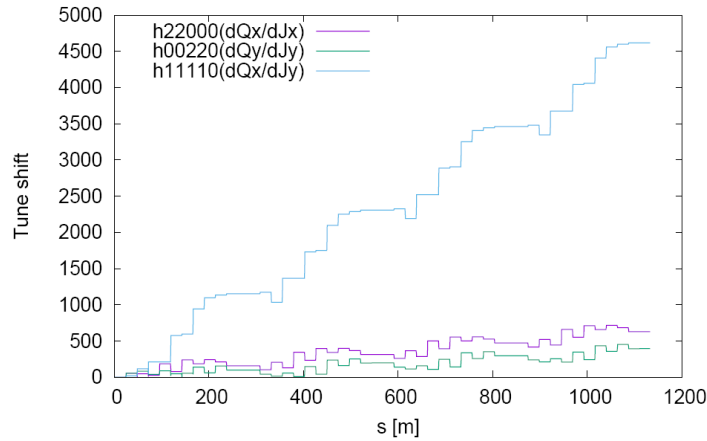
Figure 6: Tune shift due to sextupoles in ARC (24cells).

3.2.2.3 *Dynamic Aperture*

Optimize DA with Additional Sextupoles in IR

In the previous CEPC IR lattice, many attempts have been tried to increase the dynamic aperture for off-momentum particles. With two pairs of main sextupoles separated by -I transportation, 2 pairs of weak sextupoles and one additional sextupole, the dynamic aperture of $3\sigma x \times 20\sigma y$ are achieved for dp/p=$\pm$2%, see Fig. 7. However, it's still not enough to keep a reasonable beam lifetime and luminosity which require 20σ for on momentum particles and 5σ for off momentum particles [10]. This section will show the further optimization of the DA for large off-momentum particles.

The previous DA result shown that DA drops quickly with momentum deviation even just $\pm$0.5%. This is because of the breakdown of -I transportation. To correct this effect, a simple way is to correct the tiny chromaticity within the –I transportation. Thus we respectively put three sextupoles for the vertical and horizontal chromaticity correction section, i.e. the position (3,4,5) and (8,9,10). And three more sextupoles (2,6,7) help to correct the second order dispersion and so on. The positions of additional

sextupoles are shown in Fig. 8. 1 denotes the sextupole we have added in previous IR lattice.
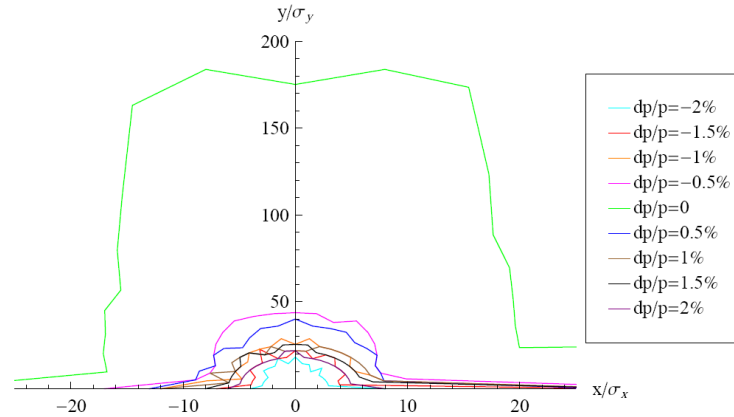
Figure 7: Dynamic aperture.
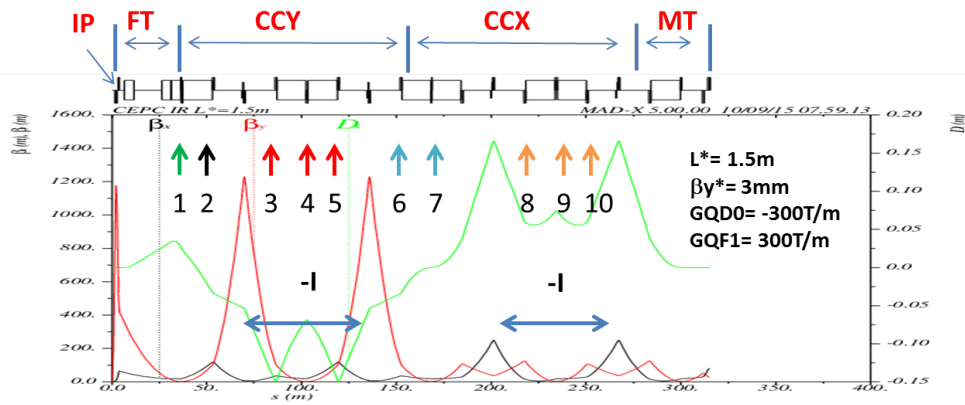
Figure 8: Optics of the interaction region with Brinkmann sextupoles.

It's difficult to correct a high order aberration while not increase other aberration. Similar to final focus of linear collider, we optimize the momentum acceptance directly in the following way [12]: In the plane of "DA vs. DP/P", the area of dynamic aperture with $|dP/P| \leqslant 2\%$ was got by tracking. A small coupling factor of 0.1% used to mainly optimize the horizontal DA. To avoid DA cut-in shape with small step of momentum deviation, as large as 19 points within $|dP/P| \leqslant 2\%$ were used. Four cases of initial phases, i.e. $(0,0)$, $(\pi/2,\pi/2)$, $(0,\pi/2)$, $(\pi/2,0)$ are considered. We maximize the area of four cases with Downhill Simplex algorithm [12]. The tracking was done with 100 turns which corresponding to around one damping time.
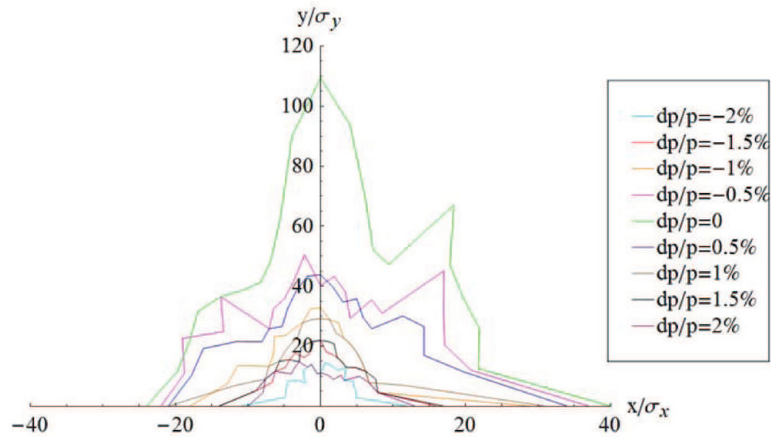
Figure 9: Dynamic aperture with Brinkmann sextupoles.

Fig. 9 shows the optimized dynamic aperture with Brinkmann sextupoles including synchrotron motion but without radiation damping and errors. The horizontal DA no longer drops quickly with momentum deviation. With dP/P = ±0.5%, the DA is still the same with on-momentum one, i.e. 20σx. The horizontal DA for dP/P = ±2% are significantly increased to around 6.5σx though the vertical one decreased to 10σy. This result has met the DA requirement we mentioned. Though thin sextuples are used in this study, there will be no significant finite length effect due to the weak sextupole strength.

Optimize DA with large families of sextupoles in ARC

We also optimized DA with large families of sextupoles in ARC by applying the differential evolution algorithm [13].

The x-z aperture of the original lattice is shown in Fig. 10, where the coupling is 0.3 %. There are only one family for SF/SD in the arc of the original lattice. Since the arc cell consists of 60/60 degree FODO lattice, we set the sextupole interleaved 180 degree one pair and there are totally 240 sextupole pairs used in the optimization. The objectives are listed in the following:

1. The tune Qx is in the range of [0.05, 0.31] and Qy in [0.10,0.31] for $\delta \in$ [-0.02, 0.02].

2. X-Z aperture objective is defined as an ellipse $\frac{x^2}{20^2} + \frac{z^2}{16^2} = 1$, where x is the transverse amplitude in unit of RMS size with 0.3% coupling, and z is unit of RMS energy spread.

3. X-Y-Z aperture objective is defined as an elliptical ball $\frac{x^2}{20^2} + \frac{y^2}{50^2} + \frac{z^2}{16^2} = 1$.

The optimized solution seems enlarge the dynamic aperture significantly, as shown in Fig. 11.
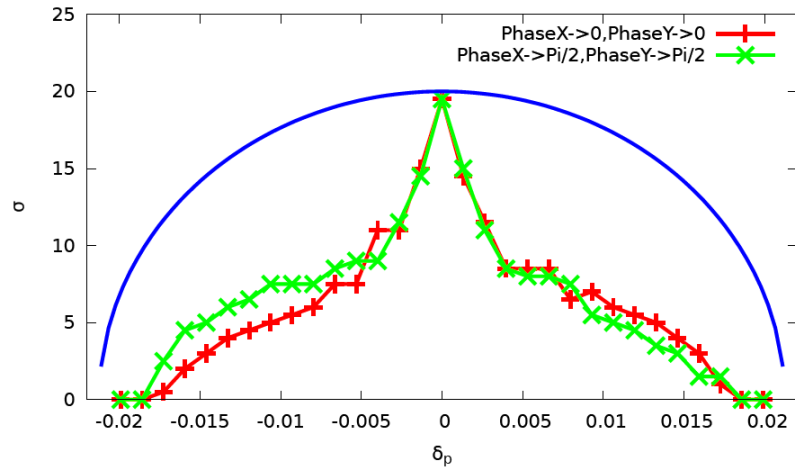
Figure 10: Dynamic aperture of CEPC before optimization.
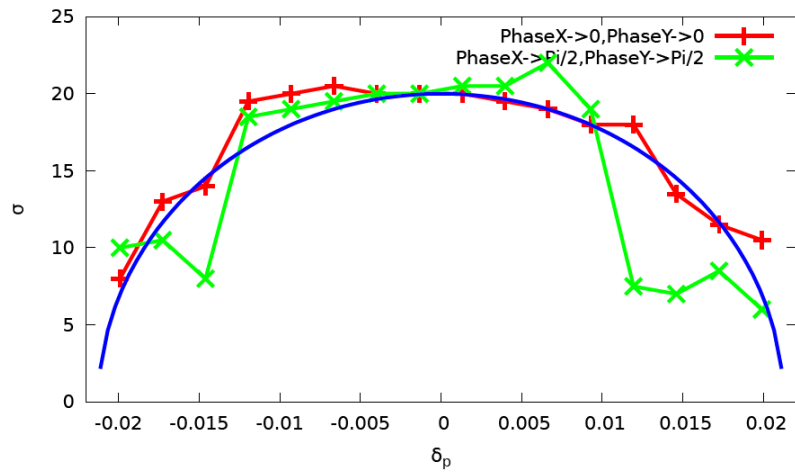
Figure 11: Dynamic aperture of CEPC after optimization.

Since there exist strong synchrotron radiation in the higgs factory, the radiation effect on DA should be also studied. The tracking shows that the damping really helps especially for large momentum offset particle, but the quantum fluctuation may reduce the DA for small momentum offset particle.

3.2.3 Partial Double Ring Scheme

In Pre-CDR, CEPC is a single ring machine [2]. All 50 bunches are equally spaced, and the collisions are head-on. This design requires a pretzel orbit in order to avoid parasitic collisions in the arcs. From the experience of LEP and CESR, the pretzel orbit is difficult to operate and control, and is also difficult for injection. After Pre-CDR, we developed a new idea called partial double ring scheme showed in Fig.12. Therefore, a pretzel orbit is not needed. With partial double ring scheme, we can consider crab waist

on CEPC. The most important advantage of crab waist is that the beam-beam limit can be increased greatly, see Tab. 2.

The lattice design and dynamic aperture optimization for partial double ring scheme is undergoing.
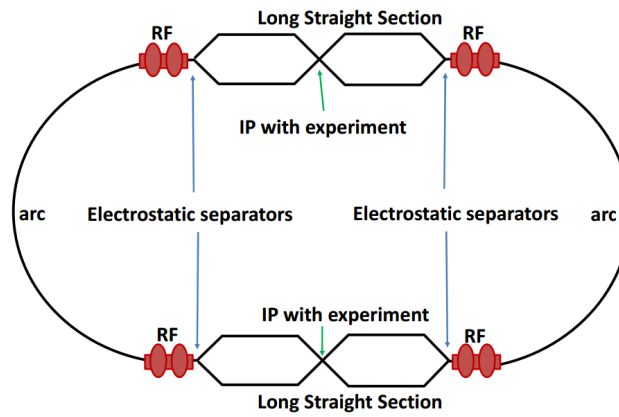
Figure 12: Dynamic aperture of CEPC after optimization [14].

Table 2: Main parameters of CEPC partial double ring scheme [15]

	Pre-CDR	H-high lumi.	H-low power	W	Z
Number of IPs	2	2	2	2	2
Energy (GeV)	120	120	120	80	45.5
Circumference (km)	54	54	54	54	54
SR loss/turn (GeV)	3.1	2.96	2.96	0.59	0.062
Half crossing angle (mrad)	0	15	15	15	15
Piwinski angle Φ	0	2.5	2.6	5	7.6
N_e/bunch (10^{11})	3.79	2.85	2.67	0.74	0.46
Bunch number	50	67	44	400	1100
Beam current (mA)	16.6	16.9	10.5	26.2	45.4
SR power /beam (MW)	51.7	50	31.2	15.6	2.8
Bending radius (km)	6.1	6.2	6.2	6.1	6.1
Momentum compaction (10^{-5})	3.4	2.5	2.2	2.4	3.5
β_{IP} x/y (m)	0.8/0.0012	0.25/0.00136	0.268 /0.00124	0.1/0.001	0.1/0.001
Emittance x/y (nm)	6.12/0.018	2.45/0.0074	2.06 /0.0062	1.02/0.003	0.62/0.0028
Transverse σ_{IP} (um)	69.97/0.15	24.8/0.1	23.5/0.088	10.1/0.056	7.9/0.053
ξx/IP	0.118	0.03	0.032	0.008	0.006
ξy/IP	0.083	0.11	0.11	0.074	0.073
V_{RF} (GV)	6.87	3.62	3.53	0.81	0.12
f_{RF} (MHz)	650	650	650	650	650
Nature σ_z (mm)	2.14	3.1	3.0	3.25	3.9
Total σ_z (mm)	2.65	4.1	4.0	3.35	4.0
HOM power/cavity (kw)	3.6	2.2	1.3	0.99	0.99
Energy spread (%)	0.13	0.13	0.13	0.09	0.05
Energy acceptance (%)	2	2	2		
Energy acceptance by RF (%)	6	2.2	2.1	1.7	1.1
n_γ	0.23	0.47	0.47	0.3	0.24
Life time due to beamstrah-lung_cal (minute)	47	36	32		
F (hour glass)	0.68	0.82	0.81	0.92	0.95
L_{max}/IP (10^{34}cm^{-2}s^{-1})	2.04	2.96	2.01	3.09	3.09

3.2.4 Acknowledgement

3.2.5 References

1. Y. Wang, Y. Zhang, S. Bai, et. al. , "Dynamic aperture study of the cepc main ring with interaction region", THPOR012, Proceedings of IPAC2016, Busan, Korea, May 2016.

2. The CEPC-SPPC Study Group, "CEPC-SPPC preliminary conceptual design report: volume II-accelerator", IHEP, Beijing, China, Rep. IHEP-AC-2015-01, Mar. 2015.

3. Y. Wang et al., in Proc. IPAC'15, pp. 2019-2021.

4. Y. Wang et al., "Optimization of the chromaticity correction section for CEPC FFS", IHEP, Beijing, China, Rep. IHEPAC-LC-Note2015-003, 2015.

5. A. Bogomyagkov et al., "Nonlinear properties of the FCC/TLEP final focus with respect to L*", Seminar at CERN, Mar. 2014.

6. K. Oide, "Final focus system for TLC", SLAC, USA, Rep. SLAC-PUB-4806, Nov. 1986.

7. Y. Cai, private communication, Apr. 2014.

8. Y. Cai, "Charged particle optics in circular Higgs factory", SLAC, USA, Rep. SLAC-PUB-16232, 2015.

9. K. L. Brown, "First and second order charged particle optics", SLAC, USA, Rep. SLAC-PUB-3381, Jul. 1984.

10. Y. Wang et. al., "Dynamic aperture optimization of CEPC with additional sextupoles in the interaction region", IHEP, Beijing, China, Rep. IHEP-AC-LC-Note2015-015, Dec. 2015.

11. J. Bengtsson, "The sextupole scheme for the Swiss light source (SLS): An analytic approach", PSI, Switzerland, Rep. SLS-Note-9-97, Mar. 1997.

12. K. Oide, private communication, Sep. 2015.

13. Y. Zhang, D. Zhou, "Application of differential evolution algorithm in future collider optimization", TUOBA03, Proceedings of IPAC2016, Busan, Korea, May 2016.

14. M. Koratzinos, "Mitigating performance limitations of single beam-pipe circular e + e − c colliders", TUPTY058, Proceedings of IPAC2015, Richmond, VA, USA, May 2015.

15. D. Wang, J. Gao, F. Su, M. Xiao, et al, "Parameter choice and partial double ring design", THPOR010, Proceedings of IPAC2016, Busan, Korea, May 2016.

16. R. Brinkmann, "Optimization of a final focus system for large momentum bandwidth", DESY, Germany, Rep. DESY-M-90-14, 1990.

3.3 Review of final focus designs for crab waist colliders

Anton Bogomyagkov, Eugene Levichev

Mail to: A.V.Bogomyagkov@inp.nsk.su

Budker Institute of Nuclear Physics (BINP),

Prospect Lavrentieva 11, Novosibirsk 630090, Russia

3.3.1 Introduction

Invention of the crab waist collision scheme promises increase of luminosity by several orders of magnitude for specially designed collider with respect to conventional. Successful test of the scheme at existent Italian lepton collider DAФNE increased luminosity three times from 1.5×10^{32} cm^{-2}s^{-1} to 4.5×10^{32} cm^{-2}s^{-1} and proved the principle of crab waist. The moderate luminosity gain is due to limited possibility to implement all the necessary modifications. Hence, the projects of the new circular colliders exploit the crab waist interaction scheme. This review describes designs of interaction regions for already existent collider DAФNE and SuperKEKB, for new projects of SuperB in Italy, CTau in Novosibirsk and FCC-ee in CERN. Designers of the new projects (FCC-ee, CEPC in China) continuously improve them; therefore, we describe only known to us present situation.

3.3.2 Crab waist collision scheme

P. Raimondi proposed crab waist collision scheme in 2006 [1]. Three founding steps are at the heart of crab waist collision scheme [2]. In order to understand these steps, we need expressions for luminosity L, horizontal ξ_x and vertical ξ_y tune shifts [3, 4]:

$$L \propto \frac{N\xi_y}{\beta_y^*} \,, \ \xi_y \propto \frac{N\beta_y^*}{\sigma_x^*\sigma_y^*\sqrt{1+\varphi^2}} \,, \ \xi_x \propto \frac{N}{\varepsilon_x\left(1+\varphi^2\right)}, \qquad (1)$$

where N is bunch population, β_y^* is vertical beta function at the interaction point (IP), σ_x^*, σ_y^* and σ_z are horizontal, vertical and longitudinal beam sizes respectfully, using θ as a full crossing angle, Piwinski [5] angle is

$$\varphi = \frac{\sigma_z}{\sigma_x^*}\tan\left(\frac{\theta}{2}\right). \qquad (2)$$

The first step is large Piwinski angle, which requires long bunches, small horizontal emittance, and a large crossing angle. This step reduces vertical tune shift and the size of interaction area (yellow on Figure 1). Therefore, one desiring to keep vertical tune shift unchanged increases bunch population and gains in luminosity. The

second step is reduction of the vertical beta function to half-length of the interaction region but not the bunch length. This again makes vertical tune shift smaller and luminosity larger. The third is introduction of the crab sextupoles at the proper phase advances from IP: $\Delta\mu_x = \pi \cdot m, \ \Delta\mu_y = \pi / 2 \cdot (2n+1)$. The sextupoles rotate position of the vertical beta function waist along the axis of the opposite beam (Figure 2), and suppress betatron and synchrobetatron resonances [6, 7, 8, 9].
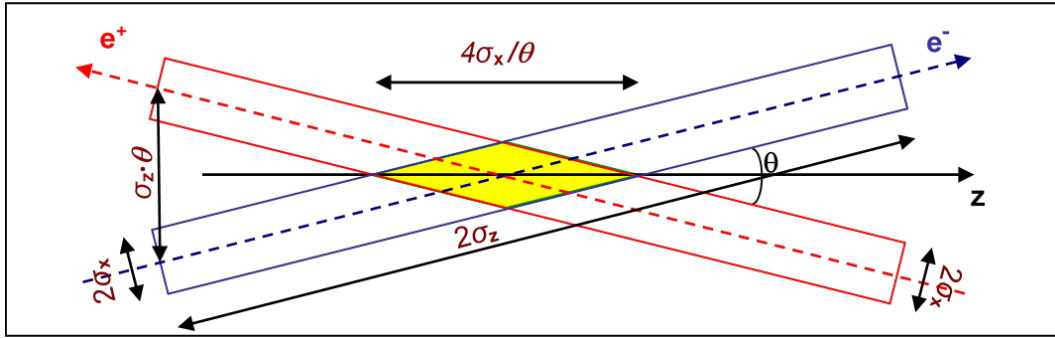
Figure 1: Layout of the crossing angle collision.
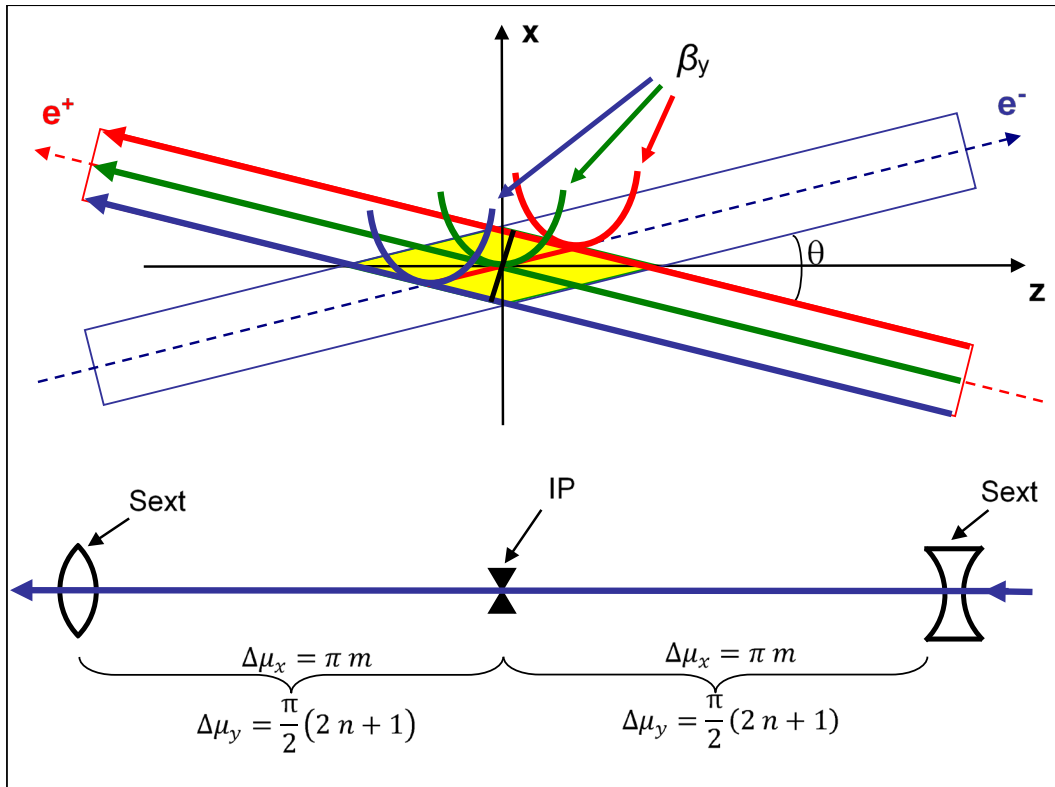
Figure 2: Crab waist collision scheme.

The integrated strength of the crab sextupoles at the place with vertical β_y and horizontal β_x beta functions is

$$K2L = \pm \frac{1}{\theta \cdot \beta_y^* \cdot \beta_y} \sqrt{\frac{\beta_x^*}{\beta_x}} \; . \tag{3}$$

The crab sextupoles cancel each other's second order geometrical aberrations because of proper phase advances and appropriate sign of the field gradient promising no dynamic aperture degradation.

The requirements of the crab waist are

1. crossing angle,

2. bunch length, horizontal size and crossing angle should provide large Piwinski angle,

3. vertical beta function comparable with the size of the interaction area,

4. sextupoles with proper strength and phase advance from IP.

The actual exploitation of the crab waist scheme in accelerator could produce some difficulties:

1. small vertical beta function and desire to minimize beta functions in final quadrupoles, despite the crossing angle, might require double aperture quadrupoles with high gradient;

2. strong final quadrupoles with large beta function are the source of large chromaticity, and need local chromaticity correction sections;

3. chromaticity correction sections and final focus quadrupoles will produce large nonlinear chromaticity limiting energy acceptance of the ring;

4. small horizontal emittance increases chromaticity of the whole ring, and raises the strength of the sextupoles correcting it, and as a result abates dynamic aperture;

5. crab sextupoles require special phase advances from IP and beta functions to reduce the strength of sextupoles, which could be difficult or impossible in the upgrade of already operating collider;

6. interference between crab sextupoles and, if present, chromaticity correction sections might limit dynamic aperture.

3.3.3 **Nonlinear detuning**

For comparison of different interaction regions, we will introduce chromaticity produced by final defocusing quadrupoles (from both sides of IP, and final quadrupole could consist of several quadrupoles)

$$\mu'_y = \frac{1}{2}\sum_i K1L_i \cdot \beta_{i,y} \,, \tag{4}$$

where $K1L_i$ is integrated strength of i-th quadrupole, $\beta_{i,y}$ is vertical beta function in the centre of the i-th quadrupole.

Detuning coefficient of the vertical plane (α_{yy}) with respect to action J_y

$$\Delta v_y = \alpha_{yy}J_y + \alpha_{xx}J_x \tag{5}$$

is the simplest characteristic describing nonlinear properties of the lattice [10, 11]. It is not the accurate attribute: even if detuning (5) is small higher orders might reduce dynamic aperture. We will consider third order nonlinearities; therefore, the first order detuning allows comparison of different lattices. Since nonlinear effects are much stronger in vertical plane, we will omit estimations of the horizontal detuning. Assuming that FF quadrupole changes sign of Twiss functions α_y we derive the quadrupole integrated strength K1L [m^{-1}]

$$K1L \cdot L_q = -\frac{2}{L^* + L_q/2}, \tag{6}$$

where L_q is quadrupole length, L^* is the distance from IP to the face of the quadrupole.

Now we estimate chromaticity as

$$\mu'_y = -\frac{L^* + L_q/2}{\beta_y^*} \,. \tag{7}$$

From the Hamiltonian of the kinematic term

$$H = \frac{\left(P_x^2 + P_y^2\right)^2}{8}, \tag{8}$$

we decipher detuning coefficient for the drift between the FF quadrupoles

$$\alpha_{yy}^k = \frac{3}{16\pi}\int\frac{\left(1+\alpha_y^2\right)}{\beta_y^2}ds \approx \frac{3}{16\pi}\frac{L^* + L_q/2}{\beta_y^{*2}} \,. \tag{9}$$

Hamiltonian of the fringe field of FF quadrupole is

$$H = K1'\frac{\left(P_x x y^2 - P_y x^2 y\right)}{4} - K1''\frac{\left(x^4 - y^4\right)}{48}, \tag{10}$$

and we obtain

$$\alpha_{yy}^f = \frac{1}{32\pi}\int K1'' \beta_y^2 ds \approx -\frac{1}{4\pi}\frac{K1 L^{*3}}{\beta_y^{*2}} \approx \frac{1}{2\pi}\frac{L^{*3}}{L_q\left(L^* + L_q/2\right)\beta_y^{*2}}. \tag{11}$$

The -I pair of sextupoles [11, 12] gives

$$\alpha_{yy}^s \approx -\frac{1}{16\pi}\left(K2 L_s\right)^2 L_s \beta_{s,y}^2, \tag{12}$$

where K2 is sextupole strength [m^{-3}], L_s is sextupole length, $\beta_{s,y}$ is vertical beta functions at the sextupole position.

3.3.4 Present colliders: DAΦNE and Super KEKB

3.3.4.1 *DAΦNE*

DAΦNE is an electron-positron collider with central mass energy of 1.02 GeV (Φ resonance) delivering luminosity since 2000 [2]. The staff upgraded the machine to implement crab waist scheme in 2007. The changes included two times larger crossing angle, 26% smaller horizontal emittance, almost two times smaller vertical and horizontal beta functions, 50% smaller bunch length. Reduction of the bunch length was not intentional and happened because of continuous work on impedance reduction. Constraints of already working machine did not allow achieving extreme parameters; nevertheless, they doubled Piwinski angle from 0.8mrad to 1.7mrad (Table1) and increased luminosity three times [2].

Table 1: Parameters of DAΦNE and SuperKEKB

	DAΦNE	SuperKEKB	
	SIDDHARTA	LER	HER
Energy, GeV	0.51	4	7.007
Circumference, m	97.69	3016.315	
$\varepsilon_x/\varepsilon_y$, nm/pm	250/750	3.2/8.64	4.6/12.9
β^*_x/β^*_y, mm	250/9.3	32/0.27	25/0.3
Crossing angle, mrad	50	83	
σ_z, mm	17	6	5
Piwinski's angle φ	1.7	25	19
Beam current e^-/e^+, A	2.45/1.4	3.6	2.6
Beam beam tune shift ξ_y	0.03	0.088	0.08
μ'_y	-61	-5400	-5400
α^k_{yy}	694	1.8×10^6	1.8×10^6
α^f_{yy}	218	9.8×10^6	9.8×10^6
α^s_{yy}		-7×10^5	-7×10^5
Luminosity, cm^{-2}s^{-1}	Achieved 4.5×10^{32}	Design 8×10^{35}	

Moderate IP beta functions and small beta functions in final quadrupoles do not require separate chromaticity correction sections, and sextupoles of the ring correct the whole chromaticity. Figure 3 shows optical functions of DAΦNE interaction region.
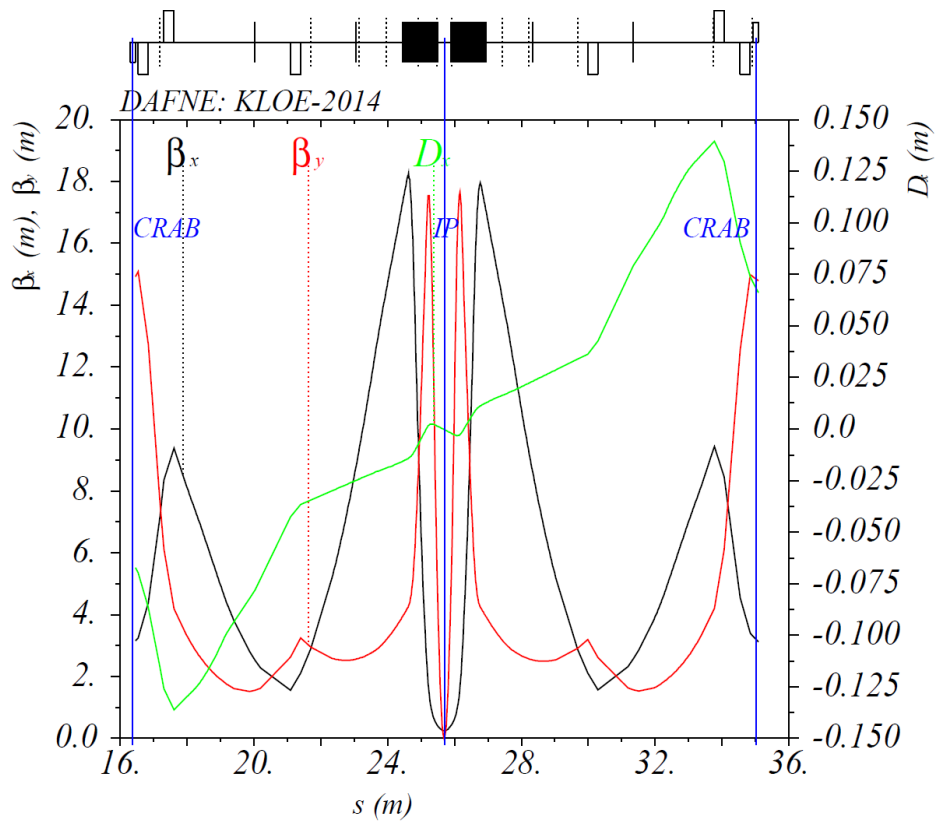
Figure 3: Optical functions of DAΦNE interaction region with crab waist sextupoles.

3.3.4.2 *SuperKEKB*

SuperKEKB [13, 14, 15] is an upgrade of KEKB B-factory [13] in the state of beam commissioning [16] with the goal to increase luminosity 40 times to 0.8×10^{36} cm^{-2}s^{-1} (Table 1). The upgrade followed the steps of crab collision scheme and, because of very small beam sizes at IP, received the name of nano-beam. Figures 5 and 6 show optical functions of the interaction region for low (LER) and high (HER) energy rings.
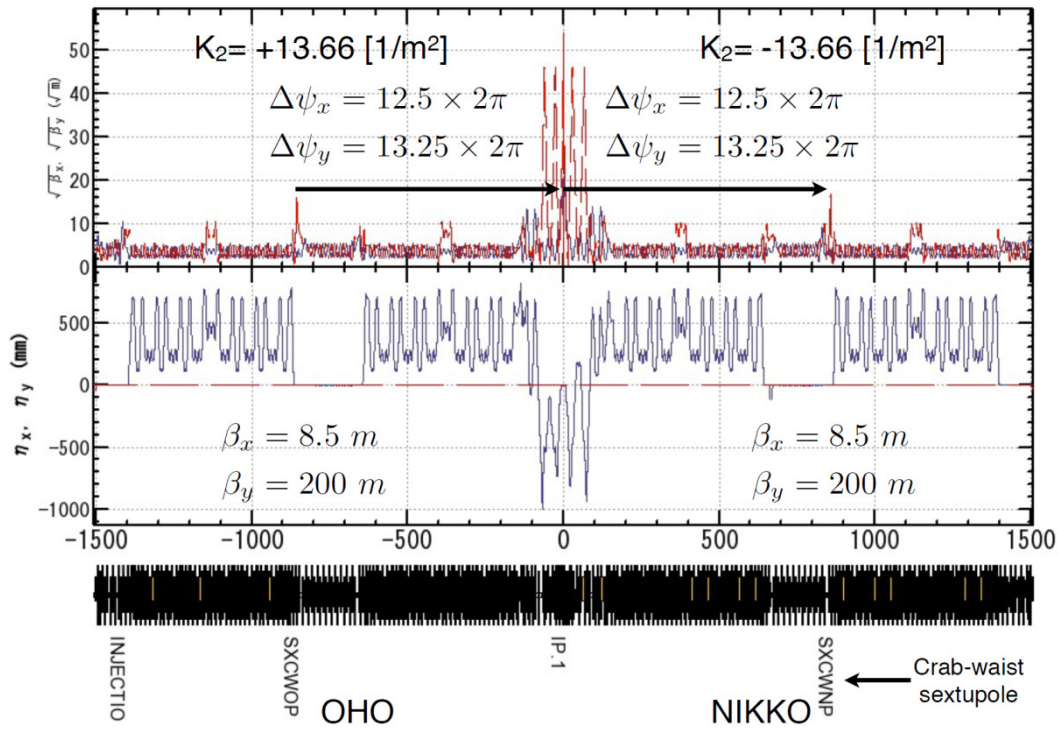
Figure 5: Optical functions of SuperKEKB LER interaction region with crab waist. sextupoles.
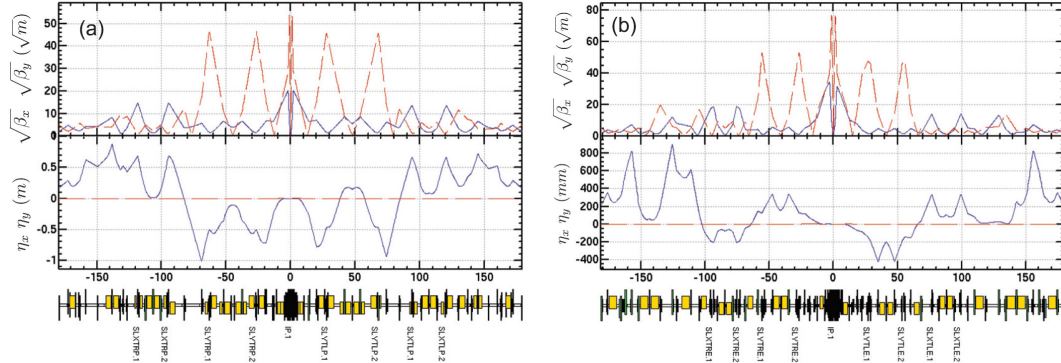
Figure 6: Optical functions of SuperKEKB interaction region (a) LER, (b) HER.

The crab sextupoles are installed before horizontal and vertical chromaticity sections, rather far from IP at $\mu_x = 12.5 \times 2\pi$ and $\mu_y = 13.25 \times 2\pi$. The interplay of crab sextupole, nonlinear fringe of final quadrupoles, and kinematic term in the IP drift reduces dynamic aperture drastically [17, 18] (Figure 7). The staff did not find a solution to regain dynamic aperture; therefore, they planned to work without crab sextupoles.
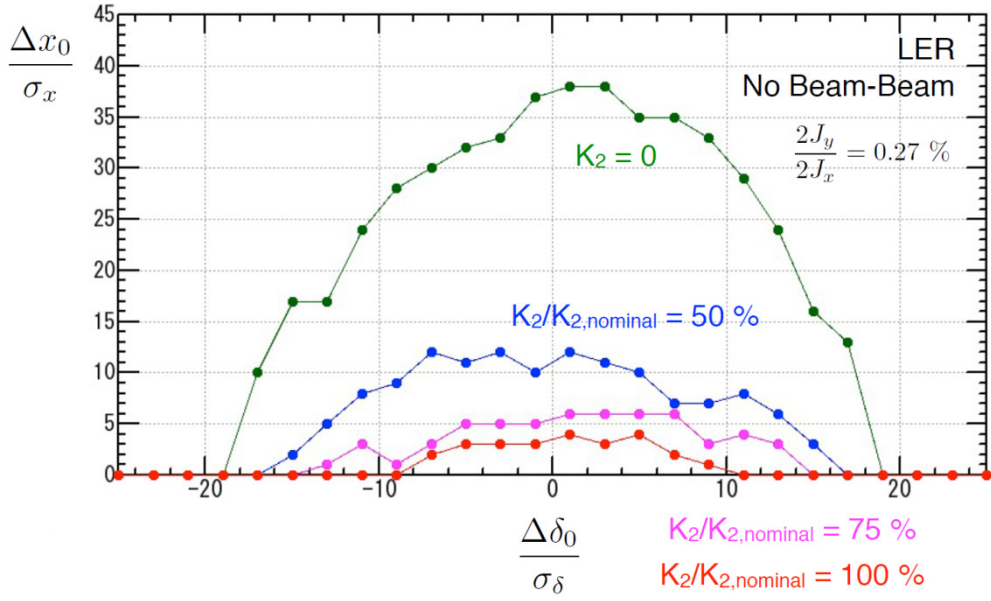
Figure 7: Dynamic aperture for LER SuperKEKB with different crab sextupole strength.

3.3.5 Future projects based on crab waist

3.3.5.1 *SuperB*

SuperB [19, 20] is an Italian project of asymmetric b factory employing crab waist collision scheme to achieve luminosity of 1×10^{36} cm^{-2}s^{-1}. The optics of the interaction region includes separate vertical and horizontal chromaticity correction sections followed by crab sextupole (Figure 8). Again, dynamic aperture shrinks under influence of crab sextupoles (Figure 9), but it is satisfactory.

Table 2: Parameters of SuperB

	SuperB	
	LER	HER
Energy, GeV	4.18	6.7
Circumference, m	1258.4	
$\varepsilon_x/\varepsilon_y$, nm/pm	2.46/6.15	2/5
β^*_x/β^*_y, mm	32/0.205	26/0.253
Crossing angle, mrad	66	
σ_z, mm	5	5

Piwinski's angle φ	19	23
Beam current, A	2.4	1.9
Beam beam tune shift ξ_y	0.097	0.097
μ'_y	-1068	-1056
α_{yy}^k	1×10^6	1×10^6
α_{yy}^f	2.8×10^5	2.8×10^5
α_{yy}^s	-5.4×10^6	-5.4×10^6
Luminosity, $cm^{-2}s^{-1}$	1×10^{36}	
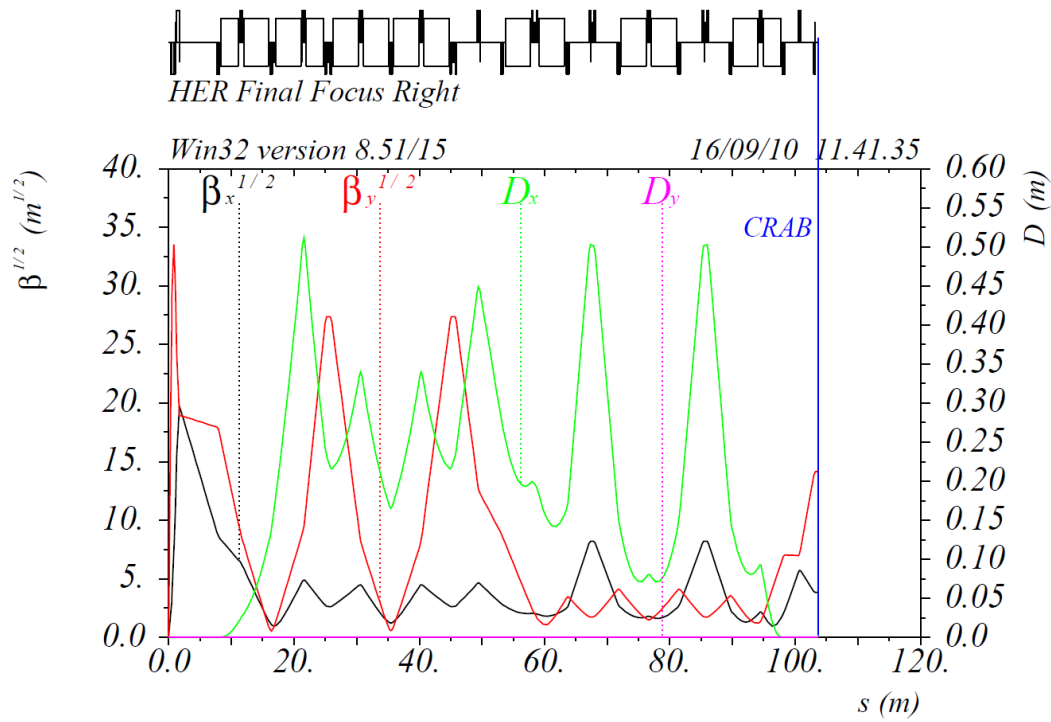
Figure 8: Optical functions of SuperB HER interaction region with crab waist sextupoles.
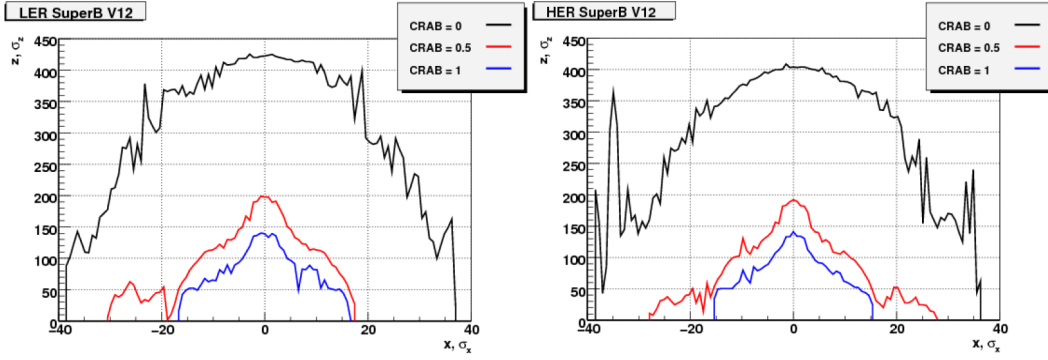
Figure 9: On momentum dynamic aperture of SuperB LER and HER: black line — crab sextupoles are off, red and blue — crab sextupoles strength of 50% and 100% of nominal respectfully.

3.3.5.2 *CTau*

Super Charm–Tau Factory is a project of electron-positron collider in the Budker Institute of Nuclear Physics (Novosibirsk, Russia) [21]. Designed center mass energy range of operation is from 2 to 5 GeV with luminosity reaching 1×10^{35} cm^{-2}s^{-1}(Table 3). It also relies on the crab waist collision scheme. China proposed similar project HIEPA [22].

Table 3: Parameters of CTau in Novosibirsk

	CTau			
Energy, GeV	1	1.5	2.0	2.5
Circumference, m	813.4			
$\varepsilon_x/\varepsilon_y$, nm/pm	8/40			
β^*_x/β^*_y, mm	40/0.8			
Crossing angle, mrad	60			
σ_z, mm	16.5	11	10	10
Piwinski's angle φ	27	19	17	17
Beam current, A	1.65			
Beam beam tune shift ξ_y	0.15	0.15	0.12	0.1
μ'_y	-697			
α^k_{yy}	1.3×10^5			
α^f_{yy}	7.7×10^5			
α^s_{yy}	-7.2×10^5			
Luminosity, cm^{-2}s^{-1}	0.61×10^{35}	0.91×10^{35}	1×10^{35}	1×10^{35}

Interaction region optics, similar to SuperB, consists of separate chromaticity correction sections (sextupoles Y1 and Y3, X1 and X3) and crab sextupole (Figure 10). The optics also includes additional sextupoles Y2 and Y4, X2 and X4 to correct reduction of dynamic aperture due to finite length of main sextupoles [12], and sextupoles X5, X6, X7 help to correct nonlinear chromaticity [23,24].
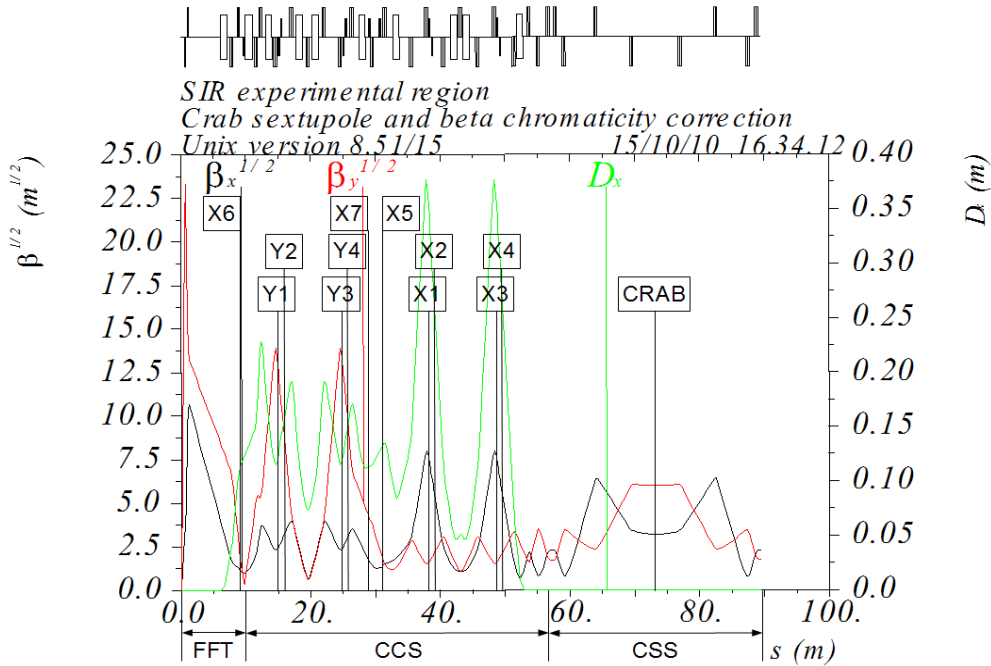
Figure 10: Optical functions of CTau interaction region.

3.3.5.3   *FCC-ee*

Future circular collider is a project in CERN of the next accelerator after LHC [25, 26]. The ultimate goal is 100 km proton-proton machine with 100 TeV central mass energy. The first possible step is e^+e^- machine — FCC-ee with central mass energy range from 80 GeV to 350 GeV and two IPs (Table 4).

Table 4: Parameters of FCC-ee

	FCC-ee			
Experiment	Z	W	H	tt
Energy, GeV	45	80	120	175
Circumference, m	100×10^3			
$\varepsilon_x/\varepsilon_y$, nm/pm	0.14/1	0.44/2	1/2	2.1/4.3
β^*_x/β^*_y, mm	500/1			
Crossing angle, mrad	30			
σ_z, mm	5.9	9.1	8.2	6.6
Piwinski's angle φ	11	9	6	3
Beam current, A	1.4	1.4	0.3	0.06
Beam beam tune shift ξ_y per IP	0.175	0.187	0.16	0.08
μ'_y	-2805			
α^k_{yy}	4.5×10^5			
α^f_{yy}	1.9×10^5			
α^s_{yy}	-1.2×10^7			
Luminosity, cm^{-2}s^{-1} per IP	211×10^{34}	36×10^{34}	9×10^{34}	1.3×10^{34}

Minimization of synchrotron radiation background towards the detector and the length of IR tunnel are important requirements; therefore, IR is asymmetric, i.e. with lower bending for the incoming beam and stronger bending for outgoing beam. Two teams developed different IR optics [27, 28].

The first variant (Figure 11) does not have horizontal chromaticity section because of geometrical constraints. The second sextupole of –I pair performs two functions: it cancels geometric aberrations of the first sextupole and, because dispersion is zero, it plays a role of crab sextupole. Individual –I pairs of arc sextupoles correct nonlinear chromaticity and dynamic aperture (Figure 12).

The second variant (Figure13) employs separate horizontal chromaticity corrections section and additional sextupoles as in CTau project. The arc sextupoles constitute two families. Dynamic aperture is comparable with the variant one (Figure14).
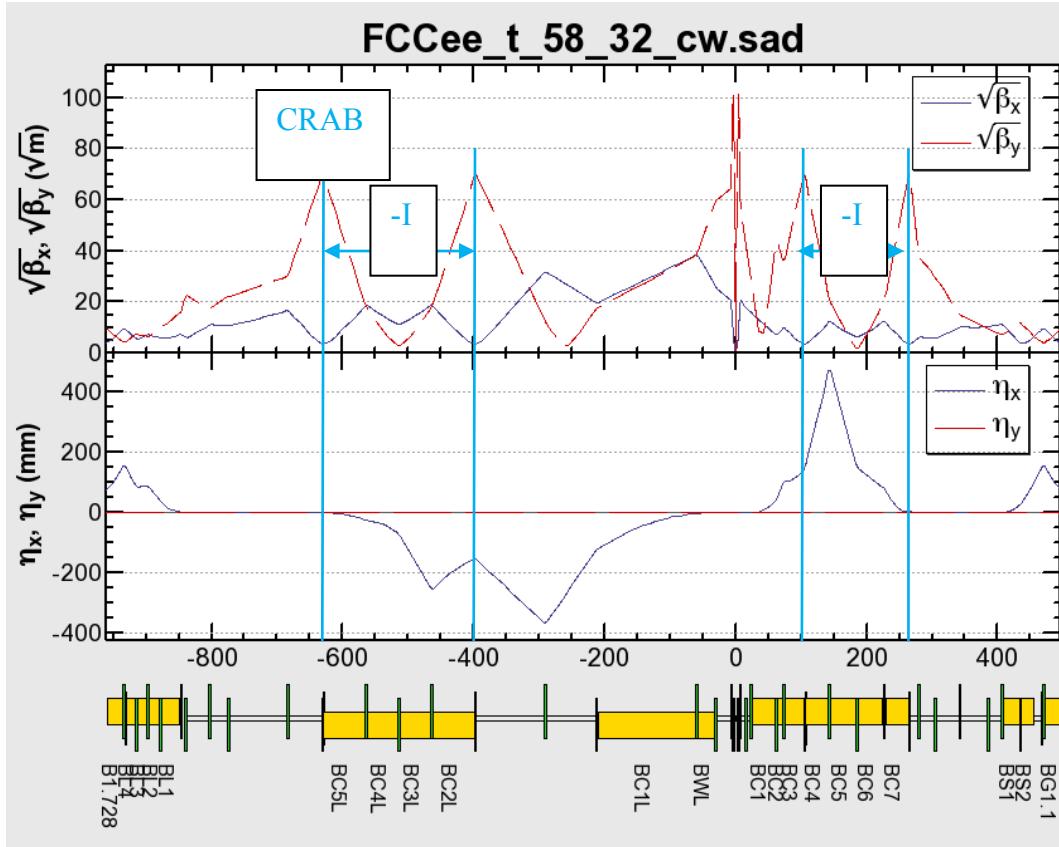
Figure 11: Optical functions of FCC-ee interaction region variant 1.
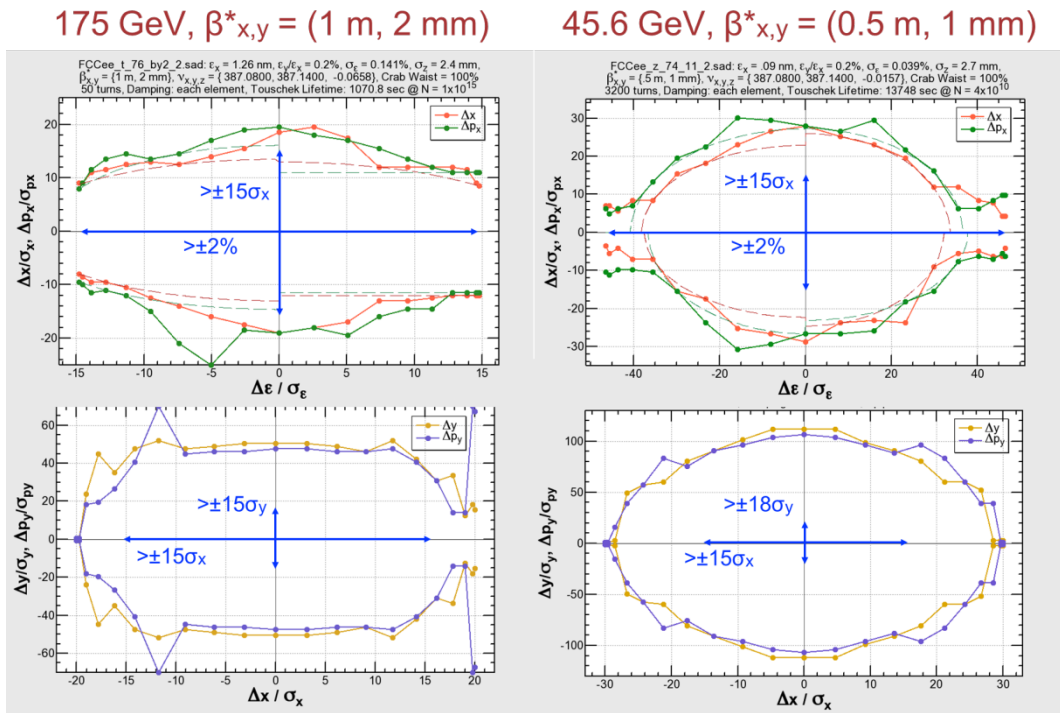
Figure 12: Dynamic aperture for FCC-ee interaction region variant 1.
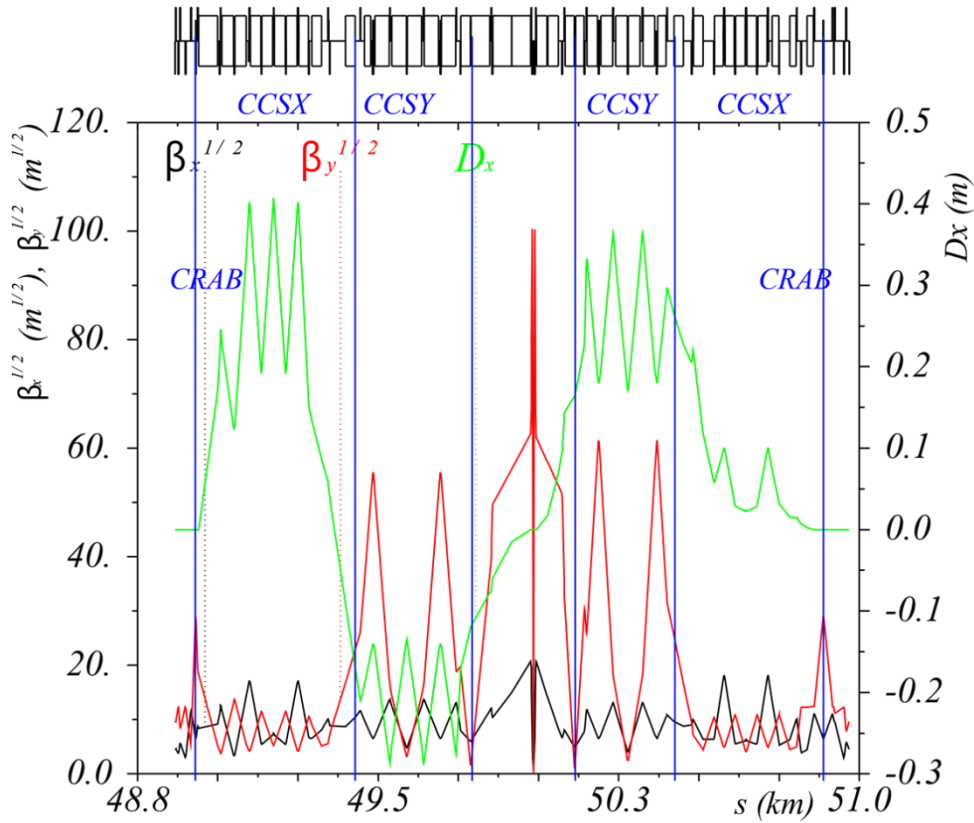
Figure 13: Optical functions of FCC-ee interaction region variant 2.
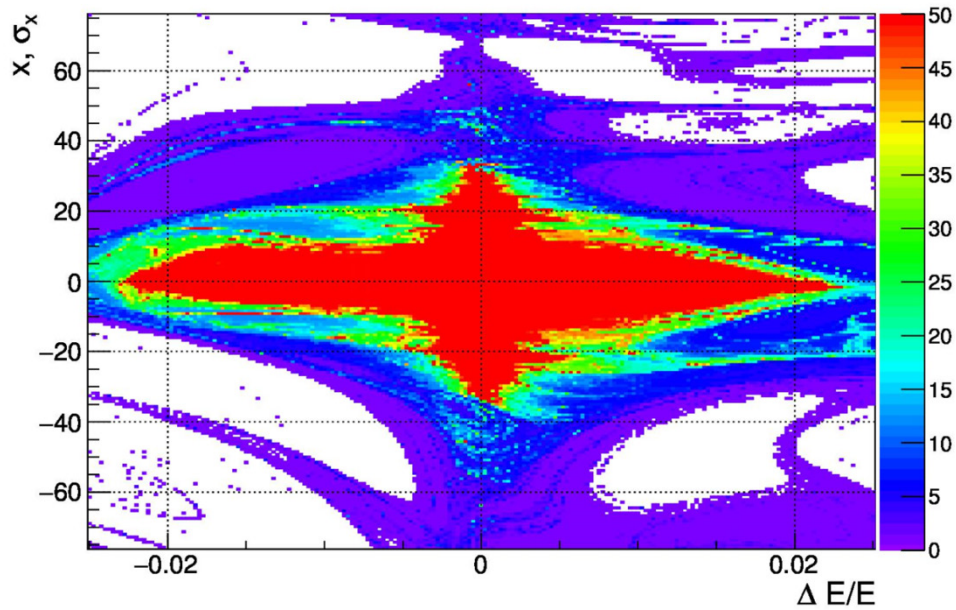
Figure 14: Dynamic aperture for FCC-ee interaction region variant 2 (50 turns, without damping, crab sextupole is off, RF is on).

3.3.5.4 *CEPC*

CEPC is Circular Electron Positron Collider in China [29, 30] with central mass energy range from 80 GeV to 240 GeV. The base line design is a single beam pipe collider with pretzel orbit scheme. In the base line design, it is not a high luminosity Z factory; therefore, the staff proposed partial double ring design [29] with crab waist collision scheme. The interaction region layout in the new proposal is similar to the second variant of FCC-ee.

3.3.6 **Discussion**

DAΦNE is the only collider among the reviewed projects, which does not report significant dynamic aperture loss from the crab sextupole. Observing detuning coefficients, we notice that SuperKEKB has the highest coefficients for kinematic term and for quadrupole fringe. The source of dynamic aperture reduction is then interference of crab sextupole with nonlinearities of kinematic terms and quadrupole fringes. To understand the nature of the dynamic aperture loss, we calculated the transfer map for a simple symmetrical case of thin crab sextupoles with strength $\pm K2L$ [m^{-2}], thin final quadrupoles with fringes $K1L$ [m^{-1}] and $K1$ [m^{-1}], two drifts of the length L^* (from quadrupole to IP) with kinematic terms (Figure 15).
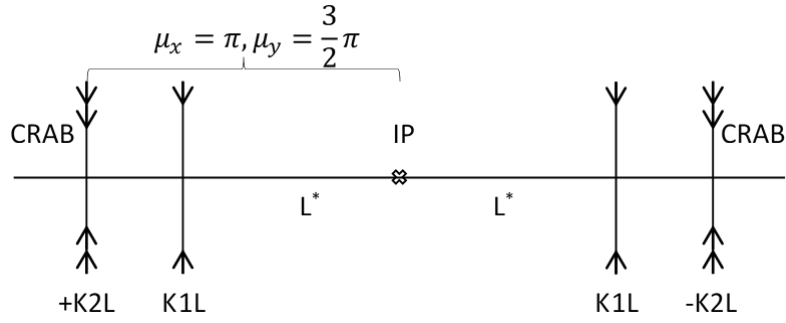
Figure 15: Layout of the simple interaction region.

Coordinates after the second crab sextupole depend on initial x_0, y_0 as

$$x = x_0 + y_0^4 \frac{L^*\left(1 + 2 \cdot K1 \cdot K1L \cdot L^{*3}\right)}{2\theta \beta_y^{*2} \beta_y^2} \sqrt{\frac{\beta_x}{\beta_x^*}} - x_0^4 \frac{K1 \cdot K1L \cdot L^{*2}}{\theta \beta_y^* \beta_y} \sqrt{\frac{\beta_x^*}{\beta_x}} -$$

$$x_0^2 y_0^2 \frac{L^*\left[\left(1 + 2 \cdot K1 \cdot K1L \cdot L^{*3}\right)\beta_x + 6 \cdot K1 \cdot K1L \cdot L^* \beta_x^* \beta_y^* \beta_y\right]}{2\theta \beta_y^{*2} \beta_y^2 \sqrt{\beta_x^* \beta_x}} \quad , \qquad (13)$$

$$p_x = -x_0^3 \frac{2}{3} K1 \cdot K1L \frac{\beta_x^{*2}}{\beta_x^2} - x_0 y_0^2 \frac{2 \cdot K1 \cdot K1L \cdot L^{*2} \beta_x^*}{\beta_y^* \beta_y \beta_x} , \qquad (14)$$

$$y = -y_0 - x_0^3 y_0 \frac{2 \cdot K1 \cdot K1L}{\theta}\left(\frac{L^{*2}}{\beta_y^* \beta_y} \sqrt{\frac{\beta_x^*}{\beta_x}} + \left(\frac{\beta_x^*}{\beta_x}\right)^{\frac{3}{2}} \right), \qquad (15)$$

$$p_y = y_0^3 \frac{L^*\left(3 + 2 \cdot K1 \cdot K1L \cdot L^{*3}\right)}{3\beta_y^{*2} \beta_y^2} + x_0^2 y_0 \frac{2 \cdot K1 \cdot K1L \cdot L^{*2} \beta_x^*}{\beta_y^* \beta_y \beta_x} , \qquad (16)$$

where we preserved the same notation for beta functions, and we chose $px_0=0$, $py_0=0$ for simplicity, and substituted crab sextupole strength (3). Introducing map notation V_{ijklm} for vector $z=\{x,p_x,y,p_y\}$ ($z_i = V_{ijklm} z_j z_k z_l z_m$), we compare the largest coefficients for different projects (Table 5). Again, we notice that SuperKEKB has the largest coefficient from the interference of crab sextupole and quadrupole fringe.

Table 5: Comparison of the map coefficients for different projects

	V_{11133}	V_{13333}
DAΦNE	$-3268 - 71 \cdot K1 \cdot K1L$	$3268 + 55 \cdot K1 \cdot K1L$
SuperKEKB	$-31481 - 51501 \cdot K1 \cdot K1L$	$31481 + 51465 \cdot K1 \cdot K1L$
SuperB	$-31849 - 2091 \cdot K1 \cdot K1L$	$31849 + 2087 \cdot K1 \cdot K1L$
CTau	$-64492 - 27894 \cdot K1 \cdot K1L$	$64492 + 27860 \cdot K1 \cdot K1L$
FCC	$-438 - 7063 \cdot K1 \cdot K1L$	$438 + 7011 \cdot K1 \cdot K1L$

Careful inspection of expressions (13, 14, 15, 16) shows that increasing vertical beta function β_y in crab sextupole decreases majority of the terms, thus providing a way to enhance dynamic aperture. Introduction of an octupole in the final quadrupole will provide the same monomials in the map; therefore, it is another way to optimize dynamic aperture.

3.3.7 Acknowledgements

3.3.8 References

1. P. Raimondi, "Status on SuperB Effort", presentation at the 2nd Workshop on Super B-Factory, http://www.lnf.infn.it/conference/superb06/talks/raimondi1.ppt

2. M. Zobov, "New generation electron-positron factories", Phys.Part.Nucl. 42: 782-799, 2011.

3. P. Raimondi and M. Zobov, DAΦNE Technical Note G-58, April 2003;

4. D. Shatilov and M. Zobov, ICFA Beam Dyn.Newslett.37:99-109, 2005.

5. A. Piwinski, "Satellite resonances due to beam-beam interaction", IEEE Transactions on Nuclear Science, vol. NS-24, no.3, June 1977.

6. D.V.Pestrikov, "Vertical Synchrobetatron Resonances due to Beam-Beam Interaction with Horizontal Crossing", Nucl.Instrum.Meth.A336:427-437, 1993.

7. P. Raimondi, D. Shatilov D and M. Zobov, "Beam-beam issues for colliding schemes with large Piwinski angle and crabbed waist", Preprint physics/0702033, 2007.

8. P. Raimondi, D. Shatilov and M. Zobov, "Suppression of beam-beam resonances in crab waist collisions", Conf. Proc. C0806233 WEPP045, 2008.

9. D. Shatilov, E. Levichev, E. Simonov and M. Zobov, "Application of frequency map analysis to beam-beam effects study in crab waist collision scheme", Phys. Rev. ST Accel. Beams 14 014001, 2011.

10. A. Bogomyagkov et al., "Analysis of the Non-linear Fringe Effects of Large Aperture Triplets for the HL LHC Project", Proceedings of IPAC2013, Shanghai, China, paper WEPEA049, pp. 2616-2617.

11. A.Bogomyagkov, E.Levichev, P.Piminov, "Nonlinear Perturbations for High Luminosity e+e- Collider Interaction Region", IAS HEP Conference, 18-21 Jan 2016, Hong Kong.

12. A. Bogomyagkov, S. Glukhov, E. Levichev, P. Piminov. Effect of the sextupole finite length on dynamic aperture in the collider final focus, Arxiv: 0909.4872.

13. K. Oide, "KEKB B-Factory, The Luminosity Frontier", Progress of Theoretical Physics, v. 122, p. 69, 2009.

14. T. Abeet al., KEK-REPORT-2010-1. 2010; arXiv:1011.0352.

15. Y. Ohnishi et al., "Accelerator design at SuperKEKB",Progress of Theoretical Experimental Physics, 03A011 (17 pages), 2013.

16. Y. Funakoshi et al., "Beam Commissioning of SuperKEKB", proceedings of IPAC16, tuoba01, http://www.ipac16.org, 2016.

17. Y. Ohnishi, "Optics Issues", 18th KEKB Review KEK, March 3-5, 2014.

18. Y. Ohnishi, "Dynamic aperture optimization at SuperKEKB", 55th ICFA Advanced Beams Dynamics Workshop on High Luminosity Circular e^+e^- colliders – Higgs factory, October 9-12, 2014.

19. Bona M. et al., Preprint SLAC-R-856, INFN-AE-07-02, LAL-07-15. 2007. 480 p.; hep-ex/0709.0451.

20. Biagini M. E. et al.,"SuperB progress report", arXiv:1009.6178.

21. V. Anashin et al., "A project of super C-τ factory in Novosibirsk" conceptual design report, https://ctd.inp.nsk.su/c-tau, 2011.

22. Z. Zhou et al., "Preliminary concept and key technologies of hiepa accelerator", proceedings of IPAC16, thpor047, http://www.ipac16.org, 2016.

23. R. Brinkmann, "Optimization of a final focus system for large momentum

bandwidth", Preprint DESY M-90-14, 1990.

24. A. Bogomyagkov, "Chromaticity correction of the interaction region", IAS Program on High Energy Physics, Hong Kong18-21 January, 2016.

25. M. Benedikt, "Future Circular Collider Study: status and parameter update", 2nd FCC week, Rome, http://fccw2016.web.cern.ch/fccw2016, 2016.

26. FCC-ee design study, http://tlep.web.cern.ch.

27. K. Oide, "Machine layout and beam optics", 2nd FCC week, Rome, http://fccw2016.web.cern.ch/fccw2016, 2016.

28. A. Bogomyagkov, "Interaction region optics solutions", 2nd FCC week, Rome, http://fccw2016.web.cern.ch/fccw2016, 2016.

29. D. Wang et al., "CEPC parameter choice and partial double ring design", proceedings of IPAC16, thpor010, http://www.ipac16.org, 2016.

30. Feng Su et al., "CEPC partial double ring lattice design", proceedings of IPAC16, thpor009, http://www.ipac16.org, 2016.

3.4   Introduction on the pretzel scheme design of CEPC

Huiping Geng

Mail to: genghp@ihep.ac.cn

Institute of High Energy Physics, 19B Yuquan Road, Shijingshan, Beijing, China

3.4.1   Introduction

After the discovery of Higgs-like boson at CERN[1,2,3], many proposals have been raised to build a Higgs factory to explicitly study the properties of the particle. One of the most attractive proposals is the Circular Electron and Positron Collider (CEPC) project in China[4,5].

CEPC is a ring with a circumference of 50-70 km, which will be used as electron and positron collider at phase-I and will be upgraded to a Super proton-proton Collider (SppC) at phase-II. The designed beam energy for CEPC is 120 GeV, the main constraints in the design is the synchrotron radiation power, which should be limited to 50 MW, the target luminosity is on the order of $\sim 10^{34}$ cm^{-2}s^{-1}.

As beam energy is high, CEPC favors a lattice with more arcs which will enable RF cavities to compensate the energy loss in the straight section, thus can reduce energy variation from synchrotron radiation. SppC needs long straight sections for collimators etc. To compromise between CEPC and SppC, the ring is decided to have 8 arcs and 8

straight sections, RF cavities will be distributed in each straight section. The layout of CEPC can be seen in Fig.1.
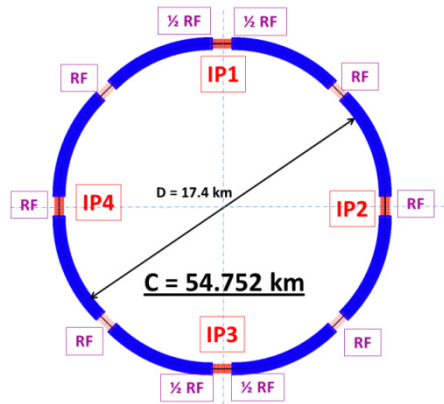
Figure 1: A schematic drawing of CEPC ring.

In the baseline design, a single ring scheme will be one of the options, besides the partial double ring scheme. In the single ring scheme, the electron and positron beam will share the beam pipes, thus a special orbit is needed to avoid the beam colliding at positions except the Interaction Points (IPs). This paper will show the latest design of the CEPC lattice, including the design of the main ring lattice and the pretzel scheme. The ring and pretzel orbit has been designed for 50 bunches, as required in the CEPC Pre-CDR. Some critical issues that we encountered when designing the lattice will be discussed. The linear optics, as well as the non-linear chromaticity compensation with the presence of pretzel orbit will be described.

3.4.2   Principles of pretzel scheme

In single ring collider, the pretzel orbit is used to avoid the beam collision at positions except the IP.

For ideal pretzel orbit, the following relationship should be fulfilled: $\phi = N \cdot 2\pi$, where ϕ is the phase advance between the adjacent collision points, N is an integer. This relation guarantees that if the beam is properly separated at the first parasitic collision point, then it can be automatically properly separated at other parasitic collision points.

For our lattice, it is comprised of 60/60 degree FODO cells, every 6 cells have a phase advance of 2π, so the distance between the adjacent parasitic points L_{pc} can be written as: $L_{pc} = N \cdot 6 \cdot 47.2 = N \cdot 283.2$ m. For 50 bunches, there are 100 collision points in total, thus the ring circumference C must be $C = 100 \cdot L_{pc} = 28320 \cdot N$ m.

As the circumference of the CEPC ring is about 50 km, the integer number N has to be 2, which means the ring circumference has to be 56640 m and there will be one collision point every 4π phase advance.

3.4.3 Design of the ring lattice

The circumference of the ring is 54km with 8 arcs and 8 straight sections. The layout of the ring is shown in Fig. 1. There are four IPs in the ring, IP1 and IP3 will be used for CEPC, while IP2 and IP4 will be used for SPPC. The RF sections are distributed in each straight section. At the IP section, the RF cavities will be symmetrically placed at the two ends of the section, at the other straight sections, the RF cavities can be located together at the middle of each straight section.

The lattice for CEPC ring has been chosen to use the standard FODO cells with 60 degrees phase advances in both transverse planes. The FODO cell structure is chosen to have a maximum filling factor. The 60 degrees phase advance is chosen to have a relatively large beam emittance, so that a relatively longer beamstrahlung beam lifetime, than the 90 degrees phase advance lattice cells. The lattice for CEPC ring has been chosen to use the standard FODO cells with 60 degrees phase advances in both transverse planes. The FODO cell structure is chosen to have a maximum filling factor. The 60 degrees phase advance is chosen to have a relatively larger beam emittance, so that a relatively longer beamstrahlung beam lifetime, than the 90 degrees phase advance lattice cells.
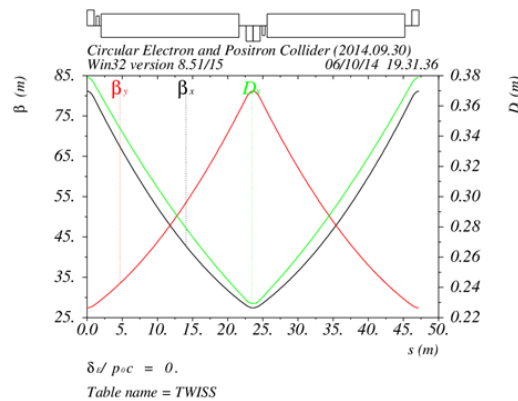
Figure 2: Beta functions and dispersion function of a standard FODO cell with 60/60 degrees phase advance in CEPC ring.

A standard FODO cell with 60 degrees phase advance is shown in Fig.2. The length of each bend is 19.6m, the length of each quadrupole is 2.0m. There is one sextupole, with a length of 0.4 m, next to each quadrupole for chromatic corrections. The distance between the sextupole and the adjacent magnet is 0.3 m, while the distance between each quadrupole and the adjacent bending magnet is 1.0 m. The total length of each cell is 47.2 m.

The dispersion suppressors are formed by pulling out the bending magnets in the second last FODO cell on each side of every arc section in CEPC ring. The beta functions and dispersion function of one dispersion suppressor is shown in Fig. 3. The dispersion suppressors are formed by pulling out the bending magnets in the second last FODO cell on each side of every arc section in CEPC ring. The beta functions and dispersion function of one dispersion suppressor is shown in Fig. 3.
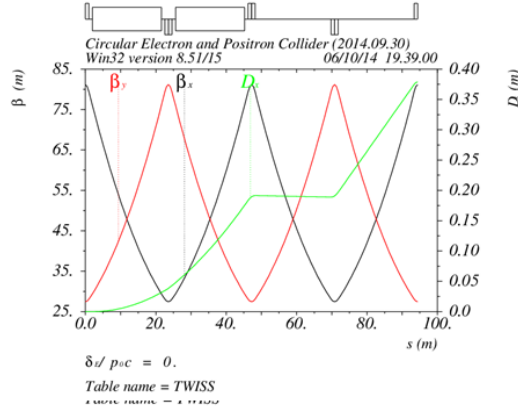
Figure 3: The beta functions and dispersion function of a dispersion suppressor in CEPC ring.

The straight sections have two different lengths, the four straight sections which have the IPs have a length of 1604.8 m, and the other straight sections have a length of 849.6 m, the circumference of the ring is 56640 m. The first four FODO cells at each end of every straight section are used for matching and working point adjustment. The beta functions and dispersion function of a short straight section in CEPC ring is shown in Fig. 4.
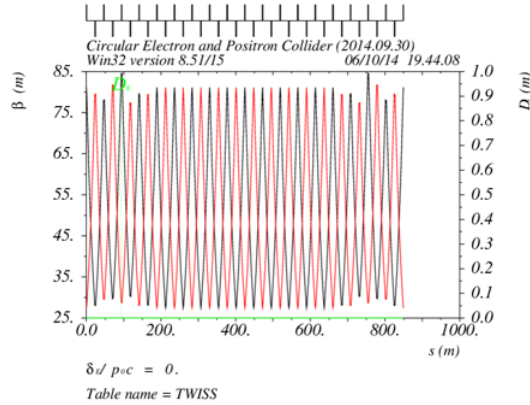
Figure 4: The beta functions and dispersion function of a short straight section in CEPC ring.

3.4.4 Pretzel scheme design

To avoid big coupling between horizontal and vertical plane, we use horizontal separation scheme to generate the pretzel orbit here. Also, in order to avoid beam instability and High Order Mode in the RF cavities, we require that there is no off-center orbit in any RF sections. Thus, we use one pair of electrostatic separators for each arc.

For each pair, the position of the first electrostatic separator is chosen such that it is $\pi/2$ phase advance before the first parasitic crossing point, and the position of the

second electrostatic separator is chosen such that it is $\pi/2$ phase advance after the last parasitic crossing point in this arc. A schematic drawing is shown in Fig.5.
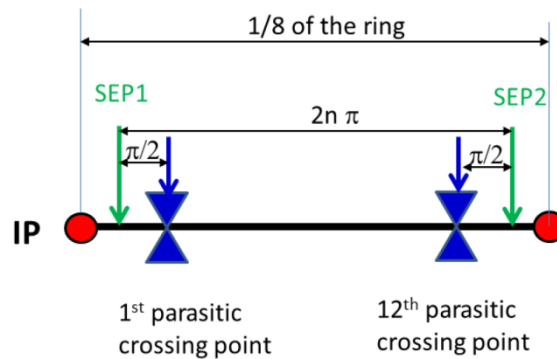
Figure 5: A schematic drawing of the positions of the electrostatic separators for 1/8th of the ring. SEP1 and SEP2 in the drawing mean the first and second electrostatic separators.

The separation distance between the two beams is about $10\sigma_x$, which is an empirical number, to allow for a reasonable beam lifetime. The final orbit of the beam is shown in Fig.6.
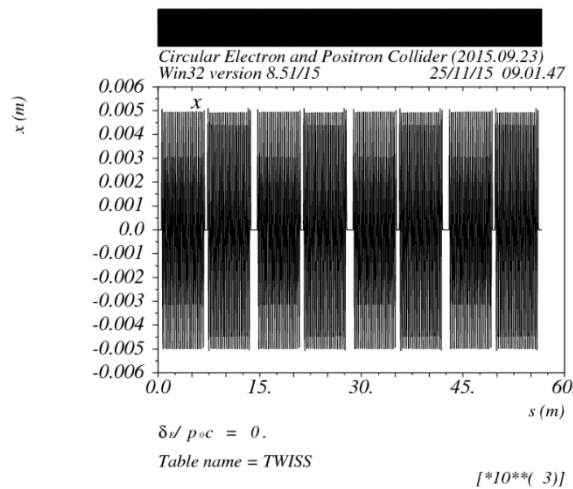
Figure 6: The pretzel orbit in the ring for one beam. The separation distance between the two beams is about $10\sigma_x$ in the horizontal plane.

3.4.5 Dynamic aperture result with pretzel orbit

When there is an off-center orbit, the beam will experience extra fields in magnets. To be specific, in quadrupole magnets, the beam will see an extra dipole filed when it is off-centered. The dipole strength can be estimated with a simple formula: $\Delta B = K_1 \cdot B\rho \cdot \Delta x$, where K_1 is the normalized quadrupole strength, $B\rho$ is the magnetic rigidity of the beam, and Δx is the orbit of the beam. With a simple calculation, we can

see that the extra dipole field seen by the off-center beam has a strength that is comparable to the strength of the main bending magnets.

In sextupole magnets, the beam will experience extra dipole and quadrupole fields. The field strength can be estimated similarly. These extra fields (dipole field in quadrupole, and both dipole and quadrupole fields in sextupole) will break the periodicity and achromatic condition of the lattice, and this effect has to be corrected.

The distortion of pretzel orbit effects on beta functions and dispersion function has to be corrected to have a reasonable dynamic aperture. Also, since the sextupoles are now coupled with quadrupoles, the chromaticity correction and the tune are coupled together, so linear lattice and nonlinear chromaticity has to be corrected at the same time. We try to find a new lattice period by taking 12 FODO cells, with symmetrically placed magnets, and require the phase advance to be 4π and the chromaticity to be zero at the same time. There is no detailed phase advance requirement in each FODO cell in this case. A new lattice can be found accordingly, the new lattice and the chromaticity correction result is shown in Fig.7 and Fig.8 .
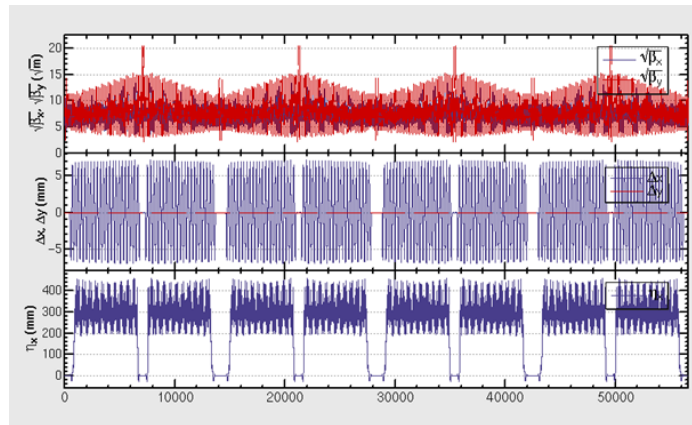
Figure 7: The beta function, dispersion function and orbit distribution along the ring after the correction of the pretzel orbit distortion on the lattice.
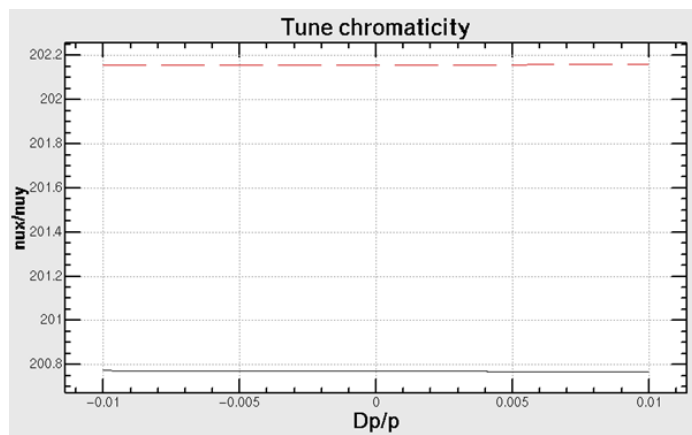
Figure 8: The tune v.s. momentum spread after the global correction of the pretzel orbit distortion on the lattice.

The dynamic aperture of the ring after correction of the pretzel orbit distortion on the lattice has been checked before the insertion of the Final Focus System (FFS). The result is shown in Fig. 9. The working point used here is (.79,.15) in horizontal and vertical planes. The plot shows that the dynamic aperture is $\sim 10\sigma_x \times 110\sigma_y$ in horizontal and vertical planes. The tracking has been done with 240 turns, which corresponds to 3 transverse damping times.

We can see that even before the insertion of FFS, the dynamic aperture of the lattice with pretzel scheme is not big enough. So we try to look at and optimize the dynamic aperture of the ring even before turn the pretzel orbit on. This work is still ongoing.
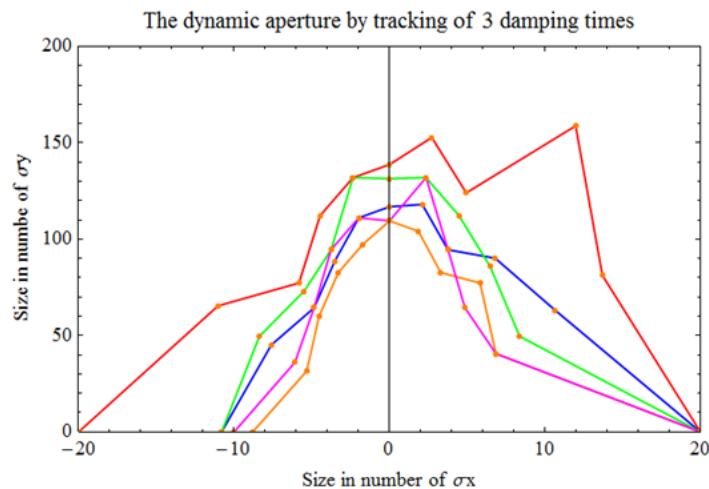
Figure 9: The dynamic aperture of the ring after correction of the pretzel orbit distortion on the lattice has been and before the insertion of the Final Focus System (FFS), the working point used here is (.79,.15) in horizontal and vertical planes.

3.4.6 Summary

In this paper, we have introduced the status of CEPC lattice design. The detailed lattice design principle and results have been showed. We have described how the pretzel orbit of 50 bunches has been designed. The distortion of lattice due to pretzel orbit has also been explained. We have also shown how the pretzel orbit distortion effect on the lattice can be compensated and the chromaticity been corrected. The work to achieve a reasonable dynamic aperture result is still ongoing.

3.4.7 References

1. Adrian Cho, "Higgs Boson Makes Its Debut After Decades-Long Search", Science 337 (6091): 141–143.

2. "Observation of a New Particle with a Mass of 125 GeV", http://cms.web.cern.ch/news/observation-new-particle-mass-125-gev.

3. CMS collaboration, "Observation of a new boson at a mass of 125 GeV with the

CMS experiment at the LHC",   Physics Letters B, 716(1):30-61

4. "Accelerators for a Higgs Factory: Linear vs. Circular (HF2012)", Fermi National Laboratory, 14-16 November, 2012.

5. S. Henderson. "Accelerators for a Higgs Factory", Report at HF2012, Fermi Lab, 14-16 November, 2012.

3.5   Booster Design for CEPC project

3.5.1   Introduction

In the baseline design of CEPC project[1] , it will utilize a linac followed by one booster ring to achieve the resuired injection energy of 120 GeV. This booster is supposed to provide both full energy electron beams and positron beams to the main collider. It will be put in the same tunnel and have almost the same circumference with the collider. A general layout of the booster ring is shown in Fig 1. The booster is composed of eight arc sections and eight long straight sections, and there are four interaction points. Only IP1 and IP3 are used for e+e- collision, while IP2 and IP4 are conserved for future pp collision. Around these interaction points, bypass lines are used to avoid the detectors. Electron and positron injection and extraction are done at the four long straight sections.
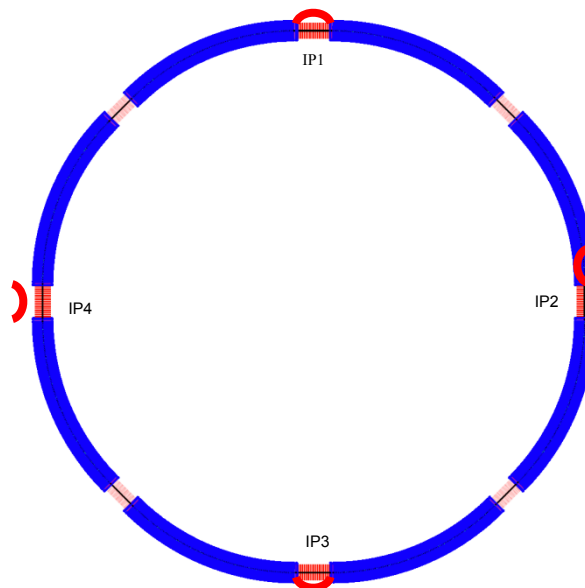
Figure 1: CEPC booster layout

The booster can do electron and positron injection into the collider every 10 seconds, which includs linac injection to the booster, energy ramp up, injection to the collider and energy ramp down. The bunch number in the booster is the same as that in the collider, and every injection can add 5% particles into each bunch.

At its low energy of 6 GeV, the low synchrotron radiation damping make the damping time hundres of seconds. We have to adpot single injection from linac to booster and this also add difficulties to the dynamic aperture optimization. The general design parameters of the booster are given in Table 1.

Table 1: General Parameters of CEPC booster

Parameters	Value
Injection Energy	6 GeV
Extraction Energy	120 GeV
Repetition Rate	0.1 Hz
Circumference	54.4 km
Bunch number	48
Bunch population	2.0E10
SR power	1.46 W

3.5.2 Lattice

A FODO cell very similar to that in the main collider is chosen to be the main lattice structure in the booster, the length of the cell is increased to decrease the number of magnets used. For considerations of noninterleaved sextupole arrangements in dynamic aperture optimization, Phase advance in each cell is chosen to be 90 degree, and the length of the cell is set to be 94.4 meters, twice of that in the main collider. Each of the eight arc sections consists of 38 FODO cells and two dispersion suppressors on its two sides, which results in zero dispersion in each of the long straight sections. Some of the general parameters are given in Table 2. Figure 2. shows lattice functions of a FODO cell and of the whole ring.

Table 2. lattice parameters of CEPC booster

Parameters	Value
FODO cell length	94.4 m
Quadrupole Strength	0.022 m^{-1}
Max beta function	162 m
Max dispersion	0.83 m
Sextupole strength SF/SD	0.45/0.44 m^{-2}
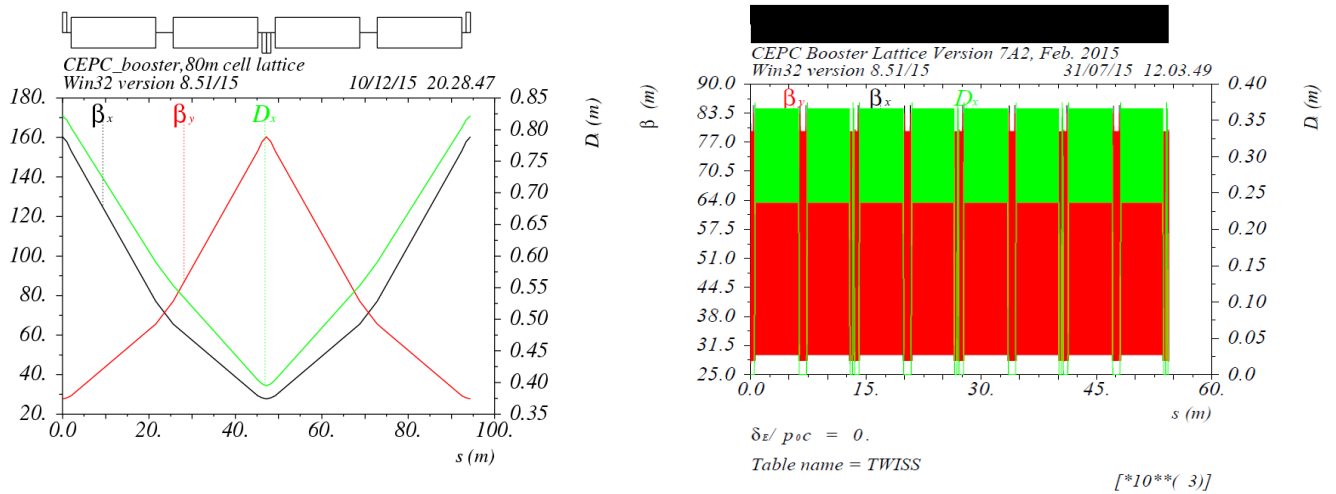
Figure 1: lattice functions of the FODO cell and the whole ring

3.5.3 Dynamic Aperture Optimization

Since the emittance of the injected beams from linac are much larger than that in a circular ring, and the damping time at low energy is very long, a large dynamic aperture with thousands of turns tracking is very important for our booster ring. Much efforts have been taken in dynamic aperture optimization, different cell structure and optimization methods have been tried. With a non-interleaved sextupole, using symbolic and numerical optimization[2,3,4], a dynamic aperture of (0.3, 0.12) is shown.

3.5.4 Low field issues

The magnetic field of dipoles in the booster is only 30 G at low energy of 6 GeV, this may cause beam instability due to magnetic field outside. In a test we did in the tunnel of BEPCII, a magnetic field of about 2 G is detected at all places far from main magnets. But the cause and work principles are still not clear, further experiments and error analysis will have to be done in the future.
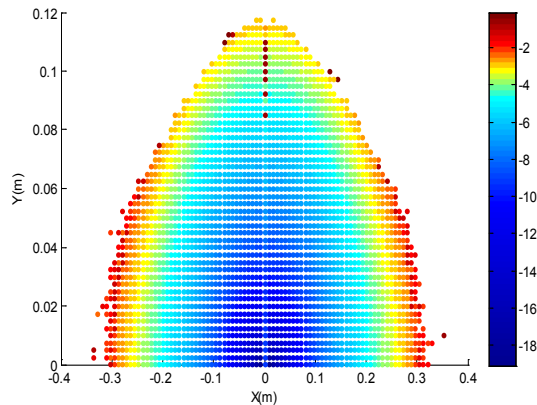
Figure 3: dynamics aperture of on momentum particles

3.5.5 Low field issues

The magnetic field of dipoles in the booster is only 30 G at low energy of 6 GeV, this may cause beam instability due to magnetic field outside. In a test we did in the tunnel of BEPCII, a magnetic field of about 2 G is detected at all places far from main magnets[5]. But the cause and work principles are still not clear, further experiments and error analysis will have to be done in the future.

3.5.6 Injection and Extraction

Electrons and positrons are injected into booster through a transfer line, a horizontal septum and a kicker downstream bend the beam onto the central position of the beam orbit. Single-turn, vertical extraction will be used. A single kicker and four orbit bump dipoles will be used to vertically displace the central orbit.

3.5.7 References

1. The CEPC-SPPC Study Group, CEPC-SPPC preliminary Conceptual Design Report, Volume II- Accelerator, IHEP-CEPC-DR-2015-01, IHEP-AC-2015-01,March 2015.

2. M. Borland, V. Sajaev, L. Emery, A. Xiao, "Direct Methods of Optimization of Storage Ring Dynamic and Momentum Aperture", proceedings of the 2009 Particle Accelerator Conference, Vancouver,BC, Canada (2009).

3. Y. Yan, J. Irwin, Y. Cai, M. Donald, and Y. Nosochkov, "Dynamic Aperture Improvement of PEP-II Lattices Using Resonance Basis Lie Generators", SLAC-PUB-10122.

4. "A. Terebilo, "Accelerator Toolbox for MATLAB", SLAC-PUB-8732.

5. C. Zhang, X. Cui, T. Bian, "Magnetic fields in the tunnel of BEPCII", IHEP Internal Report, August, 2015.

3.6　Design study of CEPC Alternating Magnetic Field Booster*

Tianjian Bian[1], Jie Gao[1], Yunhai Cai[2], Michael Koratzinos[3], Chuang Zhang[1], Xiaohao Cui[1], Yiwei Wang[1], Sha bai[1], Dou Wang[1], Feng Su[1], Ming Xiao[1]

[1]Institute of High Energy Physics, Beijing, China, [2]SLAC National Accelerator Laboratory, CA, USA, [3]University of Geneva, Geneva, Switzerland

Mail to: biantj@ihep.ac.cn

Bian Tianjian, Institute of High Energy Physics, Beijing, China

3.6.1　Introduction

CEPC (Circular Electron and Positron Collider) was proposed as an electron and positron collider ring with a circumference of 50-100km to study the Higgs boson[1][2][3]. CEPCB(CEPC Booster) is a full energy booster ring with the same length of CEPC which ramp the beam from 6Gev to 120Gev. At the injected beam energy, the magnetic field of the main dipole is about 30Gs, the low magnetic field will create problems for magnet manufacturing[4].

In the Pre-CDR[5], a preliminary design is proposed, but the problems of low field of the main dipole and dynamic aperture are not solved.

In this paper, we focus on those problems and find a reasonable solution. The wiggler scheme, which split the normal dipole to several pieces with different magnet field direction, is adopted to avoid the problem of very low dipole magnet fields[6][7][8]. An analytic map method(Differential algebra)[9] is used to derive the twiss functions of arbitrary order of energy spread, such as β function, phase advance function, dispersion function. Those functions are all analytic functions dependent of sextupole strength. Optimize the high order chromaticities, then a good dynamic aperture for both on-momentum and off-momentum particles are got.

3.6.2　Design Goal

At present, the emittance of CEPC is about $2.0 \times 10^{-9} m \cdot rad$, it is much lower than the Pre-CDR because of crab waist. That makes the CEPCB harder to design because emittance of CEPCB at high energy is also reduced, which cause the chromaticities much stronger and pose challenges to our design at the same time.

Figure 1 shows the X direction injection scheme. Asume that the dynamic aperture of CEPC at 0.5% energy spread is 20 times of sigma and the beta function is 590m.

The total space for injection:

$$\sqrt{2.0 \times 10^{-9} \times 590} \times 20 = 0.0217 (m)$$

8 sigma is retained for revolution beam to get enough quantum life time:

$$\sqrt{2.0 \times 10^{-9} \times 590} \times 8 = 0.0087 (m)$$

6 sigma is retained for injection beam to loss less particles:

$$\sqrt{3.5 \times 10^{-9} \times 590} \times 6 = 0.0086 (m)$$

In that condition, 4mm is retained for septum. So $3.5 \times 10^{-9} m \cdot rad$ seems a reasonable option for the emittance of CEPCB at 120Gev.

The design goals of CEPCB are listed:

The emittance of CEPCB at 120Gev is about $3.5 \times 10^{-9} m \cdot rad$.

1% energy acceptance for enough quantum life time.

The dynamic aperture results must better than 6 sigma (Normalized by emittance $3 \times 10^{-7} m \cdot rad$, which is decided by the beam from linac) for both on-momentum and off-momentum(1%) particles.
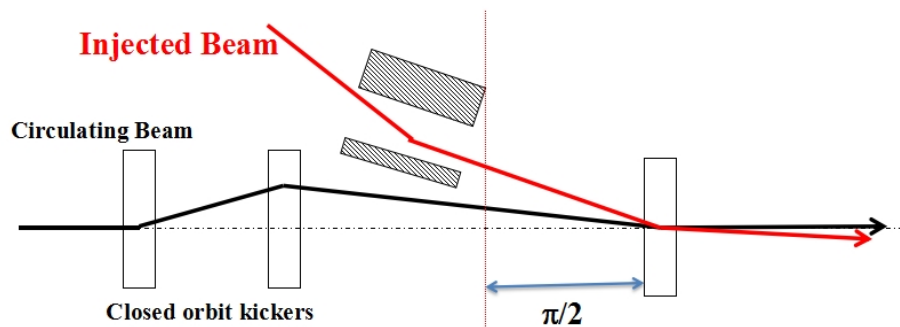
Figure 1: Injection scheme**.**

3.6.3 **Linear Lattice**

The layout of CEPCB is show in Figure 2. It is make up by 8 arcs and 8 straight section, and the total length is 63.8 km. The RF cavities are distributed in each straight section. The lattice for CEPCB has been chosen to use the standard FODO cells with 90 degrees phase advances in both transverse planes, which give us smaller emittance and clear phase relationship between sextupoles.

A standard FODO cell with 90 degrees phase advance is shown in Figure 3. The length of each bend is 30.4 m, the length of each quadrupole is 1.2 m, while the distance between each quadrupole and the adjacent bending magnet is 1.7 m. The total length of each cell is 70 m.
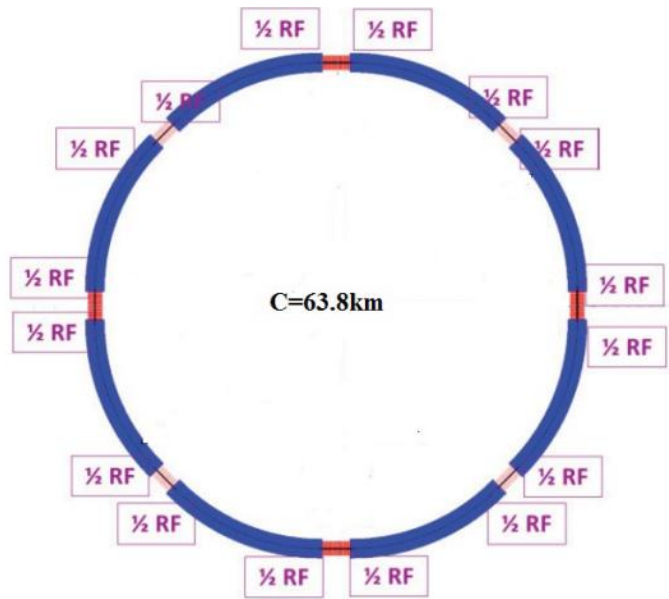
Figure 2: Layout of CEPCB.

In order to make the main dipole stronger to avoid the problem of low magnet field, we split the 30.4 m bend to 8 pieces. The adjacent dipole pieces have different magnet field direction but the integral field strength of dipole is the same as the normal dipole. And we call this scheme "wiggler scheme", as figure 4 shows. The orbit off-set(the red curve in figure 4) in dipole is became smaller as the beam ramping up until the negative dipole change it's field direction and all the dipole became normal bending magnet at 120 Gev. Figure 5 shows the bending angle of positive and negative magnet as a function of ramping time.
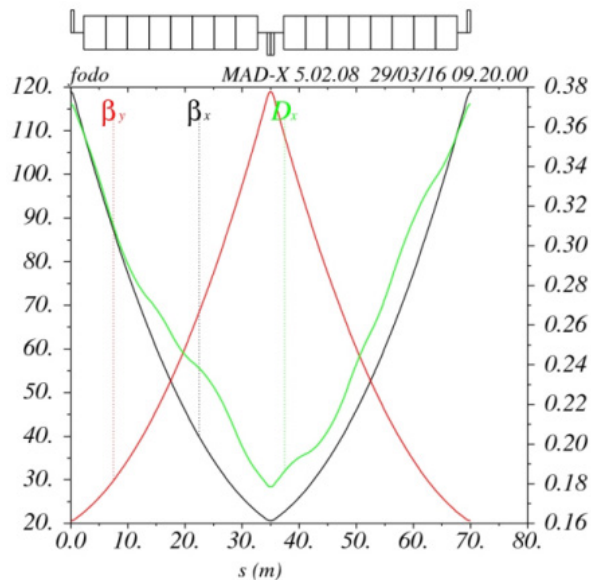
Figure 3: Beta functions and dispersion function of a standard FODO cell with 90/90 degrees phase advance in CEPCB.
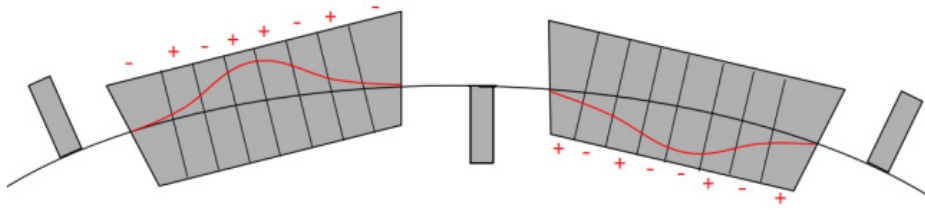
Figure 4: Twisted orbit in a FODO.
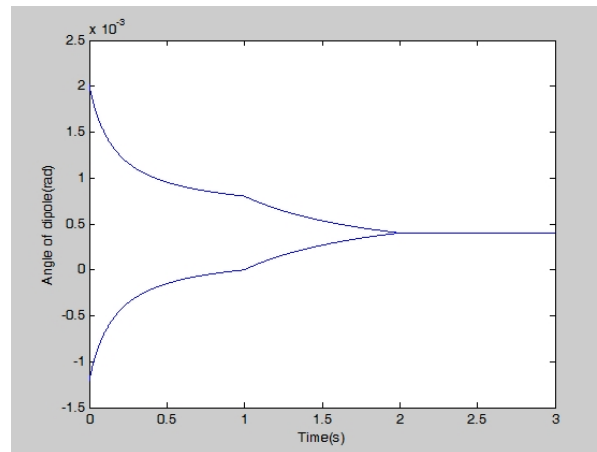
Figure 5: Positive and negative magnet as a function of ramping time.

3.6.4   Sextupole Scheme

The sextupole scheme of CEPCB is shown in Figure 6. The long space means 180 degree phase advance and the short space means 90 degree phase advance. The FODO in Figure 6 means to insert a FODO cell in two repeated sextupole arrangement. In total, 8 families of sextupoles are used.

SF1		SF1	SF2		SF2	SF3		SF3	SF4		SF4
SD1		SD1	SD2		SD2	SD3		SD3	SD4		SD4
FODO											
SF1		SF1	SF2		SF2	SF3		SF3	SF4		SF4
SD1		SD1	SD2		SD2	SD3		SD3	SD4		SD4

Figure 6: Sextupole scheme of CEPCB.

In this scheme, geometric terms are minimized because of the non-interleaved sextupole scheme. Two identical sextupoles apart by 90 degree phase advance to cancel the beta-beat effect of off-momentum particles. Our goal is reducing the 2th and 3rd order chromaticities to enlarge the energy acceptance. An analytic map method

(Differential algebra)[9] is used to derive the 2nd and 3rd order chromaticities analytically, which contain the information of the 8 sextupole families.

When we optimize the 8 sextupole families using the 2nd and 3rd order chromaticities we have derived, we find it is not enough to make the 2nd and 3rd order chromaticities as small as we expect. So tune shift between ARCs is considered. The analytic map method is also used in finding a right phase advance between two ARCs, and we find 43.3 degree is a good choice[7]. Figure 7 shows the tune as a function of energy spread.

3.6.5 Dynamic Aperture Results and CEPCB Parameters

To make the CEPCB more real, mutipole errors are added. We estimate the error of CEPCB is in the same level as LEP[10], the table 1 shows the error estimation.

The tune we are using is: 0.61/0.88, because it avoids some strong resonance line. This tune a rough estimation, tune scanning is needed to find a better tune.

With error, cavity on and 0% and 1% energy spread, the dynamic aperture result is shown in figure 8 and figure 9. In x direction, dynamic aperture is 0.06 m and 0.04 m, and in the y direction, dynamic aperture is 0.023m and 0.016 m for on-momentum and 1% off-momentum particles. Figure 8 and Figure 9 also shows the tune shift depending on amplitude, which also constraint in a reasonable rang e. The parameters of CEPCB are listed in table 2.
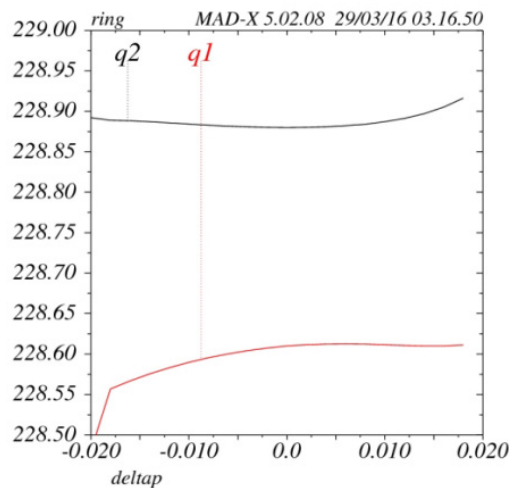
Figure 7: Tune as a function of energy spread.

Table 1: CEPCB error estimate

Parameter	bend	quad	sext
quadrupole	8e-4	...	...
sextupole	2e-4	6e-4	...
octupole	7e-5	5e-4	1.7e-3
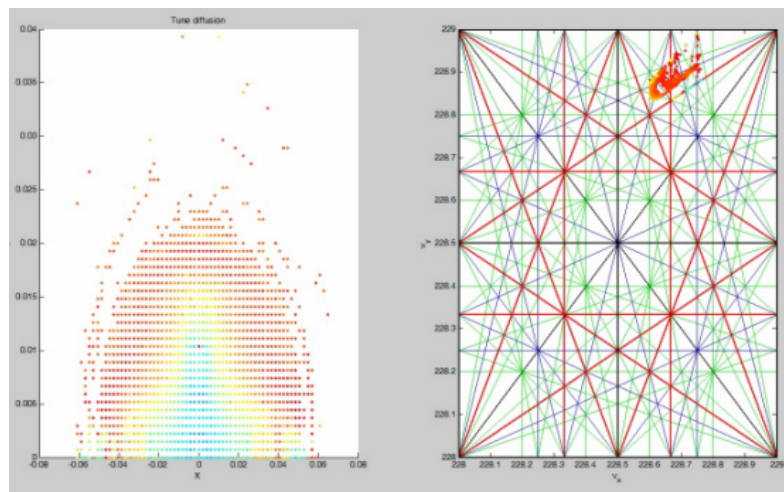
Figure 8: Dynamic aperture and tune shift for the on-momentum particles.
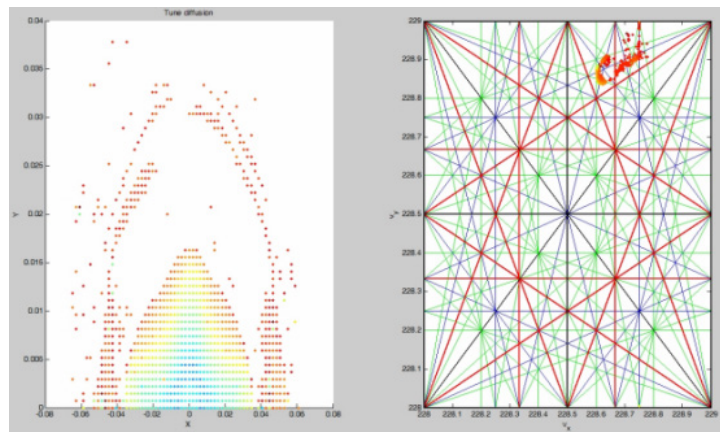
Figure 9: Dynamic aperture and tune shift for the 1% off-momentum particles.

Table 2: CEPCB parameters

6Gev	unit	value	120Gev	unit	value
Beam off-set in bend	cm	1.20	Beam off-set in bend	cm	0
Momentum compaction factor		2.33e-5	Momentum compaction factor		2.54e-5
Strength of dipole	Gs	-129/180	Strength of dipole	Gs	516.71
NB/beam		50	NB/beam		50
Beam current / beam	mA	0.92	Beam current / beam	mA	0.92
Bunch population		0.92	Bunch population		0.92
RF voltage	GV	0.21	RF voltage	GV	6
RF frequency	GHz	1.3	RF frequency	GHz	1.3
Synchrotron oscillation tune		0.21	Synchrotron oscillation tune		0.21
Energy acceptance RF	%	5.93	Energy acceptance RF	%	4.57
SR loss / turn	Gev	5.42e-4	SR loss / turn	Gev	2.34
equilibrium Energy spread	%	0.0147	equilibrium Energy spread	%	0.12
Horizontal emittance equilibrium	m*rad	6.38e-11	Horizontal emittance equilibrium	m*rad	3.61e-9

3.6.6 Summary

In this paper, a possible implementation for CEPCB is proposed. The low field problem is solved by the wiggler scheme. The strength of main dipole increase from 30Gs to -129.18/+180.84 Gs. Damping times are much shorter, which is 4.7 seconds.

With error, cavity on and 0% and 1% energy spread, dynamic aperture is 9.2 sigma and 6.6 sigma in x direction; And 9.6 sigma and 6.4 sigma in y direction.

Contrast with the design goal we have proposed in previous section, this design is reasonable and meet requirements. What we should do next is considering the effect of earth field, shielding or correcting is needed.

3.6.7 **References**

1. Gao, Jie. "Review of some important beam physics issues in electron‑positron collider designs." Modern Physics Letters A, vol. 30, no. 11, pp.1530006, 2015.

2. Wang Dou, et al. "Optimization parameter design of a circular e+ e- Higgs factory." Chinese Physics C, vol.37, no.9, pp.097003, 2013.

3. Su Feng, et al. "Method study of parameter choice for a circular proton-proton collider." Chinese physics C, vol.40, no.1, pp.17001-017001,2015.

4. Kang Wen, "Some Design Considerations and R&D of CEPCB Dipole Magnet", IHEP, Beijing, Apr. 2016.

5. The CEPC-SPPC Study Group, "CEPC-SPPC Preliminary conceptual Design Report", IHEP, Beijing, IHEP-AC-2015-01, March. 2015.

6. Michael Koratzinos, private communication, Dec. 2015.

7. Yunhai Cai, private communication, Feb. 2016.

8. Gang Xu, private communication, Feb. 2016.

9. Yunhai Cai, "Symplectic maps and chromatic optics in particle accelerators.", Nucl. Instr. Meth., vol. 797, pp. 172-181, 2015.

10. Sha Bai, "CEPC magnet error study summary", IHEP, Beijing, Dec. 2015.

3.7 **Collider-Related Lattice Design Efforts at Fermilab**

Y. Alexahin, A. Liu, M.J. Syphers[+]

Mail to: syphers@fnal.gov

Fermilab, P.O. Box 500, Batavia, IL 60510 USA

[+]*also*, Northern Illinois University, DeKalb, IL 60115 USA

3.7.1 **Introduction**

Historically the design of circular hadron collider lattices has been very much an art form, utilizing periodicity, symmetry, and anti-symmetry to help guide the development of the focusing structure of these large-scale synchrotrons. As energies and circumferences continue to climb as well as demands for ever-higher luminosities, new elements such as beam-beam tune shift limits, energy deposition rates, and synchrotron radiation effects have become primary factors as opposed to secondary considerations. Rather than the high periodicity typical of many lower-energy synchrotrons, designs for high-energy hadron colliders today tend toward large arcs with "clustered" straight

sections for more efficient utility distribution; the benefits of many super-periods to suppress resonance effects from systematic errors in lower energy rings tend to be reduced due to the very large number of magnetic elements between straight sections in the very high energy rings and the random field errors inherent of these elements. Thus, rather than containing a set of 6-8 identical equally-spaced straight sections, the new collider lattice designs tend toward large arcs of FODO cells with concentrated straight sections, each with perhaps a unique optical design created for its particular use – beam injection, extraction, collimation, acceleration, and – of course – collisions.

The abandonment of high periodicity was studied in depth during the SSC studies [1] and guided their design toward clustered interaction regions (IRs) and straight sections. The geometry of the LHC was determined by LEP and still has relatively high symmetry, but its optics does not, strictly speaking, due to the variety of straight section insertion designs for various functions. Recent FCC design efforts [2] feel the tension of this, as the hadron collider (hh) option could adopt a more SSC-like layout while the lepton collider (ee) option seeks to retain more equally spaced sections for RF; some might also argue that the hh option will require space in the "arcs" for collimation to protect machine components at such high stored beam energies. To date, much of the FCC optics has been scaled from LHC. But, since the FCC will be in a new tunnel, opportunities exist to study new long straight section layouts more congenial to the problems inherent with this very high energy storage ring.

As an example, consider one particular challenge for a 100-TeV-scale collider: the control of the energy spread of the beam during a store, where intense intra-beam scattering and other such effects will lead to longitudinal emittance growth. A system will be required for energy cleaning, most commonly performed by collimation in regions of the lattice where the dispersion function, D is large. As the energy of these storage rings increases, the relative energy spread continues to get smaller, yet the value of dispersion will remain relatively unchanged. Thus, to resolve off-momentum particles a section of the lattice should be sought that can generate large D while maintaining a small transverse betatron beam size in a region suitable for transverse collimation (See Fig. 1.)
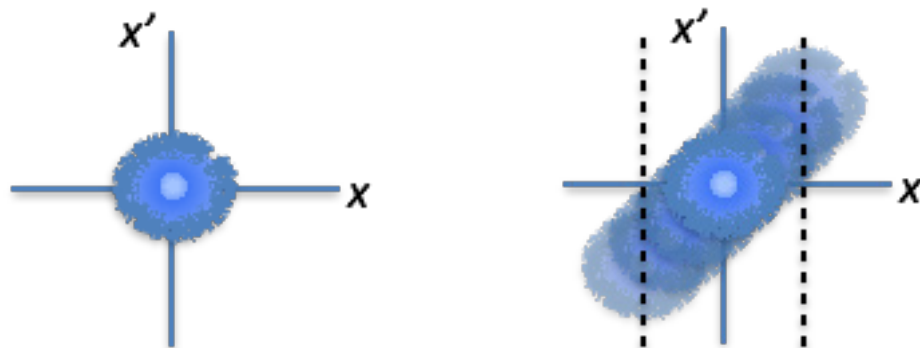
Figure 1: Illustration of transverse phase space with dispersion zero (left) and non-zero (right).

To enhance the dispersion function, dogleg bending regions using negative bending dipole magnets may be required. In the case shown in Figure 2, two arc cells of an FCC-style lattice have positive bending while the following two cells have negative bending. The amplitude of the dispersion reaches 10 m or more. By employing such a scheme one can create a constant value of dispersion within a straight section and then produce a horizontal focus in that straight section to produce a small transverse beam size for the on-momentum particles, but spread out the off-momentum particles for scraping.

Quantitatively, suppose one would like the beam size to be dominated by dispersion at the point of scraping by a factor of two, such that we want

Then, for FCC-type parameters, we may wish to design for. In the vicinity of the straight section mid-point, this ratio will beand varies by less than 20% for. In our example, this would generate a region roughly 100 m long where our condition for is met, within %.
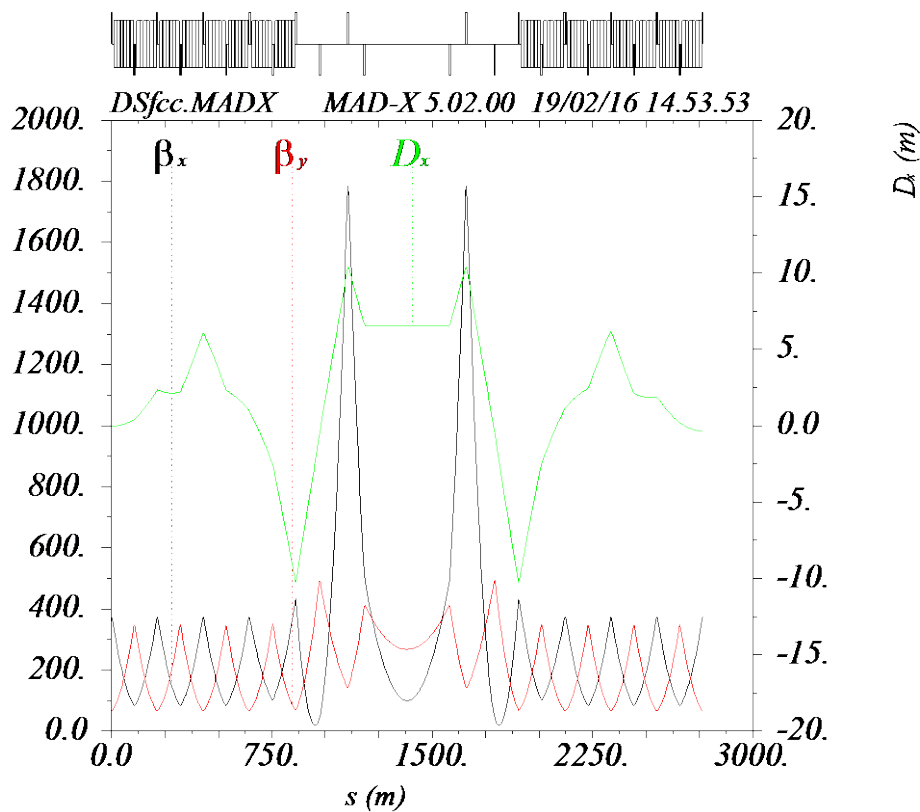
Figure 2: An example of a straight section design with large, constant dispersion, generated by positive and negative bending on either side, plus a low-beta focus in the horizontal plane.

While FCC-type efforts are gearing up at CERN, FNAL, and elsewhere, FNAL has had ongoing studies of muon collider lattices, which are reported upon in the next sections. Also of interest is the use of new optimization techniques utilizing metaheuristic algorithms to explore vast areas of the design phase space. One such

technique is reported upon here in the final section, where its use has been applied to studies pertinent to muon colliders.

3.7.1.1 *References*

1. Conceptual Design of the Superconducting Super Collider, *ed*. J.D. Jackson, SSC-SR-2020, March 1986.

   (http://lss.fnal.gov/archive/other/ssc/ssc-sr-2020.pdf)

2. Future Circular Collider Study, http://fcc.web.cern.ch.

3.7.2 **Muon Collider Lattices (Y. Alexahin)**

A Muon Collider (MC) promises unique opportunities both as an energy frontier machine and as a factory for detailed study of the Higgs boson and other particles [1]. However, in order to achieve a competitive level of luminosity a number of demanding requirements to the collider optics should be satisfied arising from short muon lifetime and relatively large values of the transverse emittance and momentum spread in muon beams that can realistically be achieved with ionization cooling (confer Table 1).

Short muon lifetime, typically ~ 2000 turns, creates a number of problems, e.g. it requires to make the ring as compact as possible to maximize the number of turns (and therefore interactions) the muons make during their lifetime, but there is a positive side to it: such short time is not enough for high-order resonances to manifest themselves. This alleviates problems with obtaining sufficiently large dynamic aperture.

3.7.2.1 *Lattices for High-Energy Colliders*

To avoid losing luminosity due to the hour-glass effect the bunch length should be small enough: $\sigma_z \leq \beta* \leq 1$ cm. Then the momentum spread will be quite high, $\sigma_p/p \sim 10^{-3}$, requiring large momentum acceptance and - to obtain small σ_z with a reasonable RF voltage - momentum compaction factor $|\alpha_c| \sim 10^{-5}$ or lower.

Requirements of large momentum acceptance and small $\beta*$ make correction of the Interaction Region (IR) chromaticity a challenging problem. It can be solved using Chromatic Correction Sections (CCS) [2]. The original approach is to employ two CCS – one for horizontal and the other for vertical correction – on each side of the Interaction Point (IP). Each CCS has a pair of sextupoles separated by *-I* transformation to achieve cancellation of spherical aberrations so the original scheme can be called a 4-sextupoles scheme.

However, the CCS are sources of significant chromaticity themselves so that the required integral strength of the two sextupoles in a CCS is higher than with a single sextupole correction. The ensuing detrimental effect on the dynamic aperture (especially vertical) can be alleviated by adding weak compensating sextupoles at some (small) distance from the main sextupoles [3].

Another problem is the optics sensitivity to magnet field errors and misalignments which is getting worse with increased number and strength of elements at high beta locations. To reduce such sensitivity a 3-sextupole scheme was proposed in [4], where the vertical chromaticity is corrected with a single sextupole placed at a low horizontal

beta-function location to reduce aberrations (see Fig. 1) while the horizontal chromaticity is still corrected with a CCS since smallness of β_y at a normal sextupole location is beneficial but does not suppress horizontal aberrations.
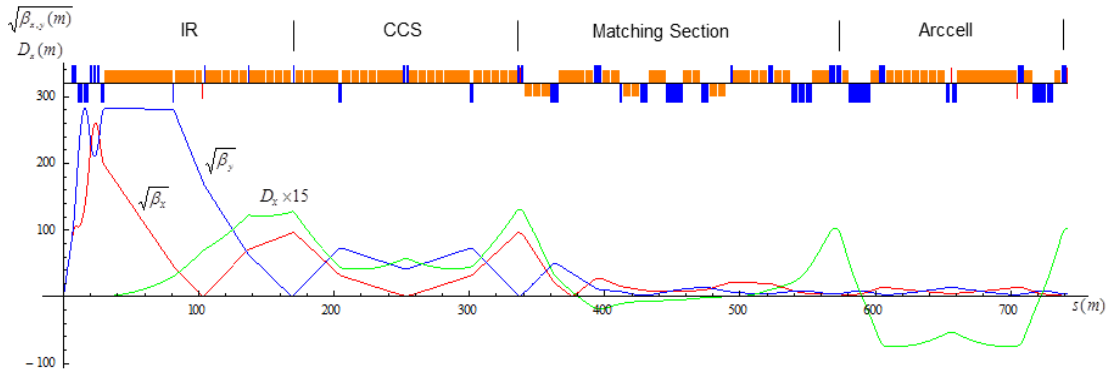
Figure 1: Layout and optics functions from IP to the end of the first arc cell in 3TeV MC.

The IR design must also provide protection of magnets from heat deposition and detectors from backgrounds created by products of muon decays. For the latter there is a dipole component in the IR quadrupoles sweeping away from the detector the charged secondaries. Since the dipole component in defocusing magnets is more efficient for this purpose it is advantageous to have the second from IP magnet defocusing.

The last from IP magnet in the Final Focus (FF) multiplet should be also defocusing in order to make the horizontal beta-function at the dispersion-generating strong dipoles smaller thus minimizing the so-called "dispersion invariant". To satisfy both requirements simultaneously the multiplet should be either a doublet or a quadruplet. The first option was used in [4] for a 1.5 TeV MC design with β∗ = 1 cm and later in [3] for a 6 TeV design with the same β∗.

To obtain smaller β∗ values at high energies with quadrupole gradients offered by the existing Nb3Sn technologies a quadruplet FF can be used [5]. Figure 1 shows the layout and optics functions in Ec.o.m.= 3 TeV MC from IP to the end of the first arccell for β* = 5mm.

Each arc consists of 6 so-called Flexible Momentum Compaction (FMC) cells of the type described in [4] which allows for independent control of all important parameters: tunes, chromaticities, momentum compaction factor and its derivative with momentum.

The matching section includes a chicane with adjustable bending field which does not perturb the orbit outside and changes the total orbit length only slightly. It allows for β* variation in wide range (3 mm-3 cm) without breaking the dispersion closure [6].

With tunes Qx ≈ Qy ≈ 19.1 the stable momentum range exceeds ± 0.6 %. Figure 2 shows the 2048 turns dynamic aperture in the plane of initial particle coordinates at IP xin, yin for indicated values of constant δp calculated with beam-beam interaction off (solid lines) and on (dashed line) using MADX PTC_TRACK routine and MAD8 TRACK LIE4 option respectively.

These results show that the three-sextupole chromaticity correction scheme can provide sufficient dynamic aperture and momentum acceptance.
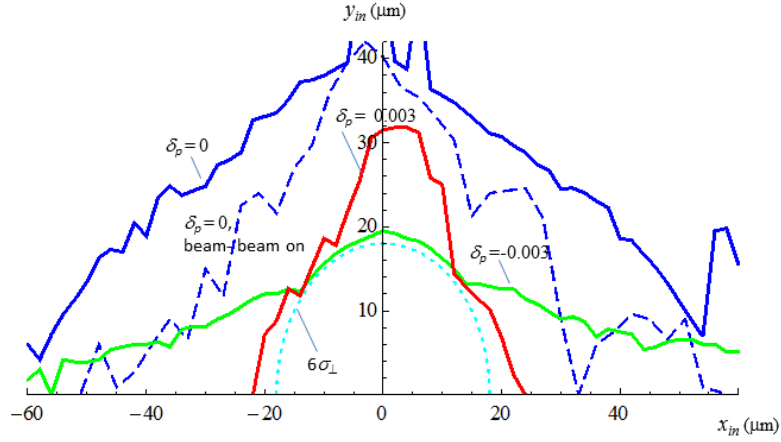
Figure 2: 3TeV MC dynamic aperture in the plane of initial particle coordinates for δ_p = 0 without and with beam-beam interaction (solid and dashed blue lines), δ_p = -0.003 (green line) and δ_p = 0.003 (red line). Dotted line shows 6σ beam ellipse for β^*=5mm.

3.7.2.2   *Specifics of the Higgs Factory Lattice*

There is a number of advantages of a muon collider as the Higgs factory [7], among them a high cross-section of the Higgs boson production in the *s*-channel and the possibility of obtaining a sufficiently low muon beam energy spread to directly measure the Higgs boson peak width which is expected to be ~4MeV.

With low energy spread being a priority, the ionization muon cooling can be stopped at the minimum longitudinal emittance – before the final cooling stage which is mostly an emittance exchange – leaving the transverse emittance relatively high (see Table 1). As a consequence quite small values of the beta-function (a few cm) at the Interaction Point are required to achieve sufficiently high luminosity resulting in a large beam size in the Final Focus quadrupoles.
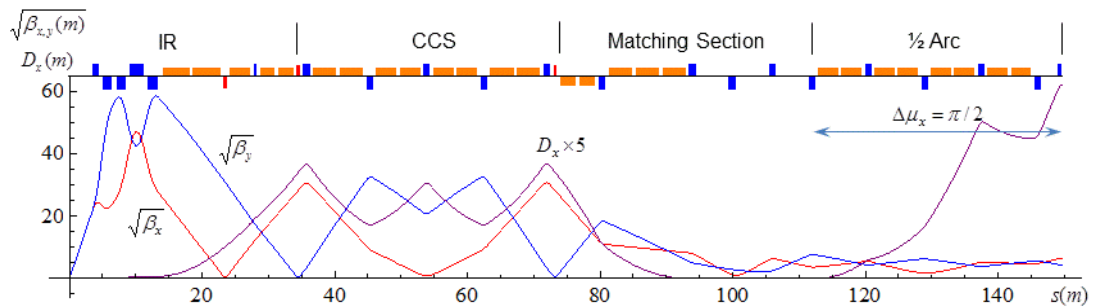
Figure 3: Layout and optics functions in half ring of the Higgs factory for β^*=2.5 cm.

There is a number of effects which can increase energy spread, among them: microwave instability, longitudinal beam-beam effect, path-lengthening due to transverse oscillations. These effects can be mitigated by a large value of the

momentum compaction factor. The latter effect is proportional to chromaticity so that the chromaticity correction is still needed despite extremely low momentum spread.

The necessity of chromaticity correction and of the beam size management in the Final Focus quadrupoles justifies the employment of the same solutions as in the high energy MC case: a quadruplet FF and CCS. The optics functions in half ring (starting from IP) are shown in Figure 3 for β*=2.5 cm. Note that with this IR design, β* can be varied from 1.5 to 10 cm by changing the gradients in matching sections without perturbing the dispersion function. The momentum acceptance of the ring exceeds ±0.5%, the dynamic aperture in absence of errors is about 8 sigma. The systematic field errors in the FF quadrupoles reduce the latter by a factor of 2 so that correction of these errors as well as of the fringe-fields is necessary [8].

Table 1: Muon collider design parameters

Parameter	Unit	Higgs Factory	High Energy Muon Colliders		
Collision energy	TeV	0.126	1.5	3.0	6.0*
Repetition rate	Hz	15	15	12	6
Average luminosity / IP	$10^{34}/cm^2/s$	0.008	1.25	4.6	11
Number of IPs	-	1	2	2	2
Circumference	km	0.3	2.5	4.34	6
β*	cm	1.7	1	0.5	0.3
Momentum compaction factor	-	0.079	$-1.3 \cdot 10^{-5}$	$-0.5 \cdot 10^{-5}$	$-0.3 \cdot 10^{-5}$
Normalized transverse emittance	(π)mm·mrad	200	25	25	25
Momentum spread	%	0.004	0.1	0.1	0.083
Bunch length	cm	6.3	1	0.5	0.3
Number of muons / bunch	10^{12}	4	2	2	2
Number of bunches / beam	-	1	1	1	1
Beam-beam parameter / IP	-	0.02	0.09	0.09	0.09
RF frequency	GHz	0.2	1.3	1.3	1.3
RF voltage	MV	0.1	12	50	150

*) The 6 TeV ring design is not completed yet, the numbers are a projection.

3.7.2.3 *References*

1. J.-P. Delahaye et al., "A Staged Muon Accelerator Facility for Neutrino and Collider Physics", in Proc. IPAC'14, Dresden, Germany, 2014, weza02.

2. J. Irwin et al., in Proc. 1991 IEEE PAC, San Francisco, 1991, p.2058.

3. M.-H. Wang et al., "Design of a 6 TeV Muon Collider", in Proc. IPAC'15, Richmond, VA, USA, 2015, TUPTY081.

4. Y. Alexahin et al., PRSTAB 14 (2011) 061001.

5. Y. Alexahin, "Muon Collider Design", MAP 2014 Spring Meeting, Fermilab May 27-31, 2014.

6. Y. Alexahin and E. Gianfelice-Wendt, in Proc. IPAC'12, New Orleans, LA, USA, 2012, TUPPC041.

7. D.V. Neuffer et al., "A Muon Collider as a Higgs factory", in Proc. IPAC'13, Shanghai, China, 2013, TUPFI056.

8. A.V. Zlobin et al., ibid, TUPFI061.

3.7.3 Applications of Metaheuristic Optimization Algorithms on Muon Facility Designs (A. Liu)

3.7.3.1 *Introduction*

Muon facilities such as a muon collider (MC), or a muon decay ring in a Neutrino Factory (NF) provide unique opportunities to study the Higgs boson and the neutrino properties. The neutrinos from STORed Muons (nuSTORM) [1, 2] facility was designed to be the simplest implementation of the neutrino factory concept [3] and was based on well-demonstrated accelerator technology. The International Muon Ionization Cooling Experiment (MICE) [4] will demonstrate ionization cooling, which is a critical step in an MC and NF design that reduces the phase-space volume occupied by a muon beam within the short muon lifetime. In both of the facility designs, the accelerator elements need to transport a muon beam with a very large phase space emittance and momentum spread ($\Delta p/p$). In such scenarios, a conventional design approach with low-order approximations does not guarantee good acceptance of the large beam. Moreover, simulations of both include pion to muon decays, and simulation of MICE includes particle-material interaction, hence conventional particle tracking tools such as MAD-X [5] cannot be used. Instead, the designs were done based on multi-particle tracking results in G4Beamline [6]. In this section, the applications of the Genetic Algorithm (GA), one of the most frequently used Metaheuristic algorithms, on nuSTORM and MICE are described.

3.7.3.2 *Basics of metaheuristic algorithms*

Genetic Algorithm is a well-demonstrated and well-accepted metaheuristic optimization algorithm, which globally searches for the optimal solution by iteration cycles that can be simply described as "propose-evaluation-repropose-reevaluation". Not like deterministic optimization algorithms, metaheuristic algorithms cannot easily be trapped in the well-known "local optimum", and usually take less computing power to find an acceptable solution. Moreover, the heuristic feature allows parallel computing such as MPI to be implemented, further improving the optimization efficiency. However, there are some disadvantages using metaheuristic algorithms. For instance, they usually do not guarantee an absolute optimal solution. They are also less efficient than deterministic algorithms considering simple systems, such as basic fitting, root finding, extremum finding for basic functions. In principal, the more chaotic a system is, the more advantageous are the metaheuristics.

For nuSTORM and MICE designs, the effects of many high order nonlinearities and stochastic processes are non-ignorable and can be well reflected by G4Beamline tracking. These effects affect each other and determine the facility performance altogether. Therefore, metaheurstic algorithms are preferable in these cases.

3.7.3.3 *nuSTORM facility design optimizations using a MOGA*

The magnetic horn is commonly used in most of the neutrino experiments, as a device to collect the secondary pions generated by bombarding a target with a proton beam [7]. The parabolic shape of the horn inner conductor obtains a path length in the horn that is approximately r^2. With $B_\phi 1/r$, the effective focusing strength of a particle passing through the horn is proportional to r. However, considering the physical length of the target, the initial longitudinal position of pions emerging from the target surface varies significantly, which also depends on the effective interaction lengths of the target. The horn design is commonly done based directly on the physics reach of the neutrino beam from decay of pions after the horn(s), using multi-variable optimizations [8].

The optimization of the nuSTORM horn was done using a Multi-Objective GA (MOGA), by converting a single objective, namely to increase the number of muons within the acceptance of the ring, to two objectives. One of the objectives was regarding the phase space acceptance of the nuSTORM pion beamline, and the tunablility of the pion beamline using the first nine quads. The linear optics and the lattice of the nuSTORM pion beamline is shown in Figure 1. The other objective was regarding the momentum acceptance of the pion beamline and also the kinematics of pion to muon decay.

96
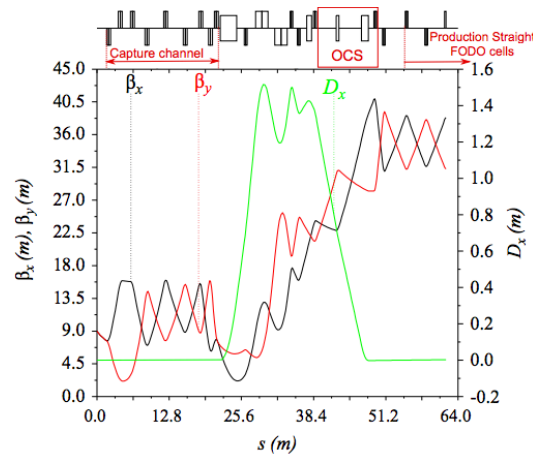
Figure 1: The nuSTORM pion beamline optics and lattice.

Using the same target (38 cm Inconel, 2.5 interaction lengths), the MOGA was able to improve the number of acceptable muons at the end of the pion beamline from the pion beam after the optimal horn by 8%, compared with the baseline target and horn combination. The pion distribution in the transverse phase space is shown in Figure 2, and the pre-optimized horn is compared with the optimized horn in Figure 3. Longer targets were investigated afterwards in order to yield more pions. Optimization was done for both 46 cm and 60 cm Inconel targets. While increasing the target from 46 cm to 60 cm did not show any improvement, 16% more acceptable muons can be obtained by increasing it from 38 cm to 46 cm. As a comparison, if only the target is lengthened but the horn is kept the same, that increment will drop to 5%.
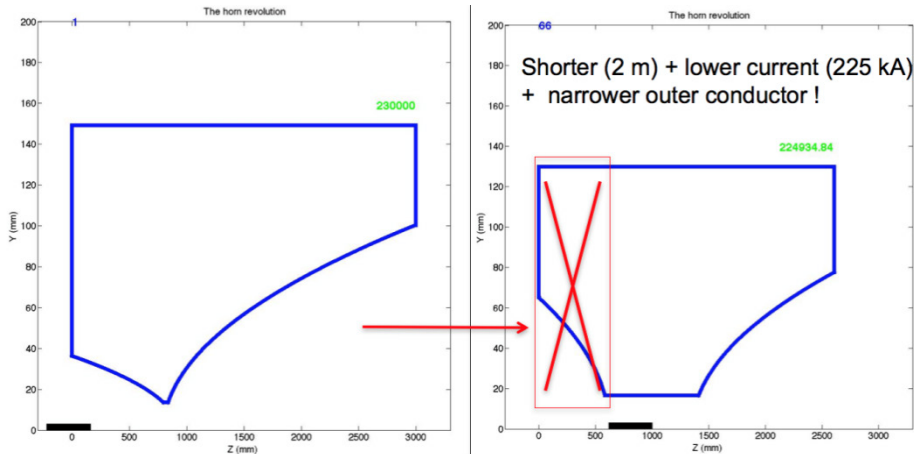
Figure 2: The pre-optimized and optimized horn for a 38 cm Inconel target. The region crossed in red does not provide useful focusing, therefore the front parabolic inner conductor can be discarded.
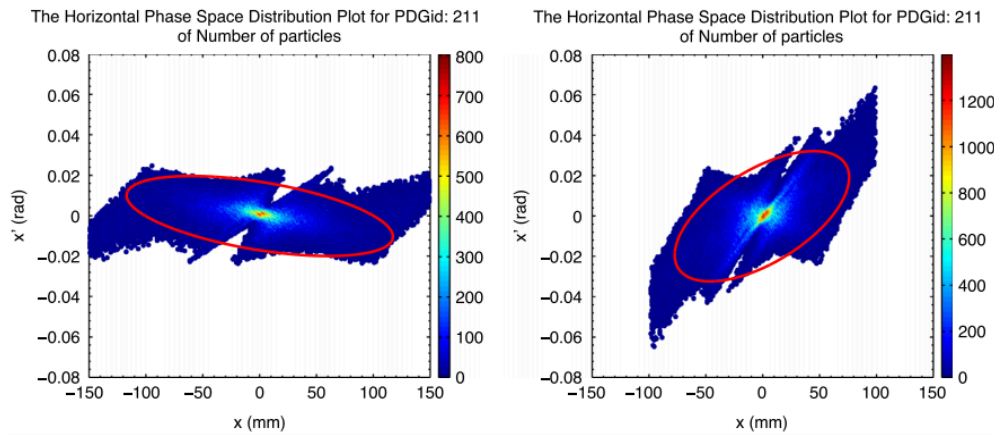
Figure 3: The transverse phase space distribution of the pions after the pre-optimized horn (left) and optimized horn (right). Because the pion beamline can provide optics matching, a positive correlation between x and x' can be accepted.

3.7.3.4 *MICE Step IV optics optimization using a SOGA*

The international Muon Ionization Cooling Experiment (MICE) will demonstrate ionization cooling, the only technique that, given the short muon lifetime, can reduce the phase-space volume occupied by a muon beam quickly enough. MICE will demonstrate cooling in two steps. In the first one, Step IV, MICE will study the multiple Coulomb scattering in liquid hydrogen (LH2) and lithium hydride (LiH). A focus coil module will provide focusing on the absorber. The schematic drawing of the key elements at Step IV is shown in Figure 4. The transverse emittance will be measured upstream and downstream of the absorber in two spectrometer solenoids (SS). Magnetic fields generated by two match coils in the SSs allow the beam to be matched into a flat-field region in which the tracking detectors are installed. An incident in September 2015 rendered matching coil #1 (M1D) of the downstream spectrometer inoperable. In this section, a new Step IV lattice without M1D and its optimization via a Single-Objective Genetic Algorithm (SOGA) will be described.
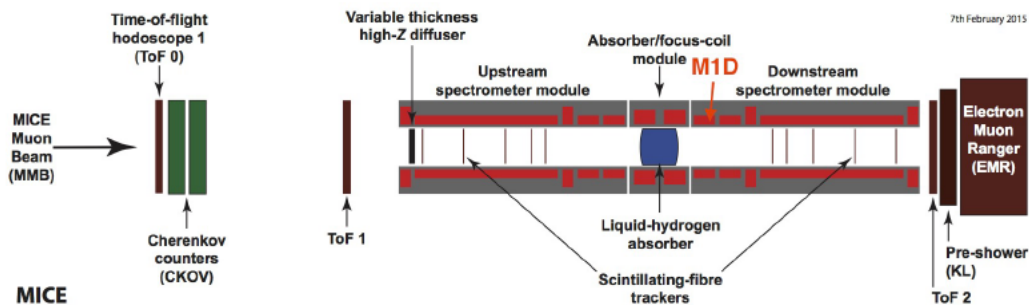
Figure 4: The schematic drawing of MICE Step IV

Due to system limitations in this optimization, 6 tunable coil currents, among the 12 coils were used as the variables in the SOGA. The optimization is based on multi-

particle tracking in G4Beamline from the upstream end of SS upstream (SSU) to the downstream end of SS downstream (SSD). G4Beamline has Geant4 implemented such that it provides an environment to model energy loss due to ionization, and also multiple Coulomb scattering.

The optimizations were done on 6 operational modes, which are combinations of three reference momenta, 140, 200, and 240 MeV/c and two solenoidal modes, flip and solenoid, where the direction of B_z flips and keeps the same in SSU and SSD, respectively. The optimization results indicated that 90% transmission can be reached with a few percent drop in the normalized rms 4D emittance. The coil currents were finely tuned to ensure stability of the lattice performance at that configuration. The 200 MeV/c, flip mode optimization result is shown in Figure 5 as an example.
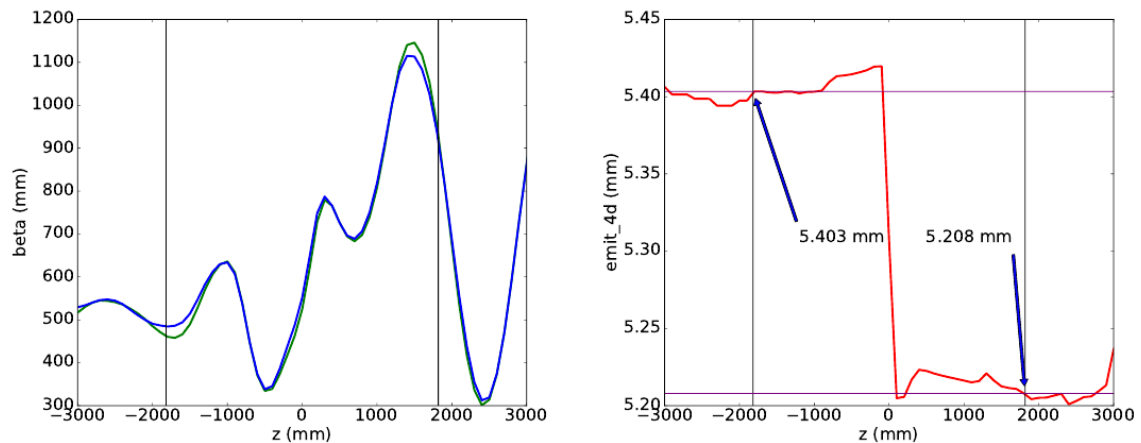
Figure 5: Optimization result of MICE Step IV 200 MeV/c flip mode optics, with β_X in blue and β_Y in green, and normalized emittance versus the longitudinal coordinate z for 200 MeV/c flip mode. Only the muons that make through the cooling channel are included in the emittance calculation. The two vertical lines mark the locations of the two reference planes, which are where the input and output emittances are defined. In this case, the transmission is 93% and the ε_n reduction is -3.7%.

3.7.3.5   *Conclusions*

Metaheuristic optimization algorithms are beneficial in muon facility designs. They are also frequently applied to many accelerator problems such as cavity design, ion source design, and so forth. Genetic algorithm, as one of the most known metaheuristic algorithms, was used to attain satisfactory improvement in the nuSTORM horn performance, and MICE Step IV optics without M1D.

3.7.3.6 *References*

1. D. Adey et al. on behalf of the nuSTORM collaboration, "nuSTORM – neutrinos from STORed Muons", Fermilab proposal 1028, 2013.

2. A. Liu, "Design and simulation of the nuSTORM facility", FERMILAB-THESIS-2015-04, 2015

3. S. Geer, "Neutrino beams from muon storage rings: Characteristics and physics potential", in Phys. Rev. D, 57, 6989, 1998

4. M. Yoshida, "The International Muon Ionization Cooling Experiment (MICE)", in Nuclear Physics B – Proceedings Supplements, 149, 94-98, 2005

5. CERN – BE/ABP Accelerator Beam Physics Group, "MAD – Methodical Accelerator Design", http://mad.web.cern.ch/mad/

6. T. Roberts and Muons Inc, "G4Beamine: a particle tracking simulation program based on Geant4", http://www.muonsinternal.com/muons3/G4beamline

7. S. van der Meer, "A directive device for charged particles and its use in an enhanced neutrino beam", in CERN-61-07

8. M. Bishai and M. Thomson, "LBNE Long-Baseline Neutrino Experiment Document 10688-v10", in LBNE-doc-10688-v10

4 Proton Proton Colliders

4.1 Lattice design of pp collider

Antoine Chance

Mail to: antoine.chance@cea.fr

CEA, IRFU, SACM, F-91191 Gif-Sur-Yvette

4.1.1 Introduction

A long list of optics and beam dynamics challenges for pp colliders includes the following: design of the interaction region with a low beta function; beam-beam effects; impedance, HOM losses and instabilities; achieving the dynamic aperture required for adequate beam lifetime, comprising the optimization of the arc optics; emittance control, including alignment and field errors, lattice nonlinearities, as well as beam-beam effects; machine protection, with dedicated halo cleaning section; injection and extraction of the beam. The lattice design has to handle these different challenges; the optimization is then multi-criteria like the machine performance or the machine cost. We will then consider here a few aspects of the lattice design like the arc optimization, some insertions like the interaction region or the beam cleaning insertions and how to tune the different regions together. To illustrate the problematics, we will use some examples coming from LHC [1], HL-LHC [2] or FCC-hh [3].

4.1.2 Layout of a pp collider

A pp collider like LHC or FCC-hh consists of a ring with two propagating beams H1 and H2. The first beam (H1) is assumed to run in the clockwise direction whereas the second beam (H2) runs in the other direction. Since both beams have the same charge, they cannot run on the same trajectory. Most magnets have then two beam chambers with opposite magnetic fields. At the interaction points (IP), both beams cross which implies a common chamber until the triplet neighboring the IP. To ensure the synchronism between both beams (and thus the same trajectory length), the layout has an even number of IPs. Two of the IPs are diametrically opposite whereas the other IPs are put symmetrically around. The collider length is chosen as a good trade-off between the feasibility of the dipole field, the geological constraints and the total cost. Parameters of different pp colliders are given in Table 1 [4].

The layout of a pp collider (see Figure 1) contains:

- High-luminosity insertions (2 in LHC and FCC-hh). They are diametrically opposite. To mitigate the beam-beam effects, the crossing angle is horizontal in one of them and vertical in the other. Some considerations on the lattice of such a section will be detailed further.

- Low-luminosity insertions (2 in LHC and FCC-hh). They are put in cluster with one of the high-luminosity insertions to mitigate beam-beam effects.

- An injection section. In LHC, both beams are injected in the low-luminosity insertions (ALICE and LHCb experiments). For FCC-hh, because of the higher injection energy, a dedicated section is under study. To minimize the needed magnetic fields, a phase of advance of 90 degrees is required between the injection septum blade and the injection kicker downstream.

- An extraction section. For machine protection, the collider must be able to extract the whole beam in few turns and to transport it up to the dump. A section is dedicated to the extraction to the dump in LHC and in FCC-hh [5].

- A cleaning section. Because of collisions, intra-beam scattering, multipole components in the magnets, or other perturbations, a halo is progressively created around the beam. That is why beam cleaning is necessary while operating. A dedicated section is then needed to do the betatron and momentum beam cleaning. In LHC, there is a dedicated section for the betatron beam cleaning (in both planes) and another for the momentum cleaning. These insertions are based on the multi-stage scheme, which will be detailed further. In the case of FCC-hh, the baseline uses a similar scheme as for LHC with the betatron cleaning in one insertion and the momentum cleaning in another. To protect the arcs from a badly extracted beam, the betatron collimation section is located downstream to the extraction section. An alternative under investigation is to have an insertion (shorter) dedicated to the extraction alone and an insertion combining the betatron and the momentum collimation.

- RF sections. Contrary to ee colliders, the synchrotron radiation stays low. Therefore, we do not need to distribute the RF sections around the machine and the needed total voltage is quite low. The RF sections are then put where there is space enough and no dispersion.

- Dispersion suppressors (DIS). Special care must be taken to have a dispersion function lower than in the momentum collimation section in the DIS upstream in order not to spoil the collimator hierarchy.
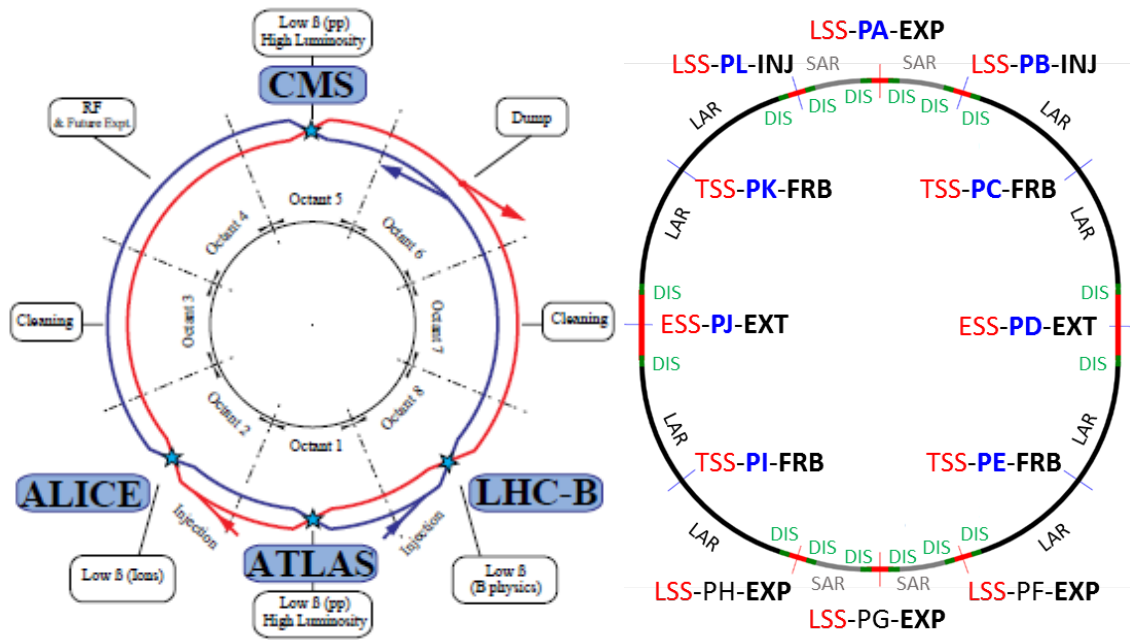
Figure 1: Layout of the LHC (left) and of the FCC-hh (right).

The pp collider cost is driven by the dipole cost and thus by the dipole magnetic field, which is directly correlated to the filling ratio of the arcs. Special care must be taken to make the arcs as compact as possible. In FCC-hh, there are short and long arcs (SAR and LAR). The length of the SAR was determined by the constraints on the injection transfer lines.

Table 1: Comparative parameters of LHC, HL-LHC and FCC-hh.

	LHC (Design)	HL-LHC	FCC-hh baseline	FCC-hh ultimate
Main parameters and geometrical aspects				
c.m. Energy [TeV]	14		100	
Circumference C [km]	26.7		100	
Dipole field [T]	8.33		16	
Arc filling factor	0.79		0.79	
Straight sections	8 x 528 m		6x1400 m+2x4200 m	
Number of IPs	2 + 2		2 + 2	
Injection energy [TeV]	0.45		3.3	
Peak luminosity* [10^{34} cm^{-2} s^{-1}]	1.0	5.0	5.0	< 30.0

Beam parameters

Number of bunches n at 25 ns/5 ns	2808		10600/53000	
Bunch population N[10^{11}] 25 ns/5 ns	1.15	2.2	1.0/0.2	
Transverse normalized emittance [μm] 25/5 ns	3.75	2.5	2.2/0.44	
Number of IPs contributing to ΔQ	3	2	2	2
Maximum total β-β tune shift ΔQ	0.01	0.015	0.01	0.03
Beam current [A]	0.584	1.12	0.5	
RMS bunch length [cm]	7.55		8	
IP beta function [m]	0.55	0.15 (min)	1.1	0.3
RMS IP spot size [μm] 25 ns /5 ns	16.7	7.1 (min)	6.8/3	3.5/1.6
Full crossing angle [μrad]	285	590	91	175

Other beam and machine parameters

Stored energy per beam [GJ]	0.392	0.694	8.4	8.4
SR power per ring [MW]	0.0036	0.0073	2.4	
Arc SR heat load [W/m/aperture]	0.17	0.33	28.4	28.4
Energy loss per turn [MeV]	0.0067		4.6	
Critical photon energy [keV]	0.044		4.3	
Longitudinal emittance damping time [h]	12.9		0.5	
Horizontal emittance damping time [h]	25.8		1.0	
Dipole coil aperture [mm]	56		50	
Beam pipe half aperture [mm]	~20		13	

* Depending on the operational scenario, the peak luminosity might increase to larger values during the run.

** The crossing angle will be compensated using the crab crossing scheme.

4.1.3   **First order optics**

4.1.3.1   *Arc cell*

Generally, we use FODO cells in the arcs because they have the advantage to be robust, to have a good filling ratio, and to have a large energy acceptance. Contrary to the LHC, the synchrotron radiation of the protons is not negligible for FCC-hh [4]. An alternative to FODO cells is multi-bend achromats (MBA) [6] which are usual in synchrotron machines. The advantage of the MBA is to have smaller equilibrium emittances. The counterpart is stronger quadrupoles and less flexibility on the location of the magnets. The beam emittance will decrease while running, counterbalancing the emittance growth from beam-beam effects. Nevertheless, the aim is to optimize the average luminosity. A too large peak luminosity (coming from a too small emittance) will increase the beam burn-off in the experiment and thus decrease the beam lifetime. Therefore, having the smallest equilibrium emittance is not necessarily the best thing for the machine operation optimization. That is why FODO lattices are used for the arc cell of pp colliders.

The layout or the half-FODO arc cell for FCC-hh is shown in Figure 2. The magnetic length of the dipole is drawn in yellow. The spool pieces (in blue) are in the dipole cryostats. Another cryostat contains the quadrupole (in green), the sextupole (in cyan), the BPM, the orbit corrector (in magenta), the trim quadrupole, and other multipole correctors.
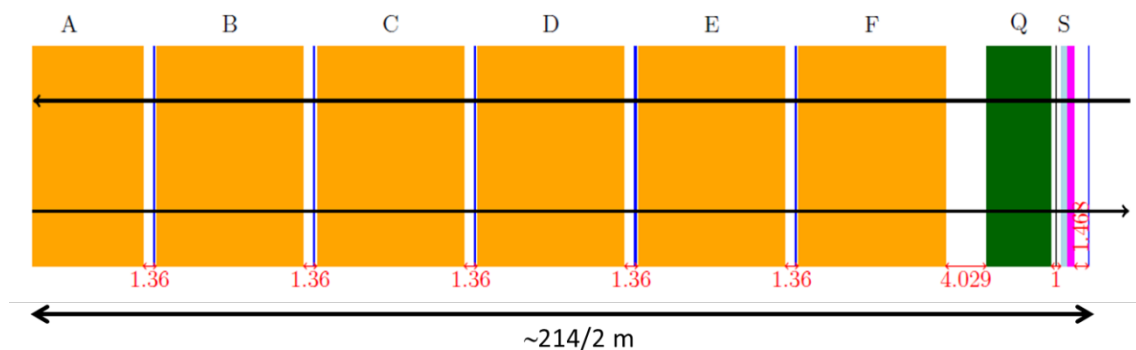
Figure 2: Layout of an arc half-cell.

In LHC [1] and in the baseline of FCC-hh, the phase advance is 90° in both planes. The optics functions of the arc cell of the FCC-hh are shown in Figure 3. The advantages of a phase advance of 90° are:

- A ratio βmax/Lcell near the minimum [7].
- A small ratio Dmax/Lcell.
- A good efficiency between the corrector and the BPM one cell downstream.
- A compensation of the sextupoles every other cell.
- A compatibility with more advanced scheme like the achromatic telescopic squeezing (ATS) [8].
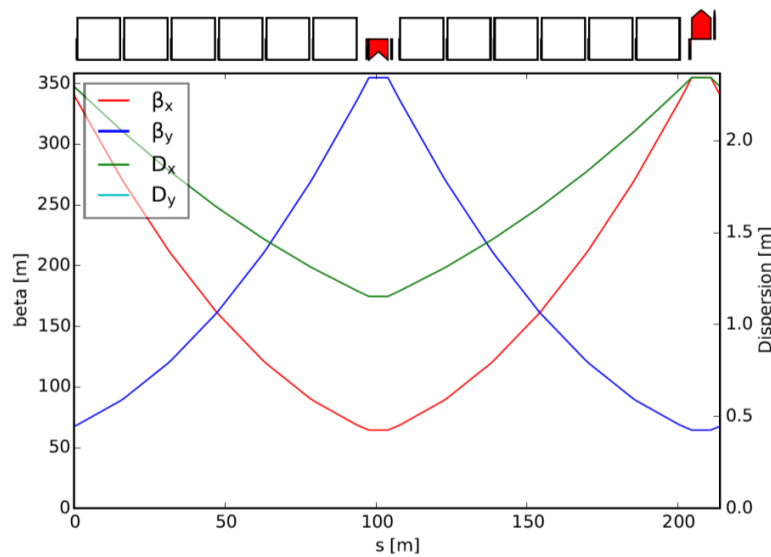
Figure 3: Optics functions of the FCC-hh arc cell.

An alternative to a phase advance of 90 degrees is 60 degrees. This phase advance is also standard and was used in LEP for example [9]. The advantages of a phase advance of 60° are:

- A smaller quadrupole gradient.
- A smaller sextupole gradient.
- A ratio βmax/Lcell near the minimum [7].
- A compensation of the sextupoles every three cells.

The drawbacks are an enlarged dispersion by a factor 1.8 and a less good efficiency of the correctors. A larger dispersion implies a decrease of the energy acceptance of the collider ring, which requires more care on the beam momentum cleaning.

The cost of the arcs is driven by the dipole and more precisely by the peak field in the dipoles. That is why the cell length is optimized to maximize the filling ratio of the collider from a list of parameters [10]:

- The collider ring length.
- The length of the insertions.
- The dipole magnetic length.
- The minimum quadrupole magnetic length.
- The spacing dipole-dipole.
- The minimum spacing quadrupole-dipole.
- The minimum magnetic quadrupole length.

The magnetic field versus the arc cell length is plotted in Figure 4 for FCC-hh. Several dipole magnetic lengths were considered from 14 m to 15 m. The upper limit is given by the transportation limitations of the cryostat.
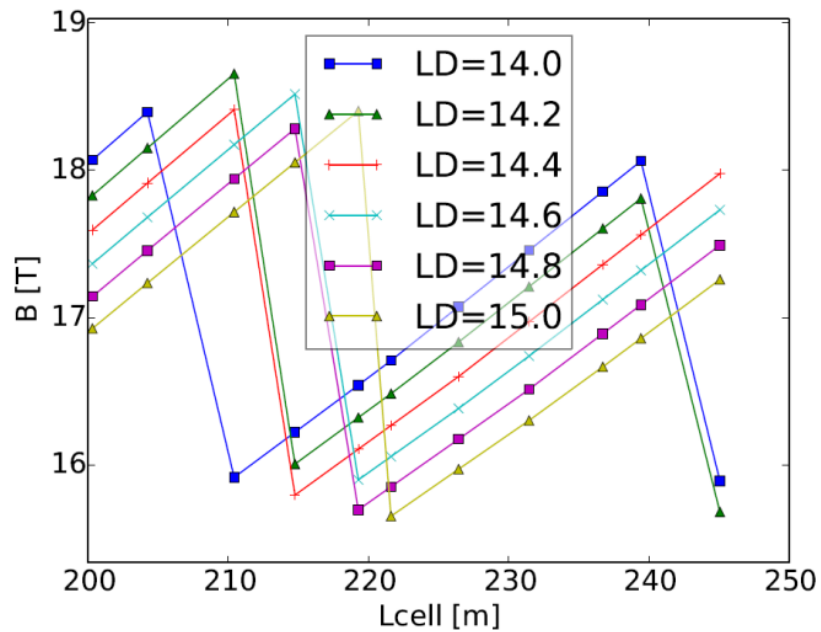
Figure 4: Variation of the dipole field with the cell length in the case of FCC-hh.

It is worth notifying that there is a dipole field minimum when a dipole is added or removed in the half-cell. Longer cells enable to reduce at once the integrated gradient (and thus their length) and the total number of arc quadrupoles. The filling ratio decreases thus a little. However, betatron functions and dispersion proportionally increase with the arc cell length. That implies that the beam stay clear will decrease at the injection. Moreover, a larger dispersion reduces the energy acceptance of the machine. The dispersion in the momentum collimation insertion must increase too to keep the collimator hierarchy: the dispersion in the DIS downstream must be lower than in this section. The cell length is thus a trade-off between energy acceptance, feasible quadrupole gradients and filling factor.

4.1.3.2 *Dispersion suppressor*

The dispersion suppressor (DIS) is used to match the dispersion (and the betatron functions) between the arcs and the insertions. The dispersion is not necessarily zero at the exit of the DIS (for instance at the entrance of the momentum collimation section in the LHC). Several kinds of dispersion suppressor can be used [7] [10] [11]:

- Half-bend DIS. The cell used for the DIS is similar to the one used in the arcs. The magnetic field in these cells is half of the one in the arcs whereas the quadrupole gradient stays the same. This kind of DIS can be used if the phase advance in the FODO cells divides 180 degrees. The advantage of this kind of DIS is to keep the same optics functions and gradients as in the arc cells by killing respectively the dispersion in 2(3) cells if the phase advance is 90(60) degrees. The drawbacks are to have a filling ratio about the half of the one encountered in the arc cells and to work only for a phase advance.

- DIS with variable magnet field. The dispersion can be suppressed in two cells if the bending angles are $\varphi_1 = \varphi\left(1 - \frac{1}{4\sin^2\frac{\mu}{2}}\right)$ and $\varphi_2 = \frac{\varphi}{4\sin^2\frac{\mu}{2}}$ where φ is the bending angle of an arc cell and its phase advance. It is worth notifying that $\varphi_1 > 0$ and $\varphi_2 < \varphi$ if $\mu > 60°$. Moreover, this DIS is equivalent to the half-bend DIS when the phase advance is 90 degrees. The advantage is to keep the same gradient as in the arc cell but the filling ratio is only the half of the arc cell.

- LHC-like DIS. This DIS was historically developed to make the DIS fit the tunnel of the LEP. It is made of one FODO arc cell, a half-FODO cell with an angle equal to the two thirds of the one in the arcs and three FODO cells of which the length if two thirds of the arc cell. A layout of this DIS is given in Figure 5. The advantage of this DIS is to be compact (near the maximum we can get) and to have some flexibility. The drawback is to need stronger quadrupoles than in the previous cases and to need to match their strength. Moreover, the dispersion can be larger than in the arcs.

- Full-bend DIS. This DIS is made of three arc FODO cells. A layout of the dispersion suppressor is given in Figure 6. The quadrupoles are used to match the dispersion and the betatron functions. The advantage is to be very compact. The drawback is that the needed gradients are stronger than in the other DIS and that the dispersion can have a peak there.

The studies for HL-LHC have shown that some off-momentum debris coming from inelastic collisions in the collimation section are not stopped before the arcs and may damage the machine [12]. That is why the layout of the DIS will be a bit modified from the LHC for 2020. One of the dipoles will be shortened (with an increased magnetic field to 11 T) to enable the insertion of a collimator, which will protect the arc entrance.

The baseline DIS for FCC-hh is the LHC-like one because it is a good trade-off between the filling ratio and the needed quadrupole gradients. From the beginning of the studies, special care must be taken to verify if the collimation section enables to collect the off-momentum debris [13]. Otherwise, the design of the DIS downstream to the collimation sections has to take into account this additional constraint. A dispersion peak is then needed in the DIS to put a collimator at this position. The full-bend DIS cannot be used in this case because of the lack of space for a collimator.
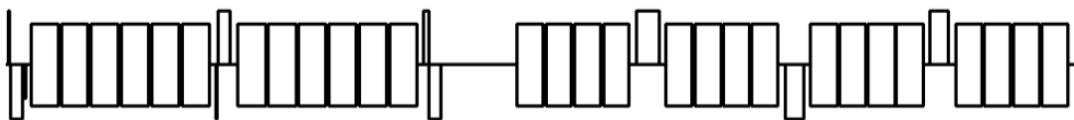
Figure 5: Layout of the LHC-like dispersion suppressor.

Figure 6: Layout of the full-bend dispersion suppressor.

4.1.3.3 *Interaction region*

The interaction region (see Figure 7) contains the detector around the IP, two triplets neighboring the IP to focus the beam in both planes, a set of four dipoles to enable the beam crossing at collision, a set of four kickers to adjust the crossing angle and a set of matching quadrupoles.

Design of the interaction region optics goes through several iterations in terms of the key parameters of the design –the achievable minimum β^* at the IP, the distance L* from the IP to the front of the first quadrupole and the triplet length. These key performance parameters include beam stay clear in the final triplet and energy deposition characteristics, which affect the lifetime of the triplet [14]. Indeed, a small β^* and a large L* imply large betatron functions in the triplet and so on a larger chromaticity and a smaller dynamic aperture (because of the triplet imperfections). The studies performed for FCC-hh show that L* and/or triplet length can easily be increased until chromaticity and dynamic aperture become the main issues, and that the triplet length has larger impact on the minimal achievable value of β^* at the IP than L* [15] [16]. Therefore, the used strategy is to select the shortest L* that does not limit the detector, and then increase the length of the triplet until it hits the limit due to dynamic aperture. The injection optics of the interaction region is then designed to have an enlarged value of the β-function at the IP to maintain the needed stay clear in the interaction region.

While colliding, both beams cross with an angle which can reach values up to $P_{\text{Xing}} = \sqrt{\varepsilon_N/\gamma\beta^*}\, n_{\text{Xing}}$ where n_{Xing} is the half-crossing angle in sigmas, and ε_N the normalized transverse emittance. The orbit excursion in the triplet generates then a residual dispersion, which must be corrected. Indeed without any correction, the dispersion peak generated by this wave is emphasized by the triplet at the next IP and can reach several meters there. There are different correction schemes for the spurious dispersion.

The first correction scheme is to match the spurious dispersion with the quadrupoles of the dispersion suppressor but we can only correct the spurious dispersion generated by a horizontal crossing angle and the needed gradients in these quadrupoles are likely to significantly increase.

In the case of HL-LHC, the entrance correctors and exit correctors of the arcs neighboring the low-β IPs are switched on [8]. The phase advance between the used correctors and the IP is near 90° modulo 90°. The closed orbit in the arc quadrupoles generates a dispersion wave which compensates the spurious dispersion after several FODO cells. The angles in the correctors are then adjusted to cancel the spurious dispersion at the exit of the arcs neighboring the low-β IPs. The quadrupoles of the DIS are matched to correct the β-beating created by the orbit excursion in the arc sextupoles (notify that this β-beating is almost nullified if you use the ATS scheme). The chromaticity created by the closed orbit in these arcs is then corrected by the sextupoles in the other arcs. The studies for HL-LHC have shown that the orbit bump you need in the arcs can be halved if you use an ATS scheme [8].

Another correction scheme was proposed for the pp collider SSC [17]. The idea is to generate a dispersion wave with trim quadrupoles located in the arcs. Indeed, the

dispersion η generated by a trim quadrupole (indexed by q) of integrated strength $K_q l_q$ at the position s is:

$$\eta_x(s) = -\eta_{qx}\sqrt{\beta_x(s)\beta_q}K_q l_q \sin\big(\mu(s) - \mu_q\big) \qquad (1)$$

By this way, if the phase advance between the trim quadrupoles is 180 degrees and their strength is opposite, the betatron wave generated by the couple of quadrupoles is zero out of the range in between and the dispersion wave is non zero. This scheme enables then to correct the spurious dispersion with a set of 4 quadrupole families. The vertical spurious dispersion is corrected by using skew quadrupoles instead of normal quadrupoles.
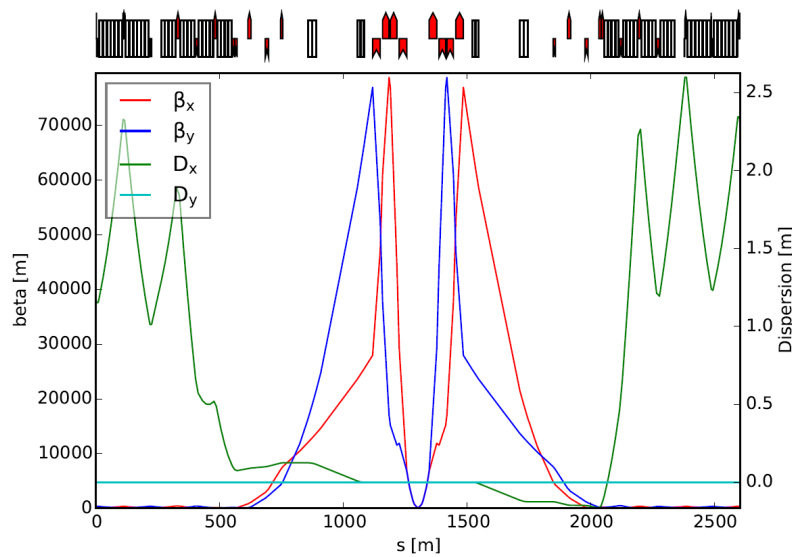
Figure 7: Optics functions of the interaction region of FCC-hh.

4.1.3.4 *Collimation section*

The collimation systems have different roles like the halo cleaning versus quench limits (for SC machines), the passive machine protection (first line of defense in case of accidental failures), the reduction of total doses on accelerator equipment (providing local protection to equipment exposed to high doses), the cleaning of physics debris (collision products to avoid SC magnet quenches close to the high-luminosity experiments), the concentration of losses/activation in controlled areas to avoid many loss locations around the collider, and to optimize background in the experiments (minimizing impact of halo losses on quality of experimental data). Because of the stored energy in the beam, the halo cleaning is a priority in colliders like LHC or FCC-hh, which makes dedicated sections for the halo cleaning mandatory [1] [18].

The strategy used in LHC is multi-stage collimation section [1]. A principle scheme is given in Figure 8. This scheme has given very good performance and is chosen as a starting point for the baseline of FCC-hh. The basic idea is to use primary collimators to give an angular kick to the halo particles which are then collected into secondary

collimators, which are put at the right phase advances to catch the secondary halo. Tertiary collimators are then used to collect the debris coming from the secondary collimators. The longitudinal and transverse positions of the different collimators are then optimized to maximize the cleaning inefficiency. This optimization needs a precise definition of the magnet aperture and tracking simulations to take into account the different interactions with the collimators (elastic and inelastic collisions).

For instance, the studies on LHC have shown that the primary betatron cleaning is to be made with three primary jaws, namely horizontal, vertical and skew [19] [20]. A reasonably good optimum is obtained with four secondary jaws per primary collimator. Figure 9 shows the corresponding optics functions in the betatron cleaning insertion for the first beam.

Particles outside the momentum range of the nominal circulating beam must be absorbed in the momentum cleaning insertion before they can be lost in the arcs. In order to decouple the momentum collimation from the betatron-collimation, the primary collimator jaws must be at a location with large dispersion and small betatron function. The optics design in this section aims at maximizing the normalized dispersion. The normalized dispersion must be large enough at the primary collimator to protect the arc aperture from off momentum particle losses [19]. Requiring further that the cut of the secondary halo is independent of the particle momentum one obtains a second constraint for the optics at the position of the primary collimator [19] [20]:

$$\frac{D'_x}{D_x} = -\frac{\alpha_x}{\beta_x} \tag{2}$$

Once the locations of the primary collimator jaw are fixed the positions of the secondary collimator jaws are constrained by the required phase advance between primary and secondary collimators. At least four secondary jaws were required in LHC to cut the secondary halo adequately [20]. Furthermore, the above constraints must be satisfied simultaneously for both beams. The optics of the momentum collimation section for the LHC is shown in Figure 10.
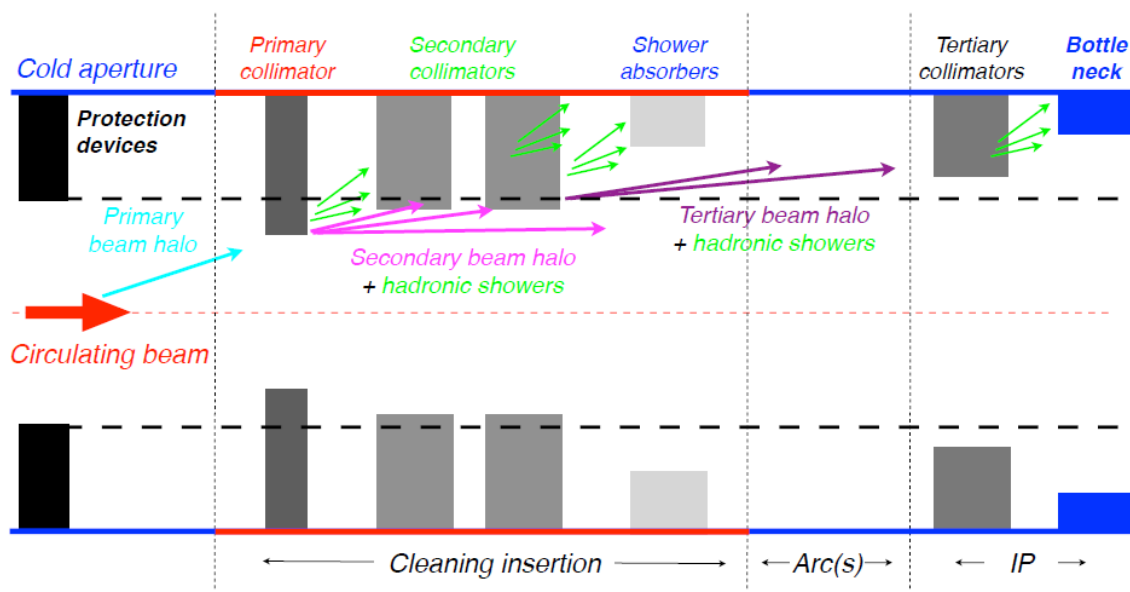
Figure 8: Principle of the multi-stage collimation.
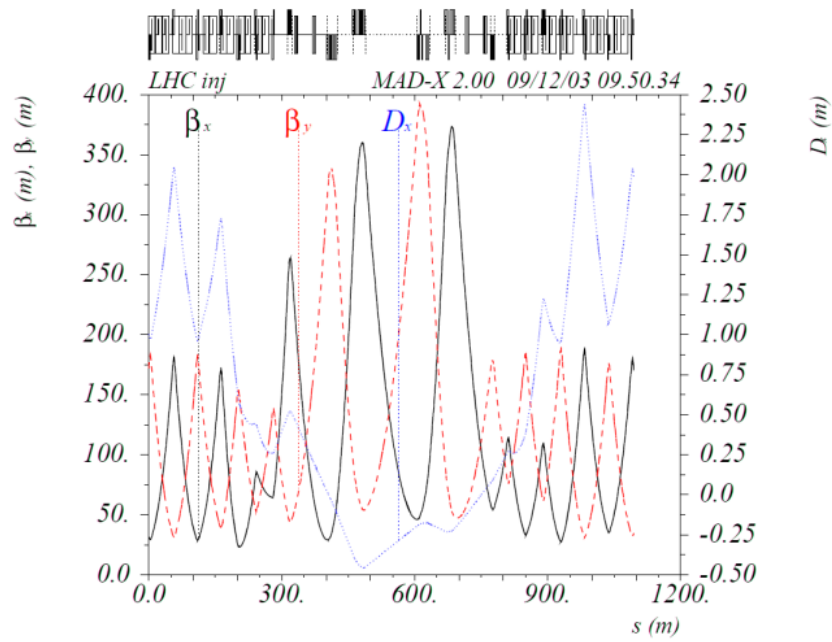
Figure 9: Optics functions in the betatron cleaning insertion of the LHC.
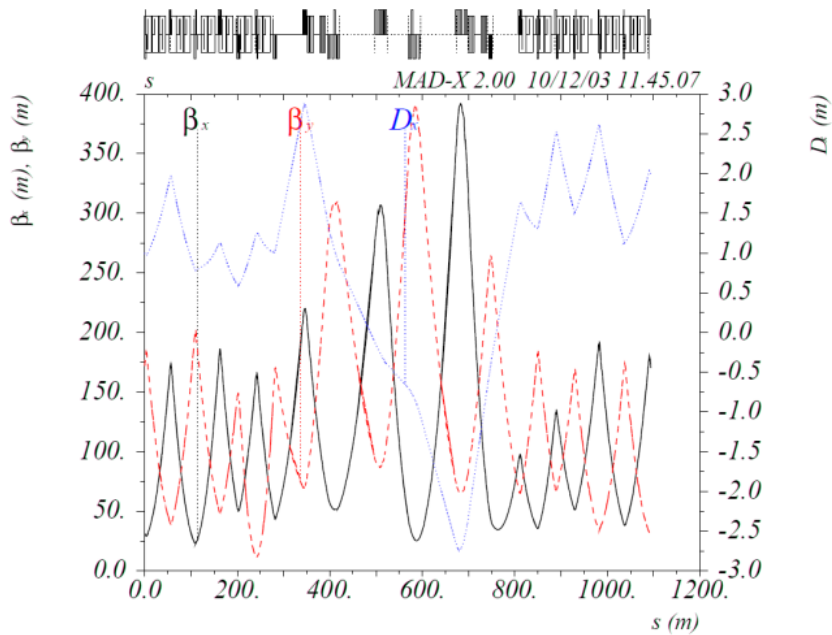
Figure 10: Optics functions in the momentum cleaning insertion of the LHC.

4.1.3.5 *Tuning of the collider*

The global tunes of machines like LHC were optimized by exploring the fractional parts of the tunes versus the dynamic aperture (at injection and at collision). The result enabled to give the baseline tune and to evaluate the operational margin on this tune [1]. The tuning of the collider can be done by tuning the insertions which do not drive the beam dynamics and dynamic aperture of the machine (for example the RF insertions). That is the strategy used in LHC. The advantage is to keep the same phase advance in

the arcs for all operation scenarios, which keep the dynamic aperture studies valid. Another possibility is to use the arcs by adding a small perturbation to the phase advance. When the number of FODO cells is large like in FCC-hh, this perturbation stays small.

In LHC, a phase advance of 90/270 degrees module 360 degrees is performed between the two main IPs to compensate the chromatic effects. By this way, a correction is made on the Montague functions [21]:

$$a_{x,y} = \frac{\partial \alpha_{x,y}}{\partial \delta} - \alpha_{x,y} b_{x,y} \tag{3}$$

$$b_{x,y} = \frac{\partial \beta_{x,y}}{\partial \delta} \tag{4}$$

$$w_{x,y} = \sqrt{a_x^2 + b_x^2} \tag{5}$$

4.1.4 Higher order optics

4.1.4.1 *Chromaticity correction*

The simplest scheme is to correct the chromaticity by two sextupole families distributed in the arcs like in LHC. The advantage of phase advance of 90 degrees in the arc cells is to have a compensation of the sextupole kick every two cell, which enables to keep a large dynamic aperture.

Nevertheless, for HL-LHC, the existing sextupoles in the LHC were not strong enough to compensate the excess of chromaticity generated in the experimental triplets (smaller beta-function at the IP). That is why a new scheme was developed: the achromatic telescopic squeeze (ATS) [8].

This idea uses the phase advance of 90 degrees in the arc cells. Indeed, if you generate a betatron wave at the entrance of the arcs (with trim quadrupoles for instance), the period of the betatron wave is exactly two FODO cells. Therefore, you have a pattern in the arcs with different optics functions every two cell. The advantage is to enable the increase of the betatron function every two sextupole by keeping the same dispersion function and thus to increase the efficiency of these sextupoles. In that aim, you need two additional sextupole families, so-called strong and weak families, located in the arcs neighboring the IP.

Nevertheless, the ATS goes further by correctly phasing the sextupoles with the IPs and by using the additional degree of freedom given by these two extra families. Firstly, in the so-called presqueezed optics, the betatron wave is not realized (the betatron functions are matched to the Twiss parameters of the FODO arc cell). The phase advance between the low-β IP and the strong family is matched to have 90+ε degrees modulo 180 degrees. The value of ε is not zero and takes into account the aspect ratio of the betatron functions (in both planes) at the sextupoles. The strength of the strong family is calculated to compensate the chromaticity generated in the triplets neighboring the low-β IPs. The residual chromaticity (generated for example in the arcs) is corrected by the sextupoles in the other arcs. The good phasing between the triplet and the strong

sextupoles makes the second order chromaticity much lower than in the nominal LHC. For the same reason, the off-momentum betatron fuction is near zero at the low-β IP. For comparison, the Montague functions are shown in Figure 11 for the nominal LHC optics and for the presqueezed ATS optics.
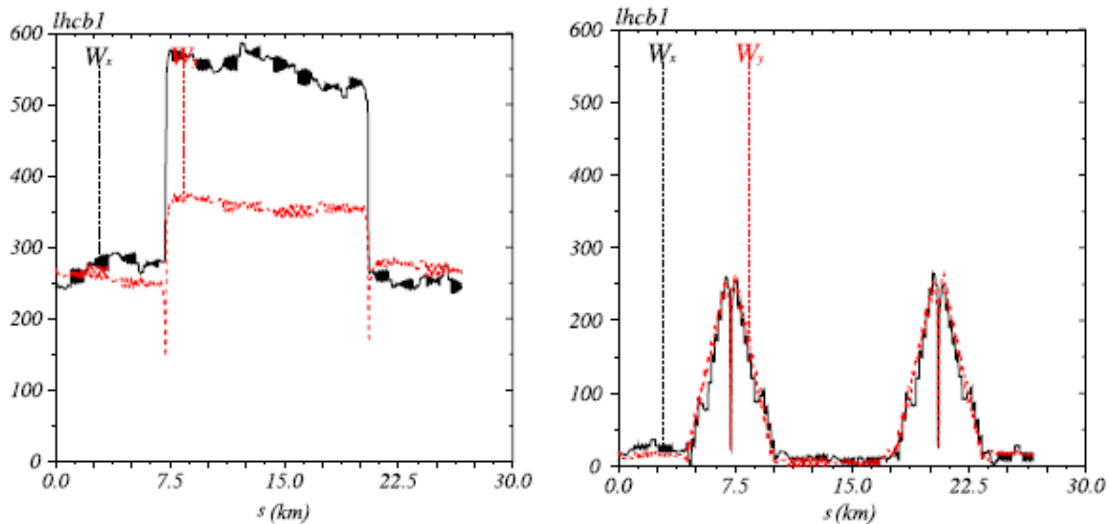
Figure 11: Montague functions along the LHC ring. The right picture stands for an ATS optics presqueezed down to β*=36 cm, compared to a nominal-like LHC optics with β*=55 cm (left).

4.1.4.2   *Dynamic aperture*

Although there is a large arsenal of theoretical tools and fast tracking techniques and computers available [22], it remains impossible to track all relevant effects for sufficiently long times. Even with present day computers it is not possible to perform a full scale simulation over 4×10^7 turns, which corresponds to one hour of beam storage time in LHC. The dynamic aperture (DA) obtained from simulations is typically 20% too optimistic when compared with dedicated beam experiments at several accelerators. Indeed, it is known from existing hadron storage rings that there are effects that limit the performance of any new machine. It is very hard to predict by how much the machine will suffer from lattice imperfections, power supply ripple and transient effects. Therefore, to ensure that particle motion is sufficiently linear in an amplitude range relevant for the collimation system, i.e. roughly 6 RMS sizes, the target DA was a factor 2 larger for the LHC, i.e 12 σ, in the absence of the very strong beam beam interaction which should be treated separately [1]. For HL-LHC a better knowledge of the machine has enabled to reduce this target value to 10.5 σ.

At injection, the DA is mainly degraded by the different multipole contributions in the main dipole magnets. The linear part perturbation is compensated by dipolar correctors and trim quadrupoles. Spool pieces powered in series are then used to compensate the systematic components up to a given multipole order; the random part stays uncorrected. A specific correction scheme is then undertaken to correct the systematic part of the multipole components [23].

It is worth notifying that it is based on a good knowledge of the magnet behavior when ramping up in energy. In the case of a large energy range between the injection and the collision energy, persistent currents can give a chaotic behavior of the magnets at injection and thus an ill correction of the dipole contributions.

At collision, the main DA degradation source mainly comes from the strong beam-beam effects at the low-β IP [24]. An additional degradation comes from the multipole contributions in the triplet because of beam offset there. A good phasing between the low-β IPs as in LHC enables to partially correct the beam-beam effects.

4.1.5 References

1. O. Brüning *et al.*, "LHC Design Report", in Optics and Single Particle Dynamics, Geneva, CERN, 2004.

2. "The HL-LHC project", http://hilumilhc.web.cern.ch/.

3. "Future Circular Collider Study", https://fcc.web.cern.ch/.

4. D. Schulte, "Preliminary collider baseline parameters", EuroCirCol-D1-1, 2015.

5. T. Kramer *et al.*, "Considerations for the Beam Dump System of a 100 TeV Centre-of-mass FCC hh Collider", in Proc. IPAC'15, Richmond, VA, USA, May 2015, 2015.

6. D. Einfeld, M. Plesko and J. Schaper, "First multi-bend achromat lattice consideration", Journal of Synchrotron Radiation, vol. 21, no. Pt 5, pp. 856-861, 2014.

7. E. Keil, "Lattices for Collider Storage Rings", in Handbook of accelerator physics and engineering, World Scientific, 2006, pp. 76-78.

8. S. Fartoukh, "Achromatic telescopic squeezing scheme and application to the LHC and its luminosity upgrade", Phys. Rev. ST Accel. Beams, vol. 16, p. 111002, 2013.

9. J. A. Uythoven, "A LEP (60,60) optics for energy calibration measurements", CERN-SL-97-058-OP, CERN-SL-97-58-OP, 1997.

10. A. Chance *et al.*, "First results for a FCC-hh ring optics design", Tech. Rep. CERN-ACC-2015-0035, CERN, Geneva, 2015.

11. B. Dalena *et al.*, "First Considerations on Beam Optics and Lattice", in Proc. IPAC'15, Richmond, VA, USA, May 2015, 2015.

12. R. Bruce *et al.*, "Energy deposition simulations for upgraded collimation layouts", CERN-ACC-2014-0009, 2014.

13. J. Molson, P. Bambade, S. Chance and A. Faus-Golfe, "Simulation of the FCC-hh Collimation System", in Proc. IPAC'16, Busan, Korea, 2016.

14. R. Martin, M. I. Besana, F. Cerutti and R. Tomás, "Radiation load optimization in the final focus dystem of FCC-hh", in Proc. IPAC'16, Busan, Korea, 2016.

15. R. Martin, R. Tomás and B. Dalena, "Interaction Region for a 100 TeV Proton-Proton Collider", in Proc. IPAC'15, Richmond, VA, USA, 2015.

16. A. S. Langner, Developments on IR baseline design, presented at the FCC week, Rome, Italy, 2016.

17. Y. Nosochlov and D. M. Ritson, "The provision of IP crossing angles for the SSC", in Proc. PAC-1993, Washington, DC, USA, 1996.

18. R. Appleby *et al.*, "Collimation system", in High-Luminosity Large Hadron Collider (HL-LHC) Preliminary Design Report, CERN-2015-005, 2015, pp. 109-130.

19. T. Trenkler and J. B. Jeanneret, "The principles of two-stage betatron and momentum collimation in circular accelerators", Part. Accel., vol. 50, pp. 287-311, 1995.

20. J. Jeanneret, "Optics of a two-stage collimation system", Phys. Rev. ST Accel. Beams, vol. 1, n° 18, p. 081001, 1998.

21. G. Brown, The Physics and Technology of Ion Sources, 2nd, Revised and Extended Edition.

22. E. McIntosh, T. S. Pettersson and F. Schmidt, "A Proposal for a Numerical Accelerator Project", Part. Acc., vol. 55, pp. 107-118, 1996.

23. B. Dalena *et al.*, "First evaluation of dynamic aperture at injection for FCC-hh", in Proc. IPAC'16, Busan, Korea, 2016.

24. D. Angal-Kalini *et al.*, "Machine Layout and Performance", in High-Luminosity Large Hadron Collider (HL-LHC) Preliminary Design Report, CERN-2015-005, 2015, pp. 21-60.

25. A. Chance *et al.*, "Status of the Beam Optics of the Future Hadron-Hadron Collider FCC-hh", in Proc. IPAC'16, Busan, Korea, 2016.

4.2 The Right Optics Concept for the Right Dimension of the High Luminosity LHC Project

Stéphane David Fartoukh

Mail to: stephane.fartoukh@cern.ch

CERN, Geneva, Switzerland

4.2.1 Introduction

The High Luminosity LHC (HL-LHC) [1] is being designed to deliver an integrated luminosity of at least 250 fb^{-1}/year in each of the two general purpose detectors ATLAS and CMS of the LHC, while operating the other two experiments, Alice and LHCb, at a very low (~10^{31} cm^{-2} s^{-1} [2]) and moderate ($1 - 2 \times 10^{33}$ cm^{-2} s^{-1} [3]) instantaneous luminosity, respectively. This ambitious performance target cannot be met without pushing to some extreme both the optics, namely β^*, and the nominal parameters of the LHC beam (see Tab. 1).

Upgrading the beam parameters at the entry of the LHC, in order to meet the HL-LHC targets in terms of bunch spacing, bunch charge, and emittance forms the scope of the LHC Injector Upgrade (LIU) project [4]. The main focus of HL-LHC project is then to enable an aggressive and performance efficient reduction of β^*, thanks to

  i. the appropriate dimensioning, in particular the aperture, of the new hardware in order to preserve the transverse acceptance of the new high-luminosity insertions (IR) for collision optics with unprecedentedly low β^* down to 10-15 cm, or even less for flat optics, compared to 55 cm for the nominal LHC [5] (already reduced to β^*=40 cm in 2016),
  ii. the implementation in the layout of so-called head-on collision tools in order to reduce as much as possible the Piwinsky angle, and therefore mitigate its detrimental impact onto the luminosity, despite of the crossing angle which is needed to warrant a sufficient transverse separation of the two beams after the collision.

In this respect, the HL-LHC relies on a certain number of very challenging new equipment and innovative technologies, such as

  i. new larger aperture super-conducting magnets, and in particular new inner triplet quadrupoles with a 150 mm coil aperture, more than doubled with respect to the existing NbTi triplet, but still operating at a gradient of 130-140 T/m thank to the Nb3Sn technology, and therefore still 'reasonably' short in order to facilitate their integration,
  ii. crab-cavities, which are high-frequency RF transverse deflectors and aims at pre- serving the luminosity gain with $1/\beta^*$ by ensuring head-on collisions at the

inter- action point (IP), despite of the crossing angle which is needed to separate the two beams later on, in particular in the inner triplet.

Table 1: HL-LHC baseline parameters compared to LHC for proton-proton operation. Performance related quantities such as virtual luminosity, levelling time, line pile-up density have been calculated following Ref. [6]. The numbers in parentheses refer to an ultimate β^* of 10 cm.

Parameter	Unit	LHC	HL-LHC
Energy /beam	TeV	7	7
Bunch spacing	ns	25	25
Number of bunches	-	2808	2748
Bunch charge	10^{11} p/bunch	1.15	2.2
Beam curent	A	0.58	1.09
Bunch length r.m.s.	cm	7.55	7.5
Number of collisions at IP1 and IP5	-	2808	2736
Normalized emittance	μm	3.75	2.5)
β^* at IP1 and IP5	cm	55	15 (10)
Full Crossing angle	μm	285	590 (720)
Full Crossing angle	[σ]	9.4	12.5
Peak luminosity (w/o crab cavity)	10^{34} cm^{-2}s^{-1}	1.0	7.2 (9.0)
Virtual luminosity (peak with crab cavity)	10^{34} cm^{-2}s^{-1}	1.2	19.6 (26.9)
Levelled luminosity	10^{34} cm^{-2}s^{-1}	-	5.0
Levelling time @ 5×10^{34} (with crab cavity)	h	-	8.3 (9.5)
Pile/up event/crossing @ 5×10^{34}	-	27	138
Size of Luminous region r.m.s. at $\beta^* = 15$ (10) cm	cm	4.5	4.4 (4.1)
Peak line pile up density at $\beta^* = 15$ (10) cm	event/mm	0.24	1.25 (1.37)

The maximum possible peak luminosity is however limited in practice by several factors, in particular the number of pile up events per bunch crossing which can rapidly degrade the quality of the data collected for the physics analysis. In this respect, the HL-LHC relies on a constant instantaneous luminosity, not exceeding 5×10^{34} cm^{-2}s^{-1} and corresponding to approximately 140 events in average per bunch crossing for operation with 25 ns bunch spacing ($\sim$ 2'750 collisions at IP1 and IP5 per revolution period). This is achieved through challenging luminosity leveling techniques, for instance via a gradual reduction of β^* in order to compensate for the proton burn off during the physics coast. In order to sustain such a high luminosity, over typically 8 to 10 hours of stable beam, the beam parameters, in particular the total beam current, shall correspond to a so-called virtual luminosity which is 4 to 5 times higher than the actual (levelled) luminosity. This virtual luminosity would be attained if all the other parameters, in particular β^*, were pushed to their respective limits at the very beginning of a physics fill. In this perspective, the HL-LHC parameters listed in Tab. 1 include some key quantities such as the virtual luminosity introduced above and an indicative leveling time at 5×10^{34} cm^{-2}s^{-1}, which has been calculated assuming no emittance growth and a total hadron cross-section of 100 mb. The numbers in parentheses in the right column of Tab. 1 correspond to an ultimate β^* of 10 cm, for which most of the new components would be pushed to the limits, in particular in terms of protect-ability of the cold aperture of the new triplet and of crab-cavity voltage when operating at $\beta^* = 10$ cm and with the corresponding increase of the crossing angle.

The HL-LHC objectives and strategy being formulated, a strong reduction of β^* however requires in principle longer final focus systems (FFS), or one should say longer low-β insertions, in order to enable a smooth matching of the optics between the interaction point (IP) and the regular lattice of the machine, i.e. the arcs. For a machine which is still in its design phase, this step is in general feasible, but a priori far from being neutral in terms of cost and planning. On the other hand, appropriate solutions, or even acceptable compromises, might be very hard, if not impossible to find, when strongly relying on this approach for upgrading an already existing machine, the LHC in the present case. Another pre-requisite to reduce β^* might also be a net reduction of L^*, which is the distance between the last final focus quadrupole and the interaction point. This intervention aims at mitigating the inevitable increase of the chromatic aberrations due to the larger peak β-functions reached in the final focus quadrupoles at smaller β^*, more precisely the linear and non-linear chromaticities, the so-called off-momentum β-beating, and the spurious dispersion induced by the crossing angle imposed at the IP. Sharper modifications might also consist in a complete redesign of the chromatic correction system initially foreseen, making it stronger and more efficient, which, for circular machines, generally means an intervention into the heart of the lattice, i.e. all the arcs of the ring, by replacing the existing chromaticity sextupoles by new ones much stronger. The situation was therefore very complicated for the LHC ring, with in addition hard constraints on L^* imposed by the size of the existing ATLAS and CMS

detectors, and strictly no flexibility for a possible extension of the low-β insertions which are obviously defined by the geometry of the existing tunnel. This was without counting on a new non-standard optics scheme, the so-called Achromatic Telescopic Squeezing (ATS) scheme [7, 8, 9] which offered a complete, cost efficient and robust (achromatic), solution to the above issues.

After reviewing the main limitations of the present LHC optics, the basic idea and principle of the ATS scheme will be presented and its features illustrated in the case of the HL-LHC optics.

4.2.2   The LHC optics limitations: a change of paradigm was needed

4.2.2.1   *The LHC ring at a glance*

As many circular machines, the LHC consists of a certain number of arcs, forming a periodic lattice which is interrupted by service and experimental (low-β) insertions:

- IR3 and IR7 hosting the momentum and betatron cleaning insertions, respectively,
- the RF insertion in IR4, containing as well most of the beam instrumentation,
- the dump insertion in IR6,
- the low luminosity insertions IR2 and IR8 housing the Alice and LHCb experiments, also used to inject Beam1 and Beam2 rotating clockwise and anti-clockwise, respectively,
- and finally the two high luminosity insertions IR1 and IR5 housing the ATLAS and CMS experiments (see Fig. 1)
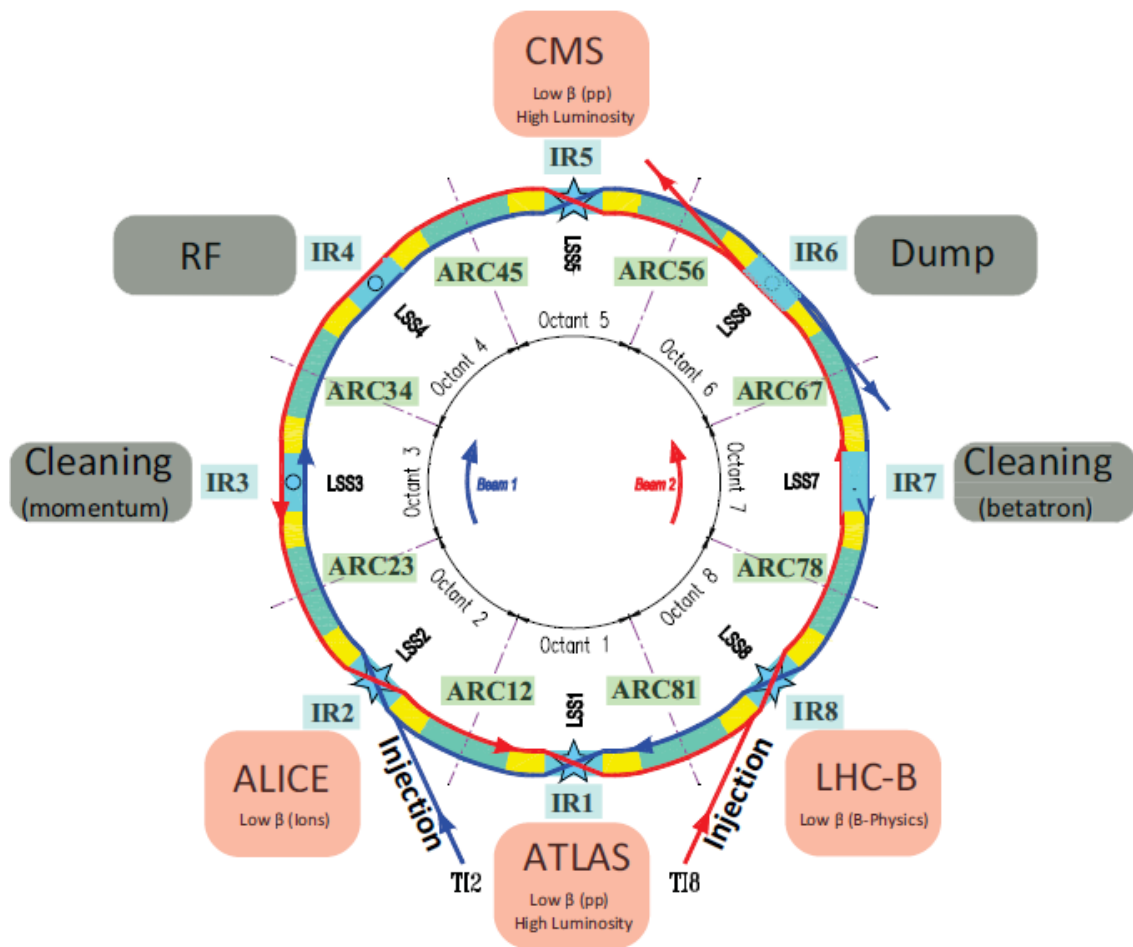
Figure 11: Schematic layout of the LHC.

4.2.2.2   ***The LHC experimental insertions in brief, with the ATS already put into perspective***

The two LHC beams circulate in separated apertures in most part of the ring, except in the experimental insertions where they share the same vacuum chamber between the IP and a so-called Y-chamber located in between the separation and recombination dipoles D1 and D2 (see Fig. 2). The main field of the final focus quadrupoles therefore impacts in an opposite way on the two counter rotating LHC proton beams. Aiming at simultaneous optics solutions for both beams led to the design of an optics which is antisymmetric between the left and the right sides of the IP for a given beam, and between Beam1 and Beam2 on a given side of the IP, and to a layout solution with a final triplet rather than with a final doublet.

The four experimental insertions of the LHC are based on the same conceptual layout. From the optics point of view, these IRs contain three main parts:

- a region which is shared by the two beams from the IP to the separation dipole D1, with the inner triplet in between installed at L^*=23 m,
- the so-called matching section, starting at the recombination dipole D2 and containing three standalone two-in-one quadrupole magnets Q4, Q5 and Q6,
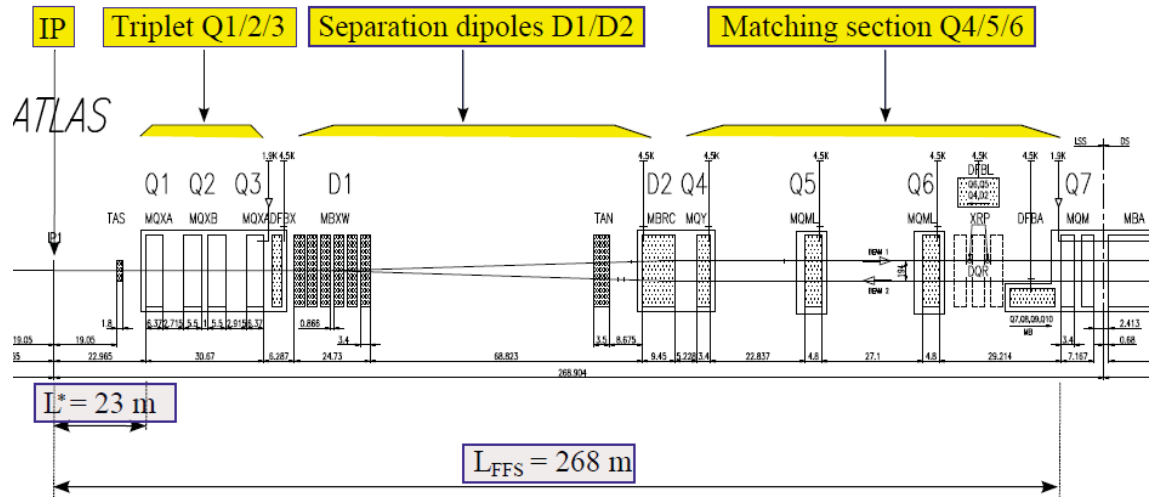
Figure 12: Typical LHC experimental insertion from the interaction point (IP) to the entry of the dispersion suppressor (Q7).

- the dispersion suppressor starting with Q7 followed by the first arc dipoles, and containing four standalone two-in-one aperture quadrupole magnets (Q7 to Q10). Strictly speaking, the dispersion suppressor extends up to Q13, with the arc quadrupoles Q11, Q12 and Q13 equipped with three individually powered trim quadrupoles.

The linear optics then becomes strictly periodic as of Q13 on the left and right side of each LHC insertion, where the arc quadrupoles are arranged into 21 regular FODO cells. In practice, as for most of the modern colliders, matching the optics of an LHC low-β insertion consists in satisfying a certain number of constraints including $β^*$, but not only, and using the standalone quadrupoles of the matching section and dispersion suppressor, while the gradient of the inner triplet is kept quasi-constant. More precisely, starting from the periodic optical functions of the arcs on the left side of the insertion at Q13.L, a total of 14 optics constraints shall be fulfilled, namely:

i. the horizontal and vertical betatron phase advances from Q13.L to Q13.R which are kept constant for any $β^*$, in order to keep the betatron tunes constant during the transition, the so-called optics squeeze, from the injection to the collision optics,

ii. and the Twiss parameters, $β_{x,y}$ and $α_{x,y}$, and the dispersion and angular dispersion, D_x and D_{px}, both at the IP (6 constraints), and at the exit of the

insertion, more precisely at Q13.R, where these parameters shall again coincide with the periodic conditions of the next arc.

As it will be presented later, the ATS scheme will complement this concept for the so-called pre-squeezed optics (with two additional constraints imposed individually on the left and right phase advances of the insertions, i.e. not only the overall phase across the iR). The ATS will then completely modify this approach for the second, so-called telescopic, part of the squeeze in order to reach unprecedentedly small β^*, with no chromatic limit (at least in term of first order linear chromaticity Q') .

4.2.2.3 *The LHC arc optics and chromatic correction system in brief*

The chromatic correction system of the LHC is hosted in the arcs, with two interleaved families of sextupoles, in each of the two transverse planes and each of the eight sectors of the ring. This makes a total of 32 independent sextupole families per beam
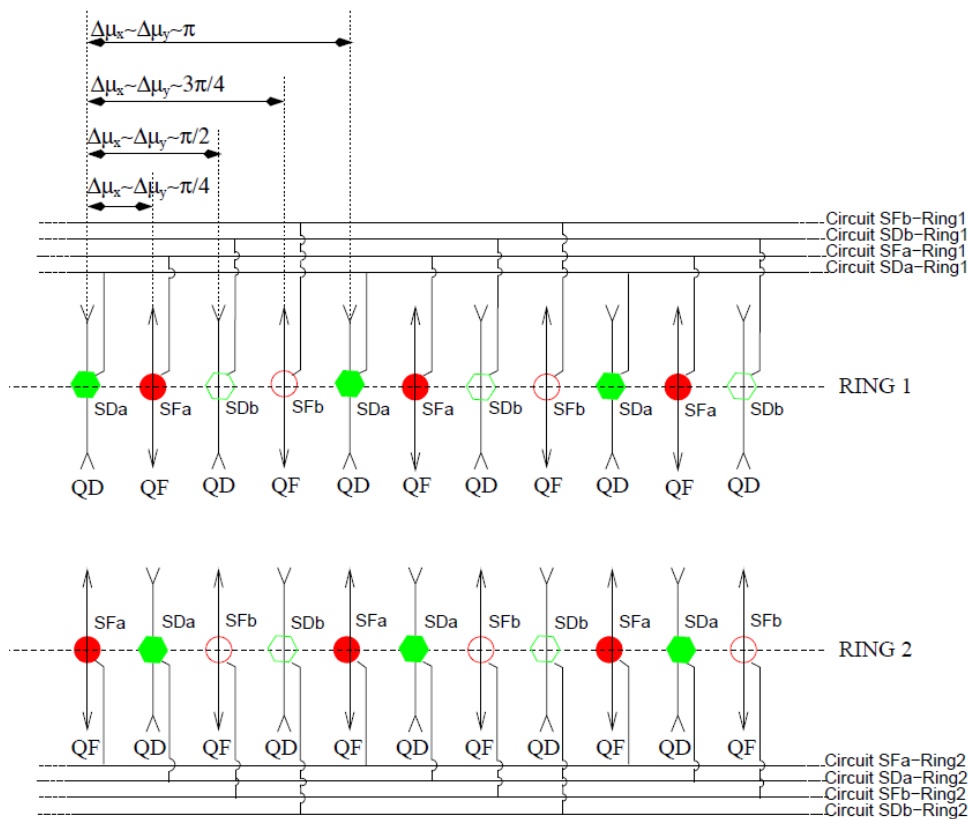
Figure 13: Schematic layout of the LHC arc sextupole powering scheme.

For the entire ring (see Fig. 3). The nominal LHC optics is matched with betatron phase advances close, but not exactly equal, to 90 degrees in the arc cells, inducing a phase split of about $\Delta\mu_x - \Delta\mu_y \sim \pi$ in each sector of the ring, and contributing to about 80% of the overall integer tune split of 5 ($Q_{x/y}$=64.31/59.32 in collision). This strategy

was implemented in the early design of the machine (see e.g. [10]), and kept unchanged since then. The initial goal was to mitigate the impact of the non-linear resonance driving terms which could have been driven by possibly large systematic field imperfections in the LHC main dipoles. A posteriori, this optics choice is however non longer justified, with a field quality much better than initially anticipated in the main magnets, which de facto would allow to come back towards phase advances much closer, if not strictly equal to $\pi/2$ in the LHC arc cells. On the contrary, preserving such an optics would prevent to use efficiently the flexibility offered by the existing LHC sextupole powering scheme, where only one of the two sextupole families available per plane will actually be used (see later) in order to control properly the chromatic aberrations of the collision optics at very low β^*. In comparison, the present LHC optics uses all these families as only two independent knobs to compensate globally the linear chromaticity in the horizontal and vertical planes, with no attempt to treat quantities like Q'' or the off-momentum β-beating, which of course become more and more relevant when pushing β^*.

4.2.2.4 *The challenge of reducing β^**

In the LHC context described above, a strong reduction of β^* leads to a series of limitations, driven on one side by the mechanical aperture available in the inner triplet (IT) and, on the other side, coming from all the rest of the ring.

Concerning the demand on the mechanical acceptance of the inner triplet, one can always find a solution based on sufficiently large aperture quadrupoles, by weakening their gradient and making them longer (at more or less constant integrated gradient), regardless of β^* and of the technology chosen for the triplet [11, 12]. Indeed decreasing the operational gradient G of the inner triplet at constant β^* and integrated strength, the aperture needed for the beam roughly scales like $1/G^{1/4}$. Said differently, the peak β-function β_{max} reached in the IT is found to increase with

(and idem with the induced chromaticity). While this smooth degradation with the triplet gradient is detrimental for the second set of limitations described below, the triplet coil aperture can therefore in principle be increased with $1/G$ at constant peak field, which is then much faster than the above scaling in $1/G^{1/4}$. This means that the possible aperture of a sufficiently long (and weak) triplet could in principle accommodate any reduction of β^* (of course to some extent given by integration constraints), but still without offering any motor for the β^* reduction proper.

The real optics challenges for low β^* are then actually elsewhere, one should say on the "non-triplet side" of the machine where a series of limitations were clearly identified and classified in the framework of the former upgrade project of the LHC, the so-called Phase I Luminosity Upgrade project [13, 14]. While of very different nature, these limitations can be quantified by the maximum possible peak β-function which is

permitted in the inner triplet, namely β_{max}. Indeed, this β_{max} shall then be matched to the regular optics of the arcs within the fixed distance given by the length of the low-β insertion, and within the aperture and gradient limits of the IR magnets (quadrupoles of the matching section and of the dispersion suppressor). Finally, a clear strategy shall be established to ensure a proper control of the chromatic aberrations induced, without exceeding the available strength of the lattice sextupoles. The beam observables to be corrected are not only the linear chromaticity Q', which is increasing linearly with β_{max} but also the non-linear chromaticities Q'', Q''',…, the off-momentum β-beating $\partial\beta/\partial\delta$ (i.e. the chromatic variations of the β-functions, at least to first order), and the spurious dispersion induced by the crossing angle in the low-β insertions.

Assuming an upgrade of the LHC optics and layout which would essentially rely on the replacement of the existing inner triplets, and no deep conceptual changes in general beam optics for circular colliders, these limitations can rapidly turn into hard limits driven by the existing hardware in large parts of the ring, and given by:

- the mechanical acceptance of the existing matching section,
- the gradient limits of the matching quadrupoles, where some of them are pushed to very high gradients, as Q7, while others reach unmanageable low gradients or even tend to change of polarity in the matching section, as Q5 and mainly Q6,
- and the strength limits of the arc sextupoles.

Taking these considerations into account, the maximum possible β_{max} permitted in any new LHC triplet was found to be around 11 km [13] (limited by the sextupole strength for the correction of the off-momentum β-beating, and with the optics matchability limit just behind). This β_{max} limit of 11 km can be directly compared to the value of 4.5 km which is reached for the nominal collision optics of the LHC (where this sophistication of the chromatic correction is not needed and therefore not implemented). This defined at that time an optimal aperture of 120 mm for the next generation of LHC triplet, regardless of the technology chosen, and in which case an upgrade of the matching section aperture was not yet needed. The corresponding minimum possible β^* was then found to be for the NbTi technology (120 T/m-120 mm triplet), and, according to the scaling law given in (1), only 20% less, that is cm, for the Nb3Sn technology a priori compatible with a 50 % higher gradient (180 T/m-120 mm triplet). In view of these sharp limitations, the basic principles of a novel optics scheme, the ATS scheme, were worked out and first ATS optics were developed rather rapidly afterwards (see e.g. [7]). These optics offered the possibility to go well beyond in terms of β^* reach, and therefore completely modified the above conclusions to give a solid background to the HiLumi Design Study [15] and now to the HL-LHC project.

4.2.3 The ATS Scheme as Baseline for the HL-LHC Optics

4.2.3.1 *Qualitative description*

Concerning the first optics limitation mentioned above, the only solution is to equip the LHC matching sections with new two-in-one magnets of larger aperture. Concerning the poor optics flexibility observed at low β^* in the experimental insertions IR1 and IR5, with some quadrupoles being pushed to very low, and others to very high gradients, one possibility is to allow floating matching conditions at the boundaries of these two insertions. More precisely the idea is to maintain the dispersion matching constraints at the entry and exit of the low-β insertions (from Q13.L to Q13.R), but to allow the ``supporting'' insertions on either side (IR8/2 for IR1 and IR4/6 for IR5, see Fig .1) to contribute as well to the matching of the β-functions, at least below a certain value of β^*. As a result, β-beating waves are generated in the sectors adjacent to the low- β insertions (sectors 45 and 56 for IR5, and sectors 81 and 12 for IR1). Assuming a phase advance per arc cell strictly matched to $\pi/2$ in these sectors (contrary to the present LHC optics), and if correctly phased with respect to the IP, these waves will reach their maximum at every other sextupole, i.e. at the sextupoles belonging to the same electrical circuit (see Fig. 3). Consequently, the chromatic correction efficiency of these sextupoles will drastically increase at constant strength which, de facto, will be a definite cure for the third limitation previously mentioned.

This novel squeezing approach is particularly well-suited to the LHC for the two following reasons. First, due to the large dynamic range of machine energy, from 450 GeV to 7 TeV, and the reduction in proportion of the transverse emittances during the ramp, the peak β-functions in the arcs could in principle be increased by a factor of about 16 at top energy without exceeding any aperture-related limits (in practice a bit less since it is advisable to increase the margins at higher energy). Moreover, at flat top energy, the quadrupole magnets of the supporting insertions are presently either moderately pushed, which is the case for the experimental insertions IR8 and IR2 assuming a β^* not less than a few meters in p-p collision mode, or not pushed at all, in the case of IR4 and IR6 for which the injection optics is kept unchanged during the whole LHC cycle. Therefore all the ingredients are already available in the existing LHC machine to blow up the β-functions in the arcs 81/12/45/56 at 7 TeV, and to implement the principle of the ATS scheme.

A comprehensive description of the scheme can be found in [9], in particular concerning the constraints imposed on the betatron phases over the left and right side of the low-β insertions, and describing in details the sequence of the optics squeeze which is achieved in a two-stage telescopic mode (see Fig. 4):

- first of all, a so-called *pre-squeeze*, which is "quasi-standard" optics squeeze (within some additional phase matching constraints), acting only on the matching quadrupoles of the low-β insertions proper and on the arc sextupoles,

till reaching some strength limitations, either in the insertion magnets (optics limit), or in the chromaticity sextupoles of the arcs (chromatic limit),

- then the **telescopic squeeze**, by acting only on the matching quadrupoles belonging to the neighboring insertions (IR2/8 for squeezing IR1, and IR4/6 for squeezing IR5), and keeping constant the strength of the chromaticity sextupoles in between (i.e. in the sectors 81, 12, 45 and56). In this scenario the peak β-functions in the arcs 81, 12, 45 and 56 are increased by the same (resp. different) factor in both transverse planes for round (resp. flat) collision optics with (resp. with), i.e. in proportion with the additional β^* reduction with respect to the pre-squeezed optics.

With the exception of the Q5 matching quadrupoles in IR6 (which, for some telescopic optics, may need to be made 20% stronger at 7 TeV [7]), and heavier interventions obviously needed in the matching sections and inner triplets of IR1 and IR5 [1], the ATS scheme has been found to be fully compatible with the existing LHC hardware and layout, in order to produce and ensure the chromatic correction of collision optics with β^* values down to 5-10 cm, i.e. incomparably small with respect to the former limit of 25-30 cm.

ATS optics were then built in practice assuming several possible triplet layouts, e.g. taking in [7] the 120 T/m (120 mm) NbTi triplet proposed for the former Phase I LHC upgrade project [14], then two other intermediate triplet layouts with an aperture increased up to 140 mm and compatible with the NbTi or Nb3Sn technology [16] (i.e. with an operating gradient of 100 T/m or 150 T/m, respectively), and more recently with one of the latest (140 T/m, 150 mm) triplet layout foreseen for the HL LHC [17, 18]. The main difference between these different cases is the so-called pre-squeezed β^*, ranging from 50 to 40 cm [again with an approximate scaling like $1/G^{1/2}$, as given in (1)], and below which the telescopic techniques of the ATS need to be deployed in order to reduce β^* further down (and ``achromatically'' although at nearly constant strength for all the chromaticity sextupoles of the lattice).

A completely new version of the LHC optics based on the ATS scheme was also developed, strictly compatible with the existing layout of the LHC, in particular with its existing (200 T/m - 70 mm) NbTi inner triplets. This allowed testing and successfully validating with beam, the basic principles of this novel optics scheme via a series of dedicated machine studies which took place in 2011 at 3.5 TeV/beam [19], and culminated in 2012 with 4 TeV/beam, where a β^* of nearly 10 cm was reached and measured at IP1 and IP5 [20]. These machine studies were of course achieved in very specific conditions which are not suitable for nominal operation, in particular with small intensity (pilot) beam, and without crossing angle in order to preserve the mechanical aperture of the existing IR magnets at such low β^*. For the present LHC Run II, ATS beam experiments will be resumed at 6.5 TeV/beam and higher intensity, in order to gain experience and confidence with this new optics scheme in view of the HL-LHC.
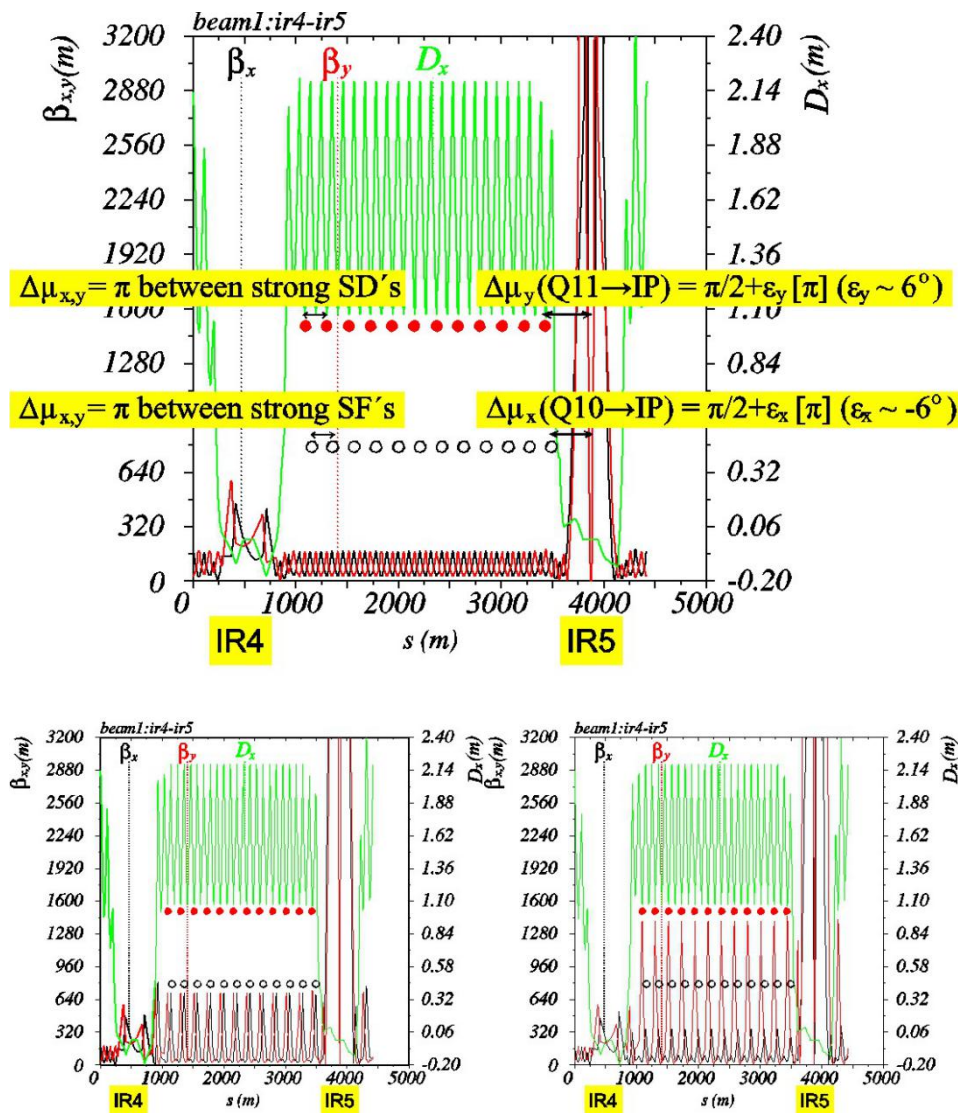
Figure 14: Typical LHC pre-squeezed optics (top) zoomed from the RF insertion IR4 to the exit of the CMS insertion IR5, with specific phasing conditions emphasized and a typical β^* of 40 cm at IP5, followed by two possible telescopic optics further reducing β^* in a symmetric (β^*, bottom left) or asymmetric (β^*, bottom right) way.

The dispersion function remains matched in the arcs for the telescopic optics, but the β-functions are mismatched reaching their maximum at every other sextupole, i.e. at the sextupoles belonging to the same LHC electrical circuit (see Fig. 3). The relative increase of these maxima with respect to the pre-squeezed optics is inversely proportional to the additional reduction of β^*. As a result, during the telescopic squeeze, the chromatic correction of the inner triplet can be achieved at nearly constant sextupole strength.

4.2.3.2 *Illustration for (HL-)LHC*
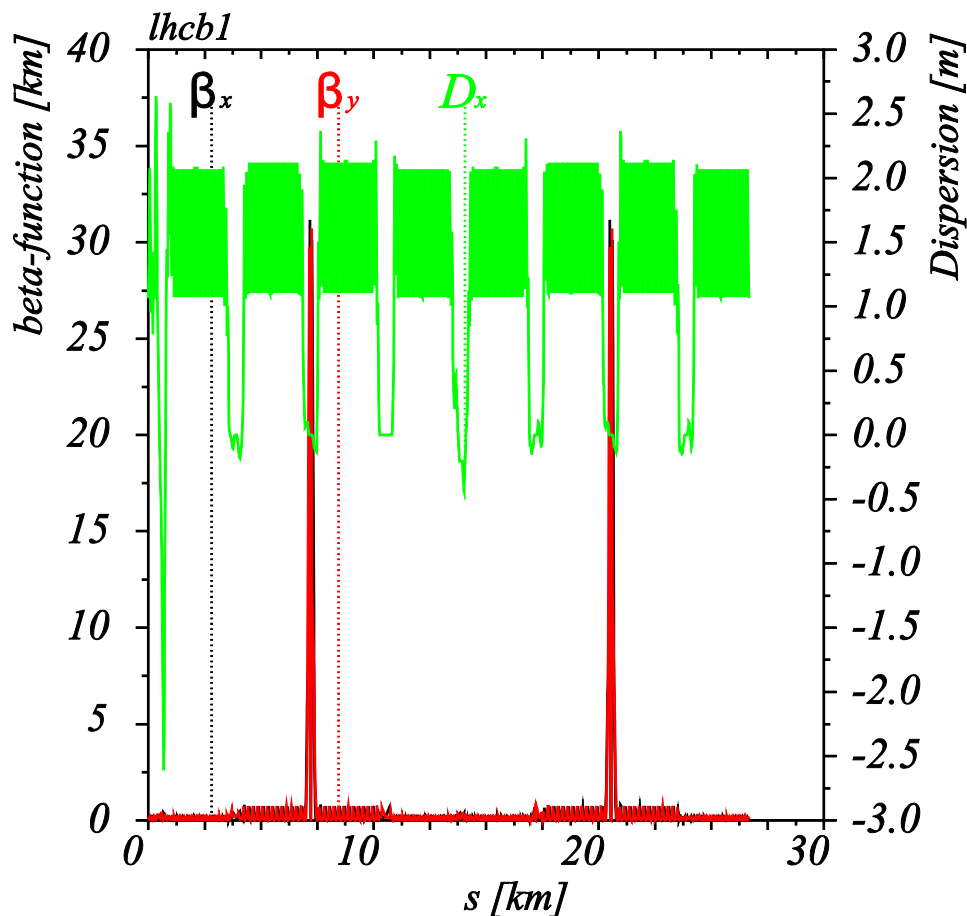
Figure 15: Typical ATS collision optics with β^*=10 cm at IP1 and IP5 (the machine is cycled from IP3). In this particular case the crossing scheme are switched off in the experimental insertions and the horizontal dispersion function remains perfectly matched in the eight sectors of the ring. On the other hand, β-beating waves are generated and clearly visible in the four sectors on either side of the two low-β insertions ATLAS and CMS. These wave are one of the main signatures of the ATS scheme.

Assuming one of the latest Nb3Sn triplet layout developed for the HL-LHC (150 mm, 140 T/m), a typical round ATS collision optics is shown in Fig. 5, with β^* pushed to its ultimate value of 10 cm at IP1 and IP5. The peak β-function β_{max} of 31 km reached in the inner triplet is impressive, i.e. already a factor of 3 larger than the limit of 11 km [13] previously mentioned. Equivalent flat collision optics with a typical β^* aspect ratio of 4, i.e. with β^*=20 cm in the crossing plane and down to 5 cm in the other plane, can also be produced with the ATS techniques, therefore leading to peak β functions exceeding 60 km in the inner triplet for a given plane, i.e. more than one order of magnitude larger than the 4.5 km reached for the nominal LHC collision optics at β^*= 55 cm [5].

In practice, the minimum possible pre-squeezed β^* is found to be around 44 cm in the case of 140 T/m for the triplet gradient (slightly degraded in comparison with the value of 36 cm found for the 205 T/m existing LHC triplet, limited in both cases by the strength of the arc sextupoles). This means that a mismatch of the β-functions by 440 % is generated in the arcs 81, 12, 45 and 56 (i.e. with peak β-functions increased in both transverse planes by a factor 4.4), in order to pass from β^* =44 cm to β^* =10 cm, as clearly visible in Fig. 5. Provided that the sextupole circuits participating to the chromatic correction of the triplet contain an even number of magnets [7], therefore forming π-pairs to mitigate the geometric aberration induced, the level of field quality of the LHC arc magnets (dipole and quadrupole) has been rapidly found appropriate for such β-mismatch in four arcs of ring, with visible but still acceptable impact onto the dynamic aperture (see e.g. [21]).

A zoomed view of the 10 cm collision optics is presented in Figs. 6(a)-(c), for the four experimental insertions of the HL-LHC, namely

- LHCb (IR8) squeezed to an intermediate β^* of 3 m, which is more than enough for sustaining over about 10 hours a luminosity levelled to $1 - 2 \times 10^{33}$ cm^{-2}s^{-1} (assuming the HL-LHC beam parameters given in Tab. 1),
- Alice (IR2) with β^*=10 m, where halo collisions (with a large beam-beam separation at the IP of more than 5 σ) is requested in proton-proton collision mode, in order to limit the instantaneous luminosity below 10^{31} cm^{-2}s^{-1},
- ATLAS and CMS (IR1 and IR5) with β^*= 10 cm, where a factor of more than 4 in β^* reduction is actually supported by the β-beating waves generated and absorbed by the matching quadrupoles located on the right of IP8 (resp. IP4) and on the left of IP2 (resp. IP6) for ATLAS (resp. CMS).

Starting from the same injection optics as the one used to build up the 10 cm ATS optics described above, the nominal functionality of the LHC experimental insertions is still preserved: IR2 and IR8 can still be squeezed in the standard way, and in particular at constant overall betatron phases, down to their nominal β^* (50 cm), and even slightly below for IR1 and IR5 (~ 45-50 cm), assuming ion or proton-ion physics at the era of the HL-LHC [see Figs. 6(d)-(f)].

4.2.3.3 *Chromatic Properties*

The chromatic properties of ATS optics are particularly interesting to analyze. Pushing β^* down to 10 cm, the chromatic variations of the betatron tunes are only moderately perturbed by a slight third order chromaticity Q''' showing up over a momentum range of δ_p= ± 1.5 ×10^{-3} [i.e. about 5 times the momentum acceptance of the LHC RF bucket at 7 TeV, see Fig. 7(a)].

The chromatic Montague functions (giving the amplitude of the first order chromatic derivative of the β-functions) are nicely vanishing in the collimation

insertions IR3 and IR7 and at IP1 and IP5 [see Fig. 7(b)], therefore with no impact on the collimation hierarchy, nor on the machine performance. Another relevant aspect is related to the fact that the off-momentum β-beating waves induced in the two transverse planes by the lattice sextupoles are exactly out of phase by π/2 with respect to the β-functions themselves, in particular in the triplet and its neighboring magnets. Therefore, no further degradation of the off-momentum mechanical aperture is induced in the arcs, the matching section and the inner triplet (except the usual one coming from the contribution of the dispersion, which remains perfectly matched in the ATS scheme).

Finally, an extremely important quantity to control is the spurious dispersion induced by the crossing scheme in IR1 and IR5. This dispersion can indeed reach up to 20 m in the new triplets when pushing β^* down to 10 cm and with a full crossing angle increased up to 720 μrad (see Tab. 1). This dispersion is produced by feed-down effects
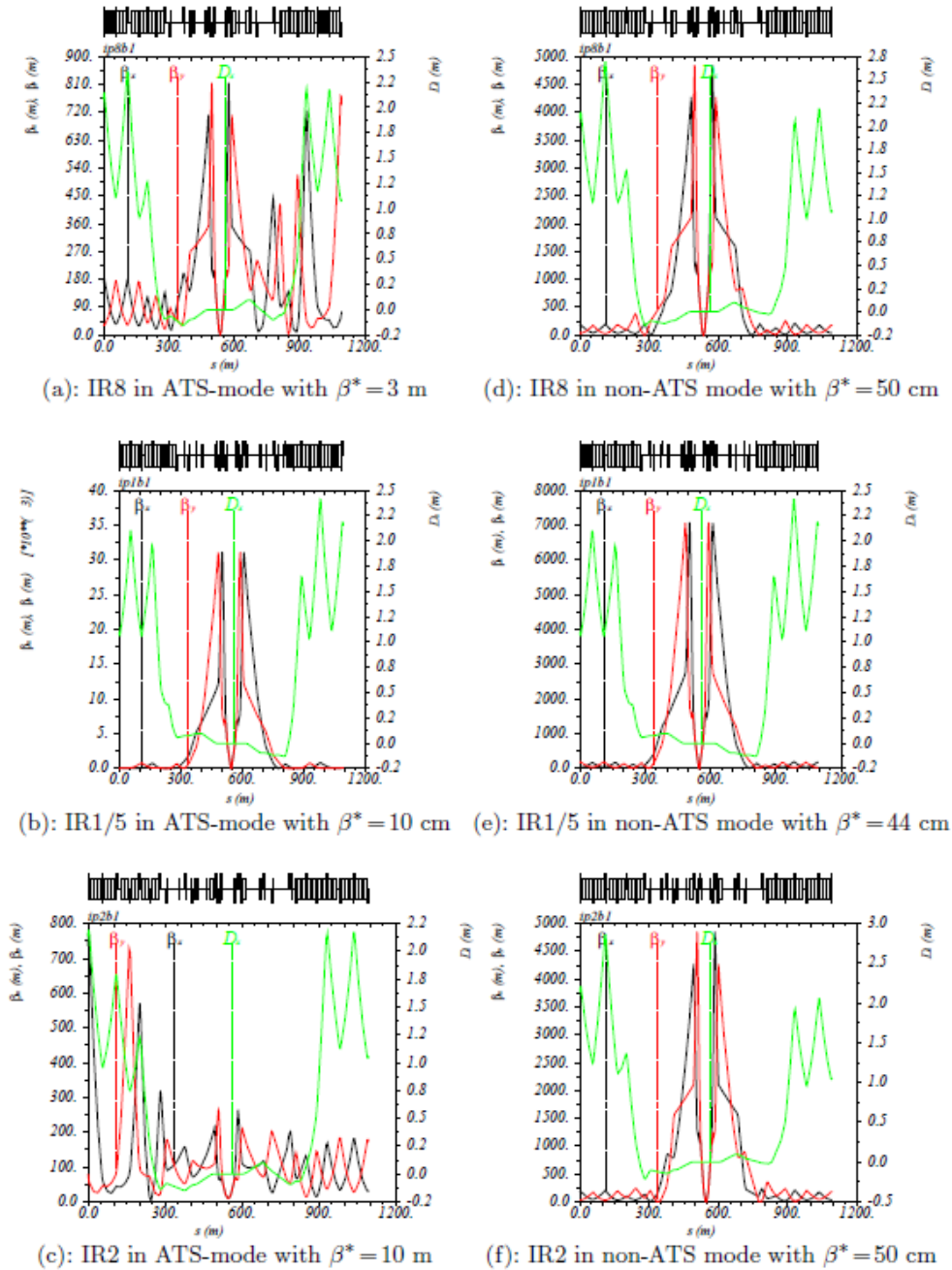
Figure 16: Zoomed view of collision optics in IR8, IR1/5 and IR2 running the LHC in ATS-mode for proton-proton physics (left pictures), and in non-ATS mode for ion or proton-ion physics (right picture). In ATS-mode, -beating waves are initiated on the right side of IR8 and absorbed on the left side of IR2 [see Figs. (a) and (c)] in order to gain a factor of 4 to 5 in the β^* reduction at IP1.

In the inner triplets of one of the two high luminosity insertions, and then exported to the other one. Without correction, such a large dispersion would certainly degrade the performance of the HL-LHC, reducing the aperture available in the inner triplets,

possibly increasing the background to the experiments, but also inducing hardly manageable effects such as variations of chromaticity by up to ±10 units along the bunch trains, due to the long range beam-beam interactions. However, thanks to the specific phasing conditions imposed by the ATS scheme, modest H or V orbit bumps of the order of 4-5 mm generated in the sectors adjacent to IR1 and IR5 are found to be sufficient to correct this spurious dispersion back to a level of about 0.5-1 m in the inner triplet [see Figs. 7(c) and (d)].

(a)

(b)

(c)

(d)
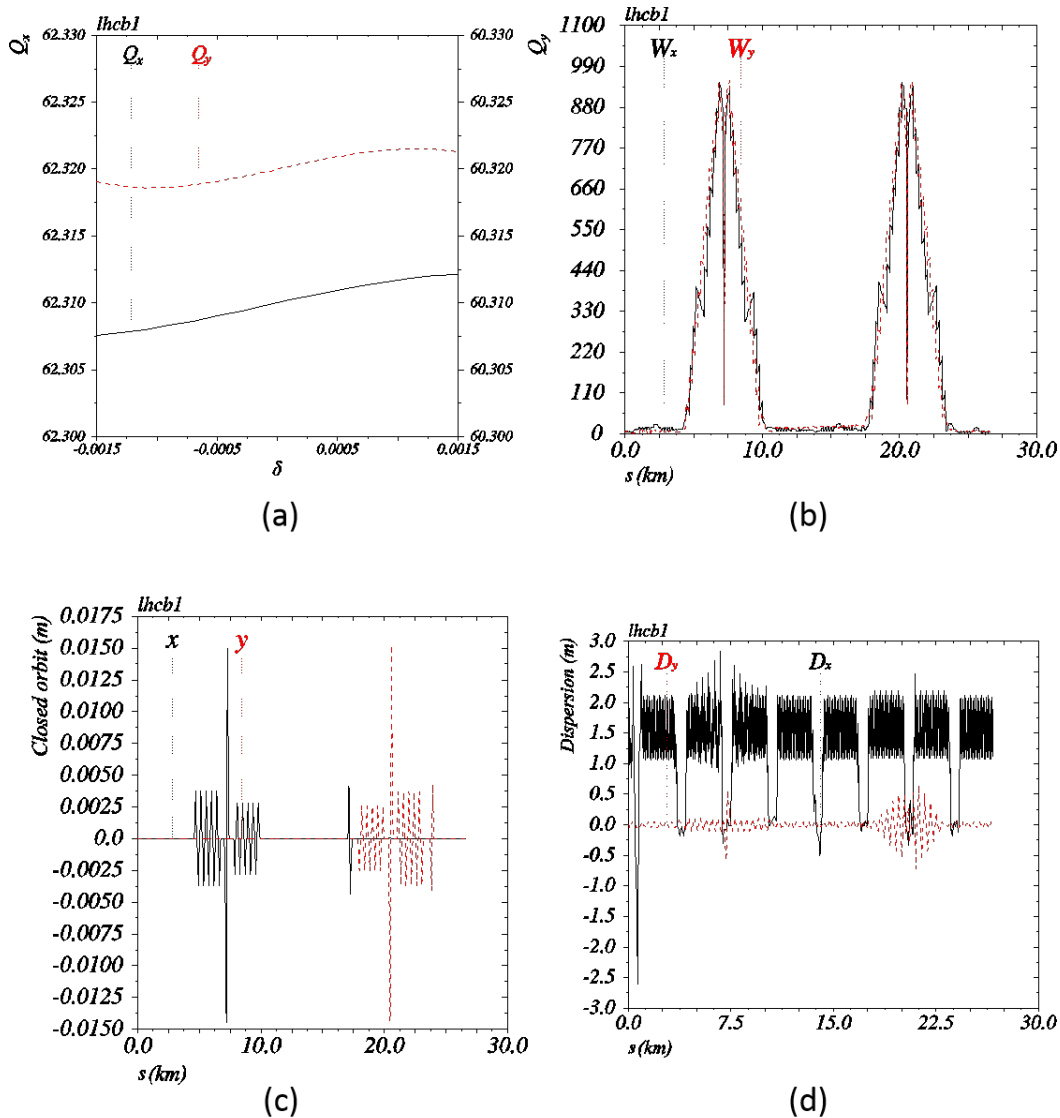
Figure 17: Chromatic properties of the 10 cm ATS optics: (a) chromatic variations of the betatron tunes (assuming the linear chromaticity to be matched to 2 units using standard Q' knobs), (b) Montague functions $W_{x,y}$ around the LHC ring (with IP3 chosen as the origin), and (d) residual horizontal and vertical dispersion mismatch induced by the horizontal and vertical crossing angles at IP1 and IP5, but minimized thanks to orbit bumps generated in the arcs 81, 12, 45 and 56 (c).

4.2.4 Summary and outlook

The Achromatic Telescopic Squeezing scheme is an essential ingredient to the LHC Luminosity Upgrade, which constituted a solid background to the HiLumi Design Study [15], recently transformed into the HL-LHC project [1]. The ATS justifies most of the hardware choices taken by the project, in particular in terms of new magnets of the largest possible aperture and of crab-cavities, (i) to be compatible and (ii) to profit from a strong reduction of β^*, which, without the ATS, would not be possible to produce otherwise. As for the HL-LHC, this scheme will likely become a built-in feature for the upgrade and/or the design of the next generation of high energy circular colliders. In this perspective, the HE-LHC (or a so-called LHC energy doubler under study to be installed into the LHC tunnel) is an another excellent example, where the minimum possible β^* would otherwise be strongly degraded with the increase of the collider energy, more precisely by the limited physical length of the arcs, and even reduced space in the long straight sections of the experimental insertions (after triplet and also, possibly L^*, lengthening), which will be available for chromatic correction and standard squeezing techniques.

4.2.5 References

1. G. Apollinari *et al.*, *High-Luminosity Large Hadron Collider (HL-LHC): Preliminary Design Report*, **CERN-2015-0005**, CERN, Geneva, Switzerland, Dec. 2015.

2. The Alice Collaboration, *Upgrade of the ALICE Experiment*, Letter Of Intent, **CERN-LHCC-2012-012**, CERN, Geneva, Switzerland, 2012

3. The LHCb Collaboration, *LHCb VELO Upgrade Technical Design Report*,

    CERN-LHCC-2013-021, also available in **LHCB-TDR-013**, CERN, Geneva, Switzerland, 2013.

4. J. Abelleira *et al., LHC Injectors Upgrade, Technical Design Report – Volume I: Protons*, **CERN-2014-0337**, CERN, Geneva, Switzerland, Dec. 2014.

5. O. Brüning, P. Collier, P. Lebrun, S. Myers, R. Ostojic, J. Pool and P. Proudlock (Ed.), *LHC Design Report, v.1: the LHC Main Ring,* **CERN-2004-003-V-1,** CERN, Geneva, Switzerland, 2004.

6. S. Fartoukh, *Pile up management at the high-luminosity LHC and introduction to the crab-kissing concept,* **Phys. Rev. ST Accel. Beams 17**, **111001**, 2014.

7. S. Fartoukh, *Towards the LHC Upgrade using the LHC well-characterized technology*, **SLHC-Project-Report 49**, CERN, Geneva, Switzerland, 2010.

8. S, Fartoukh, *Breaching the Phase I optics limitations for the HL-LHC*, **CERN-ATS-2011-005**, pp.302-316, Chamonix 2011 Workshop on LHC Performance, Chamonix, France, 24 - 28 Jan 2011, CERN, Geneva, Switzerland, 2011.

9. S. Fartoukh, *Achromatic Telescopic Squeezing Scheme and its application to the LHC and its luminosity upgrade*, **Phys. Rev. ST Accel. Beams 16, 111002**, 2013.

10. J.-P. Koutchouk, *The LHC dynamic aperture*, in Proc.'s of the 18th Biennial Particle Accelerator Conference, New York, NY, USA, 29 Mar - 2 Apr 1999, pp. 372.

11. J.P. Koutchouk, L. Rossi, E. Todesco, *A solution for Phase-one upgrade of the LHC low-beta quadrupoles based on Nb-Ti*', **CERN-LHC-Project-Report-1000**, CERN, Geneva, Switzerland, 2007.

12. O. Brüning, R. De Maria, R. Ostojic, *Low gradient, large aperture IR upgrade options for the LHC compatible with Nb-Ti magnet technology*, **CERN-LHC-Project-Report-1008**, CERN, Geneva, Switzerland, 2008.

13. S. Fartoukh, *Optics Challenges and Solutions for the LHC Insertion Upgrade Phase I*, **CERN-ATS-2010-026**, pp. 262-290, Chamonix 2010 Workshop on LHC Performance, Chamonix, France, 25 - 29 Jan 2010, CERN, Geneva, Switzerland, 2011.

14. R. Ostojic, *Overview of IR upgrade scope and challenges*, **CERN-ATS-2010-026**, pp. 253-257, Chamonix 2010 Workshop on LHC Performance, Chamonix, France, 25 - 29 Jan 2010, CERN, Geneva, Switzerland, 2011.

15. http://hilumilhc.web.cern.ch

16. S. Fartoukh, R. De Maria, *Optics and Layout Solutions for HL-LHC with Large Aperture NB3SN and NB-TI Inner Triplets*, in 3rd International Particle Accelerator Conference 2012, New Orleans, LA, USA, 20 - 25 May 2012, pp.145.

17. R. De Maria, S. Fartoukh, A. Bogomyakov, M. Korostolev, *HLLHCV1.0: HL-LHC layout and optics models for 150 mm Nb3Sn triplets and local crab cavities*, in 4th International Particle Accelerator Conference 2013, Shanghai, China, 12 - 17 May 2013.

18. R. De Maria, S. Fartoukh, M. Fitterer, *HLLHCV1.1: Optics Version for the HL-LHC Upgrade,* in 6th International Particle Accelerator Conference 2015, Ricmond, VA, USA, 3 – 8 May 2015.

19. S. Fartoukh, *First demonstration with beam of the Achromatic Telescopic*

Squeezing (ATS) scheme, **CERN-ATS-2012-069**, pp.128-134, Chamonix 2012 Workshop on LHC Performance, Chamonix, France, 6 - 10 Feb 2012.

20. S. Fartoukh*, et al*., *The 10 cm beta* ATS MD*, **CERN-ATS-Note-2013-004 MD**, CERN, Geneva, Switzerland, 2013.

21. R. de Maria, S. Fartoukh, *SLHCV3.0: layout, optics and long term stability*, **SLHC-Project-Report 50**, CERN, Geneva, Switzerland, 2010.

4.3   Novel Lattice Solutions for the LheC

S.A. Bogacz[2], O. Brüning [1], E. Cruz-Alaniz[3], A. Latina[1], D. Pellegrini[1], D. Schulte[1], R. Tomás [1], A. Valloni[1,3]

[1]CERN, [2]Jefferson Lab, [3]University of Liverpool

bogacz@jlab.org

4.3.1   Introduction

Unprecedently high luminosity of 10^{34} cm^{-2}s^{-1}, promised by the LHeC accelerator complex poses several beam dynamics and lattice design challenges. As part of accelerator design process, exploration of innovative beam dynamics solutions and their lattice implementations is the key to mitigating performance limitations due to fundamental beam phenomena, such as: synchrotron radiation and collective instabilities. This article will present beam dynamics driven approach to accelerator design, which in particular, addresses emittance dilution due to quantum excitations and beam breakup instability in a large scale, multi-pass Energy Recovery Linac (ERL). The use of ERL accelerator technology to provide improved beam quality and higher brightness continues to be the subject of active community interest and active accelerator development of future Electron Ion Colliders (EIC). Here, we employ current state of though for ERLs aiming at the energy frontier EIC. We will follow conceptual design options recently identified for the LHeC. The main thrust of these studies was to enhance the collider performance, while limiting overall power consumption through exploring interplay between emittance preservation and efficiencies promised by the ERL technology. This combined with a unique design of the Interaction Region (IR) optics gives the impression that luminosity of 10^{34} cm^{-2}s^{-1} is indeed feasible.

4.3.2   Challenges of 60 GeV ERL

4.3.2.1   *Principles and Design Considerations for High Energy ERLs*

Energy Recovery Linacs accelerate electron bunches of linac quality, and then recover beam energy (after the collision) by deceleration through the same linac, before dumping the bunches at low (injection) energy. Energy recovery has the benefits of supporting high beam energy and power while maintaining high beam quality, including

small beam sizes as delivered by linacs; minimizing activation by dumping low-energy (and thus low-power) beam; and ensuring power efficient accelerator operation.

An ERL would also allow for more 'disruptive' applications than the ones that would be tolerable by a ring and can achieve a smaller machine footprint. However, there is a 'payback' in terms of increased complexity, which exceed the ones for both rings and linacs.

Both the acceleration and deceleration can take place simultaneously in the same RF cavities, typically with interleaved bunches, which minimizes the fluctuations of the power stored in the cavities. This scheme requires both the accelerating and decelerating beam to travel in the same direction; therefore a recirculating arc is necessary to connect the two ends of the linac. Eventually, the machine can be arranged in a racetrack configuration with a second linac in the opposite straight section.

In order to reach higher energies, multi-turn recirculation can be adopted, with more passages on the accelerating and on the decelerating phases. A number of bunches at different energies will then coexist in the machine, requiring optics solutions capable of accommodating all of them. The choice of the number of recirculating passes and the machine size (linac length and arc radius) is driven by the desired energy, with constraints mostly coming from the impact of synchrotron radiation. In general, one can estimate the arc radius by fixing the maximum energy loss in the highest energy arc, according to beam quality issues and power considerations. The total number of passes at lower energies should then be limited by similar considerations. This allows one to fix the required voltage in the linac and therefore the machine size. Due to the scaling of the radiation effects, high energy designs tend to converge towards very small pass numbers and powerful linacs, while lower energy ones can afford to bend the beam in many passes.

These considerations might not apply if the machine is to be installed into an existing tunnel, which may pose other constraints. However, since the current in the linac scales with the number of turns, one may still want to limit these in order to allow for higher beam currents without incurring in instabilities caused, for instance, by long range wakefields and the ion/electron cloud.

The material presented in the following sections is adapted from [1,2,3], where more details and in-depth explanations can be found. The lattice solutions have been tested with extensive beam dynamic simulations.

4.3.2.2 *Layout of the LHeC*

The ERL design for the LHeC electron facility is sketched in Fig. 1. The machine is arranged in a racetrack configuration hosting two superconducting linacs in the parallel straights and three recirculating arcs on each side. The linacs are 1 km long and the arcs have 1 km radius, additional space is taken up by utilities like spreading, matching and compensating sections. The total length is 9 km: 1/3 of the LHC circumference.
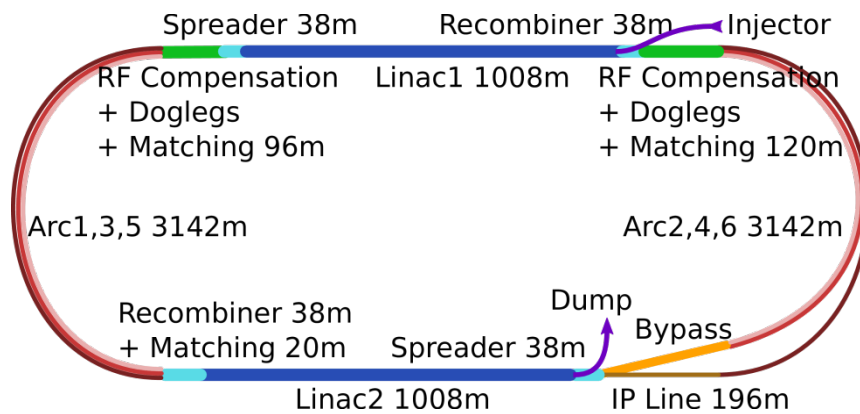
Figure 1: Scheme of the LHeC ERL layout.

Each of the two linacs provides 10 GV accelerating field, therefore a 60 GeV energy is achieved in three turns. After the collision with the protons in the LHC, the beam is decelerated in the three subsequent turns. The injection and dump energy has been chosen at 500 MeV.

4.3.2.3 *Linac Design and Optimization*

Each 1 km long linac hosts 72 cryomodules, each containing 8 cavities for a total of 576 cavities per linac operating at 802 MHz. In the baseline design a quadrupole is placed every two cryomodules providing a FODO configuration. Note that the optics of a high gradient linac can be substantially perturbed by the additional focusing coming from the RF [4]. It is therefore important to make sure that it is properly modelled.

Energy recovery in a racetrack topology explicitly requires that both the accelerating and decelerating beams share the individual return arcs. This in turn, imposes specific requirements for TWISS function at the linacs ends: the TWISS functions have to be identical for both the accelerating and decelerating linac passes converging to the same energy and therefore entering the same arc.

To visualize beta functions for multiple accelerating and decelerating passes through a given linac, it is convenient to reverse the linac direction for all decelerating passes and string them together with the interleaved accelerating passes, as illustrated in Fig. 2. This way, the corresponding accelerating and decelerating passes are joined together at the arcs entrance/exit. Therefore, the matching conditions are automatically built into the resulting multi-pass linac beamline.

The optics of the two linacs are symmetric, the first being matched to the first accelerating passage and the second to the last decelerating one. In order to maximize the BBU threshold current, the optics is tuned so that the integral:

$\langle \beta E \rangle = \int \text{Acceleration } \beta/E \, ds$

is minimized. The resulting phase advance per cell is close to 130°. Non-linear strength profiles and more refined merit functions were tested, but they only brought negligible improvements.

More consistent improvements were obtained doubling the number of quadrupoles in the linacs (placing one every cryomodule) as show in Fig. 2. This has two benefits: enhances the BBU threshold and contains the beam sizes; which can possibly result in a smaller injection and dump energy.
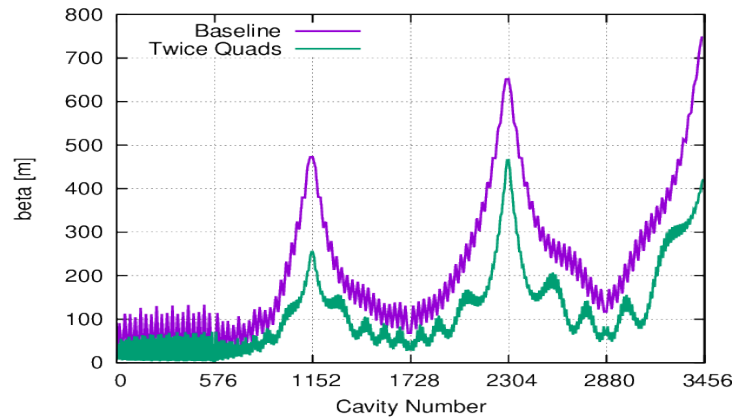
Figure 2: Beta function in the optimized LHeC Linacs during the acceleration. The linac contains 576 cavities. Only the first passage is well matched, the beams at higher energies need to be re-matched in dedicated sections (not shown here).

4.3.2.4   *Recirculating Arcs*

All six arcs (three on each side) are accommodated in a tunnel of 1 km radius. Their lattice cell adopts a flexible momentum compaction layout that presents the very same footprint for each arc. This allows us to stack magnets on top of each other or to combine them in a single design. The dipole filling factor of the cell is 76%; therefore, the effective bending radius is 760 m.

The tuning of each arc takes into account the impact of synchrotron radiation at different energies. At the highest energy, it is crucial to minimize the emittance dilution; therefore, the cells are tuned to minimize the dispersion in the bending sections, as in a theoretical minimum emittance lattice. At the lowest energy, it is possible to compensate for the bunch elongation with a negative momentum compaction setup which, additionally, contains the beam size. The intermediate energy arcs are tuned to a double bend achromat (DBA)-like lattice, offering a compromise between isochronicity and emittance dilution. Fig. 3 illustrates all three settings of the arc cells. Tapering will be required in particular for arc6, where the beam loses more than 1% of its total energy.
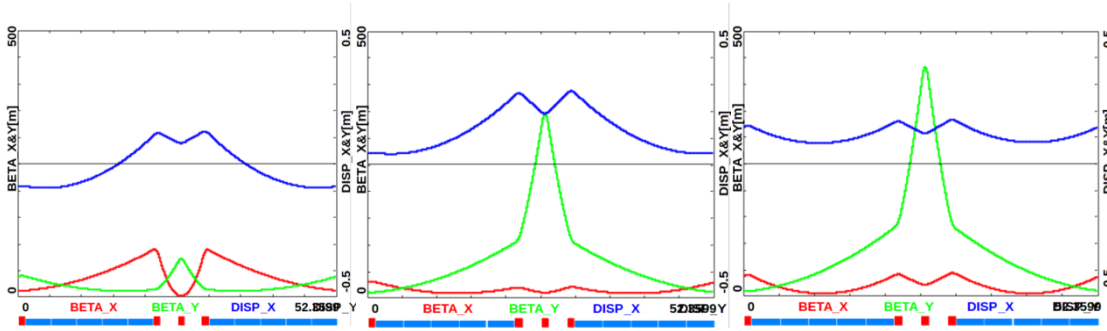
Figure 3: Different tunings of the arc cells at different energies. From left to right: low energy negative momentum compaction, middle energy DBA-like, high energy TME-like.

Before and after each arc a matching section adjusts the optics from and to the linac. Adjacent to these, additional cells additional cells are placed, hosting the RF compensating sections. The compensation makes use of a second harmonic field to replenish the energy lost by synchrotron radiation for both the accelerating and the decelerating beam, therefore allowing them to have the same energy at the entrance of each arc.

Path length-adjusting chicanes were also foreseen to tune the beam time of flight in order to hit the proper phase at each linac injection. Later investigations proved them to be effective only with the lowest energy beam, as these chicanes triggers unbearable energy losses if applied to the higher energy beams. A possible solution may consist in distributing the perturbation along the whole arc with small orbit excitations.

An alternative design based on FFAG have been proposed and explored. It allows one to transport multiple energies in the same beam pipe, although only a very specific energy is bent with a constant radius. A drop-in FFAG arc tuned to the 60 GeV energy showed promising results when substituted in the lattice, mainly because of the much higher bending filling factor, which mitigates synchrotron radiation. Nevertheless the LHeC would still need at least two FFAG arcs on each side and it is not yet clear if the benefits compensate for the added complexity.

4.3.2.5 *Spreaders and Recombiners*

The spreaders are placed after each linac, and they separate the bunches at different energies in order to route them to the corresponding arcs. The recombiners do just the opposite, merging the beams into the same trajectory before entering the next linac.

The spreader design consists of a vertical bending magnet, common for all beams, that initiates the separation. The highest energy, at the bottom, is brought back to the horizontal plane with a chicane. The lower energies are captured with a two-step vertical bending adapted from the CEBAF design [5]. This two-step design simplifies the suppression of vertical dispersion; however, it induces a non-negligible energy loss, especially for arc4, and also it drives the horizontal β function to very high values.

In order to mitigate this, a single-step design was developed. It employs seven quadrupoles to control the dispersion between the two bending dipoles. The energy loss

is reduced by factor of 5, and at the same time both the dispersion and the β functions are reduced. To avoid magnet interference, the quadrupoles of the two beam lines were appropriately shifted longitudinally. The maximum quadrupole gradient of 80 T/m will probably require superconducting magnet technology, however the cryogenics is readily available from the nearby linacs.

A comparison of the two designs for the arc2 spreader is shown in Fig. 4. Both of them provide a final vertical separation of ∼0.5 m between the three arcs.
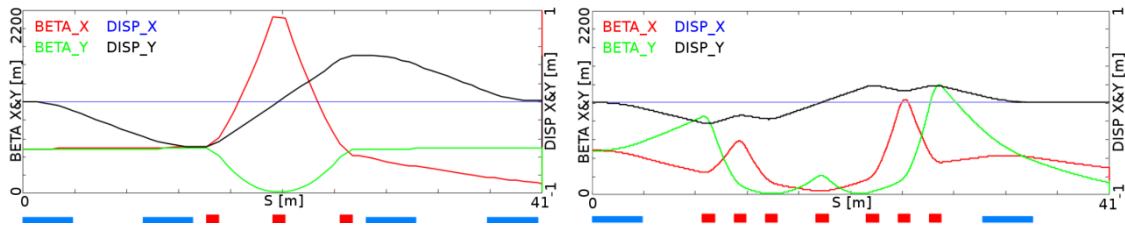
Figure 4: Comparison between the two spreader designs. Left: the CEBAF-like one, in two steps and Right: the single step developed to mitigate synchrotron radiation.

4.3.2.6 *The Bypass*

While after the last spreader the 60 GeV beam can go straight to the interaction region, the lower energies beams, at 20 and 40 GeV, needs to be further separated in order to avoid interference with the detector. Different design options for the bypass section were explored and the one that minimizes the extra bending has been chosen and installed in the lattice.

Ten arc-like dipoles are placed very close to the spreader, to provide an initial bending, which results in 10 m separation from the detector located 150 m downstream. The straight section of the bypass is approximately 300 m long. In order to join the footprint of arc6, 10 of the 60 standard cells in arc2 and arc4 are replaced with seven higher field cells. The number of junction cells is a compromise between the field strength increase and the length of additional bypass tunnel, as can be inferred from the scheme in Fig. 5.
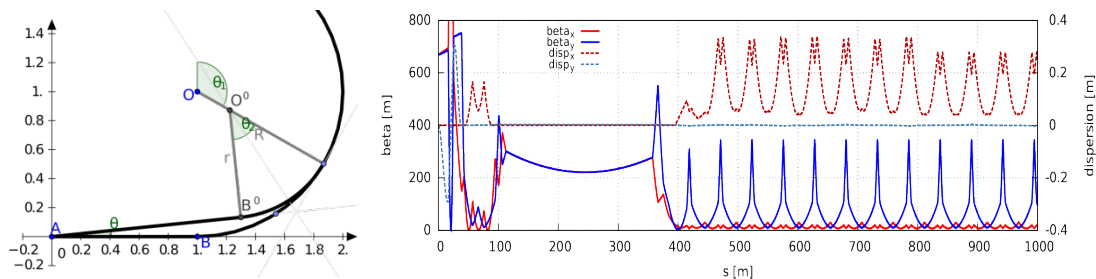
Figure 5: Layout of the bypass and Twiss along the line. One can recognize: the matching section from the linac, the initial bending, the long straight, the dispersion suppressor, seven cells with higher bending field and four regular arc cells.

The stronger bending in the junction cells creates a small mismatch which is corrected by adjusting the strengths of the quadrupoles in the last junction cell and in the first regular cell.

4.3.3   Interaction Region Optics: Integration into the HL-LHC ATS Optics

4.3.3.1   Nominal Design

The design of the LHeC interaction region (IR) aims at focusing the counter-clockwise rotating proton Beam2 colliding it with the electron beam of the ERL while the clockwise proton Beam1 bypasses the interaction.

A first conceptual design of the LHeC Linac-Ring IR was discussed in [6]. The aim of this design was to achieve head-on electron-proton collisions in the interaction region at a luminosity $L = 10^{33}$ cm^{-2}s^{-1}, requiring a low β^* (β function at the interaction point) of 10 cm. This low β^* was achieved by implementing a new inner triplet (IT) of quadrupoles which was positioned as close as possible to the interaction point (IP) to reduce chromaticity.

An illustration of the three beams passing through the inner triplet is shown in Fig. 6. The closest quadrupole to the IP (Q1) is based on a half aperture design to minimize the synchrotron radiation produced by the electron beam. A new type of magnet has been proposed for the Q1 to overcome some of the present challenges of the design [7].
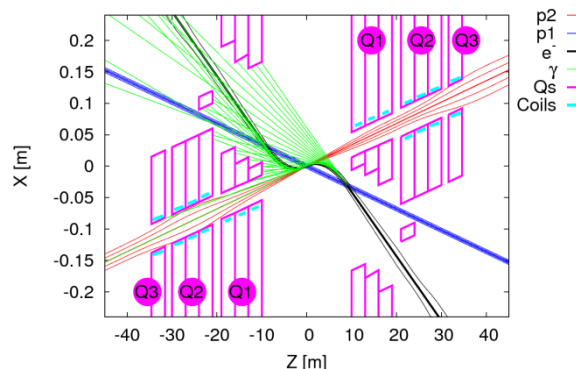
Figure 6: Focussed proton Beam2 (red) colliding with electron beam (black) while the unfocussed proton Beam1 bypasses the interaction. Each proton and electron beam passes through its corresponding aperture in the inner triplet.

It was initially hoped that a compact Nb$_3$Sn triplet at a distance (L*) of 10 m from the interaction point would allow the use of a conventional scheme for chromaticity correction using the arc sextupoles. However, after matching the new triplet to the LHC and correcting the chromaticity the chromatic beta beating at dp/p = ±0.001 is about 100%, which is not tolerable regarding collimation and machine protection issues [6].

The challenge consists in developing an optics that not only achieves the β^* of 10 cm while leaving the HL-LHC insertions undisturbed but that also provides a dedicated chromaticity correction scheme.

4.3.3.2 **Implementation of the LHeC into the ATS scheme**

The Achromatic Telescopic Squeezing scheme is a novel technique proposed for the HL-LHC project in IR1 and IR5 (ATLAS and CMS respectively) to reduce the β*, overcoming the limitations of the optics given by the quadrupole strengths in the IR's and the chromatic correction efficiency limits [8].

The ATS consists of creating and absorbing a β-beating wave in the arcs adjacent to the low β insertions. By adjusting the phase advance in the arc cell to π/2, this β-beating wave is carefully constructed in a way that will increase the β function at the location of every alternate sextupole in the arcs, and consequently increase its efficiency for chromatic correction, at the same rate than the β* gets reduced.

Although reducing β* increases the IR chromaticity, the improvement in sextupole efficiency in the arcs leads to a net benefit.

Following a proposal to integrate the LHeC IR into the HL-LHC lattice using the ATS scheme [9], a first study of the required proton optics for the nominal case was presented in [10]. This procedure involved extending the β-beating wave in the arc between IR2 and IR3 by adjusting the arc cells in sector 23 to the phase advance of π/2 and imposing the ATS matching conditions for proton beam 2 for the left and right phase advance of IR2 (with respect to IP2) resulting in a β* of 10 cm in IR2 for the LHeC and a β* of 15 cm in IR1 and IR5 for the HL-LHC. The β functions along the LHC with this optics are shown in Fig. 7.
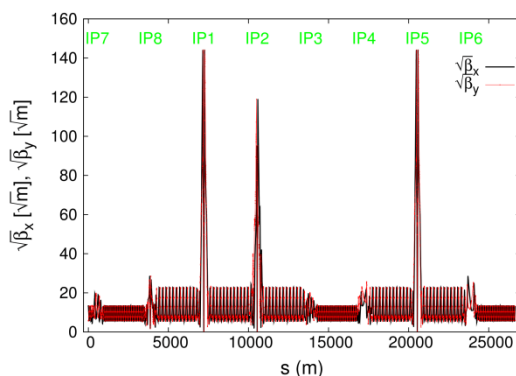
Figure 7: LHeC ATS collision optics for beam 2 with $\beta^* = 10$ cm and $L^* = 10$ m in IP2 and $\beta^* = 15$ cm in IP1 and IP5.

4.3.3.3 **Flexibility of the design**

The flexibility of the design described above (based on the ATS scheme) is of great interest because of the benefits that could be obtained in terms of synchrotron radiation power and luminosity.

Two methods were used to assess the flexibility. First β^* is reduced as far as possible, to determine the maximum luminosity that can be achieved. Second, L^* is increased as far as possible, to reduce the synchrotron radiation power from the electron beam: with larger L^*, less bending is required to guide the electron beam into the field-free aperture

of the proton inner triplet. This is illustrated in Fig. 8, where the synchrotron radiation power is given as a function of L* with a β^* of 10 cm.
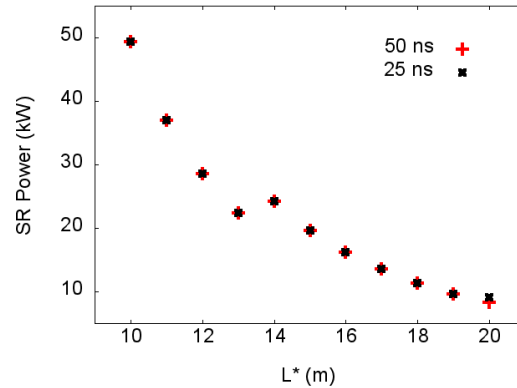
Figure 8: Synchrotron radiation power as a function of L*. The black and red symbols (almost overlaid in the image) show the synchrotron radiation for the minimum beam separation for bunch spacing of 25 ns and 50 ns respectively, and both for the case of the CDR luminosity of $L = 10^{33}$ cm^{-2}s^{-1}.

Keeping the optics parameters at either end of IR2 fixed, the strengths of the quadrupoles in the IR2 can be used as variables to find solutions for different values of β^* and L^*.

Stable solutions for optical designs with L^* between 10 m and 20 m and β^* fixed at 10 cm have been found, as well as the cases with $\beta^* = \{5, 6, 7, 8, 9, 10, 20\}$ cm and L^* fixed at 10 m [11].

4.3.3.4 *Chromaticity Correction*

The chromaticity correction for the HL-LHC case was achieved using only one family of sextupoles at each side of the IPs. However, in the LHeC, an imbalance exists due to the β wave produced to perform the telescopic squeeze in both IP1 and IP2. The path to follow is then trying to achieve a global correction that might break the locality of the chromatic correction but that will certainly bring benefits in terms of controlling the chromatic aberrations.

The strengths of all sextupole families are varied to fix the horizontal and vertical chromaticities to values $Q'_x = Q'_y = 2$, and to reduce the chromatic betatron amplitude functions in the collimation insertions IR3 and IR7 to W_x, $W_y < 200$.

Chromatic correction including control of the tune spread to avoid resonances up to order 9 was achieved for a minimum β^* of 8 cm with $L^* = 10$ m, and a maximum L^* of 18 m with $\beta^* = 10$ cm.

The natural chromaticity for the different optical designs in terms of L^* and β^* along with the limit of the chromatic correction is shown in Fig. 9.
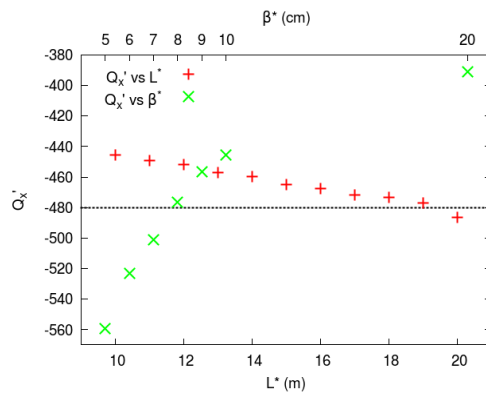
Figure 9: Limit of the chromatic correction (black dashed line) overlaid in the plot Qx' vs L* (red) and Qx' vs β*(green).

4.3.3.5 *Tracking studies*

Dynamic Aperture (DA) studies were performed to study the impact of the different lattices on long term stability of the beam. The DA calculations were carried out in SixTrack[1] over 10^5 turns and considering 60 different realizations (seeds) of the LHC magnet errors. So far, the errors of the new IT and recombination dipoles D1 and D2 for IR1, IR2 and IR5 have not been included, as well as the errors for the additional quadrupoles Q4, Q5 for the HL insertions IR1 and IR5.

Figure 10 shows the minimum dynamic aperture for all sees and angles as a function of L^* with $β^*$ fixed at 10 cm. A small reduction of DA is observed for the case $L^* = 15$ m but it is still very close to the DA found for $L^* = 10$ m. However, for $L^* > 15$ m the higher β functions reached in the location of the inner triplet causes aperture losses and therefore a significant reduction of DA.
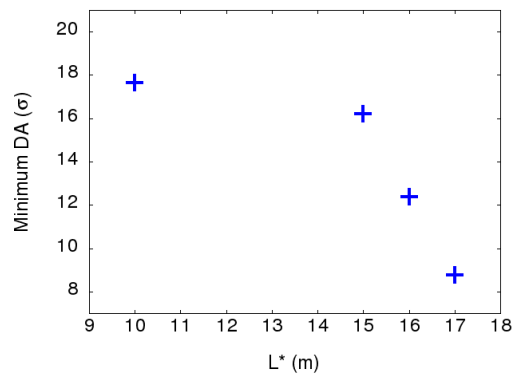
Figure 10: Minimum dynamic aperture over 60 seeds and 5 angles as a function of L^* for LHeC lattices with collision optics ($β^* = 15$ cm at IP1 and IP5, $β^* = 10$ cm at IP2) over 10^5 turns. Cases with L* = 10 m, 15 m, 16 m and 17 m are shown.

---

[1] http://sixtrack.web.cern.ch/SixTrack

Figure 11 shows the minimum dynamic aperture for all seeds and angles now as a function of β^* all with L^* fixed at 10 m. Results show a reduction in dynamic aperture for cases with $\beta^* < 10$ cm, with similar results between the cases with $\beta^* = 8$ and $\beta^* = 9$ cm, but a clear reduction for the case with $\beta^* = 5$ cm.
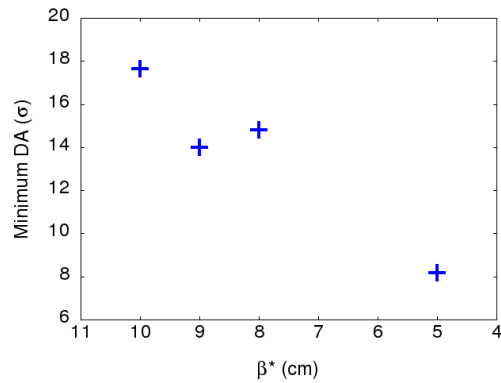
Figure 11: Minimum dynamic aperture over 60 seeds and 5 angles as a function of β^* for LHeC lattices over 10^5 turns. Cases with $\beta^* = 5$ cm, 8 cm, 9 cm and 10 cm (all with L* = 10m) are shown.

In summary, we have demonstrated the feasibility of integrating the LHeC into the HL-LHC by extending the ATS scheme. For the CDR luminosity of $L = 10^{33}$ cm^{-2}s^{-1} studies show the possibility of increasing L* up to 15 m, bringing benefits in terms of the synchrotron radiation power and magnet design. On the other hand the upgraded luminosity of 10^{34} cm^{-2}s^{-1} is within reach but further studies are required to produce a feasible design.

4.3.4 PERLE a Proposed ERL Test Facility at CERN

4.3.4.1 *Design Concept and Parameters*

PERLE stands for Powerful Energy Recovery Linac Experiment [16]. The test facility aims at a 1 GeV beam energy, which can be achieved in a recirculating SC linear accelerator operating with high currents in multi-pass (3) energy recovery mode. Independently, it could be used for variety of physics applications

PERLE is envisioned as a staged project. The final baseline design (**Error! Reference source not found.**2) would consist of the following basic elements:

- A 5 MeV injector;
- Two 150 MeV linacs consisting of eight 5-cell SC structures;
- Optics transport lines including spreader regions at the exit of each linac to separate and direct the beams via vertical bending, and recombiner sections to merge the beams and to match them for acceleration through the next linac;
- Beam dump at 5 MeV.
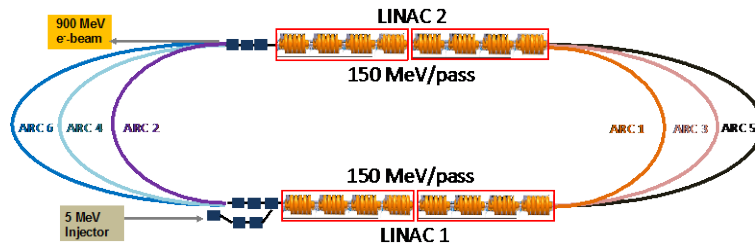
Figure 12: ERL accelerator complex of two parallel linacs consisting of two 4-cavity cryomodules each achieving 150 MeV acceleration per linac (300 MeV per pass).

Each beam recirculates up to three times through both linacs to boost the energy to about 900 MeV. To enable operation in the energy recovery mode after acceleration the beam is phase shifted by 180° and then sent back through the recirculating linac at a decelerating RF phase. The set of main parameters incorporated into the ERL prototype is shown in Table 1.

The first phase of the staged construction would only use two 4-cavity cryomodules and a single pass – it could reach 150 MeV and be used for injector studies and SC RF tests. A subsequent upgrade would involve installation of two additional arcs on each side to raise the beam energy up to 450 MeV. This configuration accommodates additional space available for implementation of feedback, phase-space manipulations, and beam diagnostic instrumentation. In phase 3, four additional cavities in each linac are added to permit energy recovery recirculation tests at full energy.

Table 1: Basic Parameters of PERLE

TARGET PARAMETER	VALUE
Injection Energy	5 MeV
Maximum Energy	900 MeV
Normalized Emittance $\gamma\varepsilon_{xy}$	< 25 mm mrad
Average Beam Current	> 12.8 mA
Beam charge	320 pC
Bunch Spacing	25 ns
RF frequency	801.58 MHz
Duty Factor	CW

4.3.4.2 *Injector*

The injector of the ERL test facility needs to deliver beams with an average current of 12.8 mA (with possibility of future upgrades to deliver polarized electrons or larger currents) and the energy of ~ 5 MeV. Bunches with a charge of 320 pC or higher follow with a repetition rate of 40.1 MHz (20th sub-harmonic of 801.58 MHz). There are

several possibilities to meet these specifications. One option is to use a grid modulated thermionic gun followed by a multi stage bunching-accelerating structure. This choice however will rule out any future upgrade to deliver polarized electrons. Photocathode guns where electrons are emitted from the photocathode illuminated with laser light are more flexible in terms of the beam charge and temporal structure and allow operation with both polarized and un-polarized photocathodes. Presently, only DC technology may be considered as mature and applicable to an ERL test facility.

To deliver beams with the parameters required for PERLE, preliminary simulations indicate the possibility of using a 350 kV DC gun operating with a Cs_3Sb photocathode. An optimal beam emittance of $2\pi \cdot mm \cdot mrad$ can be obtained with a laser pulse with hat top spatial distribution with a diameter of 3 mm and a flat top 80ps laser pulse. The RMS bunch length at 1 m from the photocathode is 8.5 mm (36 ps) and depends only slightly on the laser pulse length.

Once emerged from the gun, an energy chirp should be introduced to longitudinally compress the bunch and compensate the bunch elongation due to the space charge repulsion (typically done with an RF buncher). In order to provide linear energy modulation the frequency of the buncher should be selected to have a bunch flight time at the buncher shorter than 10° of its RF phase. At 320 pC and rms buncher flight time of 36 ps the required frequency should be less than 775 MHz. Practically attractive is 400.8 MHz - the first sub-harmonic of the ERL frequency. Gradual beam compression and acceleration can be provided with a booster consisting of a series of single cell 801.58 MHz cavities with individual coupling and control of amplitude and RF phase.

4.3.4.3   *Transport Optics*

Appropriate recirculation optics is of fundamental concern in a multi-pass machine to preserve beam quality. The design consists of three different regions, the linac optics, the recirculation optics and the merger optics. A concise representation of multi-pass linac optics is illustrated in Fig. 13.
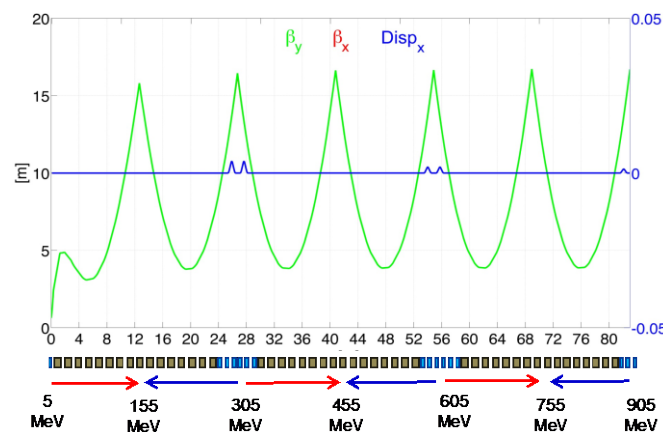
Figure 13: ERL multi-pass linac optics. The requirement of energy recovery puts a constraint on the exit/entrance Twiss functions for the two linacs. Green and blue curves show, respectively, the evolution of the beta functions amplitude and the horizontal dispersion for Linac 1. Red and blue arrows indicate the passages of acceleration and deceleration.

Due to the demand of providing a reasonable validation of the LHeC final design a Flexible Momentum Compaction (FMC) cell based lattice has been adopted. Specifications require isochronicity, path length controllability, large energy acceptance, small higher-order aberrations and tunability. An example layout, which fulfils these conditions, is shown in Fig. 14 and represents the lowest energy arc optics as example. It includes a two-step achromatic spreader and a mirror symmetric combiner to direct the beam into the arc. The vertical dispersion introduced by the first step bend is suppressed by the quadrupoles located appropriately between the two stages. The switchyards separate all 3 arcs into a 90 cm high vertical stack; the highest energy arc is not elevated and remains at the linac-level. A horizontal dogleg, used for path length adjustment and made of 3 - 13 cm long dipoles, is placed downstream of each spreader providing a tunability of ± 1 cm (10° of RF).
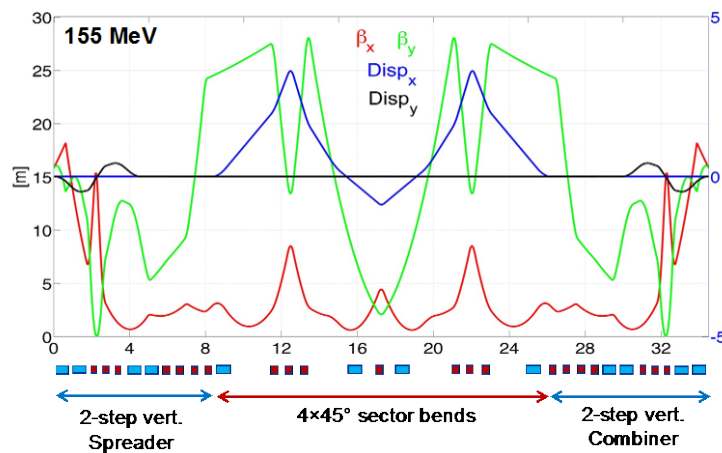
Figure 14: Optics based on the FMC cell for the lowest energy return arc. Horizontal (red curve) and vertical (green curve) beta-function amplitudes are illustrated. Blue and black curves show, respectively, the evolution of the horizontal and vertical dispersion.

The recirculating arc at 155 MeV is composed of 4 - 70 cm long dipoles to bend the beam by 180° and of a series of quadrupoles (two triplets and one singlet). A complete first-order layout for switchyards, arcs and linac-to-arc matching sections has been accomplished for all the arcs. Injection into the racetrack at 5MeV is accomplished through a rectangular chicane, configured with four identical rectangular bends and 11 quadrupoles distributed in a mirror symmetric fashion, leaving six independent quadrupole gradients to control: betas and alphas at the beginning of the linac (4 parameters), momentum compaction (1 parameter) and the horizontal dispersion (1 parameter). The chicane optics features a horizontal achromat, by design, with tunable momentum compaction to facilitate bunch-length control and finally with Twiss functions matched to the specific values required by the linac.
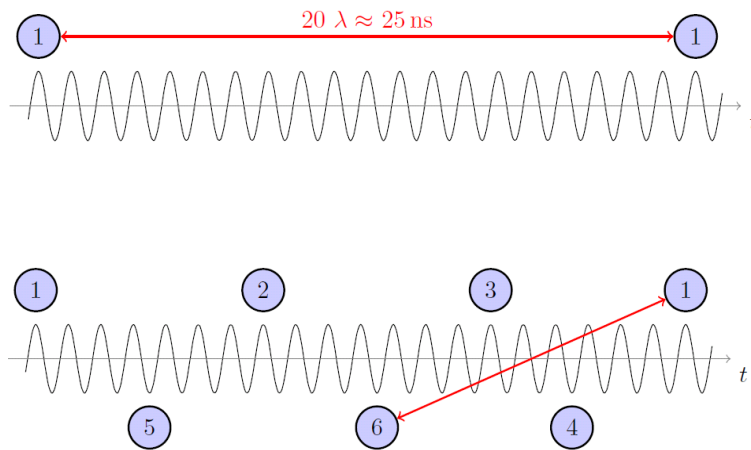
Figure 15: (Top) Basic RF structure, without recirculation with bunches injected every 25 ns. (Bottom) When the recirculation is in place, both linacs are populated with bunches at different turns. Presented recombination pattern maximizes the separation between the two low energy bunches (at the first and sixth turn).

The path length of each pass is chosen to be precisely an integer number of RF wavelengths except for the highest energy pass whose length is shifted by half an RF wavelength to recover the energy through deceleration. In order to minimize collective effects, the number of RF wavelengths that determines the arc's lengths has been tuned to avoid different bunches in the same bucket, like it would happen with a full turn length equal to an integer number of 20 λ. The lattice is therefore adjusted to achieve nearly constant bunch spacing. Special care has been taken to select a pattern that maximizes the distance between the lowest energy bunches circulating into the machine at the first and last turn (bunches 1 and 6 in Fig. 15). This comes from the fact that, with a nearly constant β function, the kicks from HOMs are more disruptive at lower rigidities, thus if two low energy bunches follow each other, the Beam Break Up (BBU) threshold current can be reduced. Fig. 16 is obtained following a test bunch in its path from the injector to the dump. The energy profile shows that the arcs' lengths are properly tuned to obtain the maximum acceleration and deceleration.

The total beam path for a full 3 pass accelerating cycle is around 300 m leading to an approximate footprint of 43m × 16m of the ERL itself.
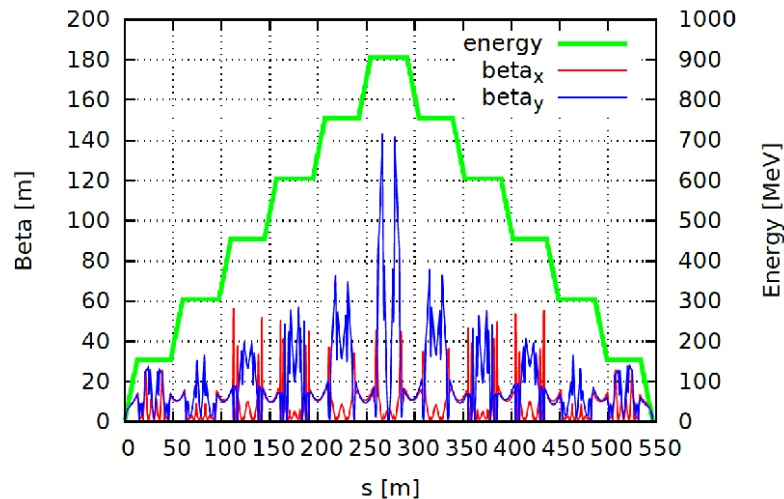
Figure 16: Energy and Twiss parameter tracked for the whole lattice.

In conclusion, the case for PERLE is quite compelling; it will serve as a unique 'testbed' for demonstrating validity of innovative beam dynamics solutions proposed for the LHeC. In particular, scaling of energy recovery to a large-scale SRF installation raises concerns about multi-pass BBU, an instability that has previously been seen and studied in detail in the Jefferson Lab FEL [12]. There are still open questions about scaling of instability thresholds to higher beam energies and a large-scale SRF installation [13] that could be addressed at PERLE. We propose PERLE to experimentally address these challenges with unique new additional accelerator capability. The facility would enable experimental exploration of multiple-passes and high current operation.

4.3.5 **Summary and Outlook**

Here, we discussed novel approach to meet the LHeC challenges of adding new accelerator capabilities (ERL with multiple-passes, tens of GeV at high current, tens of mA). They were addressed through exploration of innovative lattice solutions. Effective implementation of Energy Recovering Linac technology requires: proper design of multi-pass optics, fine control of beam stability and losses (halo), preservation of 6D bunch quality, energy recovery efficiency, multiple-beam diagnostic devices, and development of ERL-specific commissioning and optics tuning procedures[14, 15].

Scaling of energy recovery to multi-GeV energies also encounters incoherent synchrotron radiation energy loss and spread, which asymmetrize accelerated and decelerated beam energies and profiles. These asymmetries substantially complicate multi-pass energy recovery and matching, and ultimately they limit the energy reach of the ERL due to recirculating arc momentum acceptance. Scaling of energy recovery to a large-scale SRF installation also raises concerns about multi-pass BBU. We propose PERLE to experimentally address these issues as well.

Presented unique design of the IR optics gives the impression that luminosity of 10^{34} $cm^{-2}s^{-1}$ is within reach.

4.3.6 References

1. D. Pellegrini, A. Latina, D. Schulte, S.A. Bogacz, "Beam-dynamics driven design of the LHeC energy-recovery linac", PRSTAB (2015).

2. D. Pellegrini, "Beam Dynamics Studies in Recirculating Machines", Ph.D. Thesis, EPFL, Switzerland, 2016.

3. O. Brüning et al, "DEVELOPMENT OF AN ERL BASED TeV ENERGY ep AND eA COLLIDER AT CERN" ICFA Beam Dynamics Newsletter No 68, December 2015.

4. J. Rosenzweig and L. Serafini, "Transverse particle motion in radio-frequency linear accelerators", Phys. Rev. E, vol. 49, Feb 1994.

5. 12 GeV CEBAF Upgrade, Reference Design, www.jlab.org/12GeV

6. J. L. Abelleira Fernandez *et al.* (LHeC Study Group), "A Large Hadron Collider at CERN", J. Phys. G. 39 (2012) 075001.

7. B. Parker, presentation in the LHeC Workshop, Chavannes-de-Bogis, 2015, https://indico.cern.ch/event/356714/.

8. S. Fartoukh, "Achromatic telescopic squeezing scheme and application to the LHC and its luminosity upgrade", Phys. Rev. ST Accel. Beams 16, 111002 (2013).

9. R.Tomás, in the Meeting on LHeC with Daresbury group, Daresbury, UK, 2012, https://indico.cern.ch/event/207665/.

10. M. Korostelev, E. Cruz-Alaniz, D. Newton, A. Wolski, O. Brüning, and R. Tomás, "LHeC IR optics design integrated into the HL_LHC lattice", in Proceedings of the 4th International Particle Accelerator Conference, Shanghai, China, 2013, MOPWO063.

11. E. Cruz-Alaniz, D. Newton, R. Tomás and M. Korostelev, "Design of the Large Hadron Electron collider interaction region", Phys. Rev. ST Accel. Beams 18, 111001 (2015).

12. S.A. Bogacz, A. Hutton et al., "CEBAF-ER Experiment Proposal", Je_erson Lab, PAC22 proposal PR-02-102, June 2002.

13. G. Hoffstaetter and I. Bazarov, "Beam-breakup Instability Theory for Energy Recovery Linacs", in Phys. Rev. ST Accel. Beams, 7, p. 054401, 2004.

14. ICFA Beam Dynamics Newsletter on ERL Technology, No. 68, Eds. J. Wang and W. Chou, Dec. 2015.

15. T. Powers and C. Tennant, "Implications of Incomplete Energy Recovery in SRF-Based Energy Recovery Linacs", in Proc. of ERL'07, Daresbury, UK, p. 75.

16. PERLE, Conceptual Design Report, 2015, unpublished

4.4 Lattice Design for Super Proton Proton Collider (SPPC)

Feng Su, Jie Gao, Yukai Chen, Jingyu Tang, Dou Wang,

Yiwei Wang, Sha Bai, Tianjian Bian, Dengjie Xiao

Mail to: sufeng@ihep.ac.cn

Institute of High Energy Physics, Chinese Academy of Sciences, Beijing, China

4.4.1 Introduction

With the discovery of the Higgs boson at the LHC, the world high-energy physics community is investigating the feasibility of a Higgs Factory as a complement to the LHC for studying the Higgs and pushing the high energy frontier. CERN physicists are busy planning the LHC upgrade program, including HL-LHC and HE-LHC. They also plan a more inspiring program called FCC, including FCC-ee and FCC-hh. Both the HE-LHC and the FCC-hh are proton-proton (pp) colliders aiming to explore the high energy frontier and expecting to find new physics [1, 2, 3]. Chinese accelerator physicists also plan to design an ambitious machine called CEPC-SPPC (Circular Electron Positron Collider-Super Proton Proton Collider). The CEPC-SPPC program contains two stages. The first stage is an electron-positron collider with center-of-mass energy 240 GeV to study the Higgs properties carefully. The second stage is a proton-proton collider at center-of-mass energy of more than 70 TeV [4]. The SPPC design is just starting, and first we developed a systematic method of how to make an appropriate parameter choice for a circular pp collider by using an analytical expression of beam-beam tune shift, starting from the required luminosity goal, beam energy, physical constraints at the interaction point (IP) and some technical limitations [5, 6]. Then we start the lattice design according to the parameter list and have the first version SPPC lattice.

4.4.2 SPPC Parameter Choice

The energy design goal of the SPPC is about 70-100 TeV, using the same tunnel as the CEPC, which is about 59 km in circumference [7, 8, 10]. A larger circumference for the SPPC, like 100 km, is also being considered. It is planned to use superconducting magnets of about 20 T [4]. We obtain a set of parameters for the 59.2 km SPPC. In this set of parameters, the full crossing angle θc keeps the separation of 12 RMS beam sizes for the parasitic crossings. The luminosity reduction factor due to the crossing angle is larger than 0.9 and the ratio of β^* and σ_z is about 15. We also give a set of parameters for the larger circumference SPPC, considering both 80 km and 100 km. Table 1 is the parameter list for the SPPC. We choose the dipole field as 20 T and get a center-of-mass energy of 70 TeV. If we want to explore the higher energy, we should make the

circumference larger. To explore a center-of-mass energy of 100 TeV while keeping the dipole field at 20 T, the circumference should be 80 km at least. With this condition, there is hardly any space to upgrade, so a 100 km SPPC is much better because the dipole field is then only 15.52 T. If the dipole field is kept at 20 T in a 100 km SPPC, we can get a center-of-mass energy as high as 130 TeV [9, 11].

Table 1: SPPC Parameter List.

	SPPC(Pre-CDR)	SPPC-59.2Km	SPPC-100Km	SPPC-100Km	SPPC-80Km
Main parameters and geometrical aspects					
Beam energy[E_0]/TeV	35.6	35.0	50.0	65.0	50.0
Circumference[C_0]/km	54.7	59.2	100.0	100.0	80.0
Dipole field[B]/T	20	19.70	15.52	19.83	19.74
Dipole curvature radius[ρ]/m	5928	5921.5	10924.4	10924.4	8441.6
Bunch filling factor[f_2]	0.8	0.8	0.8	0.8	0.8
Arc filling factor[f_1]	0.79	0.78	0.78	0.78	0.78
Total dipole length [L_{Dipole}]/m	37246	37206	68640	68640	53040
Arc length[L_{ARC}]/m	47146	47700	88000	88000	68000
Straight section length[Lss]/m	7554	11500	12000	12000	12000
Physics performance and beam parameters					
Peak luminosity per IP[L]/ cm^{-2}s^{-1}	$1.1{\times}10^{35}$	$1.20{\times}10^{35}$	$1.52{\times}10^{35}$	$1.02{\times}10^{36}$	$1.52{\times}10^{35}$
Beta function at collision[$\beta*$]/m	0.75	0.85	0.99	0.22	1.06
Max beam-beam tune shift [ξy]/IP	0.006	0.0065	0.0068	0.0079	0.0073
Number of IPs contribute to $\triangle$Q	2	2	2	2	2
Max total beam-beam tune shift	0.012	0.0130	0.0136	0.0158	0.0146
Circulating beam current[I_b]/A	1.0	1.024	1.024	1.024	1.024
Bunch separation[$\triangle$t]/ns	25	25	25	25	25

Number of bunches[n_b]	5835	6315	10667	10667	8533
Bunch population[N_p] (10^{11})	2.0	2.0	2.0	2.0	2.0
Normalized RMS transverse emittance[ε]/μm	4.10	3.72	3.62	3.10	3.35
RMS IP spot size[σ^*]/μm	9.0	8.85	7.86	3.04	7.86
Beta at the 1st parasitic encounter[β_1]/m	19.5	18.70	16.36	68.13	15.31
RMS spot size at the 1st parasitic encounter[σ_1]/μm	45.9	43.20	33.31	55.20	31.03
RMS bunch length[σ_z]/mm	75.5	56.60	65.68	14.88	70.89
Full crossing angle[θc]/μrad	146	138.23	106.60	176.66	99.28
Reduction factor according to cross angle[Fca]	0.8514	0.9257	0.9247	0.9283	0.9241
Reduction factor according to hour glass effect[F_h]	0.9975	0.9989	0.9989	0.9989	0.9989
Energy loss per turn[U_0]/MeV	2.10	1.97	4.45	12.71	5.76
Critical photon energy[Ec]/keV	2.73	2.60	4.11	9.02	5.32
SR power per ring[P_0]/MW	2.1	2.01	4.56	13.01	5.89
Transverse damping time [τ_x]/h	1.71	1.946	2.08	0.946	1.28
Longitudinal damping time [τ_ε]/h	0.85	0.973	1.04	0.473	0.64

4.4.3 SPPC Lattice Consideration

4.4.3.1 *ARC length consideration and limitation*

According to the SPPC physicists, we want to find some new physics on this big ambitious machine. The center-of-mass energy should be 70 TeV at least and between 70 TeV and 100 TeV will be much better. We will use high field dipole in ARC and its strength will be 20T. Now we estimate the circumference length. If we choose the lowest CMS energy 70 TeV, then we have the smallest Bρ *(116635.29Tm)*. We use the highest strength of dipole 20T, then we have the smallest dipole radius *ρ(5831.76m)* and the smallest total dipole length (36.6 km). If the arc filling factor in ARC is 0.8, an usual choice and much reasonable number, then we can get the total ARC length (L_{ARC}

=47.8 km). There are 8 long straight sections and 2 of them are about 3 km long at IP1 and IP3 for ee integration region. And now the other 6 long straight sections are about 1km in the same length. So the circumference will be about 59.5 km.

4.4.3.2   *Layout consideration*

According to the Pre-CDR and CEPC partial double ring layout [10, 11], in the future, SPPC is in the same tunnel with CEPC and may be running at the same time. So the layout of SPPC should consider the CEPC layout. Fig. 1 shows the layout of SPPC according the layout of CEPC partial double ring scheme.
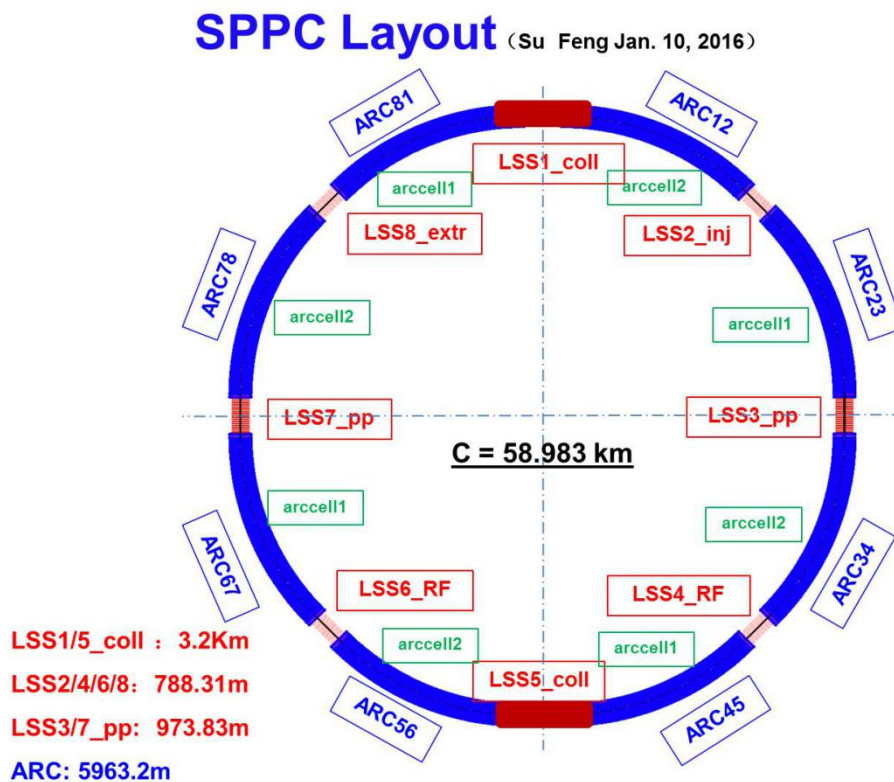
Figure 1: SPPC Lattice Layout.

4.4.4   **SPPC Lattice Design**

4.4.4.1   *ARC and FODO cell*

In this part, we introduced the preliminary lattice design of SPPC. There are 8 arcs and 8 long straight sections. We use FODO in the ARC, and Fig. 2 shows the parameters of FODO cell in ARC. Each cell has 8 dipoles whose length is 14.8 m and strength is 20 T. The total cell length is 144.4 m, maximum beta function is 244.8 m, minimum beta function is 42.6 m and phase advance is 90 degree in both horizontal and vertical. The quadrupole gradient and dipole parameter is reasonable according to the

Pre-CDR choice. And the aperture of quadrupole is also reasonable for both injection and collision energy. Fig. 3 and Fig. 4 is the optics of FODO cell and ARC.

ARC CELL

	LQ	DQS	LS	DSB	LB	DBB
SPPC	4m	1m	0.5m	1m	14.8m	1m
FCC-hh	6.3137m	1m	0.5m	2.184m	14.3m	1.36m

B max [T]	G max [T/m]	k1	k2
19.61	582.156	4.9899E-3	0

Pre-CDR：

Dipole: L=15m   B=20T

Quadrupole:

D = 45 mm   B$_{pole}$=16 T

G=711.1T/m   K1=6.097*10^-3

Betax: 244.878/42.57
Betay: 42.569/244.869   (ϵ_n =4.1um)

E (Collision：35TeV) $\epsilon = \dfrac{\epsilon_n}{\gamma}$
**   (Injection：2.1TeV)**

ϵ **(Collision：1.099*10^-10m=0.1099nm)**
（Injection：1.83*10^-9m=1.83nm）

σ **（Collision：1.66*10^-4m=166um）**
（Injection：6.76*10^-4m=676um）

R=20*σ$_{Inj}$=13.52mm

D=27.04

Figure 2: SPPC FODO cell parameter choice.
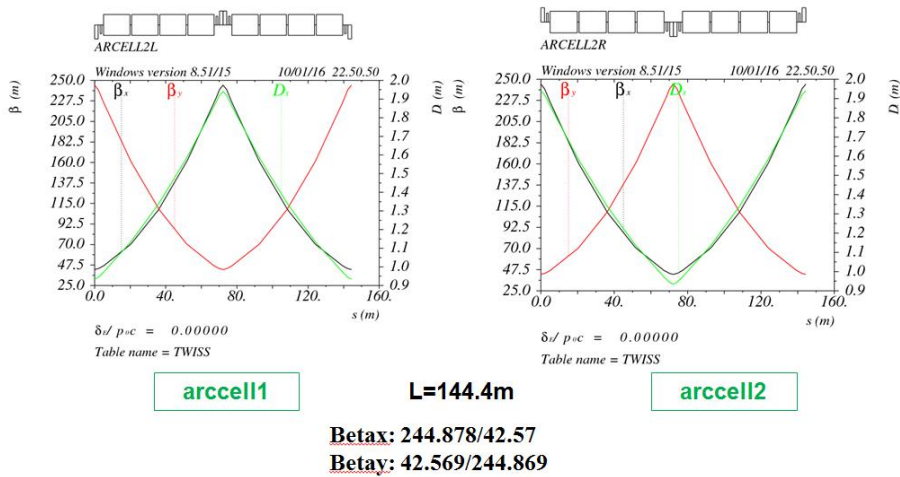
Figure 3: SPPC FODO cell optics.
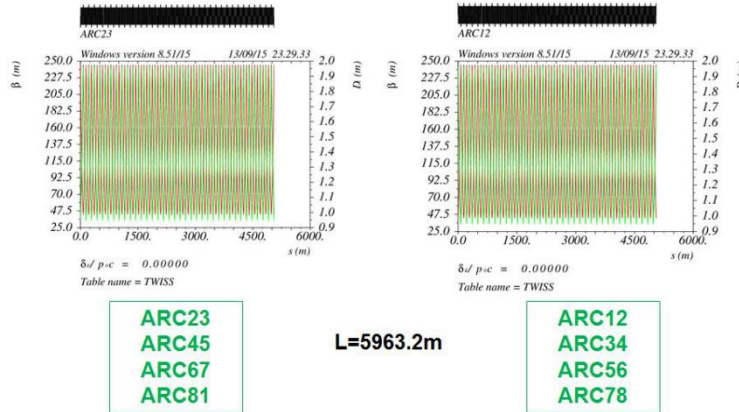
Figure 4: SPPC ARC optics.

4.4.4.2 *Dispersion Suppressor Section*

For 90 degree phase advance FODO cell, the dispersion suppressor section has three schemes, called full-bend scheme, half-bend scheme and missing-dipole scheme. Fig. 5 shows these three schemes for SPPC. And in our design we choose the missing-dipole scheme as the space can be used for collimation in the future.

	BDSP1L	BDSP2L	BDSP1R	BDSP2R	B0	
(1)	9.805	9.805	9.805	9.805	19.61	(T)
(2)	18.93	18.93	18.93	18.93	19.61	(T)
(3)	19.61	19.61	19.61	19.61	19.61	(T)
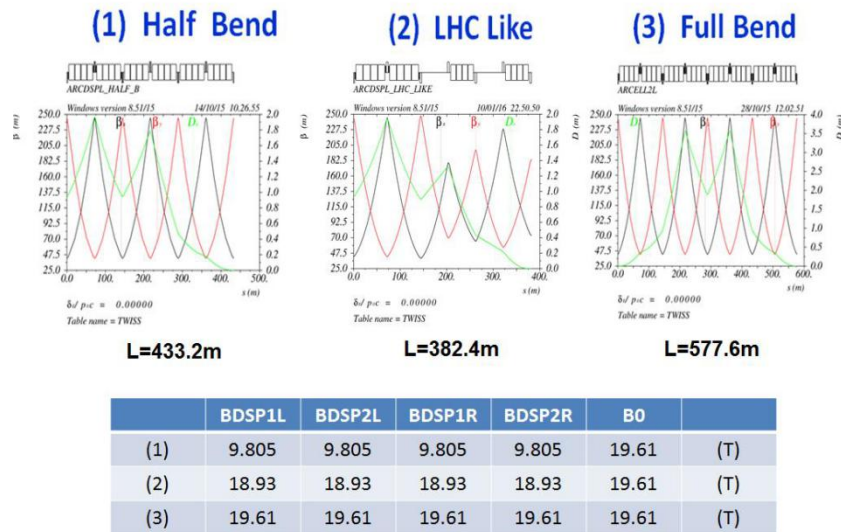
Figure 5: Dispersion suppressor section for SPPC.

4.4.4.3 *Long Straight Section and Interaction Region*

There are 8 long straight sections in SPPC lattice which are named as LSS1_coll, LSS2_inj, LSS3_pp, LSS4_RF, LSS5_coll, LSS6_RF, LSS7_pp and LSS8_extr. Long straight section 3 and 7 are for low β pp collision, long straight section 1 and 5 are for collimation using the long space as 3.2 km, long straight section 4 and 6 are for RF system and long straight section 2 and 8 are for injection and extraction. Fig. 6 7 8 9 show the optics of these long straight sections. Fig. 10 shows the quadrupole strength of

LSS3_pp and LSS7_pp, and the gradient and aperture are reasonable according to the Pre-CDR parameter choice for quadrupoles.
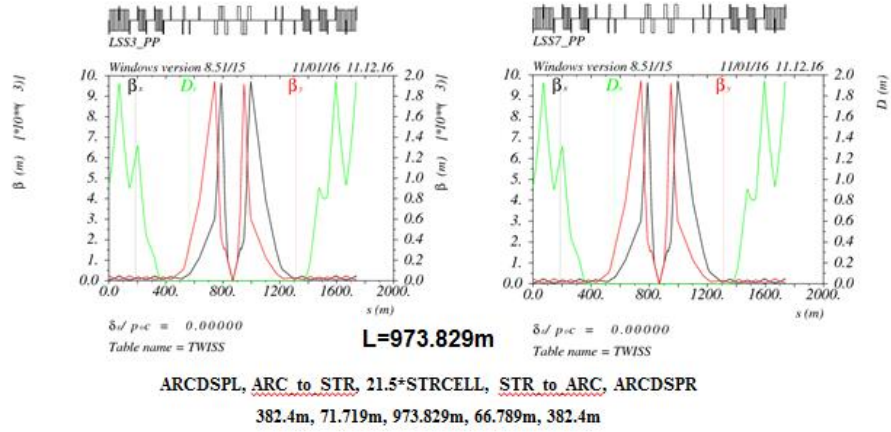
Figure 6: Long straight section for low β pp collision.
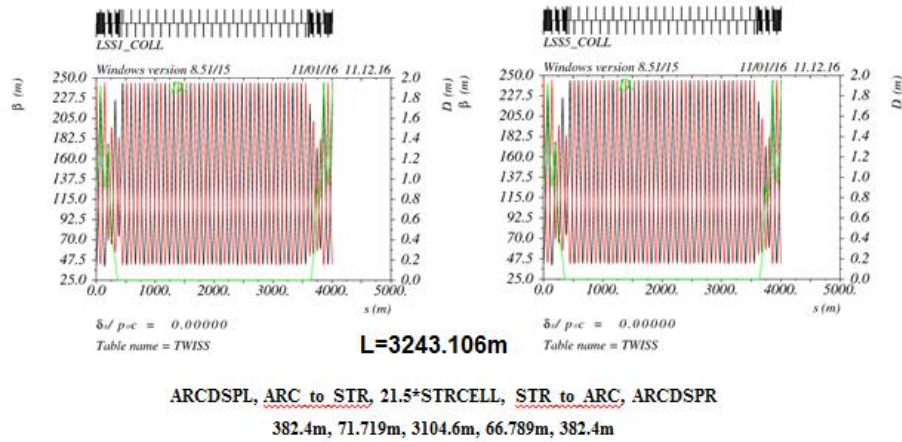
Figure 7: Long straight section for collimation.
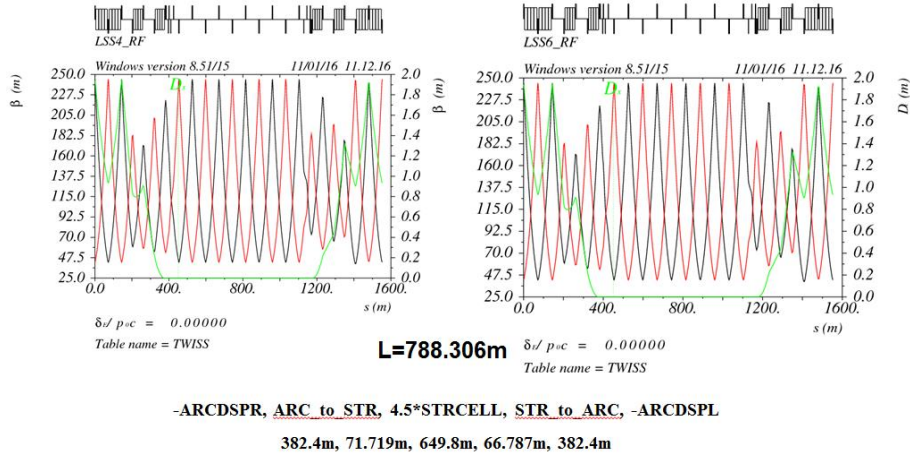
Figure 8: Long straight section for RF system.
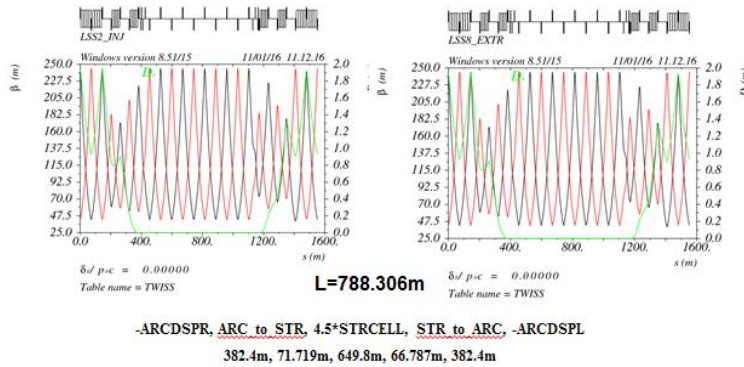
Figure 9: Long straight section for injection and extraction.

R	K1(m^-2)	G （T/M）	L(M)	βmax	L	K1(m^-2)	G （T/M）	L(M)	βmax
K1.QT.1R	4.9751e-03	580.428	6	3543.69	K1.QT.1L	-4.9751e-03	-580.428	6	3543.69
K1.QT.A2R	-5.2595e-03	-613.668	9	9601.686	K1.QT.A2L	5.2595e-03	613.668	9	9601.686
K1.QT.B2R	-5.2595e-03	-613.668	9	9601.686	K1.QT.B2L	5.2595e-03	613.668	9	9601.686
K1.QT.3R	5.3434e-03	623.369	8	9731.53	K1.QT.3L	-5.3434e-03	-623.369	8	9731.53
K1.QM.4R	-2.2804E-04	-266.04	4	3798.29	K1.QM.4L	2.2804E-04	266.04	4	3798.29
K1.QM.5R	8.8592E-04	103.36	4	1506.53	K1.QM.5L	-8.8592E-04	-103.36	4	1506.53
K1.QM.6R	-1.2144E-03	-141.68	4	587.87	K1.QM.6L	1.2144E-03	141.68	4	587.87
K1.QM.7R	1.0640E-04	124.133	4	531.25	K1.QM.7L	-1.0640E-04	-124.133	4	531.25
K1.QM.8R	-4.2431E-03	-495.028	4	162.20	K1.QM.8L	4.2431E-03	495.028	4	162.20

Figure 10: Quadrupole gradient and aperture in LSS3_pp and LSS7_pp.

4.4.5 Dynamic Aperture Study and Beam Dynamics

Dynamic aperture study is a very important and interesting issue in pp colliders. The Dynamic aperture is divided into 2 kinds. One is called Real-World-Dynamic-

Aperture (RW-DA) which is defined as the largest amplitude at which particles remain in the accelerator over a time range of interest. The other one is called Potential-Dynamic-Aperture (PO-DA) which is defined as the onset of global chaos, also means the largest amplitude with mainly regular motion. Insignificant chaotic layers within the regular regime will be ignored. However considerable wide "chaotic spikes" have to be taken into account. It turns out that the PO-DA is typically too small as RW-DA estimate. The chaotic motion is measured by the evolution of initially close-by particles. And the Lyapunov exponent is a sensitive signal for DA tracking.
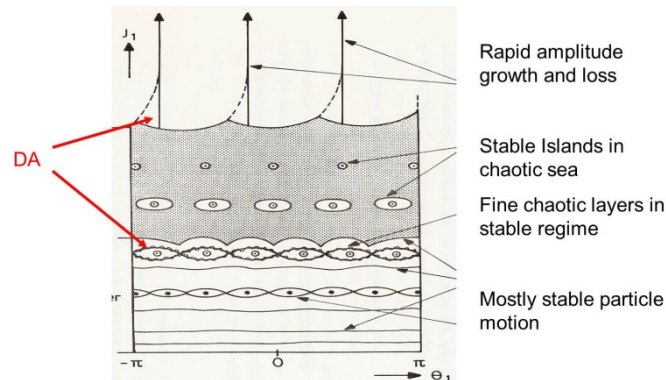
Figure 11: Dynamic Aperture Scheme

4.4.5.1 *Dynamic Aperture without Interaction Region*

At first, we studied the dynamic aperture of SPPC main ring without interaction region. There are 8 arcs in the main ring and 8 long straight sections. Now we use simple FODO in the long straight section, latter we should optimize the long straight section design for difference use like RF system, injection, extraction and collimation.

Following is the dynamic aperture from Sixtrack. Figure 12 is a 4-Dimension phase space for the regular and the chaotic motion. The solid tie shape shows the regular particles motion which has the largest amplitude, if the amplitude becomes a little larger, the motion will become chaotic, and the diffusion points around the solid tie show the chaotic motion. This largest amplitude is the dynamic aperture we want to study. Figure 13 shows the evolution of the distance of phase space for regular (left) and chaotic (right) motion. Figure 14 and Figure 15 show the horizontal and vertical phase space projections for the regular (left) and the chaotic (right) cases. Figure 16 show the physical phase space projections for the regular (left) and the chaotic (right) cases. Figure 17 and Figure 18 show the horizontal and vertical tune FFT-analysis for the regular (left) and the chaotic (right) cases. We can get from the figures that the dynamic aperture is about 22.58 mm (346 σ_x) in horizontal and 49.16 mm (315 σ_y) in vertical.
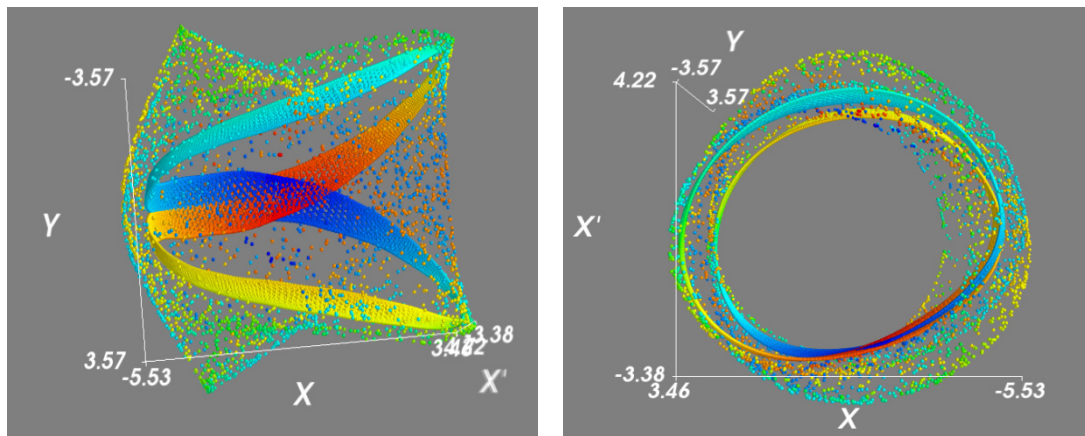
Figure 12: 4-Dimension phase space for regular and chaotic motion (cm).

(The solid tie shape shows the regular particles motion which has the largest amplitude, if the amplitude becomes a little larger, the motion will become chaotic, the diffusion points around the solid tie show the chaotic motion. This largest amplitude is the dynamic aperture we want to study.)
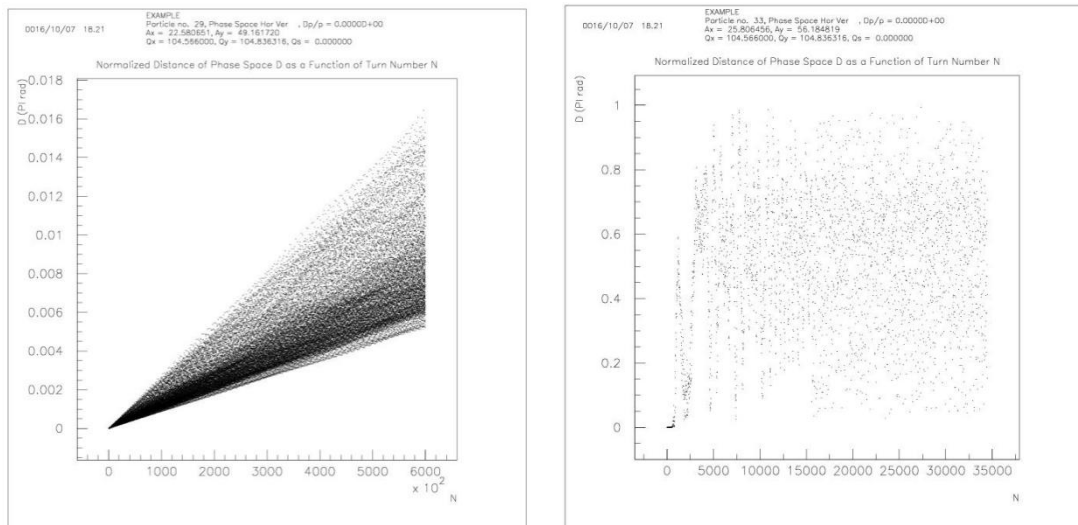
Figure 13: Evolution of the distance of phase space for regular (left) and chaotic (right) motion.

162
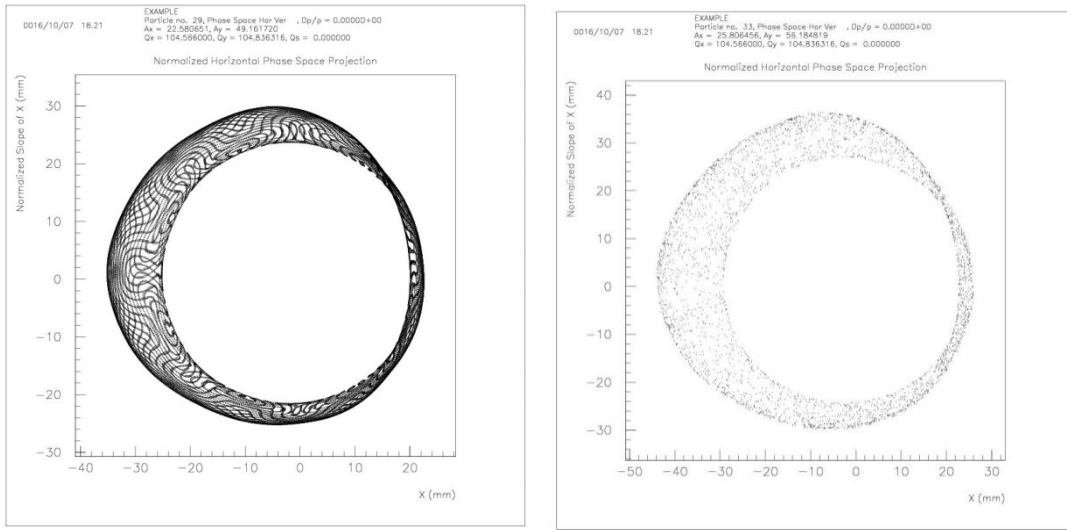
Figure 14: Horizontal phase space projections for regular (left) and chaotic (right) cases.
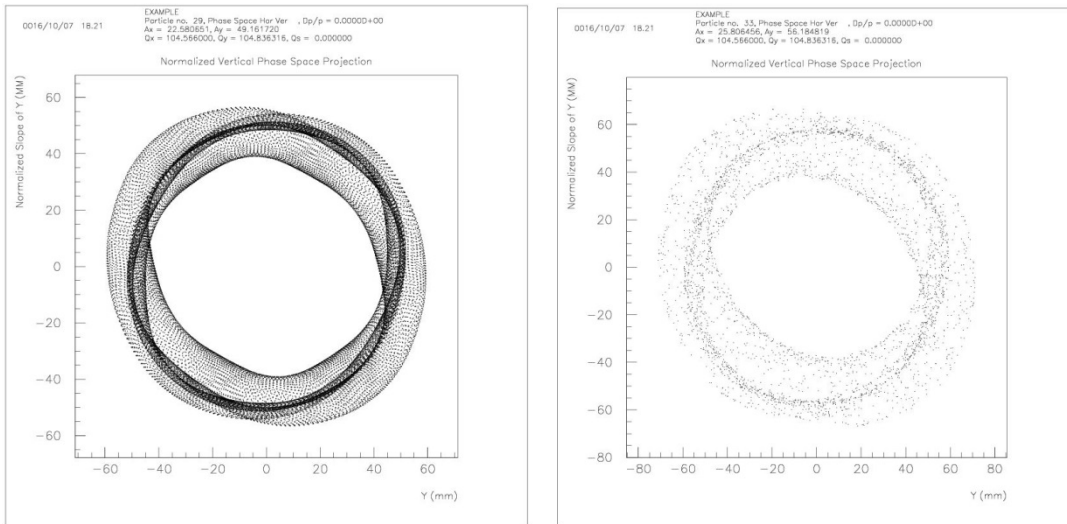
Figure 15: Vertical phase space projections for regular (left) and chaotic (right) cases.
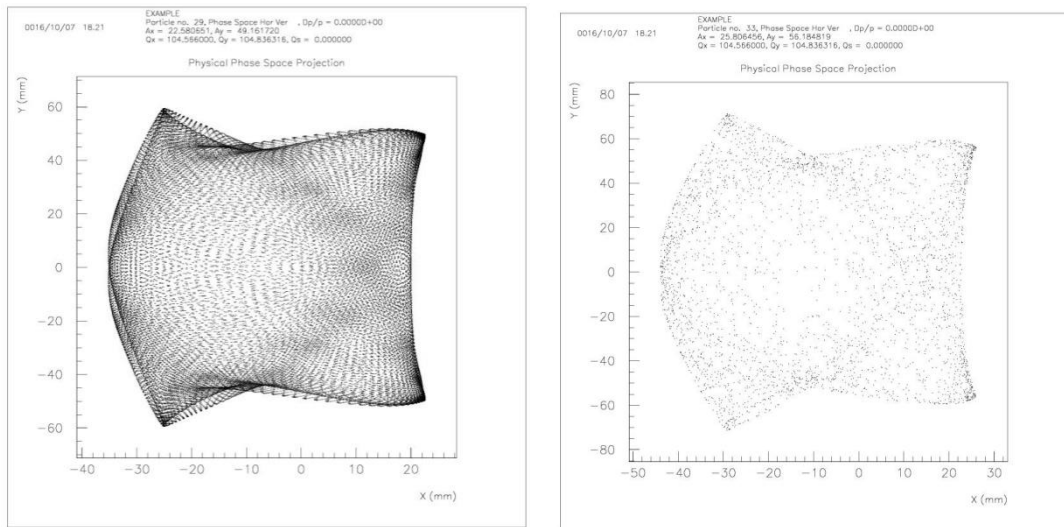
Figure 16: Physical phase space projections for regular (left) and chaotic (right) cases.
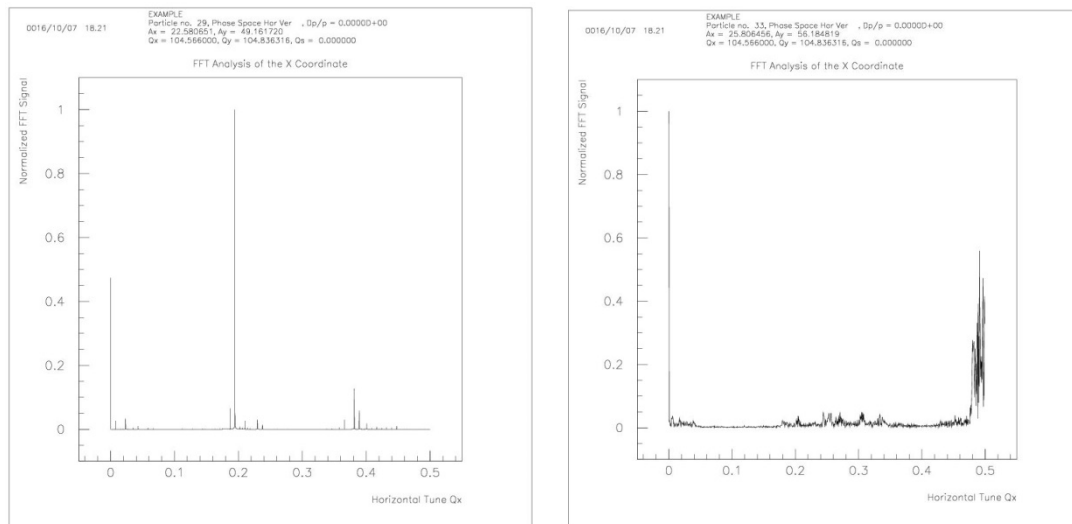
Figure 17: Horizontal FFT-analysis for the regular (left) and the chaotic (right) cases.
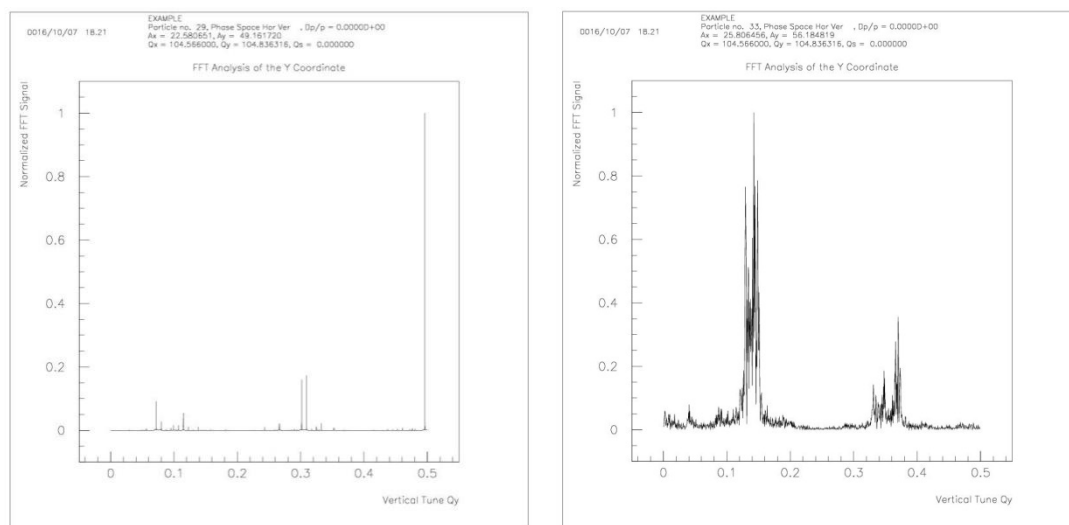
Figure 18: Vertical FFT-analysis for the regular (left) and the chaotic (right) cases.

4.4.5.2 *Dynamic Aperture with Interaction Region*

Following is the dynamic aperture with low beta pp interaction region. The beta function at IP is 0.75m. The maximum beta function in this region is about 9.6 km. The dynamic aperture becomes smaller, 8.22 mm (126 σx) in horizontal and 19.73 mm (126 σy) in vertical (we keep the same observation point for comparison with the DA without low beta pp IR). At the low beta pp IP, the dynamic aperture is only 1.089mm (126 σ) in both horizontal and vertical because the beam size is very small (8.647um).
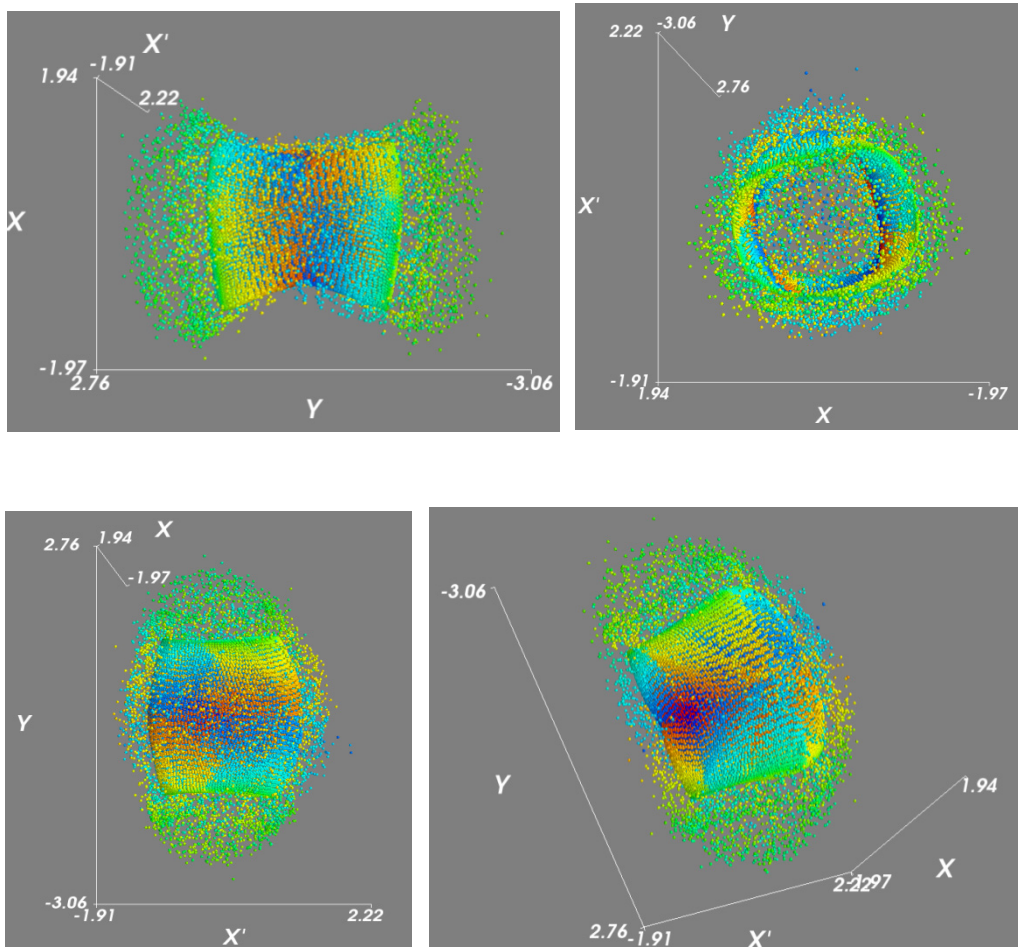
Figure 19: 4-Dimension phase space for regular and chaotic motion (cm).
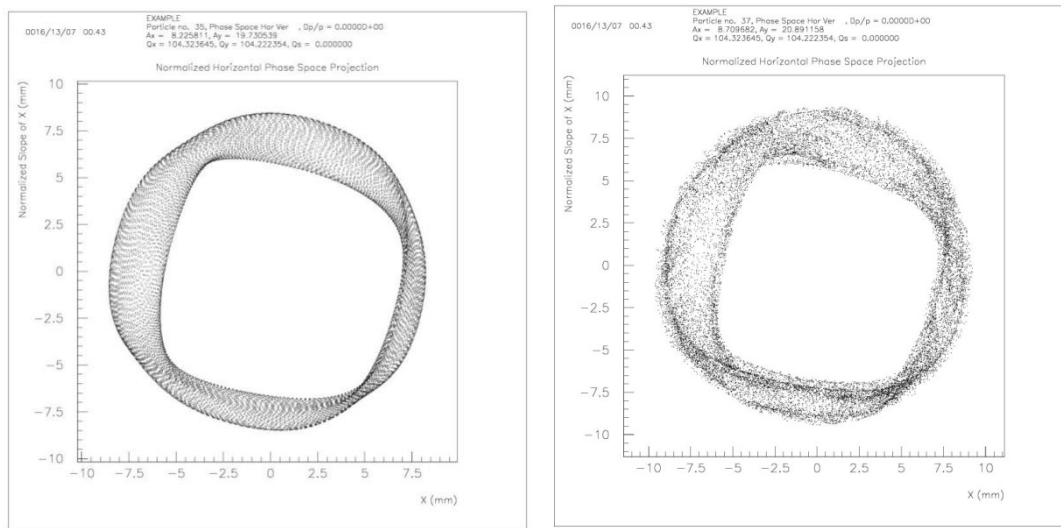
Figure 20: Horizontal phase space projections for regular (left) and chaotic (right) cases.
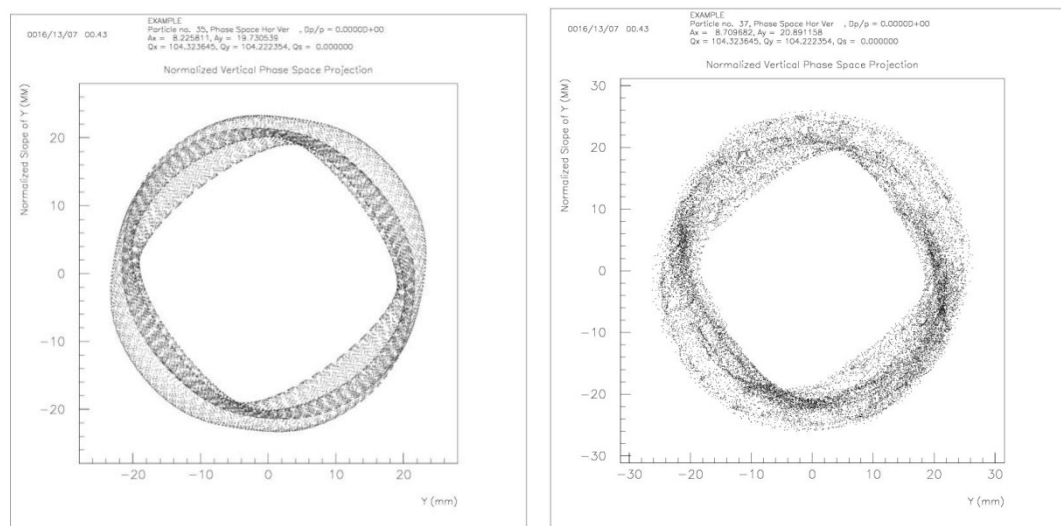
Figure 21: Vertical phase space projections for regular (left) and chaotic (right) cases.
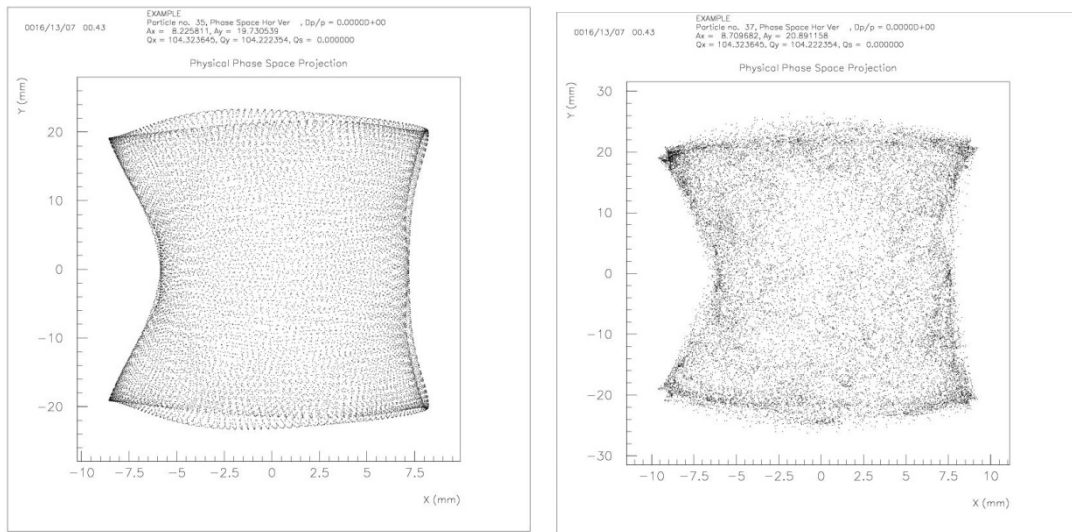
Figure 22: Physical phase space projections for regular (left) and chaotic (right) cases.

4.4.6 **Summary**

In this paper, we showed a set of parameters for SPPC with different circumferences like 59km, 80 km or 100 km and different energies like 70TeV or 100TeV. We also showed the first version of SPPC lattice including ARC, dispersion suppressor section and long straight sections. We also showed the first dynamic aperture and beam dynamic studies of SPPC main ring with and without low beta pp interaction region although it needs lots of work to do and to be optimized.

4.4.7 **References**

1. F. Zimmermann, "HE-LHC & VHE-LHC accelerator overview (injector chain and main parameter choices)", Report of the Joint Snowmass-EuCARD/AccNet-HiLumi LHC meeting, Switzerland, 2013.

2. F. Zimmermann et al., "FCC-ee overview", in Proc. HF2014, Beijing, China, Sep. 2014, p.6-15.

3. Layout and Performance, in LHC Design Report Volume 1, European Organization for Nuclear Research, 2004, p21-22.

4. The Science of the CEPC and the SPPC, in CEPC-SPPC: Pre-CDR, Volume II - accelerator, The CEPC-SPPC Study Group, Mar. 2015, p.28-35.

5. J. Gao, "Review of some important beam physics issues in electron positron collider designs", Modern Physics Letters A, Vol. 30, No. 11, p. 1530006, 2015.

6. F. Su et al., "Method study of parameter choice for a circular proton-proton collider", Chinese Physics C, Vol. 40, No. 1, p. 017001, 2016.

7. D. Wang et al., "Optimization Parameter Design of a Circular e+e- Higgs Factory", Chinese Physics C, Vol. 37, No. 9, p. 97003-0970, 2013.

8. M. Xiao et al., "Study on CEPC performances with different collision energies and geometric layouts", Chinese Physics C, Vol. 40, No. 8, 2016.

9. F. Su, J. Gao et al, "SPPC Parameter Choice and Lattice Design", TUPMW001, Proceedings of IPAC2016.

10. F. Su, J. Gao et al, "CEPC Partial Double Ring Lattice Design", THPOR009, Proceedings of IPAC2016.

11. F. Su, J. Gao, *etc.*, "CEPC partial double ring lattice design and SPPC lattice design", IAS White Paper, submitted for publication, Apr. 2016.

5   Ligh Sources

5.1   Overview of Lattice Design and Evaluation for the APS Upgrade

M. Borland, L. Emery, R. Lindberg, V. Sajaev, Y.-P. Sun, A. Xiao

Mail to: borland@aps.anl.gov

Argonne National Laboratory, 9700 South Cass Avenue, Argonne IL, 60439

5.1.1   Introduction

The Advanced Photon Source (APS) is a 7-GeV synchrotron light source that has been in operation since 1996. Since that time, the effective emittance has been decreased from 8 nm to 3.1 nm, which is very competitive for a 3rd-generation light source. However, newer facilities such as PETRA-III [1], NSLS-II [2], and MAX-IV [3] are pushing the emittance to significantly smaller values. MAX-IV in particular has set the current benchmark with an emittance of about 300 pm at 3 GeV. This was accomplished by use of a multi-bend achromat lattice [4], which takes advantage of the $1/M^3$ scaling of the emittance with respect to the number of dipoles M [5].

In order to ensure that our facility remains competitive, APS is pursuing a major upgrade, which involves replacement of the existing double-bend lattice with a seven-bend achromat lattice, promising a 40-fold reduction in emittance. This paper describes the process of developing and evaluating candidate lattice designs. Two candidate 6-GeV lattices are described: one providing a natural emittance of 67 pm [6] and the other providing 41 pm. Our analysis includes single-particle dynamics as well as single- and

5.1.2   Design goals and constraints

The new lattice is constrained in a number of ways by the parameters of the existing facility. Like the existing ring, it must have 40 straight sections, with 35 reserved for insertion device (ID) beamlines. Both ID and bending magnet (BM) beamlines must point in the same direction as now. The goal is that the ID straight sections accommodate 4.8-m long IDs as in the present ring, and that the ID straight sections do not move transversely relative to their present position. The latter goal implies that the circumference of the ring must change and that the BM lines must move transversely.

Another goal for the ID straights is the ability to accommodate very small apertures in the horizontal plane. This will permit horizontal-gap vertically-polarizing undulators (HGVPU) [7] and round-bore devices such as helical SCUs [8]. Such devices are not readily incorporated into 3rd-generation storage rings, but are considered an important new capability for a next-generation ring.

The emittance requirement for the new ring is less than 150 pm, with the goal being half of this value. In order to provide increased flux and support for timing experiments as well as higher brightness, the design current goal is 200 mA in as few as 48 bunches. At the same time, we need sufficient lifetime to obviate the need for significant changes to the shielding configuration; this implies a lifetime of about 5 hours at 200 mA and 6 GeV. We also require sufficient injection aperture for on-axis swap-out injection [9, 10], at a minimum; accumulation-based injection is nominally a desirable option, but not a requirement.

Of course, emittance is not the only determinant of brightness. Having close-to-ideal beta functions at the IDs is also a goal, though this is easiest to achieve in the vertical plane. An additional goal is to minimize the beta functions around the ring in order to reduce the effective impedance.

5.1.3 Lattice concepts and linear optics

For the APS-U MBA (multi-bend achromat) lattice design, three different types of lattice concepts were explored: a MAX-IV style with uniform TME cells [2]; an ESRF-II hybrid-lattice style with dispersion bump with -I phase separation [11]; and a SIRIUS-inspired lattice [12] that is in some sense a combination of MAX-IV and ESRF-II. Following the design goals and constraints discussed above, options from five-bend achromat (5BA) to eight-bend achromat (8BA) lattices were investigated and compared in terms of their requirements on the various techinical systems (magnets, vacuums, injection/extraction kickers, injectors) and their beam dynamics performance.

After considering the various lattice concepts discussed above, it was determined that the ESRF-II hybrid-lattice style [11] provides the lowest equilibrium emittance by a factor of two compared to the other concepts, and at the same time allows sextupole magnets that are three-to-four times weaker than the other concepts, leading to the adoption of this concept for the APS-U lattice. A 67-pm H7BA (hybrid seven-bend achromat) lattice is the current official design for APS-U. It employs four longitudinal gradient dipole magnets (each has five segments) for lower emittance and higher dispersion bump, plus three transverse gradient dipoles at the center of the sector. Three pairs of sextupole magnets are placed in the dispersion bump for chromaticity correction. The phase advance between the sextupole pairs gives close to -I transport, resulting in near-cancellation of geometric sextupole kicks. In each sector, there are 16 quadrupole magnets, 14 BPMs (beam position monitors), 4 horizontal/vertical fast correctors, 10 horizontal/vertical slow correctors, and 4 skew quadrupoles. The skew quadrupoles and fast correctors are combined into a single magnet.

With the addition of reverse dipole fields in focusing quadrupole magnets [13, 14], it is possible to partially separate horizontal dispersion function matching from horizontal beta function matching. This allows greater freedom in tuning for low

emittance. Reverse bending magnets also help to tune the damping partitions, i.e., increasing the damping partition in horizontal plane. A 41-pm emittance H7BA lattice was derived from the 67-pm H7BA lattice with the adoption of six reverse bends per sector. The peak dispersion was increased from 74 mm to 90 mm, which helps to reduce the sextupole magnet strengths, thus improving the nonlinear beam dynamics performance. The momentum compaction was reduced compared to the 67-pm H7BA lattice. The major parameters of the 67-pm and 41-pm lattices are listed in Table 1.

The lattice functions of the 67-pm and 41-pm lattices are shown in Fig. 1. It is observed that the 41-pm lattice has better-optimized beta functions at the insertion device straight section where the undulators are located. The photon beam brightness of the 41-pm lattice is increased by roughly 50% compared to the 67-pm lattice.
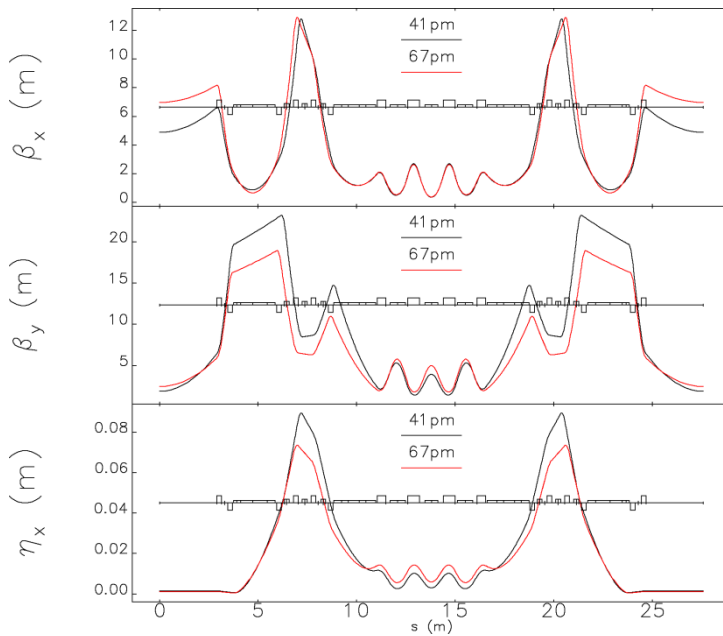
Figure 18: Lattice functions for 67- and 41-pm lattices for the APS upgrade.

Table 9: Comparison of 67- and 41-pm lattices.

	67-pm	41-pm	
Betatron motion			
v_x	95.125	95.091	
v_y	36.122	36.165	
$\xi_{x,nat}$	-138.580	-129.704	
$\xi_{y,nat}$	-108.477	-123.027	

Lattice functions			
Maximum β_x	12.9	12.8	m
Maximum β_y	18.9	23.2	m
Maximum η_x	0.074	0.090	m
Average β_x	4.2	3.7	m
Average β_y	7.8	9.5	m
Average η_x	0.030	0.032	m
Radiation-integral-related quantities at 6 GeV			
Natural emittance	66.9	41.4	pm
Energy spread	0.096	0.129	%
Horizontal damping time	12.1	7.2	ms
Vertical damping time	19.5	15.8	ms
Longitudinal damping time	14.1	19.6	ms
Energy loss per turn	2.27	2.80	MeV
ID Straight Sections			
β_x	7.0	4.9	m
η_x	1.11	1.47	mm
β_y	2.4	1.9	m
$\epsilon_{x,eff}$	67.0	41.8	pm
Miscellaneous parameters			
Momentum compaction	5.66×10^{-5}	3.78×10^{-5}	
Damping partition J_x	1.61	2.20	
Damping partition J_y	1.00	1.00	
Damping partition J_δ	1.39	0.80	

Lattice alternatives were also developed with relaxed goals for the equilibrium emittance, which promises to allow better beam dynamics performance than the nominal lattices, including the possibility of off-axis accumulation. A 90-pm H7BA lattice [15] was noteworthy in this category, offering better single particle dynamics performance (larger dynamic acceptance and longer Touschek lifetime) plus more free space for installation of injection kickers and other accelerator components. However, this lattice was ruled out due to its 2-fold lower brightness compared to the 67-pm lattice and, more importantly, issues with collective effects when accumulating high single bunch charge (see below).

5.1.4   Multi-objective optimization of nonlinear dynamics

A tracking-based multi-objective genetic algorithm (MOGA) [16, 17, 18, 19] was employed to directly optimize the linear optics and sextupole magnets for better beam dynamics performance. The normal optimization objectives include: large dynamic acceptance to accommodate the chosen injection method; long Touschek lifetime as computed from local momentum acceptance simulation; and the desired positive chromaticity, motivated by 48-bunch high charge mode. Unlike theoretical nonlinear dynamics optimization approaches, this method includes the effects of magnets errors, synchrotron radiation damping and longitudinal motion, plus the vacuum chamber apertures which are relatively small in the APS-U MBA ring. The nominal tracking time is one to two synchrotron periods. In order to reduce the time required for optimization, the tracking simulations use Pelegant [20], the parallel version of elegant [21]. This code includes parallelized dynamic and local-momentum acceptance search, parallel tune footprint computation, and parallel lattice matching.

The algorithm is optionally allowed to vary the linear optics, using either a direct variation of the quadrupole magnets gradients or a variation of linear optics targets (e.g., emittance, tunes, beta functions, phase separation between sextupole pairs). On top of that, typically 12 families of sextupole magnets are varied to optimize dynamic acceptance and local momentum acceptance. Recently chromatic detuning is introduced as another optimization objective in MOGA, which seems to be highly relevant for the robustness of the lifetime of the MOGA-derived solution. In particular, it was found that delaying crossing of the integer resonance helps robustness of the momentum acceptance, even though in MOGA it may not have a strong impact; this seems to imply that MOGA can tune sextupoles for a particular error seed to limit the impact of this resonance, but that this tuning does not extend to other seeds. However, insisting that the momentum tune footprint did not cross the half-integer resonance was found to be detrimental during MOGA, resulting in smaller momentum acceptance in the high-dispersion region [6].

After MOGA optimization, an ensemble evaluation is performed to check the solution using results of the commissioning simulations, as discussed in the following sections.

5.1.5 Commissioning simulation

APS has a large user community who understandably desire that facility "dark time" during the upgrade is minimized. To satisfy this requirement, APS is targeting 12 months for removal, installation, and commissioning. Of this 12 month period, only three months are set aside for commissioning of the new multi-bend achromat ring. As a result, we need to ensure that fast commissioning is possible for this lattice.

Several factors complicate the commissioning. The new lattice has focusing that is much stronger than in the present ring. For example, maximum quadrupole strengths increase nearly five-fold in the new lattice. Stronger focusing inevitably leads to larger natural chromaticity and smaller dispersion, which in turn requires a nearly seven-fold increase in sextupole strength. This results in rather small dynamic aperture and short lifetime even for the ideal lattice. Misalignments of the strong quadrupoles generate large orbit errors, which in the presence of very strong sextupoles lead to large lattice and coupling errors. Add to this the smaller vacuum chamber gaps that are required to achieve high gradients in the magnets and small-gap insertion device vacuum chambers that will be installed prior to commissioning, and the required rapid start-up may seem doubtful. To make sure that fast commissioning is possible, we simulated the entire process of commissioning from the first injection into the ring to the final lattice correction [22].

While the effect of individual lattice imperfections on accelerator performance can be estimated or calculated analytically, including all errors together is beyond the realm of analytical estimations. To understand how combined errors impact commissioning, a start-to-end simulation of machine commissioning was performed taking into account as many errors as possible. All simulations were done using elegant. Table 2 lists the errors included in the simulations. Misalignment for magnetic elements is generated the following way: the upstream and downstream ends of the girder are independently randomly misaligned by 100 μm rms, and the magnets on the girder are assigned displacements following the straight line connecting the ends of the girder. Individual magnets are then additionally misaligned by 30 μm rms.

Table 10: Rms errors used in commissioning simulations.

Errors imparted prior to commissioning	
Misalignments	Girders: 100 μm, Elements within girder: 30 μm
Fractional strength errors	Dipoles: 10-3, Quadrupoles: 10-3
Tilt errors	0.4 mrad for dipoles, quadrupoles, and sextupoles
Initial BPM offset errors	500 μm
Errors used during simulated lattice measurement	
BPM gain error	5%
Orbit measurement noise	0.1 μm
Corrector calibration error	5%
BPM and corrector tilt errors	1 mrad

If we neglect nonlinear effects coming from sextupoles, or asume that the sextupoles are turned off at the beginning of commissioning, we can estimate the expected closed orbit error at a particular location, for example, at location of a small-gap insertion device vacuum chamber. The amplification factors required for that estimate can be calculated using lattice functions or simple simulations in the case of girders. Using errors from Table 2 and orbit amplification factors, rms orbit errors are estimated to be 7 mm in horizontal and 4 mm in vertical planes. Considering that there are 35 insertion device chambers around the ring, it is likely that orbit errors could achieve two times the rms estimated above, which would exceed the vacuum chamber gap by a factor of 2. Based on this orbit error estimation, it is clear that first-turn trajectory correction will be required to send the beam through the ring.

The simulated commissioning procedure closely follows the steps that will be performed during real commissioning. Before proceeding with the commissioning, the quadrupole strengths are adjusted to move betatron tunes away from the integer and coupling resonances to reduce their effect during initial steps of the commissioning (the design fractional tunes are 0.12 in both planes;they are adjusted to 0.18 and 0.24). The procedure consists of the following major steps: (1) Generate errors for all elements according to Table 2 using Gaussian distributions with 2σ cut off; (2) Correct the trajectory until a closed orbit is found; (3) Correct the closed orbit down to an acceptable level, if needed adjust tunes in the process; (4) Correct optics and coupling; (5) Adjust coupling to obtain a 10% emittance ratio. The lifetime is calculated at several points along the procedure to ensure that the next step is practical.

Early in the commissioning simulation study, it was realized that the required orbit corrector strengths could easily exceed the corrector limits. Therefore, one of the goals of the trajectory correction procedure was to minimize the required corrector strengths. This goal is achieved by running correction (both trajectory and orbit) in two nested loops. The inner loop increases the number singular values used in the response matrix inversion, while the outer loop increases the number of corrector magnets used in correction. At every iteration, the best orbit and trajectory is recorded.

We found that this procedure finds a closed orbit in 100% of cases with error levels given in Table 2. We need to mention here, that if the errors are increased compared to Table 2 or girders are split into shorter units, the success rate of the trajectory correction procedure goes down. In those cases, more sophisticated correction methods are needed, which we would not describe in this article. Having a closed orbit, however, does not guarantee that the lifetime is long enough to allow for orbit correction. In real life, this would correspond to a situation when the beam completes only a few turns. Assuming that no reasonable measurements are possible at this point, a simplex optimization is performed that varies the betatron tunes and the lowest beta function harmonics using predefined quadrupole knobs. In real life, this optimization will try to maximize the number of turns that the beam is able to survive; in the simulation procedure, we maximize the transmission of a bunch consisting of five particles with 0, ±0.5%, and ±1% momentum errors. We have found that after this transmission optimization, the lifetime is longer than one minute with 90% certainty. It is rather short due to large lattice errors, but should be adequate to start orbit correction.

During the orbit correction step, after the first few iterations of the outer loop, it is assumed that the beam lifetime is long enough to permit BPM offset measurements. The BPM offset measurement is simple enough, and therefore it is not simulated in this procedure. Instead, the previously-generated random BPM offsets are simply reduced by a factor of ten from 500 μm rms to 50 μm rms. The goal of the orbit correction is to bring the maximum orbit errors below 0.5 mm, this goal is achieved in 98% of cases. The procedure reduces the rms orbit errors to about 100 μm, which most likely is defined by the 100-μm girder misalignment. The lifetime after orbit correction step increases to 15 minutes median lifetime (or 8 minutes with 90% certainty).

After the orbit correction is complete, the optics correction is performed. A standard correction procedure that was developed for the present APS is used [23], which is based on the response matrix fit [24, 25]. The simulated response matrix is generated with BPM noise, BPM gain errors, corrector calibration errors, and BPM and corrector tilts. For measurement and calculation speed, only ten correctors per plane are used. Based on the present experience, the measurement should not require more than five minutes.

   Beta function and horizontal dispersion correction is calculated using ideal beta function response matrix (rather than using direct inverse quadrupole errors from the response matrix fit), as this allows for simple correction strength control using different numbers of singular values. Coupling is corrected by minimizing the cross-plane orbit response matrix together with vertical dispersion. All quadrupoles and four skew quadrupoles per sector are used for beta function and coupling correction. Lattice and coupling correction is performed in several iterations while increasing number of SVs. After every iteration, orbit correction is also performed. After the lattice and coupling correction is complete, the coupling is adjusted to achieve a target emittance ratio of $\kappa =$ 10% by exciting the nearest difference resonance using skew quadrupoles. At this point, if necessary, $\kappa = 100\%$ can be achieved by just moving the tunes to the coupling resonance.

   The procedure is typically run for 200 different error seeds. Results of the commissioning simulation for the 67-pm lattice are shown in. Figure 2 shows the histograms of the final rms orbit errors, the relative errors of beta functions, and the final horizontal beam emittance. One can see that the design horizontal emittance of 67 pm is achieved after the lattice correction. Similar results are obtained for the 41-pm lattice.
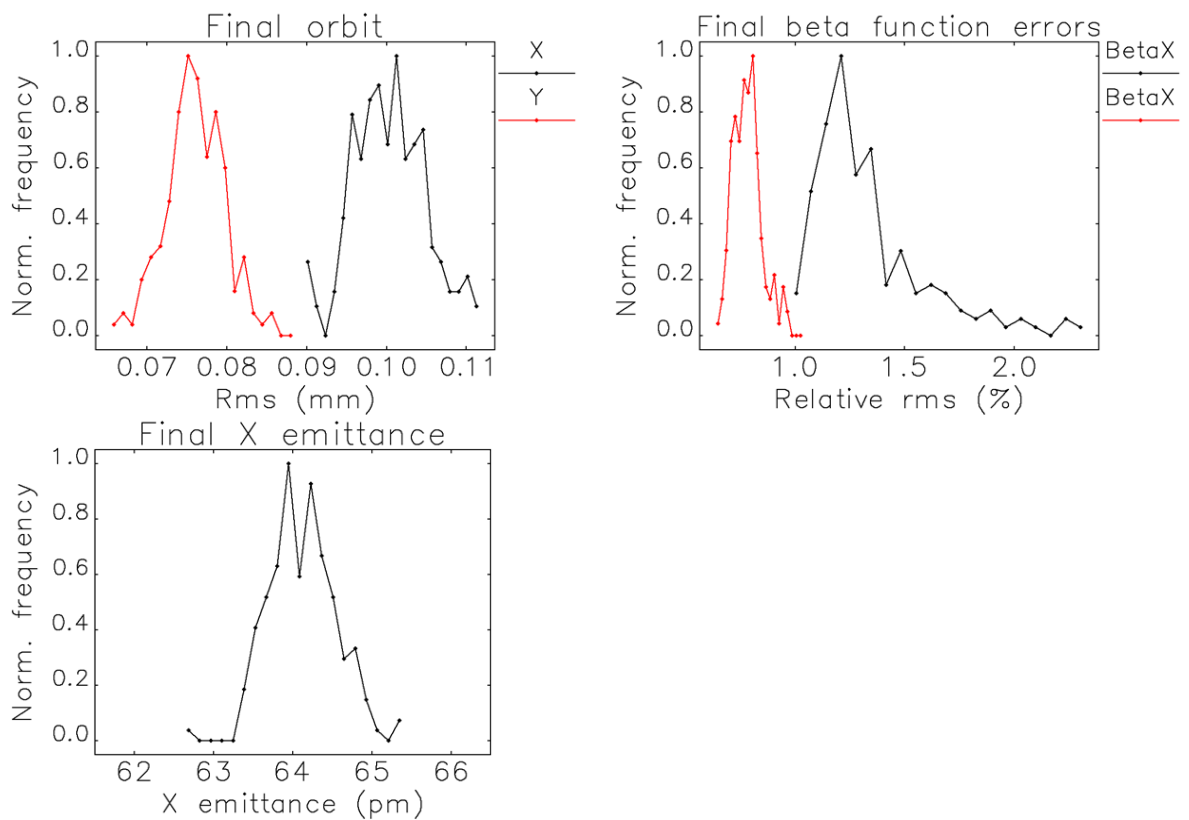
Figure 19: Performance of commissioning algorithm in terms of final rms orbit, final beta function errors, and final horizontal emittance, for the 67-pm lattice.

5.1.6   **Evaluation of commissioned configurations**

The commissioning simulations described in the last section not only provide assurance that the lattice can be commissioned in a reasonable time using realistic constraints, they also provide a set of post-commissioning configurations that can be used to assess the robustness of the lattice [6, 26], In particular, these configurations are used to predict dynamic acceptance (DA), local momentum acceptance (LMA), injection efficiency, emittances, Touschek lifetime, and gas-scattering lifetime. Injection modeling with and without collective effects is covered in subsequent sections. In this section, we describe results for the other performance measures just listed.

For each of the error ensembles, we used Pelegant to perform 1000-turn tracking with main and harmonic rf cavities, element-by-element synchrotron radiation, physical apertures, and multipole errors to determine the DA and LMA. Tracking for additional turns was not found to change results significantly. The DA is determined at the reference momentum only, which is appropriate given that the anticipated momentum spread from the injector is small. The LMA is used to assess off-momentum performance, since it allows direct computation of the Touschek lifetime.

The physical apertures include a 10-mm-radius round aperture in the arcs. In addition, we include ID apertures, which are a mixture of several types: elliptical apertures with semi-axes of 10 mm and 3 mm, n=6 super-elliptical apertures with semi-axes of 4 mm and 3 mm, and round apertures with a radius of 4 mm. These apertures were chosen based on tracking studies and in consideration of expected ID designs. They were found to have a modest effect on the DA and LMA.

Tracking was performed for the first 100 post-commissioning ensembles for each lattice. Before tracking, global knobs are used to move the tunes to the linear difference resonance to provide round beams. Similarly, the chromaticities are adjusted to the ideal value of 5 in both planes using symmetric adjustment of the sextupoles. After DA tracking, we performed statistical analysis of the DA to provide percentile contours, such as shown in Fig. 3. Also plotted are 2- and 3-sigma ellipses for the injected beam, including a conservative assumption for the emittance and margins that account for trajectory jitter (see the next section for details).
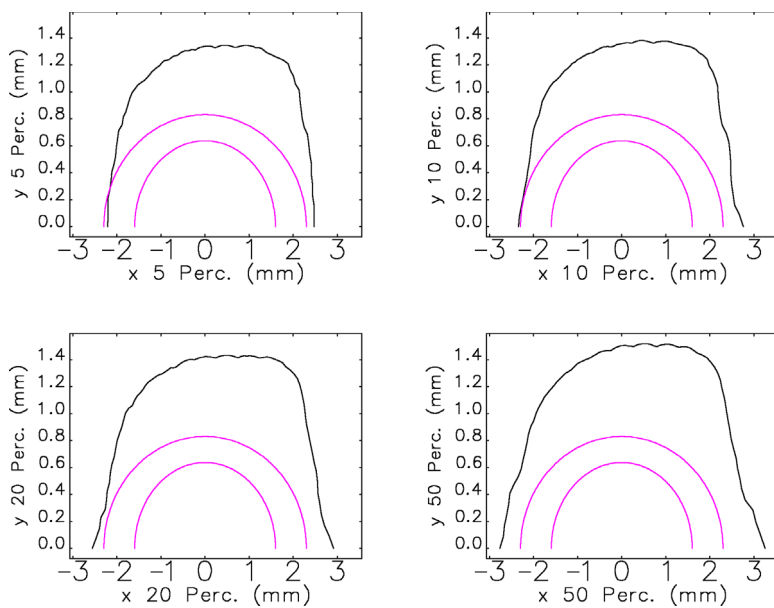
Figure 20: Dynamic acceptance contours for the 41-pm lattice using post-commissioning error ensembles. The ellipses show conservative 2- and 3-sigma beam sizes from the injector, as well as initial trajectory errors.

Using the LMA for each of the ensembles allows computing the distribution of expected Touschek lifetimes. Rather than simply use the rms bunch length and energy spread, a slice-based lifetime computation was performed that includes the effects of intrabeam scattering, impedance, and the higher-harmonic cavity (HHC) [26, 27]. This gives longer lifetime by virtue of the bunch-lengthening effects of the impedance and the beam size increase in the dispersive regions from the IBS- and microwave-instability-inflated energy spread. Table 3 summarizes results for the 67- and 41-pm lattices. Included in the lifetime estimates is the gas scattering lifetime after 1000 A*h of operation [28]. In 324-bunch mode, lifetimes are relatively long, whereas in 48-bunch mode the 10th percentile lifetime is about 2 hours. Further analysis suggests that the shorter lifetime configurations from the distributions are those for which the lattice correction was less successful, which suggests that in an operational ring it will be possible to increase the lifetime through iteration of the correction procedure.

In addition, more recent efforts have shown the possibility of increasing the Touschek lifetime by nearly a factor of two, albeit with some reduction in the DA. This indicates that operation with flat beams will also be practical when 324 bunch fills are used. Figure 4 shows a comparison of brightness envelopes for APS today, with existing insertion devices, and two APS upgrade lattices assuming a 10% emittance ratio. In the latter case, we show the envelopes over possible 3.7-m-long superconducting undulators. Thus, the curves do not show the brightness available from any single device, but over a selection of possible devices. The potential brightness increase exceeds two orders of magnitude.

Table 11: Summary of simulated beam properties at 200 mA, total beam lifetime, and corresponding injection intervals for two APS upgrade lattices with two different fill patterns.

Lattice	Bunches	X emittance	Y emittance	Energy spread	10th percentile lifetime	Injection interval
	#	pm	pm	10^{-4}	h	s
67-pm	48	45.2	44.9	14.5	2.3	17.6
	324	42.5	42.2	9.6	8.2	9.1
41-pm	48	31.4	31.1	18.6	2.1	15.5
	324	29.3	29.0	13.0	7.8	8.6
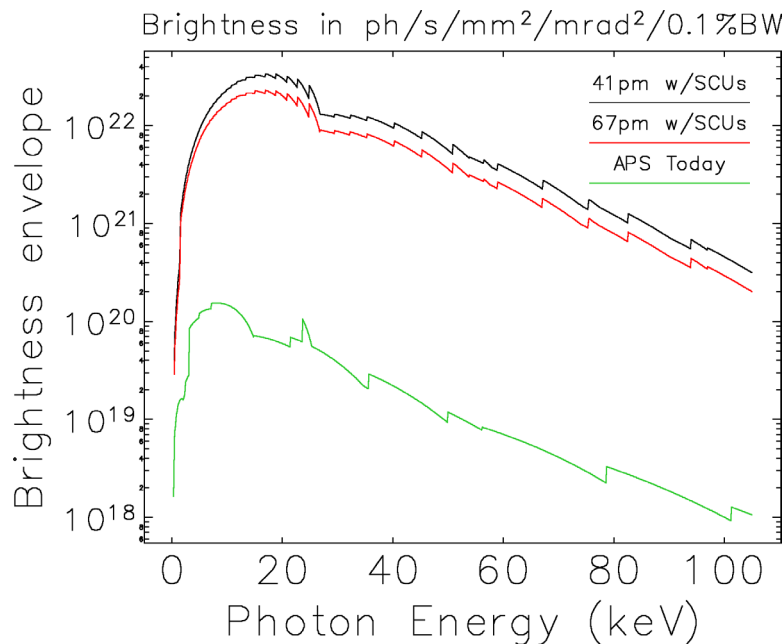
Figure 21: Comparison of x-ray brightness envelopes (over many devices) for the APS today and two APS upgrade lattices.

5.1.7 Injection design and modeling

In addition to the lattice evaluation just described, we performed detailed modeling of injection efficiency [29]. On-axis swap-out injection allows the optical design to achieve a much lower emittance and provides the opportunity to employ novel types of insertion devices, such as vertically-deflecting or helical devices. Due to the complexity and strong non-linearity of the lattice, injection is done within a single straight section,

i.e., the injected beam will not be affected by the ring's optical structure before it completely merges onto the stored beam orbit. Since the planned swap-out injection method replaces one stored bunch at a time, it requires the injection kicker system to be extremely fast. For this reason a stripline type kicker with a very fast pulser will be used. The kick strength is inversely proportional to the gap of stripline kicker, which is strongly determined by the injected beam size in the same direction. Hence, the stripline is oriented to kick the injected beam vertically and a combined horizontal-vertical injection configuration is used, as illustrated in Figure 5.

Figure 22: Injection layout for on-axis injection for the APS upgrade. Injected beam from inside of storage ring is bend horizontly to the top of stored beam orbit using a Lambertson magnet, then deflected vertically using a set of stripline kickers. To make the injected beam trajectory go through the midplane of the Q1/Q2 magnets, it has a slight vertical angle at the entrance of Q2 magnet, this angle is then adjusted by slightly tilting the Lambertson magnet).

In simulating injection performance, a very conservative assumption was made about the incoming booster beam parameters, with horizontal/vertical beam emittances of 80/16 nm, bunch length of 100 ps, and energy spread of 0.12%, compared with natural beam parameters at zero current of 53 nm, 55 ps and 0.1%. Errors in the injection process were also simulated: optical mismatch, equivalent to an effective emittance blow up from 80/16 nm to 100/20 nm; energy offset and arrival-time errors, together equivalent to an energy offset; and trajectory errors. These errors were added to tracking studies of the injected beam (1000 particles with 3 sigma cut-off) through 100 optical error ensembles, with the simulations including apertures, synchrotron radiation, main rf system, and HHC. For the 67-pm lattice, the injection performance was studied

at different error levels with the resulting average injection loss at ~2% at the specified beam parameters and error levels. For the 41-pm lattice, only one beam parameter and error level assemble was studied. Results obtained with the same beam parameter and error levels for the 41-pm and 67-pm lattices are listed in Table 4, showing that the 41-pm lattice has slightly better injection performance. This is consistent with the relative DA results shown previously.

Table 12: Simulated injection efficiency for 67- and 41-pm lattices.

Lattice	Ave. Injection Efficiency (over 100 optical error sets)	Min. Injection Efficiency
41-pm	>99%	98.9%
67-pm	99%	96.3%

5.1.8 **Collective instabilities**

The goal of achieving a high-charge bunch in the presence of the ring impedance requires accurate modeling of beam dynamics using a comprehensive tracking program, such as elegant. The techniques used here are extensions of those successfully applied to the existing APS in the past [30,31,32]. Features that proved important include the linear and non-linear optics, longitudinal and transverse wake-fields/impedance, harmonic cavities, optics errors and injection beam errors, and bunch-by-bunch feedback simulation with FIR filters. The linear and non-linear optics are simulated by magnetic elements using kicks, while the main and harmonic rf cavities are modeled here as externally applied voltages at phases set to particular values (in other applications we use the voltage and phase generated self-consistently from the beam [27]). The impedance is composed of a resistive wall contribution given by analytical formulas and geometrical wake-fields calculated by the 3D codes ECHO[33] or GdfidL[34] using a Gaussian bunch of rms length $\sigma_b = 1$ mm. This is equivalent to filtering the point particle impedance by a Gaussian filter of frequency width $\sigma_f = c/(2\pi\sigma_b) \sim 48$ GHz.

Once the impedance of all the elements is determined [30], we may compute the "ring impedance" by multiplying the impedance of each element by the local beta function and summing. For the simulations discussed here, however, we typically use element-by-element tracking with 15 local impedance elements per sector. Specifically, we use a distinct impedance source located at each of the 14 BPMs that includes the impedance contributions of that BPM-bellows assembly, the resistive wall of that part of the arc, and other neighboring components like photon absorbers, flanges, etc.; the final impedance element describes the resistive wall of the narrow gap ID chamber and is located at the middle of the straight section. For the particle tracking described here, we found that using 200K macroparticles per bunch is typically required.
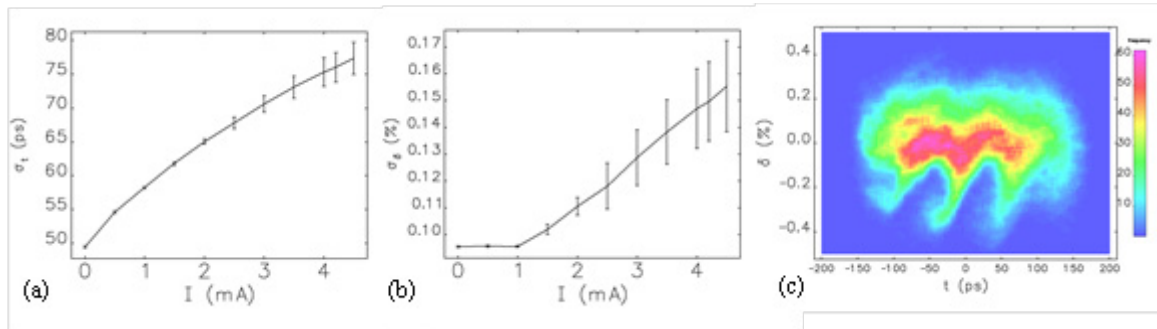
Figure 23: Predicted effects of longitudinal wakefields for the 67-pm lattice. (a) and (b) show the dependence of the bunch length and energy spread on current, while (c) shows a snapshot of the turbulent phase space at 4.2 mA/bunch.

We have applied the methods just described to simulate various collective effects in the APS-U lattice. We show the results of the predicted bunch length and current as a function of single bunch current in Fig. 6. We see that for the 0.62 mA/bunch of 324-bunch mode the impedance increases the bunch length by about 10% while remaining below the microwave instability threshold. For the 48-bunch mode with 4.2 mA/bunch the longitudinal impedance increases both the bunch length and energy spread by about 50%. The 48-bunch mode is predicted to be well above the microwave instability threshold current. While this can lead to fluctuation ~10% in both bunch length and energy spread due to the now turbulent synchrotron oscillations, it otherwise should not affect the beam dynamics or stability.

We can also use these simulation tools to predict the single bunch current limit set by transverse collective instabilities. We do this by slowly ramping the strength of the longitudinal and transverse impedance over 20,000 turns by an amount that is equivalent to increasing the bunch current from 4 to 8 mA. We found that both the 67-pm and the 41-pm RB lattice show collective instability at a single bunch current of about 7 mA, while the 90-pm lattice has a somewhat higher limit of about 9 mA. This threshold was observed at a chromaticity of 5 units, and can be increased by a few mA by increasing the chromaticity to 6 or 7. While these single bunch instability thresholds are well above the required 4.2 mA/bunch, we have found that collective effects at injection are more severe and therefore should be investigated to determine the maximum single bunch current.
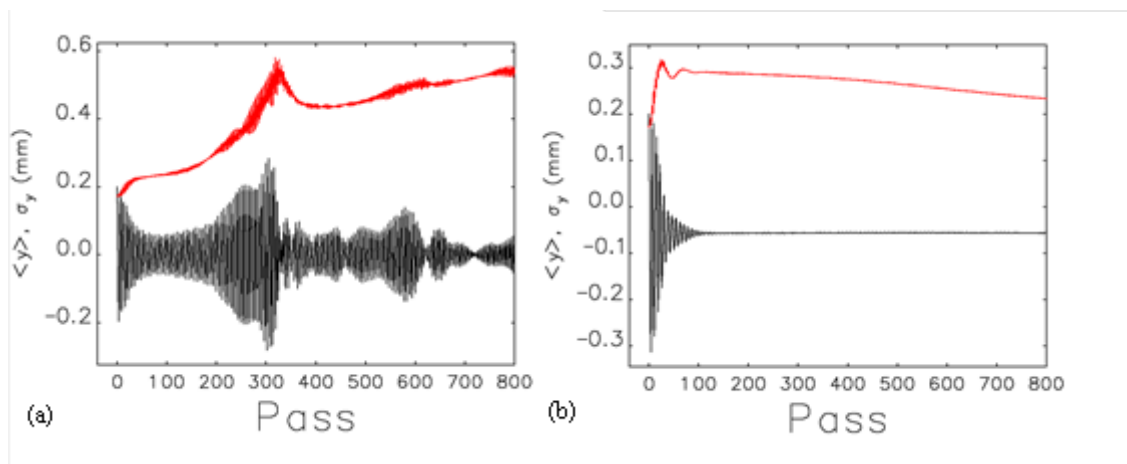
Figure 24: (a) Example of the transverse instability at injection that leads to particle loss in the 41-pm lattice. (b) shows that transverse feedback with a strength of 1 microradian cures the instability.

Collective effects at injection can significantly reduce the ability to store sufficient charge, largely because the injected beam from the booster is not matched to the MBA. First, the booster beam is temporally longer with a smaller energy spread than the MBA equilibrium. This causes the injected beam to tumble in the synchrotron bucket, which in turn leads to oscillations in the bunch length and peak current during the first few sychrotron periods. When the bunch is relatively short its increased peak current can drive large transverse wakefields that can lead to a transient instability. These wakefields are further enhanced by the large beam size at injection, since the booster emittance is three orders of magnitude larger than the MBA. Since the larger beam size is only a few times smaller than the DA, particles can be lost for even relatively small oscillation amplitudes over the first few synchrotron periods as we show in Fig. 7 (a). Finally, lattice errors can further exacerbate these problems, and we have found that some level of transverse feedback is typically required to maintain high injection efficiency.

For the lattices under study with relatively small DA, we have found that losses at injection due to collective effects make it very difficult to accumulate 4.2 mA/bunch with off-axis injection. In particular, for the 90-pm lattice designed to enable accumulation, we have found that the driven transverse oscillations lead to significant emittance growth and beam loss at high charge. Feedback appears unable to solve this problem, because either it is too weak and the stored charge gets lost, or it is too strong and essentially kicks out the injected beam. For this reason and because of its larger emittance, we have eliminated the 90-pm lattice as a candidate for APS-U.

Using on-axis swap-out injection enables the transverse feedback system to damp the transient oscillations at injection. For the perfect 67- and 41-pm lattices we have found that an injection efficiency over 99% is possible provided the feedback can provide 1 microradian of kick strength as shown in Fig. 7 (b). This conclusion appears to hold even when lattice errors are included in the 67-pm ring, while certain error sets for the 41-pm lattice showed strong transverse instabilities that were initially difficult to control with any reasonable level of feedback. We have since attributed this strong

instability to the fact that injecting into a ring with positive relative momentum error (which may occur due to residual orbit) results in smaller chromaticity for the on-momentum injected bunch due to the large second order chromaticity. This leads to insufficient chromatic (head-tail) damping for these particular 41-pm lattice error sets. Stable injection can be had by increasing the energy of the injected bunch to match the lattice, although other sextupole configurations that have smaller second order chromaticity also ameliorates the problem.

We have also investigated [35] multi-bunch collective effects by including the long-range resistive wall wakefield and the fields due to the higher-order modes (HOMs) of the main accelerating rf cavities. For this case we simulate 48 or 324 individual bunches in elegant that self-consistently drive the passive harmonic cavity, and the results in both the 67- and 41-pm lattice are quite similar. We have found that the beam is multi-bunch unstable in the transverse plane from the long-range, transverse resistive wall wakefield, and multi-bunch unstable in the longitudinal plane due to the cavity HOMs. The former resistive wall instability can easily be controlled with a small amount of transverse feedback, while the latter longitudinal instability is more difficult to suppress. This is because the bunch lengthening system results in a spread of the synchrotron frequency down to zero, while traditional feedback systems try to correct motion centered about a single synchrotron frequency. We have found [36, 35] that such a traditional feedback system does not always stabilize the longitudinal motion as we plot in Fig. 8 (a). Using a FIR filter with non-zero response down to DC eliminates the longitudinal motion as shown in Fig. 8 (b); while unconventional, this should in principle be possible. We are also investigating the degree to which we can control the frequencies of the most problematic HOMs, as we may then be able to find operating points where the longitudinal multi-bunch instability is reduced or even eliminated entirely.
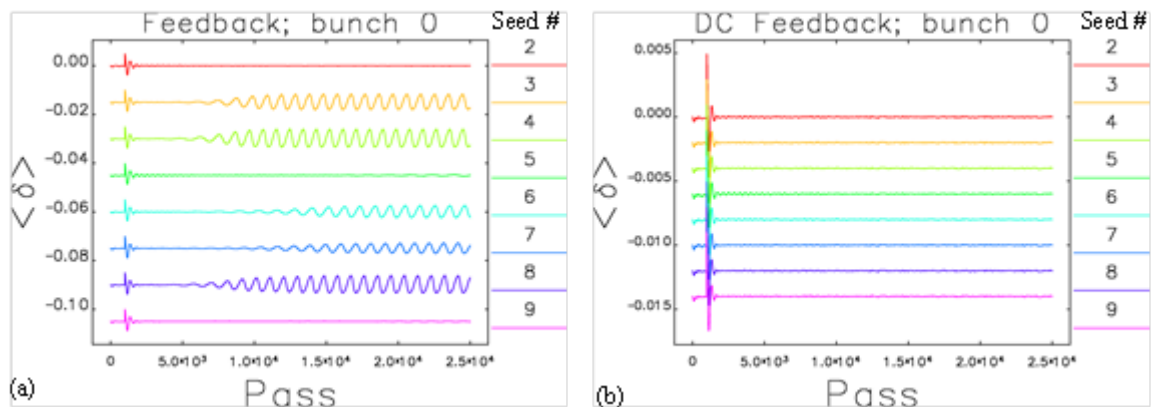
Figure 25: (a) shows that the longitudinal multi-bunch instability is not suppressed using feedback with traditional FIR filters, while (b) shows that a filter with non-zero gain down to the DC can stabilize the system.

5.1.9 Conclusion

A hybrid multi-bend achromat lattice is being developed as an upgrade to the Advanced Photon Source. Several candidate lattices have been developed and studied

using a highly integrated approach that includes tracking-based multi-objective optimization, detailed simulation of commissioning, evaluation of non-linear dynamics robustness using post-commissioning configurations, and modeling of single- and multi-bunch collective effects. Of these lattices, attention has focused on lattices that use on-axis swap-out injection, as these provide superior brightness and single-bunch current. The natural emittances of these lattices, 67 pm for the nominal lattice and 41 pm for the lattice with reverse bends, promise to deliver x-ray beams of exceptional brightness.

5.1.10 Acknowledgments

5.1.11 References

1. K. Balewski et al., PETRA-III TDR (2004).

2. J. Ablett et al., NSLS-II CDR (2006).

3. S. Leemann, A. Andersson, M. Eriksson, L.-J. Lindgren, E. Wallen, J. Bengtsson, and A. Streun, "Beam dynamics and expected performance of Sweden's new storage-ring light source: MAX-IV," Phys. Rev. ST Accel. Beams 12, 120701 (2009).

4. D. Einfeld and M. Plesko, "Design of a diffraction-limited light source," Proc. SPIE 2013 (201-212), Electron Beam Sources of High-Brightness Radiation, 201 (November 1993).

5. J. Murphy, Synchrotron Light Source Data Book, Tech. Rep. BNL-42333. (1989).

6. M. Borland, V. Sajaev, Y. Sun, and A. Xiao, "Hybrid Seven-Bend Achromat Lattice for the Advanced Photon Source Upgrade," Proceedings of the 2015 International Particle Accelerator Conference, 1776-1779 (2015).

7. N. Strelnikov, E. Trakhtenberg, I. Vasserman, J. Xu, and E. Gluskin, "Vertically-polarizing undulator with the dynamic compensation of magnetic forces for the next generation of light sources," Rev. Sci. Inst. 85, 113303 (2014).

8. Y. Ivanyushenkov, E. Baynham, T. Bradshaw, S. Carr, J. Rochford, B.J.A. Shepherd, J. A. Clarke, O. B. Malyshev, D. J. Scott, J. B. Dainton, P. Cooke, T. Greenshaw, D. P. Barber, and G. A. Moortgat-Pick, "Development of a superconducting helical undualtor for a polarized positron source," Proceedings of the 2005 Particle Accelerator Conference, 2295-2297 (2005).

9. R. Abela, W. Joho, P. Marchand, S. V. Milton, and L. Z. Rivkin, "Design Considerations for a Swiss Light Source (SLS)," Proceedings of the 1992 European Particle Accelerator Conference, 486 (1992).

10. L. Emery and M. Borland, "Possible Long-Term Improvements to the Advanced Photon Source," Proceedings of the 2003 Particle Accelerator Conference, 256-258 (2003).

11. L. Farvacque, N. Carmignani, J. Chavanne, A. Franchi, G. Le Bec, S. Liuzzo, B. Nash, T. Perron, and P. Raimondi, "A low-emittance lattice for the ESRF," Proceedings of the 2013 International Particle Accelerator Conference, 79-81 (2013).

12. L. Liu, N. Milas, A. H. C. Mukai, X. R. Resende, A. R. D. Rodrigues, and F. H. Sa, "A new 5BA low emittance lattice for SIRIUS," Proceedings ofr the 2013 International Particle Accelerator Conference, 1874-1876 (2013).

13. J. P. Delahey and J. P. Potier, "Reverse bending magnets in a combined-function lattice for the CLIC damping ring," Proceedings of the 1989 Particle Accelerator Conference, 1611-1613 (1989).

14. A. Streun, "The anti-bend cell for ultralow emittance storage ring lattices," Nuclear Instruments and Methods in Physics Research Section A, 737, 148-154 (2014).

15. Y.-P. Sun, M. Borland, R. Lindberg, and V. Sajaev, "APS-U lattice design for off-axis accumulation," Proceedings of the 2016 North American Particle Accelerator Conference, manuscript in preparation.

16. N. Srinivas, K. Deb, "Multi-objective optimization using nondominated sorting in genetic algorithms," Evol. Computing 2, 221-248 (1995).

17. I. V. Bazarov, C. K. Sinclair, "Multivariate optimization of a high-brightness photoinjector," Phys. Rev. ST Accel. Beams 8, 034202 (2005).

18. See citations in M. Borland, "Progress towards ultimate storage ring light sources," Procdings of the 2012 International Particle Accelerator Conference, 1035-1039 (2013).

19. M. Borland, V. Sajaev, L. Emery, A. Xiao, "Multi-objective direct optmization of dynamic acceptance and lifetime for potential upgrades of the Advanced Photon Source," Advanced Photon Source, ANL/APS/LS-319 (2010).

20. Y. Wang and M. Borland, "Pelegant: A Parallel Simulation Code for Electron Generation and Tracking," Proceedings of the 12th Advanced Accelerator Concepts Workshop, AIP Conf. Proc. 877, 241 (2006).

21. M. Borland, "elegant: A Flexible SDDS-Compliant Code for Accelerator Simulation," Advanced Photon Source LS-287, Sept. 2000.

22. V. Sajaev and M. Borland, "Commissioning Simulations for the APS Upgrade Lattice," Proceedings of the 2015 International Particle Accelerator Conference, 533-555 (2015).

23. V. Sajaev and L. Emery, "Determination and Correction of the Linear Lattice of the APS Storage Ring," Proceedings of the 2002 European Particle Accelerator Conference, 742-744 (2002).

24. J. Safranek, "Experimental Determination of the Linear Optics Including Quadrupole Rotations, Proceedings of the 1995 Particle Accelerator Conference, 2817-2819 (1996).

25. J. Safranek, "Experimental determination of storage ring optics using orbit response measurements," Nuclear Instruments and Methods in Physics Research A, 388, 27-36 (1997).

26. A. Xiao and M. Borland, "Intra-beam and Touschek scattering computations for beams with non-Gaussian longitudinal distributions," Proceedings of the 2015 International Particle Accelerator Conference, 559-561 (2015).

27. M. Borland, T. Berenc, R. Lindberg, and A. Xiao, "Tracking studies of a higher-harmonic bunch-lengthening cavity for the APS upgrade," Proceedings of the 2015 International Particle Accelerator Conference, 543-545 (2015).

28. M. Borland, J. Carter, H. Cease, and B. Stillwell, "Simulation of gas scattering lifetime using position- and species-dependent pressure and aperture profiles," Proceedings of the 2015 International Particle Accelerator Conference, 546-548 (2015).

29. A. Xiao and V. Sajaev, "Simulation study of injection performance for the Advanced Photon Source upgrade," Proceedings of the 2015 International Particle Accelerator Conference, 1816-1818 (2015).

30. R. R. Lindberg and A. Blednykh, "Instability thresholds for the Advanced Photon Source multi-bend achromat upgrade," Proceedings of the 2015 International Particle Accelerator Conference, 1822-1824 (2015).

31. Y. C. Chae, "The impedance database and its application to the APS storage ring," Proceedings of the 2003 Particle Accelerator Conference, 3017-3019 (2003).

32. Y. C. Chae and Y. Wang, "Impedance database II for the Advanced Photon Source storage ring," Proceedings of the 2007 Particle Accelerator Conference,

4336-4338 (2007).

33. I. A. Zagorodnov and T. Weiland, Phys. Rev. ST Accel. Beams, 8:042001 (2005).

34. W. Bruns. The GdfidL Electromagnetic Field Simulator.

35. M. Borland, T. Berenc, L. Emery, and R. Lindberg, "Simultaneous simulation of multi-particle and multi-bunch collective effects for the APS ultra-low emittance upgrade," Proceedings of the 2015 International Computation Accelerator Physics conference, 61-65 (2015).

36. L. Emery, M. Borland, T. Berenc, and R. Lindberg, "Multi-bunch stability analysis of the Advanced Photon Source upgrade including the higher-harmonic cavity," Proceedings of the 2015 International Particle Accelerator Conference, 1784-1786 (2015).

5.2 Lattice Design for the MAX IV Storage Rings

Simon C. Leemann

MAX IV Laboratory, Lund University, 22100 Lund, Sweden

Mail to: simon.leemann@maxiv.lu.se

5.2.1 Introduction

The MAX IV synchrotron radiation facility [1] will be officially inaugurated on June 21, 2016. At the time of writing the MAX IV 3 GeV linac has been commissioned and is routinely serving as both top-up injector to the MAX IV 3 GeV storage ring and driver for the MAX IV Short Pulse Facility. The MAX IV 3 GeV storage ring is presently being commissioned with its first two in-vacuum undulators installed and producing photons for beamline commissioning. The MAX IV 1.5 GeV storage ring has been almost completely installed and commissioning is scheduled to commence in September 2016.

Once the MAX IV facility is complete, it will provide users with synchrotron radiation covering a spectral range from infrared to hard X-rays and time structures from ~30 fs to ~200 ns. In addition to spontaneous radiation, spatially and temporally coherent radiation will eventually also be produced. Early on in the design process, it was established that not all of the user requirements of an advanced synchrotron radiation source can be equally fulfilled by a single machine. Instead, a global optimization of the facility based on the wide range of user demands was performed, resulting in a solution using two separate storage rings at 3 GeV [2] and 1.5 GeV [3] as well as a linac-driven short pulse facility (SPF) [4,5] which will be upgraded to an FEL in a second phase [6,7]. In addition to serving as a driver for the SPF/FEL, the MAX IV 3 GeV linac also acts as the full-energy injector to both storage rings therefore enabling top-up operation at a constant 500 mA in both rings.

This article will focus on the lattice design, optics, and electron beam properties of the two MAX IV storage rings. The following Section 5.2.2 is dedicated to the 3 GeV storage ring and is followed by Section 5.2.3 focusing on the 1.5 GeV storage ring.

5.2.2 Lattice Design for the MAX IV 3 GeV Storage Ring

The MAX IV 3 GeV storage ring is the world's first multibend achromat (MBA) storage ring to go into operation. It will serve as the main radiation source of the MAX IV synchrotron radiation facility. In order to generate high-brightness hard x-rays with state-of-the-art insertion devices (IDs), an ultralow-emittance design was targeted from the very start [8,9]. One simple and robust method to achieve ultralow emittance is the use of an MBA lattice [10-13]. The MBA exploits the inverse cubic dependence of emittance on the number of bending magnets. By choosing a very small bending angle per dipole, introducing a vertically focusing gradient in the dipoles (the emittance scales inversely with the horizontal damping partition J_x), and strong horizontal focusing between dipoles, the dispersion can be limited to very small values which leads to a dramatic reduction of emittance. The low dispersion allows the use of narrow vacuum chambers and compact magnets with strong gradients. In addition to reducing the power consumption and running cost, the compact high-gradient magnets in turn allow for a denser lattice thus closing a positive feedback, the *"MBA cycle"* [14]. Finally, by adding several families of properly optimized sextupoles and octupoles, the nonlinear optics can be tuned for large momentum acceptance and dynamic aperture rendering long Touschek lifetime and high injection efficiency despite the very low emittance [2,15,16].

The 3 GeV storage ring's 20-fold MBA lattice results in 528 m circumference and an equilibrium zero-current emittance of 328 pm rad. This emittance is further reduced when IDs are added so that ultimately about 200 pm rad horizontal emittance is expected at 500 mA (i.e. including intrabeam scattering). Moderate coupling will ensure vertical beam sizes in the IDs below the 1 Å diffraction limit. With a stored current of 500 mA held constant by continuous top-up operation, the 3 GeV storage ring is expected to become the brightest storage ring-based light source in the world.

5.2.2.1 *Linear Optics*

The MAX IV 3 GeV storage ring[2] is based on an entirely novel 7-bend achromat lattice [2]. Its 20 MBAs provide 19 user straights of 4.6 m length for IDs. An overview of one 3 GeV storage ring achromat is shown in Fig.1. Each of the achromats consists of five unit cells and two matching cells. The unit cells have a 3º bending magnet, while the matching cells at the ends of the achromat have a 1.5º soft-end bending magnet. In these soft-end dipoles, the magnetic field drop-off towards the long straight reduces the amount of high-energy radiation hitting a downstream ID therefore facilitating the

---

[2] Lattice files available at https://www.maxiv.lu.se/publications/

design of superconducting IDs. All dipoles contain a vertically focusing gradient. The lattice models both types of dipoles as arrays of gradient dipole slices so that each segment of the dipoles contains bending magnet field and vertically focusing gradients that match results from magnetic field measurements[3] [17]. In this way both the proper longitudinal gradient and the longitudinal evolution of the transverse gradients are included in modeling and beam dynamics studies.
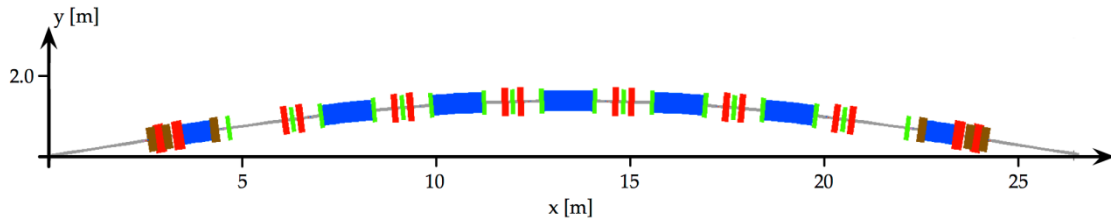
Figure 1: Schematic of one of the 20 achromats of the 3 GeV storage ring. Magnets indicated are gradient dipoles (blue), focusing quadrupoles (red), sextupoles (green), and octupoles (brown).

The matching cells at the ends of the achromat contain dedicated quadrupole doublets in order to match the achromat optics to the ID in the long straight. Each achromat also contains two 1.3 m short straights that separate the matching cells from the unit cells. These short straights are used for RF cavities and diagnostics so that all long straights but the injection straight are available for IDs. Since the vertical focusing is performed by the gradient dipoles, dedicated quadrupoles are, apart from ID matching, only required for horizontal focusing. Horizontally focusing quadrupoles are installed between the dipoles in pairs with a short space in between for a sextupole magnet. There are two families of focusing quadrupoles, one in the unit cells and one in the matching cells. Adjustment of the vertical focusing is performed by exciting a current in the pole-face strips (PFSs) that are installed in all dipoles (up to ±4% gradient variation). This results in a very compact optics with strong focusing, low beta functions, and very small peak dispersion. The optics for one achromat is displayed in Fig.2 and storage ring parameters are given in Table 1.

---

[3] In fact, even the measured multipole content evolution along the dipoles has been added to individual dipole slices in the lattice error model.
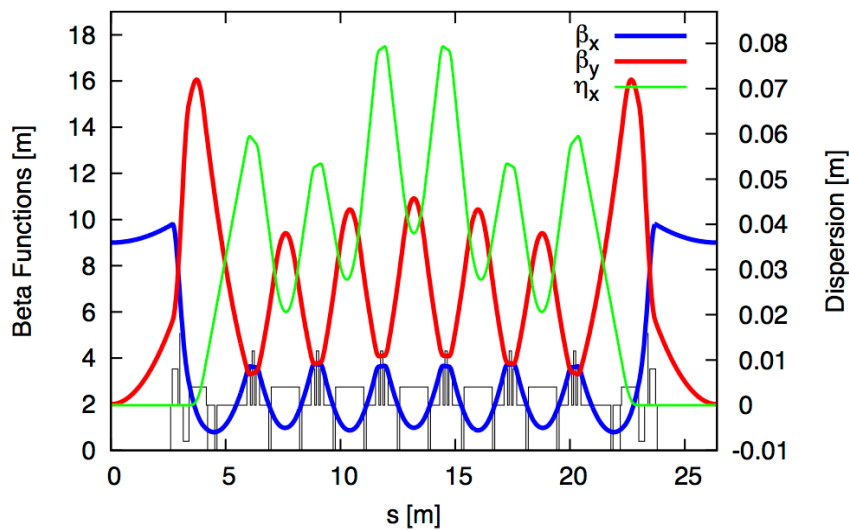
Figure 2: Beta functions and dispersion for one achromat of the 3 GeV storage ring. Magnet positions are indicated in black at the bottom.

Table 1: Parameters for the 3 GeV storage ring.

Parameter	Unit	Value
Energy	GeV	3.0
Main radio frequency	MHz	99.931
Circulating current	mA	500
Circumference	m	528
Number of achromats (straights available for IDs)	…	20 (19)
Betatron tunes (H/V)	…	42.20 / 16.28
Natural chromaticities (H/V)	…	−49.98 / −50.20
Corrected chromaticities (H/V)	…	+1.0 / +1.0
Momentum compaction factor α_c, α_2	…	3.06×10^{-4}, 1.40×10^{-4}
Horizontal damping partition	…	1.85
Horizontal emittance (bare lattice)	pm rad	328
Radiation losses per turn (bare lattice)	keV	363.8
Natural energy spread (bare lattice)	…	7.69×10^{-4}
Required momentum acceptance	…	>4.5%

The optics in the long straight sections (cf. Fig.2) has been chosen according to injection and ID requirements. In the horizontal, a beta function of 9 m at the long straight center has been selected to enable off-axis injection. In this configuration the overall horizontal acceptance is determined by the septum blade at −10 mm. In the vertical, the beta function can be selected so as to maximize photon brightness [18]. However, because of the vertical acceptance limitations this entails (up to 4 m long IDs

targeting 1 Å radiation), a vertical beta function of 2 m at the center of the long straight has been chosen instead. This choice maximizes the vertical acceptance of the machine when in-vacuum undulators (IVUs) are being operated with fully closed gaps [18].

Finally, the working point was chosen away from systematic resonances such that both fractional tunes are just above the integer and away from the most dangerous resonances. With the working point held constant during operation, the nonlinear optics can be set to minimize the chromatic and amplitude-dependent tune shifts therefore keeping the tunes of most stored beam particles clear of dangerous resonances. This shall be explained in the next section.

5.2.2.2 *Nonlinear Optics*

Despite comparably relaxed linear optics, the nonlinear optics of such an MBA lattice is demanding. The strong focusing gives rise to large negative natural chromaticities that need to be corrected to prevent head-tail instability. This can be performed with chromatic sextupoles. Because of the low dispersion in the MBA these sextupoles tend to become very strong. Although this is not a concern for the magnet design (the 25 mm nominal magnet bore allows strong gradients), it presents an optics design challenge as such strong sextupoles give rise to pronounced nonlinear, amplitude-dependent behavior, which can limit both dynamic aperture (DA) and momentum acceptance (MA). The approach followed for the 3 GeV storage ring hinges on an idea first presented in 1992 for the ESRF [19,20]: correct chromaticity where it is generated by using many distributed sextupoles thus limiting chromatic beta beating. In addition, the nonlinear lattice design separates sextupole families by appropriate phase advances in order to cancel resonance driving terms (RDTs) and limit chromatic tune shifts [21-23].

The 3 GeV storage ring contains five sextupole families, three focusing and two defocusing. The focusing sextupoles are installed between the focusing quadrupoles in the unit cells. This puts these sextupoles at locations with comparably large horizontal beta function and dispersion. The defocusing sextupoles are installed as close as possible to the maximum of the product of dispersion and vertical beta: unit cell dipoles are flanked on either side by a defocusing sextupole of one family while the defocusing sextupoles in the matching cells are installed in the short straights right next to the matching cell soft-end dipole. Because of the large number of installed sextupoles and the small magnet gap, the sextupoles can be kept short and the pole-tip fields are far from saturation.

Sextupole optimization was performed with the codes OPA [24] and Tracy-3 [25]. The linear chromaticities were corrected to +1.0 in both planes (an alternative nonlinear optics for chromaticities corrected to +4 has also been developed [26]) and the first-order RDTs along with second- and third-order chromaticity were minimized as detailed in [23]. However, amplitude-dependent tune shifts (ADTSs) are only corrected as a second-order effect in sextupoles therefore requiring a lot of sextupole gradient strength and in turn driving resonances and chromatic tune shifts. This can necessitate extra sextupoles and/or increased sextupole gradients in order to keep first-order terms in check. Apart from leading to a potential run-away problem, this is a delicate balance that is easily disturbed by IDs, alignment errors, and higher-order multipoles — all of

which exist in a real machine. In an attempt to solve this fundamental challenge of nonlinear optimization in a MBA lattice, three achromatic octupole families were introduced into the matching cells of the 3 GeV achromat in locations with appropriate beta function ratios [2,15]. These octupoles correct the three terms for ADTS *to first order*. Analogous to the linear system, which is solved to find sextupole strengths that give a certain chromaticity, a linear system can be set up to describe the ADTSs that result from an octupole in the lattice. This system can be inverted to calculate octupole strengths that give the desired ADTSs. Rather than setting the linear ADTS to zero, however, the octupoles in the achromat were adjusted so the resulting overall ADTS is minimized throughout the physical acceptance (cf. Fig.3). Because the ADTS is corrected with the octupoles, the sextupoles are freed up for first-order corrections (linear chromaticity, RDTs). Some extra weight was added to minimize second- and third-order chromaticity in an attempt to limit the chromatic tune footprint (cf. Fig.4).
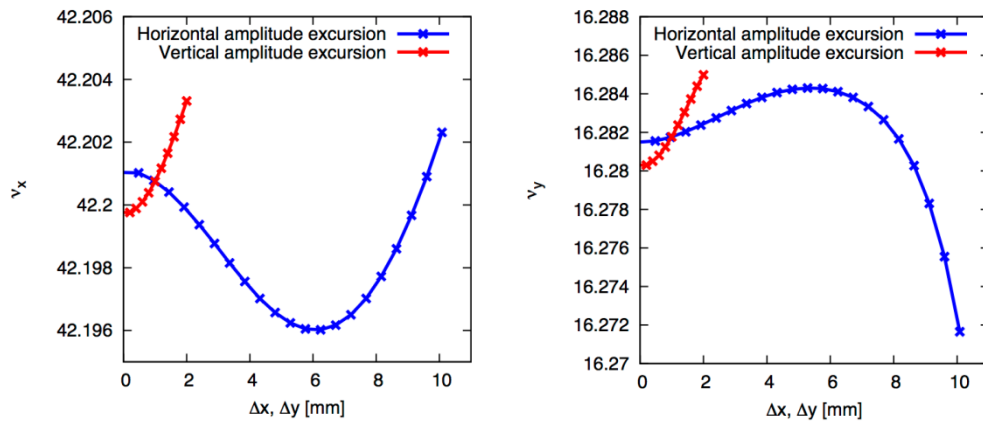
Figure 3: Amplitude-dependent tune shift in the 3 GeV storage ring with octupoles at design strength.
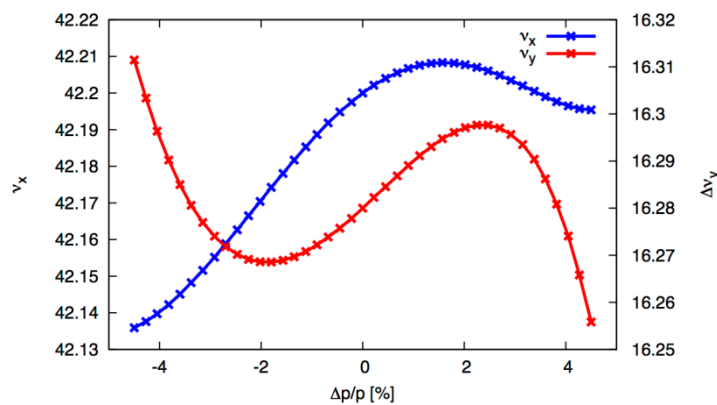
Figure 4: Chromaticity in the 3 GeV storage ring with octupoles at design strength.

The result of this nonlinear optimization is a very limited tune footprint for particles with a range of amplitudes covering the physically accessible aperture (at the center of the IDs roughly 10 mm horizontally and 2 mm vertically) and energies covering the required ±4.5% acceptance. This results in large DA and MA (cf. Fig.5 and Section 5.2.2.4), which ensure high injection efficiency and good Touschek lifetime. Frequency

map analysis confirms the "wrap-up" of tune shifts around the working point which results in this compact tune footprint. This holds also for a realistic machine, i.e. a storage ring with errors, misalignments, and IDs. This shall be discussed in the next section.
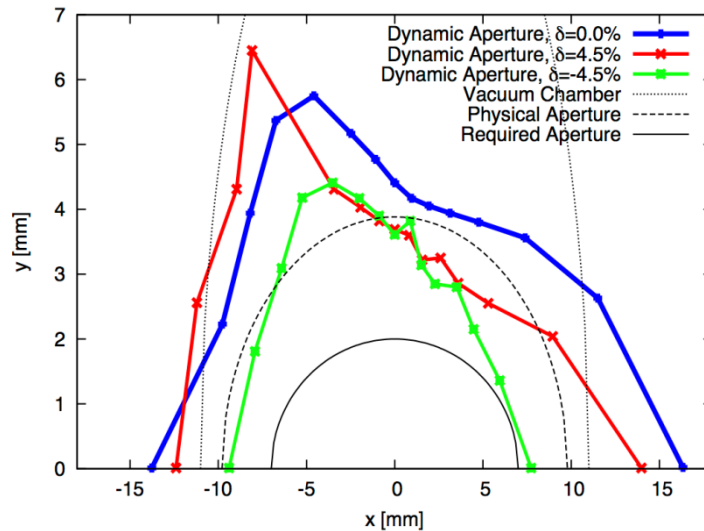
Figure 5: Dynamic aperture at the center of the long straight section in the 3 GeV storage ring (bare lattice). Tracking was performed with Tracy-3 in 6D for one synchrotron period. For comparison, the vacuum chamber, physical aperture (projection of vacuum chamber to the track point), and min. required aperture (injection, lifetime) are also indicated in the plot.

5.2.2.3   *Optics Matching and Correction*

With the quadrupole doublets in the matching cells the beta functions in the long straights can be tuned over a fairly wide range. This allows matching of the linear optics to the ID. The ID matching is performed both locally (beta functions are matched to prevent beta beats) and globally (phase advances are corrected to restore the design working point) [27, 28]. For the global correction the PFSs in the dipoles are used to adjust the vertical focusing. Because this matching results in restoring the design linear optics within the achromat, the nonlinear optics optimization is left almost undisturbed. If the multipolar content of the IDs is limited to specified values [27], neither sextupoles nor octupoles have to be adjusted with ID gap movement. In addition, skew quadrupole windings on all octupoles flanking IDs can be employed in a feed-forward scheme to compensate locally for the coupling induced by elliptically polarizing undulators (EPUs) operated in various modes and at various gaps. Tracking studies with Tracy-3 using kick maps reveal that, in the storage ring equipped with many strong in-vacuum undulators and EPUs, the DA is not substantially reduced as long as the proposed ID matching is properly performed [28].

Since all octupoles and sextupoles in the 3 GeV storage ring have been equipped with extra windings that can be powered in different ways, dispersive and non-dispersive skew quadrupoles can be added to the lattice for coupling control and removal of spurious vertical dispersion. An additional mode allows powering of the extra windings as auxiliary sextupoles in order to restore the design symmetry of the nonlinear optics [23]. Finally, these windings can also be powered as upright quadrupoles, which is routinely used to calibrate BPM offsets to the magnetic centers of the adjacent sextupoles and octupoles.

Each achromat also contains 10 horizontal and 9 vertical dipole correctors as well as 10 BPMs that are included in a slow orbit feedback. Because of the vertical beam size in the user straights reaching values as low as 2 μm rms, beam stability is crucial. There are 4 dedicated fast correctors installed around each user straight which, together with the BPM system, will allow operation of a fast orbit feedback in order to cancel beam motion effectively up to roughly 100 Hz [29,30]. Tracking studies have revealed that adequate DA remains when expected misalignments and multipole errors are added to the lattice and the orbit is corrected according to the proposed orbit feedback scheme [31]. This also holds if IDs are included and ID matching is performed as detailed above. Figure 6 shows an example for the DA resulting in such a case where, in addition to alignment, field, and multipole errors, ten 3.7-m long IVUs (18.5 mm period, 4.2 mm gap, 1.1 T effective magnetic field) have been added to the 3 GeV storage ring lattice. The resulting on-energy DA including the effect of all IDs and errors still roughly matches the physical aperture of the ring and therefore exceeds requirements based on injection and lifetime concerns.
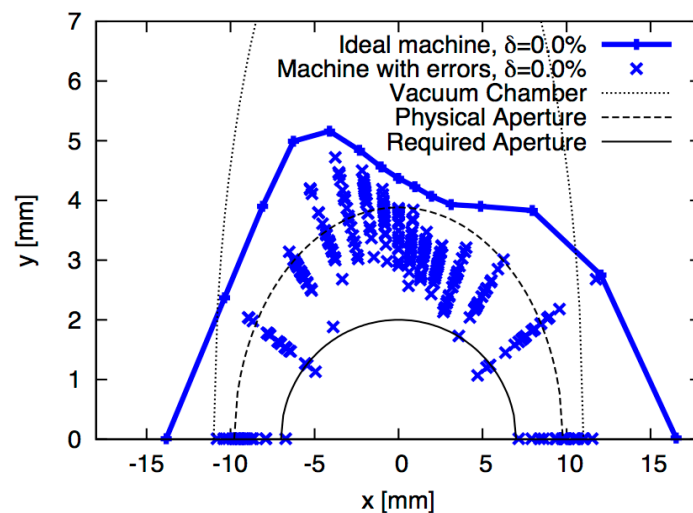
Figure 6: On-energy DA at the center of a long straight section in the 3 GeV storage ring where ten IVUs have been to the lattice. The plot shows the ideal lattice and results for 20 seeds with field and multipole errors as well as misalignments. Tracking was performed with Tracy-3 in 6D for one synchrotron period.

5.2.2.4 *Enabling Technology*

The 3 GeV storage ring lattice gives an ultralow emittance, but it requires strong magnets and compact optics, which leave little space for a conventional vacuum system. Therefore, several less conventional technology choices have been made in the 3 GeV storage ring, such as solid-iron integrated magnet blocks, a fully NEG-coated copper vacuum system, and a 100 MHz main RF system.

The magnets for the 3 GeV storage ring [32] have been designed using a technology already successfully demonstrated at MAX III [33]. The dipoles (28 mm pole gap) and quadrupoles (25 mm bore diameter) for each cell are precision-machined out of just two solid blocks of iron (CNC milling). The sextupoles, octupoles, and dipole correctors are installed into precision-machined grooves in these blocks. Each achromat cell is then built up of a lower and upper block that are brought together around the vacuum chamber. Figure 7 shows this magnet design using the matching cell as an example. This magnet technology integrates girder and magnet design, which results in reduced cost and high alignment accuracy. Furthermore, misalignments of magnets tend to be correlated [34] and can be minimized using beam-based realignment of the blocks as demonstrated at MAX III [35]. The blocks are installed on massive concrete supports at low height, which pushes vibrational eigenfrequencies of the assembly to higher frequencies thus improving beam stability.
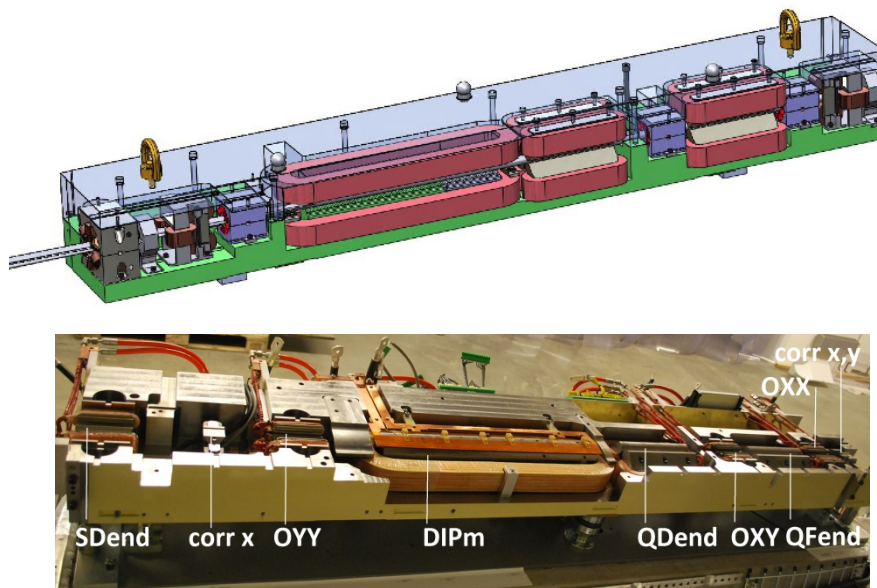
Figure 7: Top: schematic of a matching cell magnet block with soft-end gradient dipole, quadrupole doublet, defocusing sextupole (far left), three octupoles (blue), and two dipole corrector pairs. Bottom: photo [17] of an actual lower half of a matching cell magnet block.

The small magnet apertures of the 3 GeV storage ring require a narrow vacuum chamber. Such systems are often plagued by poor vacuum conductance. In addition, because of the very compact optics of the storage ring, there is no space for lumped absorbers or distributed pumping. Instead, the 3 GeV storage ring makes use of a 22/24 mm (ID/OD) circular copper tube which is uniformly NEG-coated around the entire

machine [36]. Lumped absorbers can be avoided as synchrotron radiation is distributed along long sections of the chamber. A cooling channel is electron beam-welded to the outside of the vacuum chamber. The magnet block design foresees simple removal of the chamber for activation bake-outs in the tunnel. Few small discrete pumps have been installed in straight sections. Narrow-gap chambers (8 mm full vertical aperture) for EPUs and in-vacuum IDs (4 mm minimum gap) are foreseen in user straights. Short tapers make the transition from the circular standard vacuum chamber to the ID chambers. Bellows and valves are RF-shielded. Bellows and BPM bodies (which are rigidly fastened to the magnet blocks) are manufactured from stainless steel. These bellows are also used for mounting of the fast orbit correctors, as the copper chamber is unsuited because of strong Eddy currents.

Since users are provided with short pulses from the dedicated MAX IV SPF, the MAX IV storage rings can be operated with long bunches. Without increasing the chromaticity to large values (possibly limiting the energy acceptance), this alleviates instability issues that often arise when using narrow vacuum chambers. The MAX IV storage rings therefore use a warm 100 MHz main RF system and passive Landau cavities at the third harmonic for additional bunch lengthening [37,30]. The six main cavities are an improved version of the 100 MHz cavities used in MAX II and III [38]. They are of capacity-loaded type and are HOM-damped. RF power is delivered by six stations with two 60 kW tetrode amplifiers each. This is considered a modular and cost-effective approach. The main cavities offer a maximum total gap voltage of 1.8 MV, which corresponds to an RF acceptance of up to 7.1% depending on number and type of operated IDs. The minimum required MA was specified at 4.5% which corresponds to running the cavities at 1.02 MV total gap voltage (bare lattice). Figure 8 shows the RF and lattice MA in the achromat. The lattice MA exceeds the RF acceptance except if a bare lattice is combined with maximum cavity voltage.
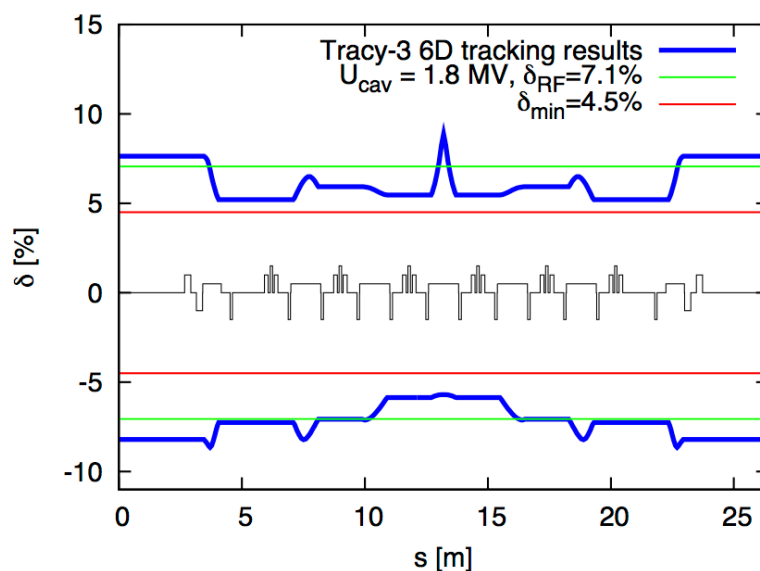
Figure 8: Lattice MA for one achromat of the 3 GeV storage ring. A bare lattice with actual vacuum chamber apertures has been used. The solid blue line shows lattice MA from 6D tracking with Tracy-3 for one synchrotron period. For comparison, the RF acceptance is also shown for cavities at maximum voltage 1.8 MV.

The Landau cavities are a new in-house development based on the main cavities' capacity-loaded design. Three warm and passive Landau cavities allow for roughly 600 kV gap voltage, thus stretching bunches by a little more than a factor of five. Not only do such long bunches increase Touschek lifetime (cf. Section 5.2.2.6) and reduce emittance growth from intrabeam scattering (cf. Section 5.2.2.5), they also make the ring more tolerant against coupled-bunch instabilities.

5.2.2.5   *Emittance and Intrabeam Scattering*

The ultralow emittance of the 3 GeV storage ring will depend on the number and type of installed IDs [16]. This is a general property of ultralow-emittance lattices based on MBAs where the power radiated in the bending magnets is low compared to ID losses. In addition, the overall equilibrium emittance at high stored current is limited by intrabeam scattering (IBS). The 3 GeV storage ring bare lattice has an equilibrium emittance of 328 pm rad, but at the shortest bunch length (i.e. at maximum cavity voltage and without Landau cavities) of 9 mm, IBS at 500 mA (even fill, 5 nC/bunch) blows up the emittance by 45%. Once the Landau cavities are tuned in and the bunches lengthened to ~50 mm as foreseen by the design, the IBS blow-up results in an emittance of 372 pm rad, i.e. 13% above the zero-current bare lattice emittance. For a moderately ID-equipped ring with cavities running at maximum voltage (giving an RF acceptance of 6%), the emittance including the effect of IBS and Landau cavities is expected to lie at roughly 270 pm rad. This figure can be further lowered by reducing the RF cavity overvoltage. On the other hand, a decrease of vertical emittance from its 8 pm rad design value will lead to an increased IBS blowup of the horizontal emittance [16]. The strong IBS mechanism in the 3 GeV storage ring results in a situation where bunch lengthening Landau cavities are not only required for lifetime and stability reasons, but most importantly also to guarantee the ultralow lattice emittance can be maintained even when storing large amounts of current.

5.2.2.6   *Lifetime*

Gas scattering lifetimes in the 3 GeV storage ring including in-vacuum IDs at 500 mA have been estimated at roughly 25 hours (elastic) and 56 hours (inelastic) where the latter has been calculated assuming a MA of only 4.5% [1]. The Touschek lifetime of the moderately ID-equipped ring at 270 pm rad is 21 hours at natural bunch length and 114 hours with Landau cavities tuned in [16]. Even factoring in alignment, field, and multipole errors as well as narrow vertical apertures from IVUs and narrow-gap EPU chambers, the Touschek lifetime should remain at 66 hours (assuming proper bunch lengthening from the Landau cavities). Overall this results in a total lifetime of about 14 hours, which equates to one top-up injection every seven minutes if a 0.5% top-up deadband is chosen.

Despite the ultralow emittance of the 3 GeV storage ring, lifetime is very good. This is the result of large MA achieved with the nonlinear optics optimization (cf. Fig.8), but also of a peculiarity of Touschek lifetime at ultralow emittance. At ultralow emittance, there are only few particles in the bunch with sufficient transverse momentum to generate Touschek losses; most of the scattering events are IBS, which blows up the emittance, but does not lead to particle loss from the RF bucket [16]. A nice example for this behavior is the observation that, as IDs are added to the 3 GeV storage ring, the

emittance (including IBS) decreases, but Touschek lifetime actually improves (cf. Fig.9).
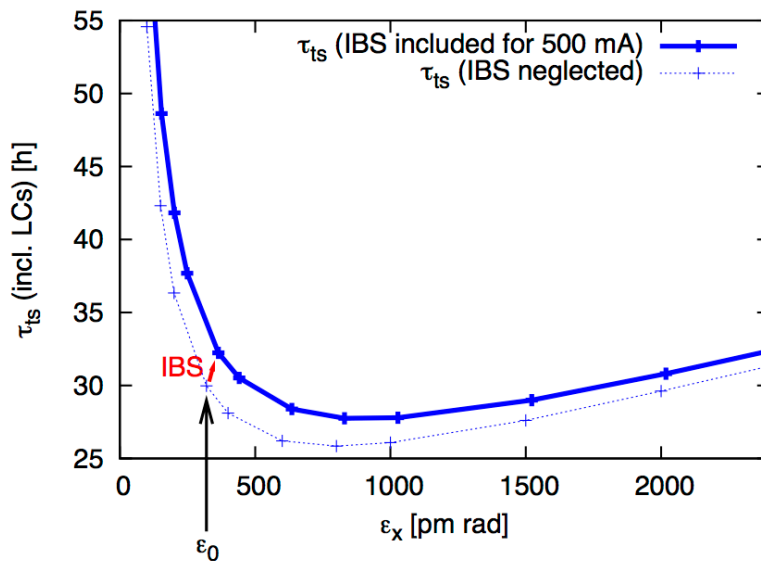
Figure 9: Touschek lifetime (including the effect of LCs) at 500 mA from 6D tracking with Tracy-3 as a function of equilibrium emittance assuming the lattice emittance could be adjusted freely while keeping the energy spread constant. The overall MA has been set to 4.5% while the vertical emittance is adjusted to 8 pm rad. The effect of IBS at 500 mA is also displayed.

Studies have indicated that the change of Touschek lifetime behavior with emittance occurs around 0.7 nm rad for the 3 GeV lattice (cf. Fig.9). Since all operation conditions foresee emittances below this value, an emittance reduction should always lead to a Touschek lifetime improvement in the 3 GeV storage ring. In consequence, having many strong IDs in the 3 GeV storage ring should not only lead to lowest emittance, but also to best lifetime. Once the 3 GeV storage ring is fully equipped with IVUs (rendering in total 213 pm rad horizontal emittance at 500 mA of stored current) 38 hours of Touschek lifetime can be expected when including the effect of errors and narrow vertical apertures [16].

5.2.2.7 *Injection*

Top-up injection into the 3 GeV storage ring will be performed by the 3 GeV linac via an achromatic vertical transfer line that connects the underground linac with the storage ring. The 3 GeV linac today routinely delivers roughly 250 pC of charge per top-up shot (a train of S-band bunches that is injected in up to ten consecutive storage ring buckets). Top-up injection can occur at 10 Hz (governed by a storage ring damping time on the order of 15 ms), thus, up to 0.3% of the storage ring current can be replenished per second—at the expected lifetime in the storage ring this will occur once every three minutes. Originally, injection into the 3 GeV storage ring was designed using a closed four-kicker injection bump around a DC Lambertson septum in the first

long straight [1]. In light of the very tight beam stability requirements in the 3 GeV storage ring there was considerable doubt that four injection kickers could be aligned, balanced, and synchronized well enough to prevent perturbation of the stored beam beyond the limits of these stability requirements. Furthermore, since the injection bump would have contained strong sextupoles and octupoles, the bump could not be closed properly for all amplitudes and all particles in the bunch.

As a result, the four-kicker injection bump was abandoned and instead an injection based on pulsed multipole injection was pursued. A first design [39] was based on a pulsed sextupole magnet (PSM) following pioneering work at KEK. Tracking studies confirmed that capture in the storage ring can be highly efficient since the emittance of the linac bunches at 3 GeV is extremely small compared to the storage ring acceptance. Meanwhile stored bunches in the ring are not perturbed beyond tolerances by the pulsed multipole as long as it is properly aligned to the stored beam. Further studies finally led to the choice of pulsed multipole injection [40,30] using a multipole injection kicker (MIK) based on a stripline-like design similar to a prototype developed for BESSY II. In this kicker the induced field around the stored beam is octupole-like, hence no kick is given to the stored beam at the magnetic center. The injected beam is, as in the case of a PSM, injected into the storage ring's acceptance within a single turn. This MIK is presently being assembled and tested [41] within a collaboration between MAX IV, SOLEIL, and HZB/BESSY. Installation into the 3 GeV storage ring is presently foreseen to take place at the end of 2016.

For commissioning purposes a single dipole kicker was retained from the original closed-bump injection scheme. This dipole kicker [42] has enabled injection, capture, and accumulation of up to 160 mA during commissioning so far. It is also used in top-up mode to ensure constant high current during machine shifts, however, since it causes considerable perturbation to the stored beam during accumulation, it is not considered compatible with user top-up operation. It will therefore be replaced by the MIK for user operation and from then on used only as a horizontal pinger during machine studies.

5.2.2.8 *Outlook*

Commissioning of the 3 GeV storage ring has progressed quite well so far [43]. The rather unconventional magnet and vacuum systems have both proven viable solutions for an ultralow-emittance storage ring. A peak stored current of 160 mA has so far been achieved. The 100 MHz main RF system and the three 300 MHz Landau cavities have been commissioned and are operating well: the resulting bunch lengthening as well as the damping of instabilities have both been demonstrated [44]. The first of two diagnostic beamlines, where transverse emittances, energy spread, and longitudinal bunch profiles are measured, has also been taken into operation [45]. The first two IVUs in the 3 GeV storage ring are now routinely producing photons for ID, beamline, and endstation commissioning. During the summer shutdown the first in-vacuum wiggler will be installed as well as the first two EPUs. These devices shall undergo commissioning starting in September 2016. Dedicated user operation at the 3 GeV

storage ring is expected to commence in 2017. By the end of 2017 the first seven beamlines (funded within the two first beamline phases) at the 3 GeV storage ring are expected to be in operation.

In terms of further machine development, several improvements have been studied and will hopefully be implemented soon after commissioning. The vertical emittance of the 3 GeV storage ring was originally set at 8 pm rad corresponding to the 1 Å diffraction limit. This calls for a rather generous 2.5% emittance coupling. Studies have shown, however, that both brightness and coherence in the vicinity of 1 Å can be substantially increased by lowering the vertical emittance to roughly 2 pm rad (0.6% emittance coupling) [18]. Ample skew quadrupoles are available in the 3 GeV storage ring for this purpose. Including imperfections, Touschek lifetime should remain beyond 27 hours even at lower coupling [16] as long as sufficient bunch lengthening from the Landau cavities is ensured. Furthermore, studies have also shown that using the many skew quadrupoles available in the 3 GeV storage ring allows adjusting the vertical emittance quite freely over a large range [46]: by exciting vertical dispersion only in the arcs, a large Touschek lifetime can be ensured while nevertheless limiting betatron coupling at the ID source points, thereby simultaneously ensuring high photon brightness and good lifetime.

Other studies have just started to investigate how timing experiments can be accommodated in the MAX IV storage rings [47,48]. While the MAX IV SPF caters to short-pulse users at 100 Hz, some high-brightness users at the storage rings are interested in synchronization, which is difficult considering that the 3 GeV storage ring has been designed to run with an even fill in multi-bunch mode using passive Landau cavities without any gaps or camshaft bunches. These recent studies have started to investigate alternate filling patterns, their effect on the storage ring, and other options to accommodate timing users at the MAX IV storage rings.

Finally, several studies have been initiated to investigate optics improvements throughout the 3 GeV storage ring. A first study [49] assumed that magnets and power supplies would be retained. By adjusting the optics in the arc to reduce the dispersion and by improving the optics matching to IDs in the long straights, the lattice emittance can be dropped by 18% and the photon brightness at 1 Å can be increased by 33%. Ongoing studies assume existing quadrupole families could be broken up and power supplies exchanged. This allows a further emittance reduction to the roughly 200 pm rad level. Lastly, first MOGA studies indicate that if DA requirements are lowered (enabled eg. by switching to on-axis injection using a ~20 ns dipole kicker to remain compatible with user top-up), we should ultimately be able to reach roughly 150 pm rad in the 3 GeV storage ring with IDs.

5.2.3 Lattice Design for the MAX IV 1.5 GeV Storage Ring

The MAX IV 1.5 GeV storage ring has a 96 m circumference, 10 user straights, and 6 nm rad emittance. It is essentially a modernized and upgraded design of the recently decommissioned MAX II storage ring [50], but employing the fully integrated magnet design first demonstrated in the MAX III storage ring [33] and now also used in the MAX IV 3 GeV storage ring (cf. Section 5.2.2.4). The MAX IV 1.5 GeV storage ring has actually been built twice: once in Lund for the MAX IV facility [1,3] and once in

Krakow, Poland for the Solaris Project [51]. While it will be injected at 1.5 GeV from the MAX IV linac in top-up mode, at Solaris injection from the linac occurs at 500 MeV and the ring is then ramped to 1.5 GeV. At MAX IV, the 1.5 GeV storage ring will serve as the source for UV and soft x-rays. In fact, a few beamlines from the recently decommissioned MAX II and III are being moved to this new storage ring.

5.2.3.1   *Linear Optics*

The MAX IV 1.5 GeV storage ring[4] is based on a double-bend achromat (DBA) lattice [3,52]. Its twelve identical DBA cells provide 10 user straights of 3.5 m length for IDs. An overview of one achromat of the 1.5 GeV storage ring is shown in Fig.10. Each of the achromats consists of two 15º bending magnets flanked by horizontally focusing quadrupoles. The dipoles contain a transverse gradient that provides vertical focusing while the quadrupoles contain a sextupole gradient for nonlinear correction. The lattice models both dipoles and quadrupoles as arrays of consecutive combined-function magnets in order to properly resolve fringe fields as well as longitudinal variations of the ratio between the design multipole components.
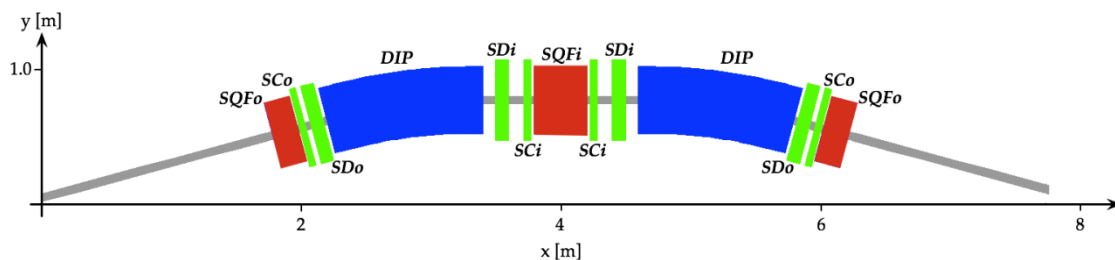
Figure 10: Schematic of one of the 12 achromats of the 1.5 GeV storage ring. Magnets indicated are gradient dipoles (blue), focusing quadrupoles with a sextupole gradient (red), and discrete sextupoles (green).

The quadrupoles are split up into two families: the SQFi family for the "inner" quadrupoles (i.e. those between the two dipoles in the arc) and the SQFo family for the "outer" quadrupoles (i.e. those in the straights). The lattice does not contain any dedicated vertically focusing quadrupoles as this is performed entirely by the transverse gradient in the dipoles. Matching of the arc optics to IDs in the straights is performed by adjusting the SQFo quadrupoles. In order to also vary the vertical focusing in the straight, the dipoles contain PFSs that allow roughly ±5% gradient variation at full excitation. The working point was chosen away from systematic resonances and so that both fractional tunes are just above the integer and away from the most dangerous resonances. The optics for one achromat is displayed in Fig.11 and storage ring parameters are given in Table 2.

---

[4] Lattice files available at https://www.maxiv.lu.se/publications/
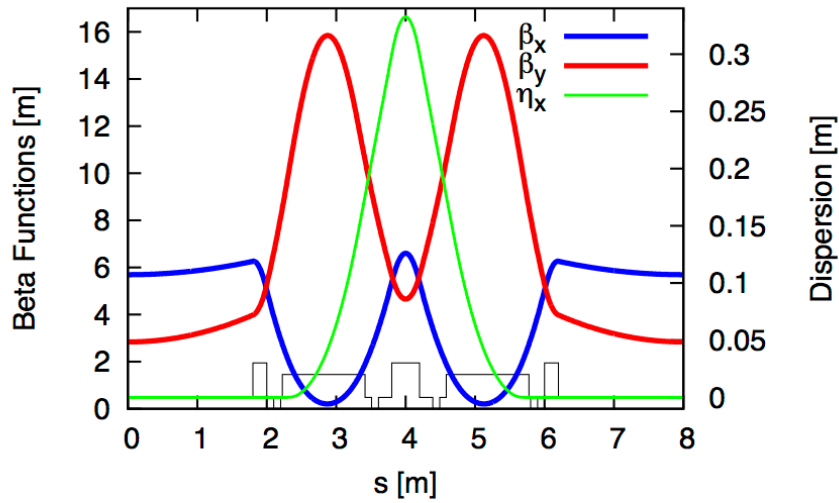
Figure 11: Beta functions and dispersion for one achromat of the 1.5 GeV storage ring. Magnet positions are indicated in black at the bottom.

The magnet design of the 1.5 GeV storage ring is very similar to the 3 GeV storage ring with two considerable differences: magnet gaps can be larger (lower gradients required by the DBA optics) and increased use of combined-function magnets, i.e. combining focusing sextupole gradients into the horizontally focusing quadrupoles. The resulting magnet design [53,54] can therefore rely on the same magnet block concept used in the 3 GeV storage ring, while a much more conventional vacuum design can be retained since magnet gaps are roughly twice the size of their 3 GeV storage ring counterparts. Figure 12 shows a schematic of the magnet block containing all magnets of one DBA of the 1.5 GeV storage ring. With this optics and magnet design the 1.5 GeV storage ring can provide two additional ID straights as well as lower emittance compared to the MAX II storage ring within essentially the same space.

Table 2: Parameters for the 1.5 GeV storage ring.

Parameter	Unit	Value
Energy	GeV	1.5
Main radio frequency	MHz	99.931
Circulating current	mA	500
Circumference	m	96
Number of achromats (straights available for IDs)	…	12 (10)
Betatron tunes (H/V)	…	11.22 / 3.15
Natural chromaticities (H/V)	…	–22.98 / –17.14

Corrected chromaticities (H/V)	…	+1.0 / +1.0
Momentum compaction factor α_c, α_2	…	3.06×10^{-3}, 6.41×10^{-3}
Horizontal damping partition	…	1.46
Horizontal emittance (bare lattice)	nm rad	5.98
Radiation losses per turn (bare lattice)	keV	114.1
Natural energy spread (bare lattice)	…	7.45×10^{-4}
Required momentum acceptance	…	>3.5%
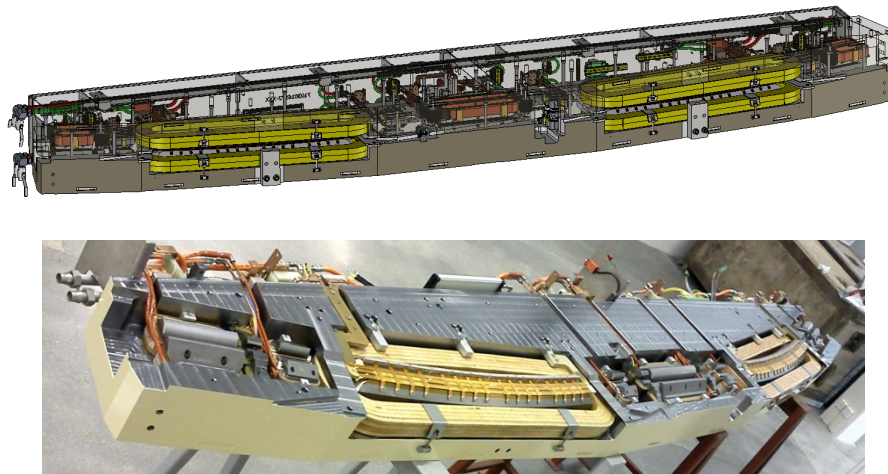
Figure 12: Top: schematic of one of the twelve magnet blocks in the 1.5 GeV storage ring. The block consists of two solid iron halves into which magnet pole faces have been machined: gradient dipoles (yellow coils), quadrupoles with sextupole gradient (red coils) as well as discrete sextupoles and dipole correctors in between. Bottom: photo of an actual lower half of a magnet block. Courtesy M. Johansson.

5.2.3.2   *Nonlinear Optics*

At least two families of sextupoles are required to correct the natural chromaticity of the lattice. In order to achieve a compact lattice, the sextupoles for the 1.5 GeV storage ring were integrated into the quadrupoles where possible. This has led to a design where both types of horizontal focusing quadrupoles contain a focusing sextupole gradient. Since only one of these quadrupoles is dispersive, only this sextupole component can be used for chromatic correction. The sextupole component in the SQFo family, is considered a harmonic sextupole and used for minimization of the RDTs and tailoring of the ADTS. The defocusing sextupoles have on the other hand been realized as discrete sextupoles. One family (SDi) is installed between the dipoles and the SQFi quadrupoles at the center of the DBA. The other defocusing family (SDo) is placed

between the dipoles and the SQFo quadrupoles. In these locations both defocusing sextupoles see beta function ratios that reduce the required sextupole gradient. Again, since only the SDi is dispersive, it is used for chromatic corrections, while the SDo family is employed for RDT minimization and tailoring of the ADTS.

Since the focusing sextupoles are realized as gradients in quadrupole magnets, an additional means of sextupole tuning is required. This has been realized by inserting thin additional sextupoles: the SCi family flanks the SQFi at the center of the DBA, whereas the SCo is installed right next to the SQFo. The underlying strategy is to use the built-in gradient of the SQFi to correct the bulk of the natural chromaticity while using the dedicated SCi for adjustments of the corrected chromaticity over a narrower range. The SCi and SCo trim sextupoles also carry three additional sets of windings: a skew quadrupole winding for correction of spurious vertical dispersion and tuning of the betatron coupling as well as dedicated coils for horizontal and vertical dipole correction that are used by the slow orbit feedback running at 10 Hz [1].

The nonlinear optics foresees correction of the linear chromaticities to +2 "in iron", i.e. using the sextupole gradient in the combined-function SQFi family and the SDi. By additionally exciting the SCi family and adjusting the SDi family, the linear chromaticities can be adjusted by roughly ±2. In the production nonlinear optics [52] this is used to set the corrected chromaticities to their design values of +1 in both planes (an alternative nonlinear optics for chromaticities corrected to +4 has also been developed [55]). The sextupole gradient in the combined-function SQFo and the setting of the SDo have been optimized in order to reduce first-order RDTs and adjust the ADTS footprint to avoid potentially dangerous resonances. This optics results in a tune footprint as shown in Figs.13 and 14. As a consequence of the very compact tune footprint and the limited RDTs, the DA both on and off energy becomes large. This is demonstrated in Fig.15.
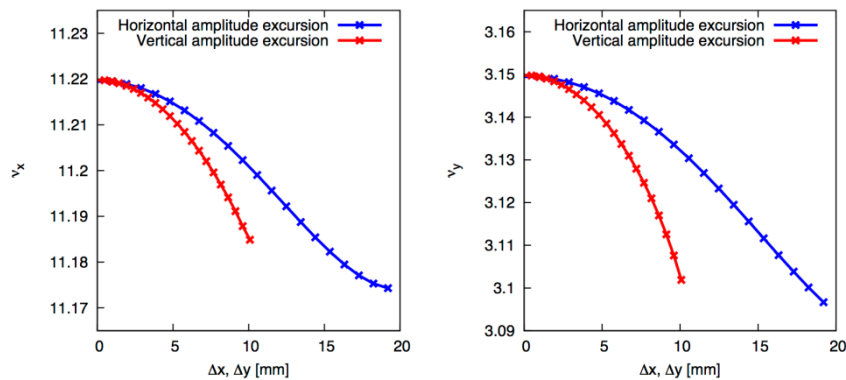
Figure 13: Amplitude-dependent tune shift in the 1.5 GeV storage ring with the design optics correcting linear chromaticities to +1 in both planes.
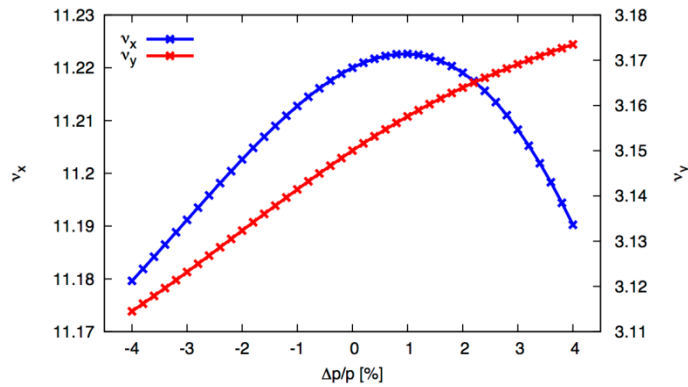
Figure 14: Chromaticity in the 1.5 GeV storage ring with the design optics correcting linear chromaticities to +1 in both planes.
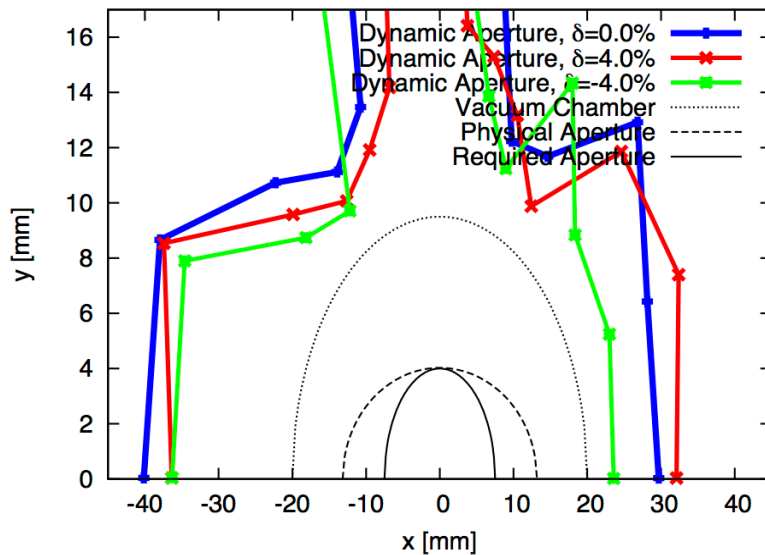
Figure 15: Dynamic aperture at the center of an ID straight in the 1.5 GeV storage ring (bare lattice). Tracking was performed with Tracy-3 in 6D for one synchrotron period. For comparison, the vacuum chamber, physical aperture (projection of vacuum chamber to the track point), and min. required aperture (injection, lifetime) are also indicated in the plot.

Similar to the approach taken for the 3 GeV storage ring, the optics in the 1.5 GeV storage ring will be matched to strong IDs [28]. PFSs and SQFo on either side of an ID can be used to match the arc optics to the ID gap and phase setting. Since changing the focusing in SQFo will also modify its sextupole gradient, the SCo can be used to compensate for this shift in the nonlinear optics if required. Skew quadrupole coils are readily available to compensate for coupling induced by EPUs in addition to cancelation of spurious vertical dispersion and the adjustment of the betatron coupling. Tracking studies with various error sources such as misalignments, field, and multipole errors in addition to adding various types of IDs to the 1.5 GeV storage ring indicate that sufficient on- and off-energy DA can be retained as long as orbit correction and ID compensation are carried out according to design (cf. Fig.16).
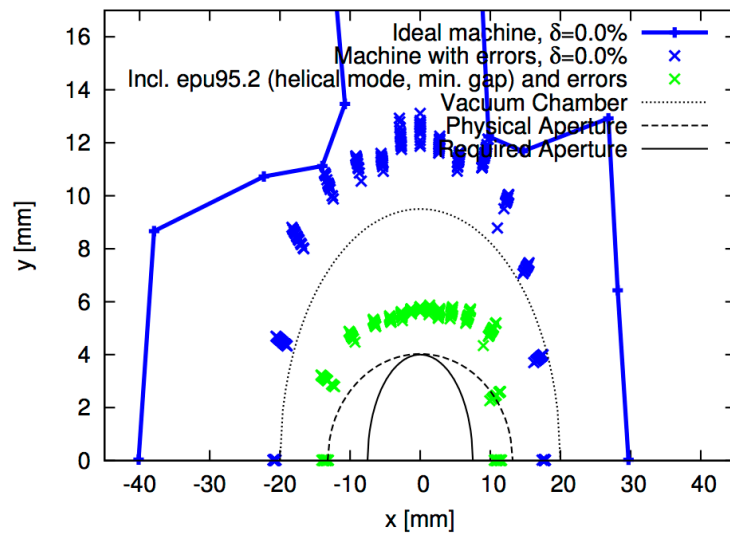
Figure 16: On-energy DA at the center of an ID straight section in the 1.5 GeV storage ring. The plot shows the ideal lattice and results for 20 seeds with field and multipole errors as well as misalignments. For comparison, results when adding an EPU (95.2 mm period, 2.6 m length, 14 mm magnetic gap) to the ring are included. In this case the EPU is assumed operating in helical mode at minimum gap (modelled with a kick map) [28]. Tracking was performed with Tracy-3 in 6D for one synchrotron period.

5.2.3.3 *RF, Lifetime & Injection*

The large off-momentum DA in conjunction with an RF system supplying sufficient RF acceptance allows for a large overall MA. The vacuum apertures at the center of the DBA were increased[5] to match the growing dispersion and in this way ensure that the overall MA remains beyond the minimum requirement of 3.5% even at the center of the DBA. The RF system makes use of the same 100 MHz cavities used in the 3 GeV storage ring. Two such cavities are installed for a maximum accelerating voltage of 560 kV which renders a maximum RF acceptance of 4.13% well matched to the lattice MA (cf. Fig.17).

---

[5] The standard full apertures at the ends of the DBA are 40 mm × 20 mm whereas towards the middle of the DBA where dispersion peaks they are increased to 56 mm x 28 mm.
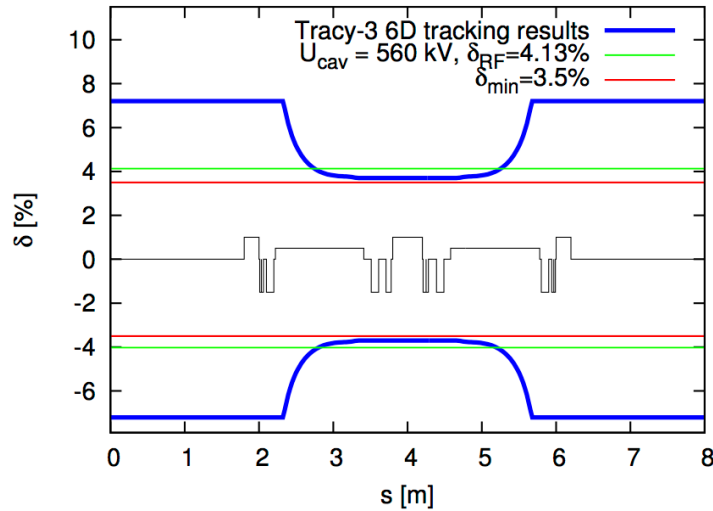
Figure 17: Lattice MA for one DBA in the 1.5 GeV storage ring. A bare lattice with actual vacuum chamber apertures has been used. The solid blue line shows lattice MA from 6D tracking with Tracy-3 for one synchrotron period. For comparison, the RF acceptance is also shown for cavities at maximum voltage 560 kV.

As a result of the large overall MA, decent Touschek lifetime despite 500 mA of stored current can be expected. To increase the resulting Touschek lifetime, two 300 MHz Landau cavities (identical to the Landau cavities in the 3 GeV storage ring) will be installed. Both 100 MHz main cavities and the two Landau cavities can be installed in a single straight section so that—together with the injection straight—only two straights cannot host IDs. The two 300 MHz Landau cavities should stretch bunches in the 1.5 GeV storage ring by roughly a factor of four. Tracking studies indicate this should result in a Touschek lifetime (at 500 mA stored current and 1% emittance coupling) between 23–34 hours depending on the exact settings of the RF cavities as well as the installed IDs and their gap settings. Together with the assumed gas lifetime of around 19 h [1], this gives an overall lifetime beyond 10 h. This is compatible with top-up injections from the MAX IV linac occurring every few minutes keeping stored current in the ring constant to within 0.5%.

Injection into the 1.5 GeV storage ring will make use of the vertical achromatic transfer line between the 1.5 GeV extraction point of the underground linac and a DC Lambertson septum in the injection straight of the storage ring. As in the 3 GeV storage ring, we have decided to avoid a four-kicker injection bump and instead inject into the ring using a single injection kicker. In the commissioning phase this will be a dipole kicker magnet [42] installed in the third straight section (capture of injected bunches is not feasible in the second straight section). This dipole kicker will allow both on-axis and off-axis injection as well as accumulation. Since it perturbs the stored beam considerably during accumulation, it will after commissioning be replaced by a MIK [39,40] to enable transparent top-up injection during user operation. The dipole kicker will then be moved to the upstream end of the injection straight where it will serve as a horizontal pinger magnet for machine studies. Since both the dipole kicker and the proposed MIK are short, the third straight remains available for a roughly 2.5 m long ID. The dipole kicker, manufactured by BINP, has already been installed in the 1.5 GeV

storage ring whereas the MIK for this ring is presently being developed within the scope of the MAX IV – SOLEIL – HZB/BESSY collaboration designing and building the MIK for the 3 GeV storage ring.

5.2.3.4 *Outlook*

At the time of writing most of the installations in the 1.5 GeV storage ring are complete. During the summer shutdown (July & August 2016) the last missing pieces will be installed: the remaineder of the 1.5 GeV transfer line from the linac as well as the last DBA before the injection straight. Once these last pieces have been installed the remaining subsystem tests can be completed so that commissioning of the 1.5 GeV storage ring should be able to commence in September 2016. Initial commissioning will be carried out with dummy chambers in the straight sections. In early 2017 the first EPU chambers will be installed so that commissioning of the first two EPUs in the 1.5 GeV storage ring can start by March 2017.

As in the 3 GeV storage ring, the 1.5 GeV storage ring was designed to operate with an even fill in constant multi-bunch mode at 500 mA with top-up injection. First studies [47, 48] have started investigating how users interested in timing and synchronization could be accommodated at the 1.5 GeV storage ring. In the meantime, the first five beamlines (funded within the two first beamline phases) will be installed and brought into operation throughout 2017.

5.2.4 **References**

1. The MAX IV Detailed Design Report.

   https://www.maxiv.lu.se/publications/

2. S.C. Leemann et al., "Beam dynamics and expected performance of Sweden's new storage-ring light source: MAX IV", Phys. Rev. ST Accel. Beams **12**, 120701 (2009).

3. S.C. Leemann, "Recent Progress on the MAX IV 1.5 GeV Storage Ring Lattice and Optics", Proceedings of IPAC'12, New Orleans, LA, USA, p.1662.

4. S. Werin, S. Thorin, M. Eriksson, J. Larsson, "Short pulse facility for MAX-lab", Nucl. Instr. and Meth. A **601**, 98 (2009).

5. S. Thorin et al., "Design of the MAX IV Ring Injector and SPF/FEL Driver", Proceedings of PAC'11, New York, USA, p.2447.

6. N. Cutic et al., "The MAX IV Injector as a Soft X-Ray FEL Driver", Proceedings of FEL2010, Malmö, Sweden, p.382.

7. F. Curbis et al., "Simulation Studies for an X-ray FEL Based on an Extension of the MAX IV Linac", Proceedings of FEL2013, New York, NY, USA, p.510.

8. H. Tarawneh, M. Eriksson, L.-J. Lindgren, B. Anderberg, "MAX-IV lattice,

dynamic properties and magnet system", Nucl. Instr. and Meth. A **508** (2003) 480.

9. M. Eriksson, et al., "Some small-emittance light-source lattices with multi-bend achromats", Nucl. Instr. and Meth. A **587** (2008) 221.

10. D. Einfeld, M. Plesko, "Design of a diffraction-limited light source", Proc. SPIE, **2013**, pp.201-212, 1993.

11. W. Joho, P. Marchand, L. Rivkin, A. Streun, "Design of a Swiss Light Source (SLS)", Proceedings of EPAC 1994, London, England, p.627.

12. D. Einfeld, J. Schaper, M. Plesko, "Design of a Diffraction Limited Light Source (DIFL)", Proceedings of PAC 1995, Dallas TX, USA, p.177.

13. D. Kaltchev, R.V. Servranckx, M.K. Craddock, W. Joho, "Lattice Studies for a High-brightness Light Source", Proceedings of PAC 1995, Dallas TX, USA, p.2823.

14. An MBA cycle schematic by A. Streun (PSI) can be found on slide 10 in https://agenda.infn.it/getFile.py/access?contribId=20&resId=1&materialId=slides&confId=9137

15. S.C. Leemann, A. Streun, "Perspectives for future light source lattices incorporating yet uncommon magnets", Phys. Rev. ST Accel. Beams **14**, 030701 (2011).

16. S.C. Leemann, "Interplay of Touschek scattering, intrabeam scattering, and rf cavities in ultralow-emittance storage rings", Phys. Rev. ST Accel. Beams **17**, 050705 (2014).

17. M. Johansson, L.-J. Lindgren, M. Sjöström, P.F. Tavares, "MAX IV 3 GeV Storage Ring Magnet Block Production Series Measurement Results", Proceedings of IPAC2016, Busan, Korea, p.1157.

18. S.C. Leemann, M. Eriksson, "Coupling and Brightness Considerations for the MAX IV 3 GeV Storage Ring", Proceedings of PAC2013, Pasadena, CA, USA, p.243.

19. W. Klotz, G. Mülhaupt, Proceeding of the Workshop on 4th Generation Light Sources, Stanford, CA, USA, 1992.

20. G. Mülhaupt, Technical Report No. ESRF/Mach-INJ/94-13, ESRF, Grenoble, France, 1994.

21. J. Bengtsson, Technical Report CER 88-05, CERN, Geneva, Switzerland, 1988.

22. J. Bengtsson, "The Sextupole Scheme for the Swiss Light Source (SLS): An Analytic Approach", PSI Internal Report SLS-TME-TA-1997-0009, PSI, Villigen, Switzerland, 1988.

23. A. Streun, "A standard method of nonlinear lattice optimization and application to the Swiss Light Source storage ring", ICFA Beam Dynamics Newsletter, Volume 57, pp.95-104, April 2012.

24. OPA lattice design code, http://ados.web.psi.ch/opa/

25. J. Bengtsson, Tracy-2 User's Manual (unpublished).

26. T. Olsson, S.C. Leemann, "High-Chromaticity Optics for the MAX IV 3 GeV Storage Ring", Proceedings of PAC2013, Pasadena, CA, USA, p.592

27. E. Wallén, S.C. Leemann, "Strategy for Neutralizing the Impact of Insertion Devices on the MAX IV 3 GeV Ring", Proceedings of PAC'11, New York, USA, p.1262.

28. S.C. Leemann, H. Tarawneh, "Impact of Insertion Devices on the MAX IV Storage Rings", Proceedings of IPAC2015, Richmond, VA, USA, p.1696.

29. M. Sjöström et al., "Orbit Feedback System for the MAX IV 3 GeV Storage Ring", Proceedings of IPAC'11, San Sebastián, Spain, p.499.

30. P.F. Tavares, S.C. Leemann, M. Sjöström, Å. Andersson, "The MAX IV storage ring project", J. Synchrotron Rad., **21**, 862-877 (2014).

31. S.C. Leemann, "Updates to the MAX IV 3 GeV Storage Ring Lattice", MAX-lab internal note 20110117, https://www.maxiv.lu.se/publications/

32. M. Johansson, B. Anderberg, L.-J. Lindgren, "Magnet design for a low-emittance storage ring", J. Synchrotron Rad., **21**, 884-903 (2014).

33. M. Sjöström, E. Wallén, M. Eriksson, L.-J. Lindgren, "The MAX III storage ring", Nucl. Instr. and Meth. A **601**, 229 (2009).

34. J. Björklund Svensson, M. Johansson, "Relative Alignment Within the MAX IV 3 GeV Storage Ring Magnet Blocks", Proceedings of IPAC2015, Richmond, VA, USA, p.57.

35. M. Sjöström, E. Wallén, M. Eriksson, L.-J. Lindgren, "Corrector-based magnet alignment procedure", Nucl. Instr. and Meth. A **597**, 170 (2008).

36. E. Al-Dmour et al., "Diffraction-limited storage-ring vacuum technology", J. Synchrotron Rad., **21**, 878-883 (2014).

37. Å. Andersson et al., "The 100 MHz RF System for the MAX IV Storage Rings",

Proceedings of IPAC'11, San Sebastián, Spain, p.193.

38. Å. Andersson et al., "The 100 MHz RF System for MAX-II and MAX-III", Proceedings of EPAC 2002, Paris, France, p.2118.

39. S.C. Leemann, "Pulsed sextupole injection for Sweden's new light source MAX IV", Phys. Rev. ST Accel. Beams **15**, 050705 (2012).

40. S.C. Leemann, L.O. Dallin, "Progress on Pulsed Multipole Injection for the MAX IV Storage Rings", Proceedings of PAC2013, Pasadena, CA, USA, p.1052.

41. S.C. Leemann, "Pulsed Multipole Injection for the MAX IV Storage Rings", 5th Low Emittance Rings Workshop, ESRF, Grenoble, France, 2015, http://indico.cern.ch/event/395487/contribution/946547/attachments/1155707/16 61128/MAX_IV_Multipole_Injection_LER2015

42. S.C. Leemann, "Injection with a single dipole kicker into the MAX IV storage rings", Nucl. Instr. and Meth. A **693**, 117 (2012).

43. M. Eriksson et al., "Commissioning of the MAX IV Light Source", Proceedings of IPAC2016, Busan, Korea, p.11.

44. G. Skripka et al., "Commissioning of the Harmonic Cavities in the MAX IV 3 GeV Ring", Proceedings of IPAC2016, Busan, Korea, p.2911.

45. J. Breunlin, Å. Andersson, "Emittance Diagnostics at the MAX IV 3 GeV Storage Ring", Proceedings of IPAC2016, Busan, Korea, p.2908.

46. J. Breunlin, S.C. Leemann, Å. Andersson, "Improving Touschek lifetime in ultralow-emittance lattices through systematic application of successive closed vertical dispersion bumps", Phys. Rev. Accel. Beams **19**, 060701 (2016)

47. S.L. Sörensen, T. Olsson, C. Stråhlman, S.C. Leemann, "Workshop on Timing Modes for Low-Emittance Storage Rings", Synchrotron Radiation News Vol.28, No.5, 2015.

48. C. Stråhlman, T. Olsson, S.C. Leemann, R. Sankari, S.L. Sörensen, "Preparing the MAX IV Storage Rings for Timing-based Experiments", Proceedings of SRI 2015, in print, http://lup.lub.lu.se/record/7791594

49. S.C. Leemann, M. Eriksson, "MAX IV Emittance Reduction and Brightness Improvement", Proceedings of IPAC2014, Dresden, Germany, p.1615.

50. Å. Andersson et al., "The MAX II synchrotron radiation storage ring", Nucl. Instr. and Meth. A **343**, 644 (1994).

51. C.J. Bocchetta et al., "Project Status of the Polish Synchrotron Radiation Facility Solaris", Proceedings of IPAC'11, San Sebastián, Spain, p.3014.

52. S.C. Leemann, "Updates to the MAX IV 1.5 GeV Storage Ring Lattice", MAX-lab internal note 20120904, https://www.maxiv.lu.se/publications/

53. M. Johansson, "Design of the MAX IV/Solaris 1.5 GeV Storage Ring Magnets", Proceedings of IPAC'11, San Sebastián, Spain, p.2430.

54. M. Johansson, "The MAX IV 1.5 GeV Storage Ring Magnet Design", MAX-lab internal note 20130712, https://www.maxiv.lu.se/publications/

55. T. Olsson, S.C. Leemann, "High-chromaticity Optics for the MAX IV 1.5 GeV Storage Ring", Proceedings of IPAC2014, Dresden, Germany, p.30

5.3 Upgrade of the Swiss Light Source storage ring based on a lattice combining longitudinal gradient bends and anti-bends

Andreas Streun, Masamitsu Aiba, Michael Böge, Michael Ehrlichman,

Ángela Saá Hernández, Haisheng Xu

Paul Scherrer Institut, 5232 Villigen, Switzerland

Mail to: andreas.streun@psi.ch

5.3.1 Introduction

The emergence of new or upgraded light source storage rings providing 1-2 orders of magnitude higher brightness and coherent flux than 3rd generation light sources obliges existing facilities, among them the Swiss Light Source (SLS), to consider upgrades too in order to stay competitive in future.

The SLS started user operation in 2001 already. The storage ring is built from 12 triple bend achromats (TBA) in a circumference of 288 m and provides an emittance of 5 nm at 2.4 GeV. An upgrade, called SLS-2, is envisaged for the period 2021-24 and should reduce the emittance by a factor of 30. This enterprise is challenged by the comparatively small circumference of the SLS storage ring, because emittance scales approximately inversely with the 3rd power of the machine circumference.

Longitudinal gradient bends (LGB), i.e. magnets where the bending field varies along the beam path, can provide significantly lower emittance than homogeneous bends, if the optical functions are properly matched. Anti-bends (AB) are small bends of opposite field polarity than the main bend and located in some distance. ABs can bring the optical functions closer to the conditions for lowest emittance in any type of main bend, and in particular, they help to exploit the emittance reduction potential of an LGB in a periodic cell structure. A multi-bend achromat (MBA) based on a LGB-AB-

cell has the potential to realize a compact low emittance lattice, hence it is the most promising candidate for an upgrade of the SLS storage ring.

5.3.2 Concept for a compact low emittance lattice

5.3.2.1 *Equilibrium emittance*

The emittance in a storage ring is determined by the equilibrium between classical radiation damping and quantum excitation. Emission of light in the direction of motion decreases transverse and longitudinal momenta of an electron, while acceleration by the radio-frequency (RF) wave restores only the longitudinal momentum, thus over many turns, the transverse momenta decay exponentially. But light is emitted in photons, taking away discrete quanta of momentum from the electron, and emission occurs only in magnetic fields, which bend particle trajectories depending on the electron momentum, an effect called dispersion. After a sudden momentum transfer to the photon an electron will start an oscillation around a dispersive orbit corresponding to its new momentum due to the presence of a focusing guiding field in the storage ring. Thus noise is introduced into the beam, and this is the source of emittance.

Low equilibrium emittance is achieved by enhancing radiation damping, for example by installation of damping wigglers, and/or by suppression of quantum excitation, which requires suppression of dispersion in regions of strong bending fields. The theoretical minimum emittance (TME) achievable with a periodic lattice cell incorporating one bending magnet of homogenous field has been studied to great detail with the well-known result that the TME scales cubically with the deflection angle of the bending magnet, because in a small bend, the dispersion cannot grow much. However the realization of the TME value leads to an impractical cell with extreme focusing, thus most light sources use relaxed TME-cells providing an emittance which is at least a factor three higher than the TME [1].

5.3.2.2 *Multi-bend achromat lattices with small beam pipes*

Modern light sources are based on MBA lattices using a very large number of rather relaxed TME-cells, such that the cubic scaling with angle over-compensates the relaxation of the conditions for minimum emittance [2]. Accommodation of many cells in a lattice of reasonable circumference requires miniaturization of components. This leads to stronger magnets, in particular quadrupoles and sextupoles: reduced focal length due to reduced cell length increases the quadrupole strength, and stronger quadrupoles and lower dispersion due to shorter cell length increase the sextupole strength. Furthermore, the strength of any magnet increases if the magnet length is reduced. The absolute magnitude of the magnetic field is limited (due to saturation in an iron dominated magnet or due to current density in a superconducting magnet), thus the strength of a $2n$-pole scales with R^{n-1}, where R is the aperture radius. So realization of high magnet strength is achieved by reduction of the beam pipe aperture. MBA lattices have been optimized in this respect until a minimum beam pipe size was reached.

The acceptable minimum beam pipe size depends on careful investigation of several aspects: Touschek scattering beam lifetime usually is not the main problem, because low dispersion in an MBA lattice provides sufficient momentum acceptance even with

small apertures. Realization of ultra-high vacuum is challenged by the low conductance of a small beam pipe, but can be achieved using modern technologies, e.g. coating with non-evaporable getter (NEG) material. The high resistive wall impedance of a small beam pipe gives a low threshold beam current for the onset of beam instabilities and thus may impose a minimum size. Finally, a scheme for off-axis injection, where the injected beam oscillates for thousands of turns around the stored beam until it eventually merges due to radiation damping, requires a minimum aperture. On-axis injection schemes have been developed to overcome this restriction, but they present other challenges like the need for fast kicker magnets or very large momentum acceptance [3], or they require additional investments such as for example an additional accumulator ring [4]. Thus off-axis schemes are not abandoned yet. Efficient and reliable injection is needed for top-up operation, which is a prerequisite for sub-micron stability of electron and photon beams.

5.3.2.3 *Small ring circumference as challenge for an upgrade of the SLS*

In contrast to new facilities, upgrades of existing storage rings are usually constrained to a given circumference. Given a lower limit for the beam pipe size the number of MBA cells is limited and with it the emittance which can be achieved. Also installation of damping wigglers in dispersion free regions for further emittance reduction requires substantial space, which may be available in a former high energy ring [5] but usually not in a 3rd generation light source. Furthermore damping wigglers efficiently reduce the emittance only if they dominate the radiated energy of the lattice, which implies low field of bending magnets and with it longer cells [6].

With 288 m circumference the SLS ring is rather compact for a 2.4 GeV machine, nevertheless an emittance in the 100—200 pm range is envisaged for the upgrade. It is planned to re-use the existing SLS booster synchrotron, which delivers a rather low emittance of only 10 nm at 2.4 GeV [7] and thus is well suited for off-axis injection into a relatively small beam pipe. On-axis injection schemes are considered as options for further upgrades [3].

Scaling existing MBA lattice solutions as established at other places to the SLS energy and circumference does not yield competitive emittances, therefore a new type of compact low emittance lattice was developed.

5.3.2.4 *Longitudinal gradient bends and anti-bends*

Recalling basic principles, quantum excitation is minimized if dispersion is suppressed in regions of high bending field. In the longitudinal gradient bend (LGB) dispersion is focused to virtually zero at a peak of highest field. In the regions before and after the focus, where the dispersion is larger, the field strength is reduced correspondingly. Since the magnetic field B_y is the source of dispersion η, because $\eta'' = eB_y/p$, both quantities are connected, and the longitudinal field variation $B_y(s)$ providing minimum emittance for given initial conditions (e.g. beta-function at focus) and constraints (e.g. maximum peak field, magnet length) can be obtained from analytical or numerical optimization procedures as detailed in [8].

Dispersion η and horizontal beta-function β_x are both subject to horizontal focusing, but the dispersion production of the bending magnet corresponds to a defocusing term

($\eta'' > 0$), so in a conventional lattice cell using only quadrupoles, η receives insufficient focusing whereas β_x is over-focused. This is the basic dilemma of the TME-cell. In order to compensate for the η-defocusing while little affecting β_x a small bending magnet of negative polarity, called anti-bend (AB), is installed out of phase with the main bending magnet: its negative dispersion production provides focusing ($\eta'' < 0$), which after $\approx \pi/2$ of horizontal betatron phase advance will result in a reduction of η at the location, where the main bend is located [9]. This concept is applicable to conventional homogenous bends as well, but it is compulsory for exploiting the low emittance of a LGB in a periodic lattice cell. In a well matched LGB the quantum excitation (as given by the 5th radiation integral I_5) is reduced by almost a factor 3 compared to a homogenous dipole of the same bending angle. Further, taking into account increased radiated power from the longitudinal field variation (for given length and deflection a bend with homogenous field radiates least), an emittance reduction by a factor >5 is possible with technically feasible LGBs [8].
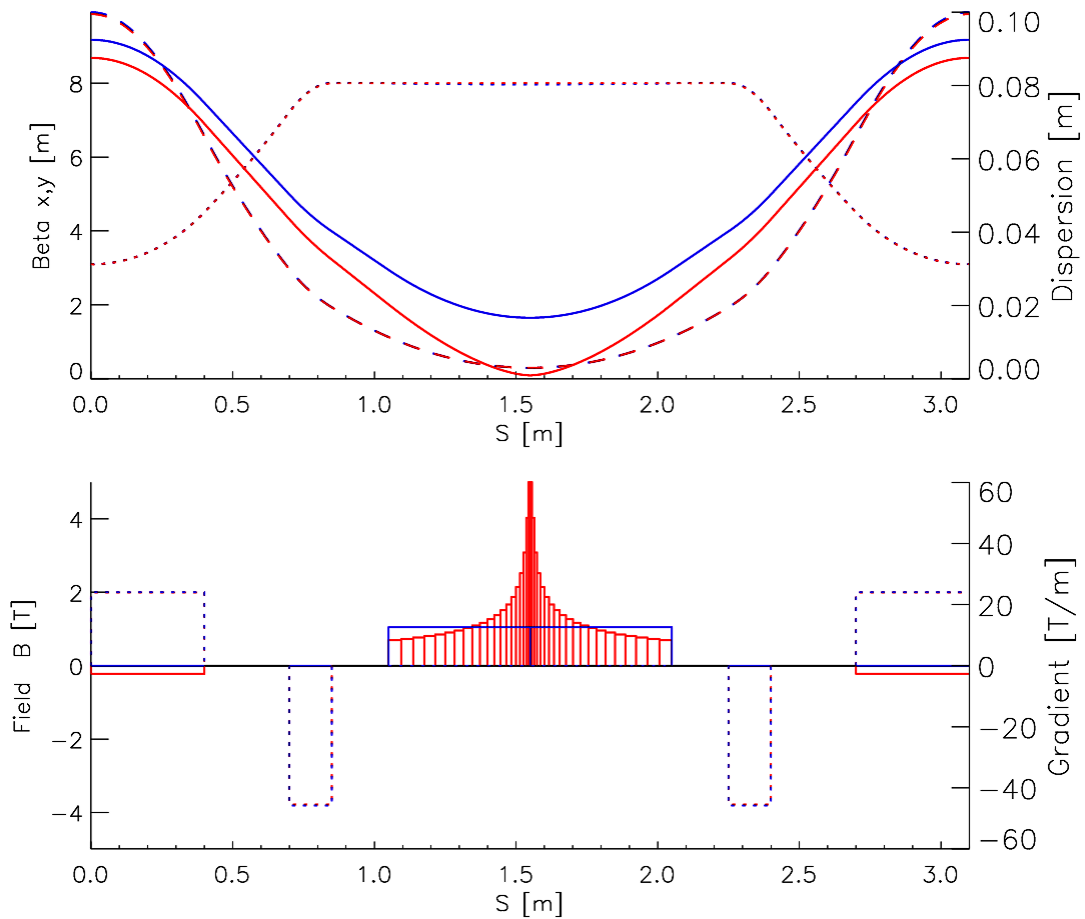
Figure 1: Comparison of a LGB/AB-cell (red) with a relaxed TME-cell (blue). The upper plot shows the optical functions (—— η, - - - β_x , $\cdots \beta_y$), the lower plot shows the magnet dipole field and gradient (—— B_y , $\cdots$ dB_y/dx).

In a lattice cell combining LGB and ABs, two effects impair the gain in emittance: the ABs, located at large dispersion, contribute to the radiation integrals too, and the

bending angle of the LGB has to be increased to compensate for the negative angles of the ABs. Nevertheless, an LGB/AB-cell may provide substantially lower emittance as illustrated in the academic example of Figure 1, comparing optical functions and magnet fields of a relaxed TME-cell and a LGB/AB-cell of same length 3.1 m, total bending angle 6.0° and cell tunes 0.428/0.087. The two AB magnets of −0.5° deflection suppress the dispersion at the cell midpoint, where the field peak of the 7°-LGB is located, while marginally affecting the beta functions. The 5th radiation integral thus is reduced by a factor 1.9 compared to the relaxed TME-cell. The radiated energy increases by another factor 1.9 due to the higher field of the LGB and due to the increase of the total absolute bending angle from 6° to 8°. The horizontally focusing gradient in the AB increases the horizontal damping partition number J_x from 1 to 1.33. In total these factors result in an emittance reduction by a factor 4.8, from 1.15 nm to 0.24 nm at 3 GeV in this example.

High dispersion and negative field in the ABs and low dispersion in the LGB cause a negative and rather small momentum compaction factor α. In this example it is reduced from $+7.1 \cdot 10^{-4}$ to $-2.2 \cdot 10^{-4}$. $\alpha < 0$ provides head-tail stability at negative chromaticity, but small $|\alpha|$ results in short bunches and requires care with regard to intra-beam scattering (IBS) and microwave instability.

5.3.3   The SLS upgrade lattice

5.3.3.1   *LGB/AB-cell based MBA*

The existing SLS storage ring is made from 12 TBA arcs. A new MBA (an arc with M bending magnets) replacing the TBA has to fulfill several, partially conflicting constraints:

1. The net deflection angle is 30° and the length ≈17 m. This is determined by the storage ring footprint.

2. The emittance should be around 150 pm. This requires a large number M or/and a high horizontal cell tune $\Delta \nu_x$.

3. The beam pipe diameter should be at least 20 mm in order to limit the resistive wall impedance. This is also compatible with off-axis injection and the needs for ultra-high vacuum. This limits the magnet gradients and thus increases the cell length.

4. The momentum acceptance should be at least 5% to obtain sufficient Touschek lifetime, this limits the maximum dispersion, which decreases with increasing number M.

5. Non-linear optics has to be considered from the beginning, since small dispersion results in strong sextupoles for chromaticity correction: all first order and most second order sextupole resonance driving terms should cancel by phase over the $(M-2)$ regular cells (the two dispersion suppressor cells at the ends of the arc have different optical functions). This requires for the cell tunes that $\Delta \nu_x$, and $2\Delta \nu_y$ are integer multiples of $1/(M-2)$.

6. Since beam lines are attached to most center dipoles of the TBAs, an odd number M is preferable to have a dipole in the arc center again.

For $M = 7$ all constraints can be fulfilled if the LGB/AB cell is used. Cell tunes $\Delta\nu_{x/y}$ of 0.4/0.1 provide resonance cancellation over 5 cells, while $\Delta\nu_x = 0.4$ is suitable to provide low emittance at moderate focusing. The LGB profile is optimized to provide minimum emittance for given values of η and β_x at the LGB center from the periodic solution with $\Delta\nu_x = 0.4$. In the base cell of Fig. 2 (left) the LGB field was limited to 2 Tesla. The low field (<1 Tesla) near the LGB edges leaves margin to introduce a transverse gradient for vertical focusing in order to save space, and to further lower the emittance by increasing J_x. Therefore the edge regions are separate pole pieces, which are enclosed by a common coil with the center LGB pole. Any of the LGBs can be exchanged by a super-LGB of 5-6 Tesla peak field as shown in Fig. 2 (right). To maintain the cell tunes a tiny adjustment of focusing (<0.5%) is done by pole face windings in the adjacent transverse gradient bends and anti-bends. The existing SLS has three super-bends of 2.9 Tesla peak field, and it is planned to have three super-LGBs at the same locations in the upgraded lattice. The high peak field would provide a brilliant source of hard X-rays, extending the photon range of the SLS up to 100 keV.
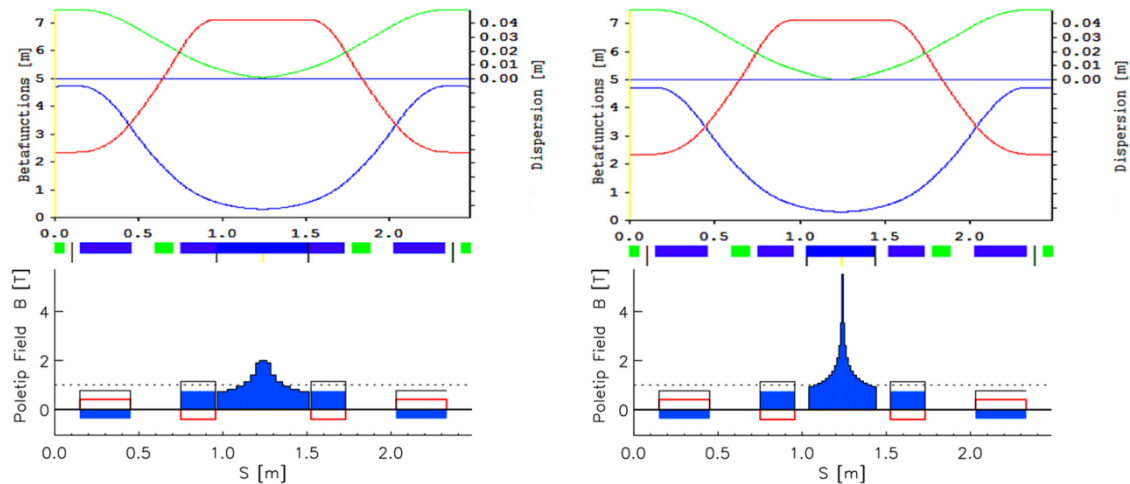
Figure 2: the LGB/AB-cell for the SLS upgrade. Optical functions (η, β_x, β_y) and magnet field component B_y at $x = 13$ mm (dipole, quadrupole, total). The left figure shows the standard cell, the right figure a cell containing a super-LGB.

5.3.3.2 *Lattice layout*

When the SLS was designed in the late 1990s it had to serve a small but heterogeneous user community. To fulfill all needs the lattice was equipped with short (4 m, S), medium (7 m, M) and long (11.5 m, L) straight sections alternating as L-S-M-S in one of three super-periods. In the meantime the demand for long straights ceased, therefore they are turned into double straights for installation of canted or twin undulators. This also alleviates matching the optics. The upgrade lattice thus will provide 6 straights of about 3 m length and 9 straights of 5 m length. Figure 3 shows the optical functions for one super-period of the new lattice and Table 1 lists the most important parameters. The transverse and longitudinal positions of all undulators can be

maintained exactly if the the lattice circumference is reduced by 0.75 m and if the straight lengths are adjusted appropriately. However, the bending magnets in the arc centers will move in radially by 0.22 m and the beam lines have to be aligned accordingly. It is not possible to maintain all source points because the new lattice is closer to a circle than the old one due to the larger number of bends. The reduction of circumference requires −260 kHz detuning of the 500 MHz cavities by inelastic deformation and switching from harmonic number 480 down to 479. This complicates the timing system for injection, because the booster RF cannot be changed.
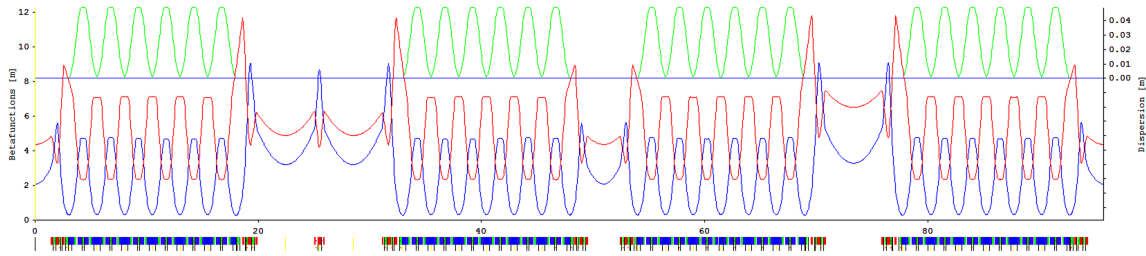
Figure 3: Optical functions for one super-period of SLS-2 (η, β_x, β_y) .

Table 1: Main parameters for the SLS upgrade lattice. The arrow ($\rightarrow$) indicates the increase due to IBS for 400 mA current in 400 bunches, assuming 10 pm of vertical emittance and stretching the bunches to 67 ps FWHM by means of a third harmonic RF-system.

Circumference [m]	287.25	Energy [GeV]	2.4
Working point $\nu_{x/y}$	37.38/10.28	Energy loss/turn [keV]	579
Chromaticities $\xi_{x/y}$	−65.0/−34.5	Emittance [pm]	137 $\rightarrow$ 150
Momentum compaction α	−1.41·10^{-4}	Energy spread [·10^{-3}]	1.03 $\rightarrow$ 1.08
Hor. damping partition J_x	1.76	Damping times $\tau_{x/y/E}$ [ms]	4.5/7.9/6.4

An alternative layout would be a period-12 lattice with 12 identical straight sections of 5–6 m length which meets well today's user needs and supports standardization of components. With regard to dynamic acceptance optimization a higher periodicity is advantageous because only few systematic resonances appear in the tune diagram. An increase of the circumference to 290.4 m, corresponding to a 4 units higher harmonic number without detuning the RF, would almost maintain the radial undulator positions at the present S- and M-straights. The undulators in the present L-straights however would move out radially by 1.7 m, which requires a modification of the storage ring tunnel. Evaluation of alternatives is in progress.

5.3.3.3 *Nonlinear Optimization*

The natural chromaticity of the lattice is moderate since the LGB/AB cell provides low emittance at relatively relaxed optics, and thanks to the negative momentum compaction factor, chromaticity would be set to negative rather than positive values for suppression of beam instabilities. Nevertheless chromaticity correction is challenged by small dispersion, which results in strong sextupoles. Drive terms for first order and some second order resonances are largely suppressed by the cell tunes as mentioned above, however higher order chromaticity and amplitude dependent tune shifts require more non-linear elements: the lattice contains 4 chromatic sextupole families and 1 chromatic octupole family located inside the MBA arcs, and 3×3 harmonic sextupole and octupole families located in the matching sections for the 3 different types of straights.

A tracking based multi-objective genetic algorithm (MOGA) was developed for direct optimization of on- and off-momentum dynamic acceptances, which makes extensive use of quickly computable quantities like chromatic tune-footprint to speed up the first phase of evolution, before switching to the computationally more intensive objectives of tracked dynamic apertures. MOGA delivers a set of solutions. From these, some were picked and tested for robustness to misalignment by further tracking studies. An on-momentum dynamic aperture of at least $(\pm 4)\times(\pm 5)$ mm^2 was obtained for all error seeds, which corresponds to 65% of the available linear aperture (projection of beam pipe to track point, not including undulator gaps) [10].

The horizontal acceptance is sufficient for off-axis injection based on a non-linear kicker: Figure 4 shows injection of the beam coming from the existing SLS booster synchrotron. The off-momentum dynamic apertures provide sufficient beam lifetime: Figure 5 shows the momentum acceptance obtained from 6D-tracking as a function of lattice position. It results in 4.5h of Touschek lifetime for the ideal lattice and >3.6h for 95% of the error seeds.

Error seeds assumed grouping of elements onto 48 girder, which are displaced by 50μm (rms, cut 2 sigma) and tilted by 50 μrad, while the elements relative to the girders are displaced by 20 μm and tilted by 50 μrad.
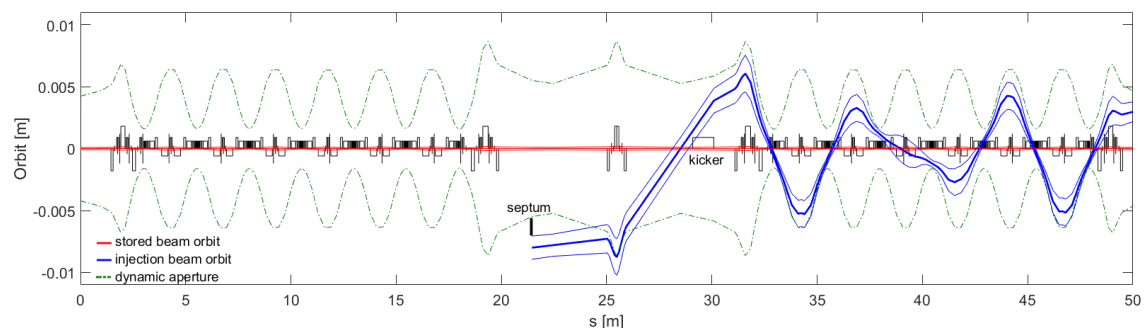
Figure 4: Injection study, showing the 5-sigma envelopes for stored and injected beam. The multipole kicker has to provide 1.5 mrad kick at 4 mm offset to keep the betatron oscillations within the dynamic aperture ($- \cdot - \cdot$) until damped.
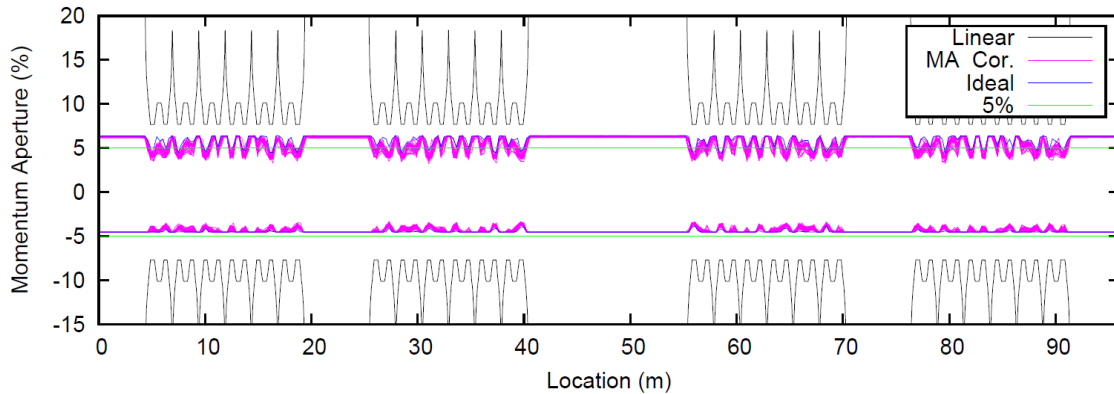
Figure 5: Momentum acceptance for one super-period of SLS-2: black ("Linear") linear acceptance; blue ("Ideal") non-linear acceptance of the error-free lattice;

purple ("MA Cor.") 30 misaligned lattices with orbit correction; green ("5%"): RF- acceptance for a cavity voltage of 1.41 MV at 500 MHz. Figure from Ref. [10].

5.3.4 Technology

Work is in progress on vacuum systems, magnets, girders and RF systems [11].

The beam pipe will be a round tube of 20 mm inner diameter probably made from copper plated stainless steel. Absorbers and a large number of small discrete pumps will be attached to an antechamber, which is connected to the beam pipe by a continuous slit. NEG-coating of the vacuum chamber is not foreseen since NEG has rather large resistive wall impedance, and activation of the coating requires local heaters or a complicated procedure to remove the magnets.

First designs for the LGBs and also for the super-LGBs have been established. The longitudinal field profile of a realistic magnet deviates slightly from the ideal profile providing minimum emittance. For the normal LGBs the effect on emittance is <2%. The 6 Tesla super-LGB is designed as a warm bore superconducting dipole. Due to the large magnet aperture it is difficult to realize a narrow high field peak as requested, nevertheless, the emittance increase due to three super-LGBs in the lattice would amount to <4% and has been included in Table 1.

The SLS storage ring is equipped with a dynamic alignment system based on 48 girders, which can be moved remotely with stored beam. It is considered to re-use this system and mount the new magnets, which will be smaller than the existing ones, on intermediate support blocks. With expected alignment tolerances of 20 μm rms for elements relative to girders and 50 μm for girders relative to the laboratory, an orbit correction based on 150 beam position monitors and 150 combined horizontal/vertical correctors results in a maximum corrector strength of <0.3 mrad and dynamic acceptances as shown in the previous section.

222

A low RF of 100 MHz as chosen in other places provides no significant advantage with regard to single bunch instabilities [12], therefore it is planned to re-use the existing 500 MHz system. A 3rd harmonic RF-system will be required, but it has not yet been decided if the existing passive system should be replaced by an active system to get better control of bunch lengthening and Landau damping.

5.3.5 Conclusion

Work is in progress for an upgrade of the SLS storage ring. The lattice provides about 150 pm emittance at 2.4 GeV and fits in the existing circumference of 288 m. Confidence has been acquired, that the lattice acceptances will be sufficient for off-axis injection and to provide several hours of beam lifetime even in the presence of misalignments.

5.3.6 Acknowledgements

This paper has a focus on beam dynamics and lattice design, but many colleagues at PSI are involved in the design of the SLS-2 storage ring and its technical subsystems. For the magnets, these are Ciro Calzolaio, Philippe Lerch, Marco Negrazus, Stephane Sanfilippo and Vjeran Vrankovic, for the RF-system Lukas Stingelin and Paolo Craievich, for the cryogenics Alexander Anghel, for impedances and instabilities Micha Dehler, for the vacuum system Andreas Müller and Lothar Schulz and for the general layout and project organization Uwe Barth, Terence Garvey, Lenny Rivkin and Albin Wrulich.

5.3.7 References

1. S. C. Leemann and A. Streun, "Perspectives for future light source lattices incorporating yet uncommon magnets", Phys. Rev. ST Accel. Beams 14, 030701 (2011).

2. M. Eriksson, L.-J. Lindgren, M. Sjöström, E. Wallén, L. Rivkin, A. Streun, "Some small-emittance light-source lattices with multi-bend achromats", Nucl. Instr. and Meth. A 587, 221-226 (2008).

3. M. Aiba, M. Böge, F. Marcellini, Á. Saá Hernández, and A. Streun, "Longitudinal injection scheme using short pulse kicker for small aperture electron storage rings", Phys. Rev. Accel. Beams 18, 020701 (2015).

4. M. Borland, "Concepts and performance for a next‐generation storage ring hard x-ray source", AIP Conf. Proc. 124, 911 (2010).

5. K. Balewski, W. Brefeld, W. Decking, Y. Li, G. K. Sahoo and R. Wanzenberg, "PETRA III: a new high brilliance synchrotron radiation source at DESY", Proc. EPAC 2014, Lucerne, Switzerland (2004).

6. W. Guo and F. Willeke, "Emittance reduction approaches for NSLS-II", Proc.

PAC 2011, New York, NY, USA (2011).

7. W. Joho, M. Muñoz, A. Streun, "The SLS booster synchrotron", Nucl. Instr. and Meth. A 562, 1-11 (2006).

8. A. Streun and A. Wrulich, "Compact low emittance light sources based on longitudinal gradient bending magnets", Nucl. Instr. and Meth. A 770, 98–112 (2015).

9. A. Streun, "The anti-bend cell for ultralow emittance storage ring lattices", Nucl. Instr. and Meth. A 737, 148–154 (2014).

10. M. P. Ehrlichman, "Genetic algorithm for chromaticity correction in diffraction limited storage rings", Phys. Rev. Accel. Beams 19, 044001 (2016).

11. A. Streun, M. Aiba, M.Böge, C. Calzolaio, M. Ehrlichman, A. Müller, Á. Saá Hernández, H. Xu, „Proposed upgrade of the SLS storage ring", Proc. IPAC 2016, Busan, Korea (2016).

12. H. Xu, M. Dehler, P. Craievic, L. Stingelin, „Study of microwave instability for SLS-2", Proc. IPAC 2016, Busan, Korea (2016).

5.4   Lattice Design and Commissioning of Taiwan Photon Source

Chin-Cheng Kuo

Mail to: cckuo@nsrrc.org.tw

NSRRC, Hsinchu Science Park, Hsinchu 30076, Taiwan

5.4.1   Introduction

This article presents an overview of the lattice design and the results of commissioning of Taiwan Photon Source (TPS), a large-scale medium-energy synchrotron-accelerator facility in Hsinchu, Taiwan. TPS has entered the stage of user operation and commissioning of the photon beamline since its first synchrotron light in 2014 December.

The TPS accelerator system consists of a 150-MeV linear accelerator, a 3-GeV booster synchrotron and a 3-GeV storage ring. The circumferences of the storage ring are 518.4 m and of the booster ring 496.8 m, installed inside the same tunnel. Before the construction of TPS, 1.5-GeV Taiwan Light Source (TLS) was established on the same campus and operated for more than two decades, since 1993. TLS has served both domestic and foreign users; the scientific output has been fruitful, but, for the future development of research with synchrotron radiation in Taiwan, a feasibility study to construct a medium-energy synchrotron ring was initiated in 2004. TPS was consequently proposed to the government in 2005 and officially approved in 2007.

A key feature of the TPS design is that the photon brightness can be one thousand times that of the existing TLS in the X-ray region. It is envisaged that TPS will further cultivate advanced research with synchrotron radiation in Taiwan.

In the evolution of the parameters of the TPS accelerators, the existing buildings of NSRRC imposed a major constraint on the ring size. To cope with such a challenge, a concentric booster ring, sharing the same tunnel with the storage ring, was adopted. Figure 1 shows an aerial view of TPS with existing buildings at the NSRRC site and a photograph inside the TPS tunnel.

The lattice design of the 3-GeV TPS has been reported [1-3]. The work on the lattice design in the storage ring and the booster injector is described here; the results of commissioning are also given in this report.

Figure 1: Aerial view of TPS and TLS at the NSRRC campus (left) and a photograph inside the TPS tunnel (right)

5.4.2   Design of the Storage Ring

The main goal in designing TPS is to obtain photon sources with extremely high brilliance and high flux covering a wide range of spectrum, from various magnets, such as dipoles, or insertion devices (IDs). The recent, advanced, third-generation, light sources have been shown to be designed at an energy about 3 GeV. These medium-energy light sources require a smaller budget for construction and can provide diverse photon energies with high photon brilliance and flux from advanced IDs.

The design goals for TPS were (1) energy 3 GeV, (2) high brilliance $\sim 10^{21}$ photon s^{-1} mm^{-2} $mrad^{-2}$ per 0.1% ($\Delta\lambda/\lambda$), (3) great flux with maximum beam current 500 mA, (4) emittance < 2 nm-rad, (5) a long beam lifetime, (6) operation in top-up mode, and (7) many straight sections for IDs.

5.4.2.1   *Lattice Structure*

Magnet lattice structures of several types and varied circumferences of the storage ring were explored. Although a multi-bend achromat (MBA) lattice structure was studied, the technical constraints prevented further investigation at the design stage. We eventually decided to adopt a double-bend achromat (DBA) lattice structure.

A structure of circumference 518.4 m with 24-cell DBA was adopted. For such a ring, it is possible to obtain a realistic horizontal natural beam emittance < 2 nm-rad with a distributed dispersion configuration. The linear optical functions are matched to fulfill the requirements for a small natural emittance and a small photon beam. Straight sections of suitable lengths are desired for the installation of injection elements, IDs and other components. Various options with varied periodicities were studied. A six-fold symmetric configuration provides six long straight sections to accommodate injection elements, long IDs etc. The working point is in a satisfactory region away from structural resonances and has a satisfactory emittance value. The lattice optical functions are depicted in Fig. 2; the major lattice parameters are listed in Table 1.
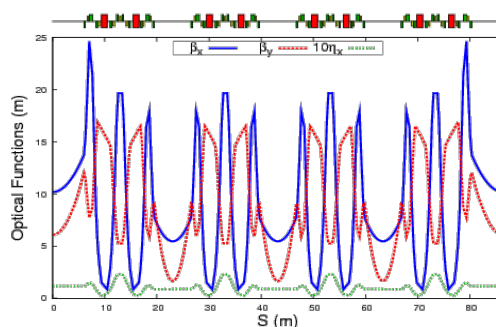
Figure 2: Optical functions of the lattice of the TPS storage ring

Table 1: Major parameters of the TPS storage ring

circumference /m	518.4
energy /GeV	3.0
natural emittance /nm-rad	1.6
straight section	12m*6+7m*18
radio frequency /MHz	499.654
harmonic number	864
SR loss/turn, dipole /MeV	0.85269
betatron tune, ν_x, ν_y	26.18, 13.28
momentum compaction , α_1, α_2	$2.4\times10^{-4}, 2.1\times10^{-3}$
natural energy spread	8.86×10^{-4}
damping partition J_x, J_y, J_s	0.9977,1.0, 2.0023
damping time τ_x,τ_y,τ_s /ms	12.20,12.17, 6.08
natural chromaticity, ξ_x, ξ_y	-75, -26

5.4.2.2 *Dynamic and Energy Aperture*

For a strongly focused and small-emittance lattice structure, large chromatic aberrations induce negative natural chromaticities; these negative chromaticities must be corrected to be slightly positive using chromatic sextupoles. Basically, in the single-resonance approach, to first order of sextupole strengths, there are four first-order chromatic terms and five first-order geometric terms in the Hamiltonian for the motion of a single particle; there are also 13 second-order driving terms in the Hamiltonian for the motion of a single particle [4]. We sought to minimize these terms, using various sophisticated codes for nonlinear optimizations and for particle tracking; these codes are OPA, BETA, Tracy-2, MAD, elegant etc. [5-9]. We adopted a scheme with six families of harmonic sextupoles together with two-family chromatic sextupoles, i.e., a scheme of eight-family sextupoles. The dynamic aperture (DA) is observed to be highly sensitive to the location and to the strength of sextupole magnets, the distribution of the optical functions etc. An iterative process between linear and nonlinear configurations was required to achieve an acceptable DA for on- and off-energy particles. Figure 3 show plots of the betatron tune shifts with horizontal and vertical amplitudes for the configuration.
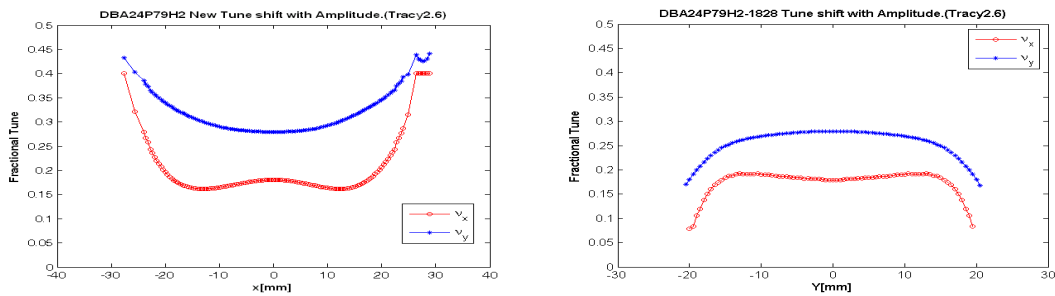
Figure 3: Betatron tune shifts with horizontal amplitude (left) and vertical amplitude (right) at the center of long straight sections

Betatron tune shifts with energy should be minimized to ensure a maximal energy acceptance, although the nonlinear synchrotron motion due to a nonlinear energy oscillation in the longitudinal plane might be the dominant factor in the energy acceptance. In the case of the present configuration, we sought an energy acceptance in a range from –4 % to 4 % without taking nonlinear energy oscillation into account. Figures 4 shows the betatron tune shifts with energy.

Figure 5 shows the DA at the center of the long straight section with 1024-turn particle tracking. With Tracy-2, we obtained a plot of tune diffusion during the DA tracking; Figure 6 presents the corresponding frequency-map analysis (FMA) in tune space. The rate of tune diffusion is defined as $D = \log_{10}((\Delta\nu_x)^2 + (\Delta\nu_y)^2)^{1/2}$, in which $\Delta\nu$ is the tune change in the first and second 512-turn particle tracking at varied initial amplitudes. FMA reveals the behavior of the beam dynamics and assists to identify dangerous resonance lines.
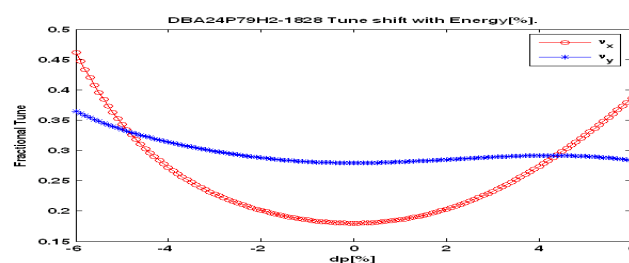
Figure 4: Tune shifts with energy
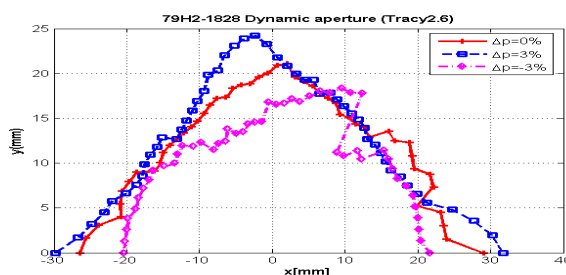
Figure 5: DA at the long straight center (on energy, ±3 % off energy); synchrotron oscillation is not included.

The effects of errors of the magnetic field include orbit distortions, tune shift, shrinkage of the DA etc. Typical error tolerances are about 10^{-4} for higher-order multipoles with respect to the main fields at radius 25 mm. With these errors of the magnetic field, we can obtain the DA using tracking codes. An acceptable DA for on- and off-energy particles is necessary.
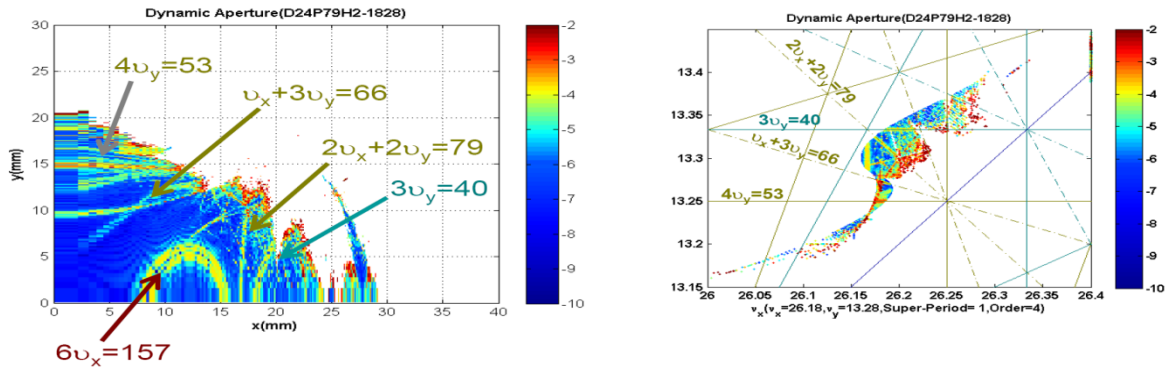
Figure 6: Tracking (Tracy-2) at the long straight center for on-energy particles (left); the diffusion of particles is evident. The rate of tune diffusion is defined as $D = \log_{10}((\Delta v_x)^2 + (\Delta v_y)^2)^{1/2}$; Δv is the tune difference between the first and second 512 turns. Red indicates a rate of diffusion greater than blue. The corresponding FMA (right).

5.4.2.3 *Closed Orbit and Coupling Correction*

Typical errors that generate closed-orbit distortions (CODs) are tight: rms errors are magnet to girder 0.03 mm, girder to girder 0.1 mm, dipole field 0.001, roll 0.1 mrad and BPM 0.1 mm. With all correctors (built in sextupoles), i.e., 168 in each plane, one can decrease residual orbits to 0.1 mm rms with respect to an ideal orbit for the case without BPM beam-based alignment (BBA). The maximum corrector strength is 1.0 mrad. With BBA, the residual orbits are tens μm rms with respect to quadrupole centers. The maximum corrector strength is decreased to 0.5 mrad.

The entire ring contains more than 96 skew quadrupoles (built-in sextupoles) so that the emittance-coupling ratio can be decreased to less than 1 % with skew strength no more than 0.2 T m^{-1} inside 25-cm sextupole magnets in the case of typical coupling errors (rms dipole roll 0.2 mrad, quadrupole roll 0.1 mrad, quadrupole and sextupole displacement 0.1 m.

5.4.2.4 *Effects in the Presence of Insertion Devices*

More than 20 straight sections can accommodate IDs to generate highly brilliant sources of synchrotron light. In the first phase of operations, seven in-vacuum undulators (IUs) and three elliptically polarized undulators (EPUs) were installed.

By using all quadrupoles for the optics and advance correction of the phase in the presence of IDs, the beta-beats become corrected to less than a few per cent and tune and phase advances are restored. The nonlinear kick map (from RADIA code) was used for dynamic tracking with Tracy-2 [10]. We obtained the on-energy DA tracking and the corresponding FMA for the condition with ID chamber aperture limits, 1 % emittance coupling and multipole errors, shown in Fig. 7.
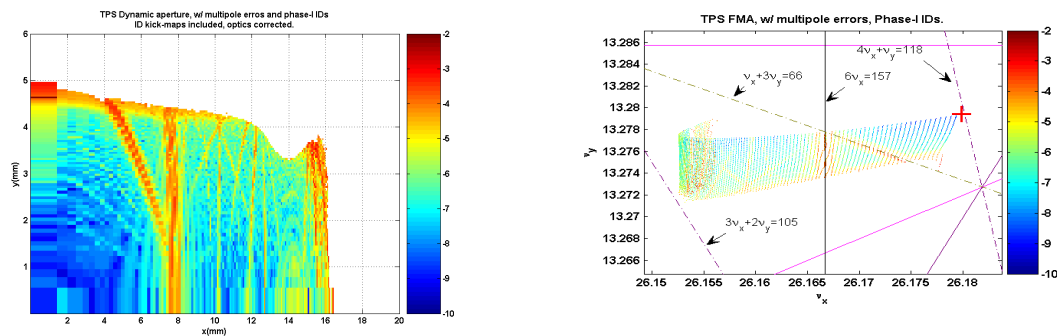
Figure 7: (left) DA (on energy) at long straight center with ID, multipole errors, 1 % emittance coupling, ID kick maps, and ID chambers. (right) Corresponding FMA.

Table 1 indicates that a large α_2 in the nominal lattice configuration induces a nonlinear longitudinal motion and a distortion in longitudinal phase space. Figure 8 shows the energy acceptance simulated with Tracy-2 and the corresponding Touschek lifetime.
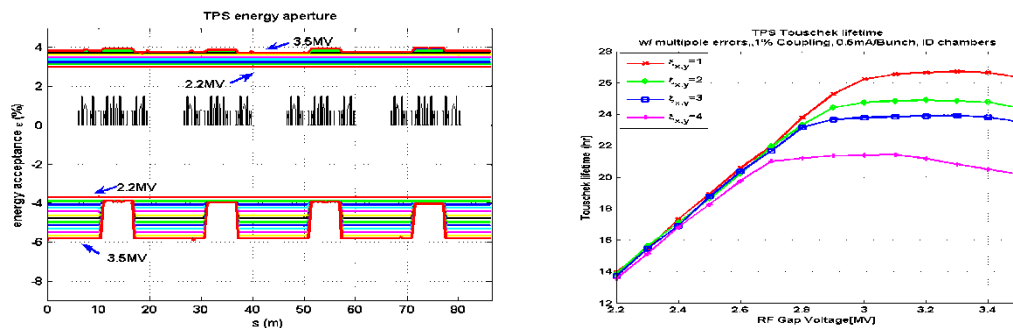
Figure 8: (left) Energy aperture for RF gap voltage from 2.2 MV to 3.5 MV with vertical ID chambers, multipole errors and 1 % betatron coupling. 6-D particle tracking was performed with Tracy-2. Chromaticities are 2.0 in both planes. (right) Touschek

lifetime as functions of RF gap voltages and chromaticity settings using Tracy-2 and the Bruck formula: bunch current 0.5 mA, ID vertical chamber inner aperture 7 mm, multipole field errors and betatron coupling 1% assumed in the simulations.

5.4.2.5   *Alternative Lattices*

The TPS lattice can be configured for several modes. Strong-field ID can cause an increased emittance and energy spread for low emittance mode 1.6 nm-rad. The lattice can be operated at slightly greater emittance in which dispersion functions in the straight sections can be decreased and the emittance changes due to strong-field ID can be minimized. The small α mode (momentum compaction, as small as 10^{-6}) provides a short bunch in a few ps with the optics shown in Fig. 9 [11].
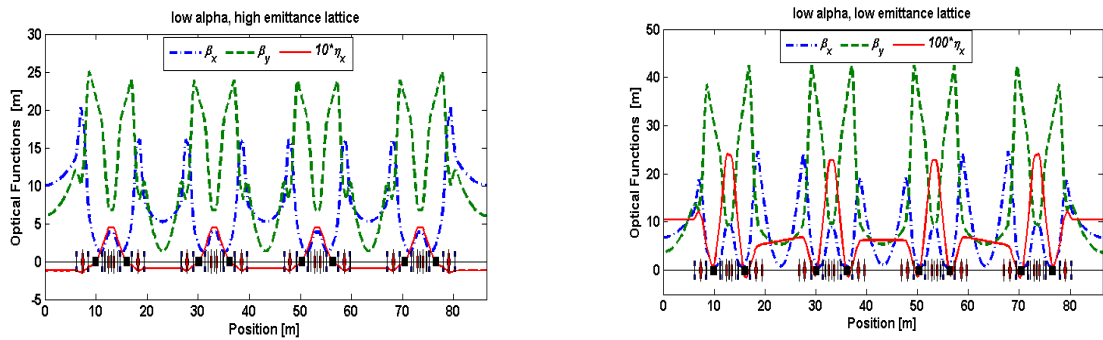
Figure 9: Small alpha lattice: $\alpha_1 = 10^{-6}$, $\varepsilon_x = 32$ nm-rad (left). $\alpha_1 = 2 \times 10^{-5}$, $\varepsilon_x = 2.5$ nm-rad (right).

Three double-vertical waists in three long straight sections are for two mini-gap IDs in each long straight section [12]. Figure 10 shows the optics and the DA-tracking result with IDs, 1 % coupling and magnet multipole errors. The Touschek lifetime calculated from the momentum-acceptance tracking with Tray-2 for Phase-I IDs is more than 12 hr.
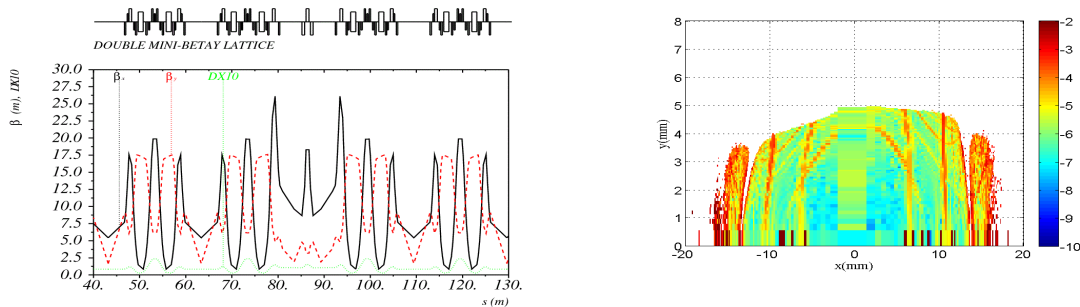
Figure 10: Double mini-β_y lattice functions (left). DA (on energy) tracked at one normal long straight center (β_x=10 m, β_y=6 m) with 1 % coupling multipole errors and IDs.

5.4.3 Injector

The injector comprises a 150-MeV linac, and a 3-GeV booster of circumference 496.8 m. The design concept of the TPS booster is similar to those of SLS and ALBA. The lattice has six superperiods, each containing seven modified FODO cells and two matching cells. Combined-function magnets are used in the booster lattice to decrease the number of magnets. Each superperiod has seven 1.6-m and two 0.8-m combined function dipoles; the natural horizontal emittance is 10 nm-rad. The embedded sextupoles in the combined-function magnets can correct chromaticity to (+1,+1). Separated function quadrupoles in the matching cells are used for optical matching; the independent sextupoles are used for chromaticity adjustment to compensate for the induced sextupole terms from the dipole-chamber eddy current during energy ramping. Satisfactory behavior of the nonlinear beam dynamics is shown in the dynamic tracking. The rate of booster ramping is 3 Hz; the emittance and energy spread can attain design values at extraction energy 3 GeV. Figure 11 shows the lattice optical functions; Table 2 gives the booster parameters [13].

The booster closed-orbit correction scheme comprises 60 BPM, 60 horizontal and 36 vertical correctors. In each modified FODO cell, the horizontal corrector and BPM are placed near a quadrupole magnet so that these three separate elements can share the same girder. Assuming 0.15-mm misalignment errors for quadrupole magnets, 0.15 mm for dipole magnets in the vertical plane, 0.2 mm for dipole magnets in the horizontal plane and 0.2 mrad for all magnet roll errors, the rms CODs are 2.8, 1.5 mm and maximum values are 10.5, 8.1 mm, both in planes x, y, respectively. The corrected orbits can be decreased to less than 0.1 mm (rms); the maximum corrector strengths are less than 0.3 mrad in both planes. The number of BPM and correctors can be decreased while still maintaining an acceptable level of residual orbit. The magnet size is minimized; the bore radius is 18 mm for quadrupole and sextupole magnets. With typical multipole errors and eddy-current-induced chromaticities included and corrected to (+1,+1), the DA as shown in Fig. 11 is large relative to the small chamber of elliptical full size 35 x 20 mm^2.
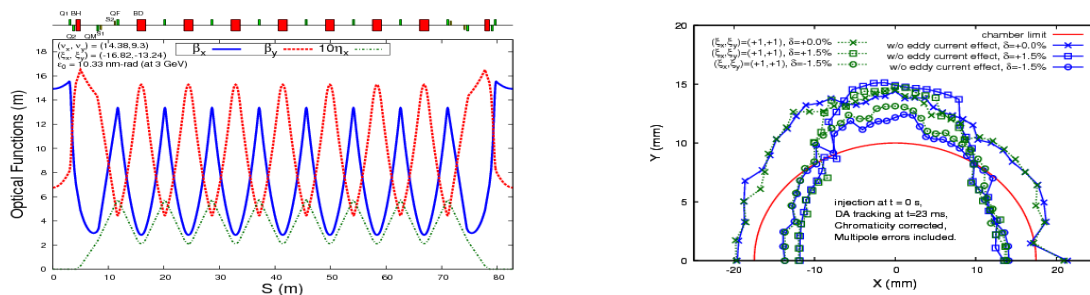
Figure 11: Lattice optical functions of the TPS booster ring (left). DA at the long straight center of the TPS booster with eddy-current effect and multipole errors (right). The bore radius of the quadrupole and sextupole magnets is 18 mm.

Table 2: Major parameters of the TPS booster ring

injection energy /MeV	150
extraction energy /GeV	3
circumference /m	496.8
harmonic number	828
betatron tune, ν_x, ν_y	14.37, 9.41
energy spread at 3 GeV	0.001
natural emittance at 3 GeV /nm-rad	10.3
momentum compaction	0.0025
damping partition, J_x, J_y, J_e	1.8, 1.0, 1.2
damping time, τ_x, τ_y, τ_e, at 3 GeV /ms	9.3, 17.0, 14.3
natural chromaticity, ξ_x, ξ_y	-16.9, -13.3
synchtrotron radiation loss/ turn at 3 GeV /keV	586
combined dipole magnets, B/T, B'/T m^{-1}, B'' /T m^{-2}, at 3 GeV	0.819, 1.73, 12.37
combined quadrupole magnets, B' /T m^{-1}, B'' /T m^{-2}, at 3 GeV	11.27, 25.75

The energy of the linac (delivered by Research Instruments) is 150 MeV. The LTB consists of one 10° dipole and 10 quadrupole magnets for optical matching. The total length is less than 22 m. As both booster and storage rings are in the same tunnel, the BTS line is minimally short, less than 25 m. Other than extraction and injection elements, there are two dipole and seven quadrupole magnets for optical matching.

5.4.4 **Commissioning**

The installation of TPS was completed and the beam test began in 2014 August. Excessive permeability of the stainless-steel chambers made difficult obtaining a stored beam at 150 MeV during testing of the booster beam. These small elliptical chambers that were cold-drawn during manufacture caused field error ten times the tolerances at injection energy 150 MeV, which resulted in a small DA and difficulty in correcting the orbit. For this reason we were unable to obtain a stored beam at 150 MeV. After heat treatment of the chambers to 1050 $^{\circ}$C and a reassembly of the vacuum tubing, the beam test resumed in mid December; we immediately obtained a stored beam. The beam

energy was ramped to 3 GeV within a few days. The CODs were corrected to less than 1 mm. The measured optics agreed satisfactorily with the model values, as shown in Fig. 12. We measured also the emittance evolution during ramping; the results were consistent with the calculations [14,15].
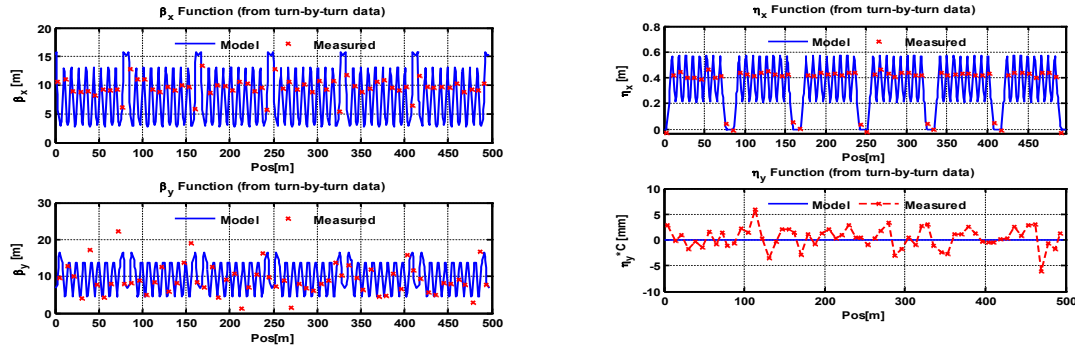
Figure 12: Comparison of model and measured betatron functions (left) and dispersion functions (right) in the TPS booster ring. BPM turn-by-turn data at 150 MeV were used.

The beam injection into the storage ring began on December 26. Due to leakage fields of the booster extraction septum, we injected a 1.5-GeV beam instead and a stored beam was achieved the next day. After repairing the septum problem, a 3-GeV, 5-mA stacked beam was obtained and the first 3-GeV synchrotron light was observed on 2014 December 31 [15].

The Phase-I commissioning of the storage ring was completed by the end of 2015 March. With two normal-conducting cavities (5-cell PETRA cavities), the beam current was limited to 100 mA. In this phase, there was no ID; dummy chambers of 20 mm in vertical were installed in the straight sections. We conducted machine tests and optimization; the topics included the optics correction, coupling correction, closed-orbit correction, energy acceptance, impedance and cure of instabilities, vacuum conditioning etc. [16].

About four months were required to install ten Phase-I IDs and SRF modules from April until August. The Phase-II commissioning of the storage ring began in mid September. The stored beam attained 520 mA on 2015 December 12. All Phase-I IDs have been tested; the associated beamlines have been commissioned [17]. Several topics of beam commissioning follow.

5.4.4.1 *Closed Orbit*

Using 166 BPM and 168 correctors in each plane, CODs were corrected. The machine-orbit response was initially found to be inconsistent with the model in the

horizontal plane; the quadrupole model required modification. With LOCO and BBA, we obtained BPM offsets with respect to the quadrupole centers, shown in Fig. 13 [18].
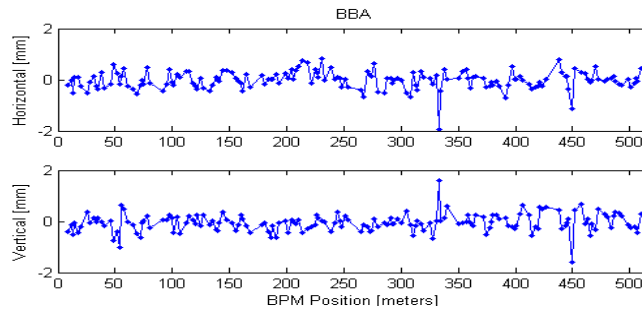
Figure 13: BPM-quadrupole center offset. H_{rms} = 0.344 mm, V_{rms} = 0.346 mm

The LOCO results revealed a few BPM discrepancies that were hence corrected. After three iterations of LOCO runs and BBA, the measured orbit without correctors was 1.78 mm rms horizontal and 1.04 mm rms vertical, as shown in Fig. 14. The *bare* CODs demonstrate the excellent work on alignment and magnets. After orbit correction, the CODs were decreased to 103 μm rms horizontal and 69 μm rms vertical (Fig. 14). Employing less than 20 eigenvalues, moderate corrector strengths less than 0.25 mrad (0.038 mrad rms) horizontal and 0.1 mrad (0.018 mrad rms) vertical were used. With additional eigenvalues and greater corrector strengths, the residual orbit can be decreased further.
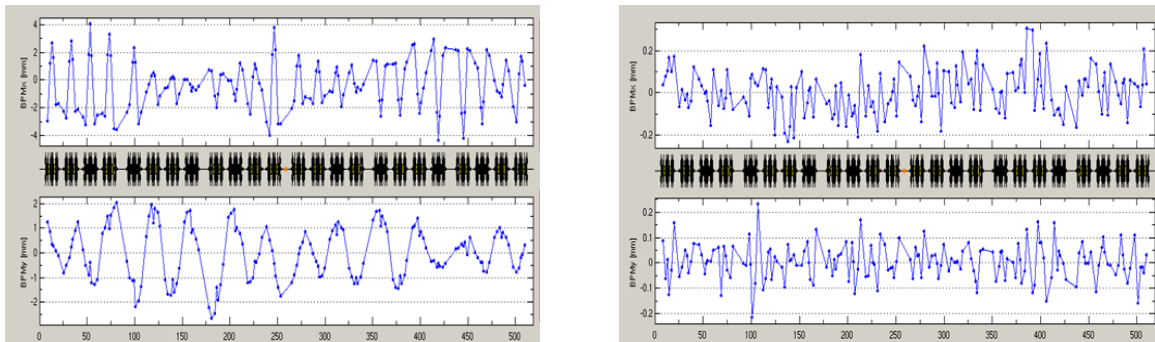
Figure 14: CODs without correctors in the TPS storage ring after three LOCO iterations and BBA (left); CODs after correction (right)

5.4.4.2   *Linear Optics and Coupling Corrections*

LOCO was the major application program for optical calibration and optimization. The deviations in the beta function were decreased from 8.91 to 1.44 % rms horizontal and from 10.94 to 0.68 % rms vertical after three iterations of corrections [16,19]. Figure 15 shows the beta beating in both planes. The horizontal dispersion function agreed satisfactorily with the model following the LOCO runs; the spurious vertical dispersion was 2.43 mm rms. Figure 16 shows the variations of the quadrupole strength deviating from hard-edge model settings. The BPM gain and roll, and the corrector gain

and tilt, were also fitted and corrected. The achromat lattice configurations were measured and calibrated accordingly.
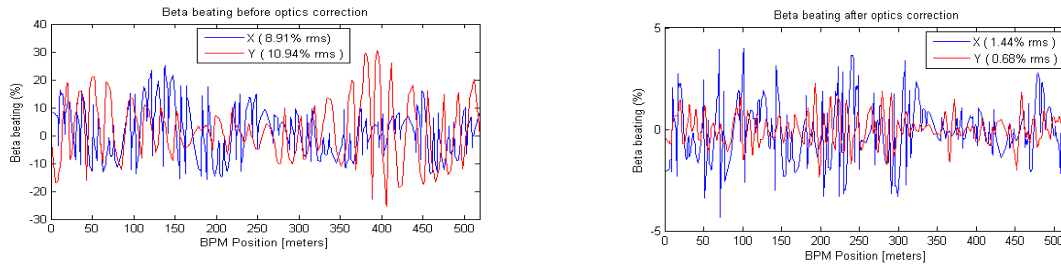
Figure 15: Beta beating before (left) and after three iterations (right) of LOCO
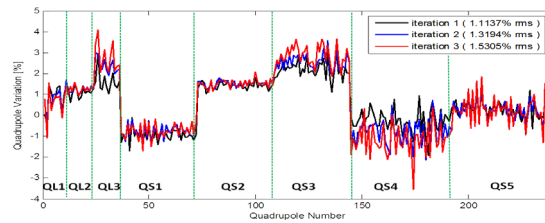
Figure 16: Variations of fitted quadrupole strength with respect to a hard-edge model after LOCO

The linear coupling was corrected in the LOCO runs. We used 168 skew quadrupoles to correct the betatron coupling and vertical dispersion. The closest tune gaps were 0.0005 and 0.0065 with and without skew quadrupole magnets, respectively, as illustrated in Fig. 18. The vertical dispersion was decreased to 1.77 mm rms with skew quadrupole corrections. Table 3 lists the emittance ratios contributed from the betatron coupling for working tune with ν_x=26.1831 and ν_y=13.2945. The vertical dispersion contributions are estimated; values measured with a pinhole camera are also shown.

Do not get panicked.
This page was inserted due to a layout screw-up.
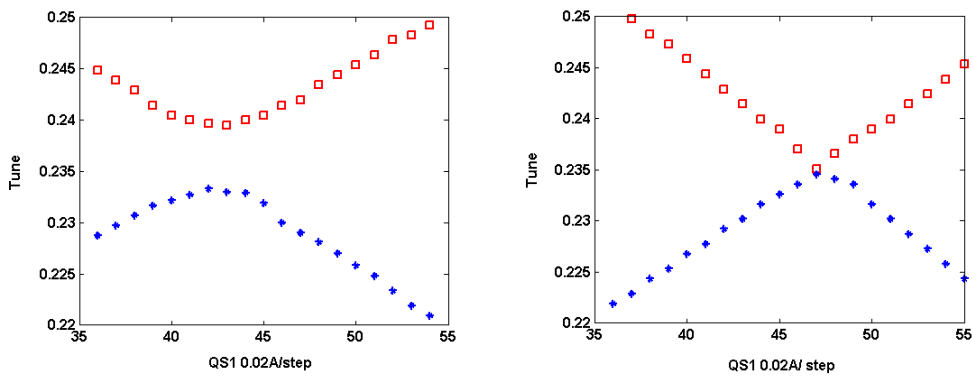
Figure 18: Tune shift vs energy of the TPS storage ring with chromaticity 2.5, 3.4 in horizontal, vertical planes.

Table 3: Emittance-coupling Ratio of TPS

emittance ratio	without skew quad	with skew quad
betatron coupling	0.170 %	0.001 %
vertical dispersion	0.156 %	0.038 %
pinhole camera measurement	1.65 %	0.96 %

The uncertainty in the measurements with the pinhole camera was due mainly to the beam-orbit noise and instabilities, and the system resolution. The measurements were conducted at a small stored beam current with a brief integration and assuming a natural energy spread.

5.4.4.3 *Nonlinear Chromaticity*

The RF frequency centering was corrected with a dispersion fit, and also on measuring the crossing in the tune shift with energy at various chromaticity settings. The measured center RF frequency differed from the nominal value by +1.228 kHz, indicating that the ring circumference was smaller by 1.27 mm in March 2015. The circumference varies with thermal and tidal effects and must be compensated with a radio-frequency feedback. The natural chromaticities were measured on varying the well calibrated strength of the dipole field. The measured natural chromaticities (horizontal, vertical) were -72.5,-25.8, near the model values -75,-26, respectively.

According to an eight-family sextupole scheme, nonlinear beam dynamics were optimized and natural chromaticities were corrected to be slightly positive. The tune

shift as a function of energy was measured on varying the RF frequency. Because of the small first-order factor for momentum compaction, the second order must be taken into account in the relation between energy and RF. Figure 18 shows that the measured acceptance of the lattice energy agrees satisfactorily with the model simulation.
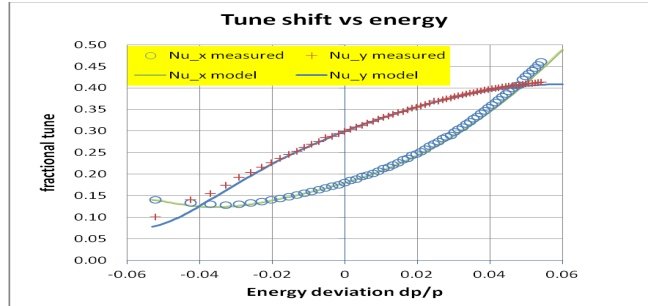
Figure 18: Tune shift vs energy of the TPS storage ring with chromaticity 2.5, 3.4 in horizontal, vertical planes.

5.4.4.4   *ID Commissioning*

All ten IDs have been commissioned with the beam using a lattice with three double vertical-waists because three long straight sections accommodate three sets of double IDs. The optics and orbit compensations during the variation of the ID gap and phase were corrected with feed-forward tables. To maintain the orbit stability in the submicrometre range, a fast orbit-correction scheme was implemented. As of 2016 May, beamline tests and user operations in the 300 mA top-up mode indicated satisfactory progress, as shown in Fig.19.
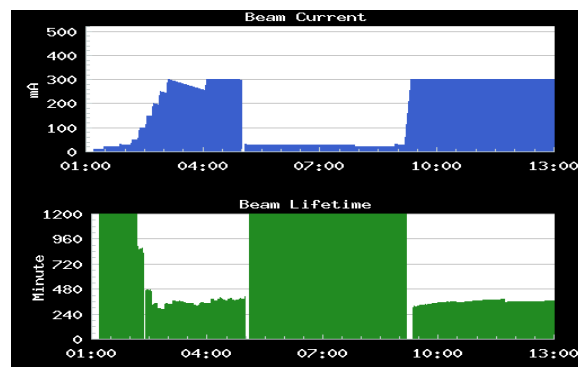
Figure 19: Beamline tests and user operations in the 300 mA top-up mode on 2016 May 27 at TPS

5.4.4.5 *Impedance and Instabilities*

A dual-sweep streak camera (C10910 Hamamatsu Photonics) was used to measure the longitudinal motion of the beam and the bunch length. The bunch length (rms) as a function of bunch current with varied RF voltage and ID chambers is shown in Fig. 20. Fitting with Zotter's potential-well distortion cubic equation below the microwave instability threshold about 2.5 mA, we obtained a longitudinal broadband impedance $|Z/n|$ = 0.09 and 0.17 Ω for the case with dummy chambers and ID chambers, respectively [20].
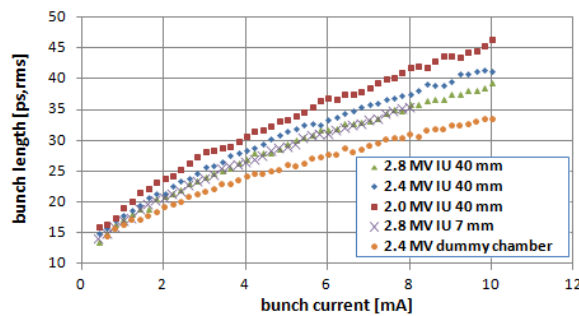
Figure 20: Bunch length as a function of bunch current for different RF voltages.

Running with PETRA cavities, both transverse and longitudinal instabilities were observed. The transverse instabilities can be suppressed with both an increased chromaticity and a bunch-by-bunch feedback damper. There was no longitudinal instability using SRF at least up to 300 mA. We expect that, according to the simulations, no longitudinal damper is required at higher beam current.

5.4.5 Conclusion

The successful beam commissioning of TPS demonstrates that the lattice design is sound. The measured parameters agree with the model values, i.e., the design codes are reliable and the engineering of components was as required. More detailed studies are necessary to optimize the future performance of TPS.

5.4.6 Acknowledgement

I thank the TPS Project Team for the efforts to make this project a success.

5.4.7 References

1. C.C. Kuo, H.P. Chang, G.H. Luo, H.J. Tsai, M.H. Wang and C.T. Chen, "Lattice Study for the Taiwan Photon Source", Proceedings of the 2005 Particle Accelerator Conference, Knoxville, Tennessee USA (2005).

2. C.C. Kuo, H.P. Chang, P.J. Chou, H.C. Chao, W.T. Liu, G.H. Luo, H.J. Tsai, J.W. Tsai, A. Rusanov, K. Liang, "Design Status of Taiwan Photon Source", Proceedings of the 2008 European Particle Accelerator Conference, Genoa, Italy (2008).

3. C.C. Kuo, H.P. Chang, H.C. Chao, M.S. Chiu, P.J. Chou, G.H. Luo, A. Rusanov, H.J. Tsai, F.H. Tseng, and C.H. Yang, "Accelerator Physics Issues for TPS", Proceedings of the first International Particle Accelerator Conference, Kyoto, Japan (2010)

4. J. Bengtsson, "The Sextupole Scheme for the Swiss Light Source (An Analytical Approach)", SLS Note 9/97 (1997)

5. A. Streun, "OPA documentation", SLS.

6. J. Payet *et al*., BETA, LNS version.

7. J. Bengtsson, E. Forest and H. Nishimura, "Tracy User Manual", unpublished (ALS Berkely); Tracy-2 is an SLS, SOLEIL and NSLS version.

8. H. Grote, F.C. Iselin, "The MAD Program", CERN/SL/90-23 (AP).

9. M. Borland, "User's Manual for elegant", Advanced Photon Source.

10. P. Elleaume, O. Chubar and J. Chavanne, "Computing 3D Magnetic Fields from Insertion Devices", Proceedings of the 1997 European Particle Accelerator Conference, Vancouver, BC Canada (1997).

11. C.C. Kuo, and H.J. Tsai, "Design of Low Momentum Compaction Lattices for the TPS Storage Ring", Proceedings of the 2013 European Particle Accelerator Conference, Shanghai, China (2013)

12. M.S. Chiu, Y.C. Lee, C.C. Chiang, C.H. Yang, H.P. Chang, C.C. Kuo , and C.T. Chen, "Double Mini-Betay Lattice of TPS Storage Ring", Proceedings of the second International Particle Accelerator Conference, San Sebastian, Spain (2011).

13. H.C. Chao, H.P. Chang, H.J. Tsai, P.J. Chou, G.H. Luo and C.C. Kuo, "Current Design Status of TPS 3 GeV Booster Synchrotron", Proceedings of the 2009 Particle Accelerator Conference, Vancouver, BC Canada (2009).

14. H.J. Tsai, J.Y. Chen, M.S. Chiu, P.C. Chiu, P.J. Chou, K.H. Hu, Y.C. Liu, F.H. Tseng, K.T. Hsu, C.C. Kuo, G.H. Luo and C.T. Chen, "Hardware Improvements and Beam Commissioning of the Booster Ring in Taiwan Photon Source", Proceedings of the 6th International Particle Accelerator Conference, Richmond, VA USA (2015).

15. H.J. Tsai, P.J. Chou, K.H. Hu, K.T. Hsu, C.C. Kuo, C.Y. Liao, Y.C. Liu, G.H. Luo, F.H. Tseng, "First Year Performance of the TPS Booster Ring", Proceedings of the 7th International Particle Accelerator Conference, Busan, Korea (2016).

16. C.C. Kuo, J.Y. Chen, M.S. Chiu, P.J. Chou, Y.C. Liu, H.J. Tsai, F.H. Tseng, K.T. Hsu, G.H. Luo and C.T. Chen, "Commissioning of the Taiwan Photon Source", Proceedings of the 6th International Particle Accelerator Conference, Richmond, VA USA (2015).

17. M.S. Chiu, et al., "The Commissioning of Phase-I Insertion Devices in TPS", Proceedings of the 7th International Particle Accelerator Conference, Busan, Korea (2016).

18. J. Safranek, G. Portmann, A. Terebilo, C. Steier, "Matlab-Based LOCO", Proceedings of the 2002 European Particle Accelerator Conference, Paris, France (2002).

19. F.H. Tseng, C.C. Kuo, Y.C. Liu, M.S. Chiu, H.J. Tsai, J.Y. Chen and C.H. Chen, "Optics Calibration During Commissioning of the Taiwan Photon Source", Proceedings of the 6th International Particle Accelerator Conference, Busan, Korea (2016).

20. C.C. Kuo, P.J. Chou, K.T. Hsu, K.H. Hu, C.Y. Liao, C.C. Liang, Z.K. Liu, H.J. Tsai, F.H. Tseng, "Impedance Study with Single Bunch Beam at Taiwan Photon Source", Proceedings of the 7th International Particle Accelerator Conference, Busan, Korea (2016).

5.5   A low-emittance lattice for the ESRF-EBS Light Source

L. Farvacque, JC. Biasci, JF. Bouteille, N. Carmignani, J. Chavanne, D. Coulon, Y. Dabin, F. Ewald, L. Goirand, M. Hahn, J. Jacob, G, LeBec, S. Liuzzo, B. Nash, H. Pedroso-Marques, T. Perron, E. Plouviez, P. Raimondi, JL. Revol, K. Scheidt, V. Serrière, ESRF, Grenoble, France

Mail to: laurent.farvacque@esrf.fr

ESRF, 71 Avenue des Martyrs

38000 Grenoble, France

5.5.1   Introduction

The ESRF is a multinational research institute located in Grenoble, France. It operates since 1992 a 3rd generation synchrotron radiation source with some 30 beamlines covering a wide range of scientific research in fields such as biology and

medicine, chemistry, earth and environmental sciences, materials and surface science, and physics. In the frame of the Phase 2 of its upgrade, the ESRF started the construction a new storage ring, referred to as ESRF-EBS (Extremely Brilliant Source), in view of significantly increasing the brightness and transverse coherence of its X-Ray beams [1]. For compatibility with the existing infrastructure, the ESRF has chosen a strategy based on well-proven technologies, resulting in a beginning of commissioning scheduled in January 2020 after about 12 months of accelerator shutdown for the lattice refurbishment.

5.5.2 The ESRF context

In order to preserve the existing facility, the new lattice must adhere to the following requirements and constraints:

- it fits in the present tunnel and keeps the insertion device source points at the same location,
- it ensures a length of at least 5 m for all the existing insertion device straight sections,
- its target horizontal emittance is around 150 pm,
- it keeps the electron energy at 6 GeV in order to preserve the spectral properties of the present beamlines,
- it preserves the time structure operation and a multibunch current of 200 mA,
- it minimizes the impact on user operation due to the downtime for installation and commissioning,
- it minimizes the radiation losses and the magnet electrical consumption, in order to decrease operating costs,
- it reuses existing hardware as much as possible (power supplies, vacuum components, diagnostics…),
- it reuses the present injector complex with minor changes.

Compared to the present lattice, the new one will provide an improvement of brightness of the order of 30-100 times for both insertion device and bending magnet beamlines. The transverse coherence fraction on insertion device beamlines will also increase by up to a factor of 30. The design allows for further "adiabatic" improvements, similar to those carried out at the ESRF over the past 20 years such as optics improvements and better undulators. This will ensure a steady improvement of the source throughout the operational life of the new storage ring.

5.5.3 Cell design

The common rule for minimizing the equilibrium emittance of an electron storage ring is to increase the number of bending magnets [2]. While most present machines are based on 2 or 3 bending magnets per cell, recent projects focus on 6 or 7 bends per cell [3]. The number of bending magnets is limited by the space to accommodate the quadrupoles providing the necessary focusing between the dipoles. But it is also well known that applying this scheme to large machines leads to very small bending angles, and so to a very small maximum dispersion function. As a consequence, the chromaticity correction needs very strong sextupoles. Apart from problems in magnet

technology, this induces difficulties to achieve a large dynamic aperture, still needed since we intend to keep the off-axis injection scheme using the present injector. In order to mitigate these difficulties, the ESRF lattice is based on a variation of the standard multi-bend achromat: instead of distributing equally the 7 dipoles along the arc, more space is left between dipoles 1 and 2, and 6 and 7. The β-functions and dispersion are allowed to grow to high values in this space, making the sextupoles more efficient. This layout is referred to as Hybrid Multi-Bend lattice (HMB). The centre part alternates 4 high-gradient horizontally focusing quadrupoles and 3 high-gradient bending magnets, which also provide vertical focusing. At each end of the cell, 2 dipoles encompass the regions with large β-functions and dispersion. Their longitudinally varying bending field helps reduce the emittance and increase the dispersion. This hybrid cell takes advantage of a large number of bending magnets to reduce the horizontal emittance (as implemented in the MAX-IV design), and regions with large localized dispersion to allow efficient correction of chromaticity, as already used in the standard double-bend achromat. The main parameters of the new source are given in Table 1:

Table 1: Main parameters of the source

	ESRF	ESRF-EBS
Lattice type	DBA	HMB
Circumference [m]	844.390	843.977
Beam energy [GeV]	6.04	6.00
Beam current [mA]	200	200
Natural emittance [pm.rad]	4000	135
Energy spread	0.106	0.095

The lattice has been optimised to achieve the minimum emittance with the following constraints:

- The straight section must be long enough to accommodate the present low-gap, 5 m-long insertion device vacuum chamber, which leaves 5.30 m between BPMs.
- The quadrupole strengths must be compatible with state-of-the-art magnet design and vacuum chamber requirements.

The lattice comprises 30 identical standard cells and two special cells that provide a higher β_x in the injection straight section. The optical functions are the same in all standard straight sections, thus disposing of the alternating high and low-beta straight sections found in the present lattice.

The nominal tunes are set to 76.21 (horizontal) and 17.34 (vertical). The natural equilibrium emittance is 132 pm and the target vertical emittance is 5 pm, corresponding to a coupling value of 3.9%. With a set of insertion devices giving an energy loss of 0.5 MeV, which is the present average value, the operation emittance values are 110 pm in horizontal and 5 pm in vertical. The insertion device source points will be kept the same as in the present lattice, this implies a reduction of the ring circumference by 413 mm and a corresponding increase of the RF frequency by 172 kHz. Figure 1 shows the optical functions of the standard cell:
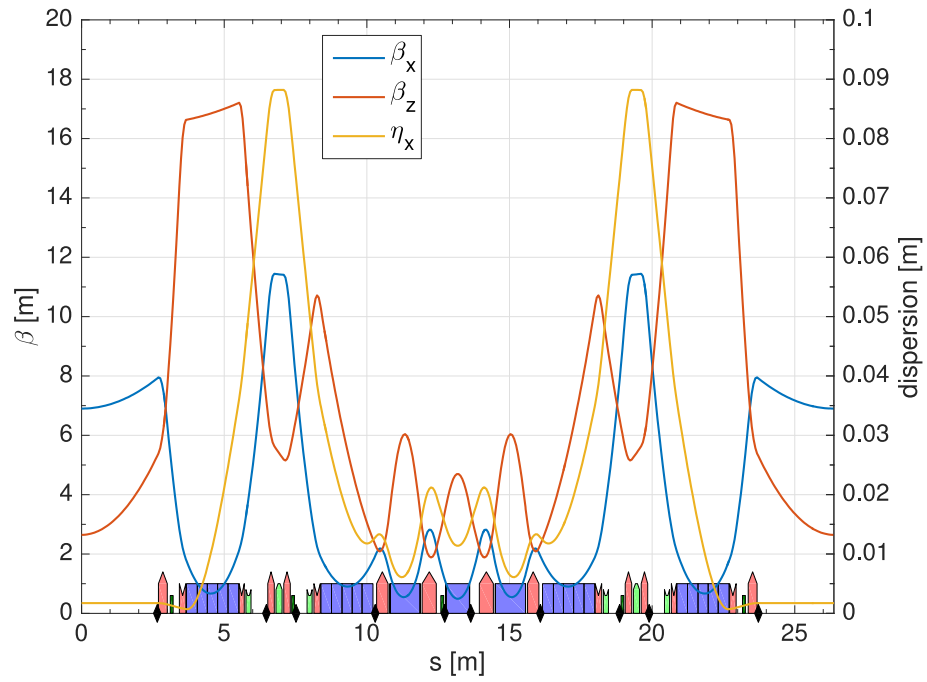
Figure 1: optical functions

The standard cell uses 16 quadrupoles grouped in 7 families, 3 combined function bending magnets (DQ), 4 permanent magnet dipoles with longitudinally varying field (DL), 6 sextupoles in 3 families and 2 octupoles (one family). Their parameters are summarized in Table 2.

Table 2: Magnet parameters

Bending magnets

	DL	DQ1	DQ2
Number	128	64	32
Field [T]	0.17 to 0.62	0.55	0.37
Gradient [T/m]	0	36.6	30.7
Gap [mm]	26	-	-
Bore radius [mm]	-	18	18

Quadrupoles

	Moderate gradient	High gradient
Number	384	128
Gradient [T/m]	≤55	≤90
Bore radius [mm]	15.9	12.8

Sextupoles

Number	192
$[T/m^2]$	≤3600
Bore radius [mm]	19.2

Octupoles

Number	64
$[T/m^3]$	≤78000
Bore radius [mm]	18.6

5.5.4 Beam stay-clear

3 regions have been considered for specifying the beam stay-clear: in the central part the β-values are small and the beam stay-clear can be reduced, making the magnet design easier for reaching the very high required gradients. In the end parts the beam stay-clear is wider but the required quadrupole strengths are smaller. Figure 2 shows the resulting aperture values.
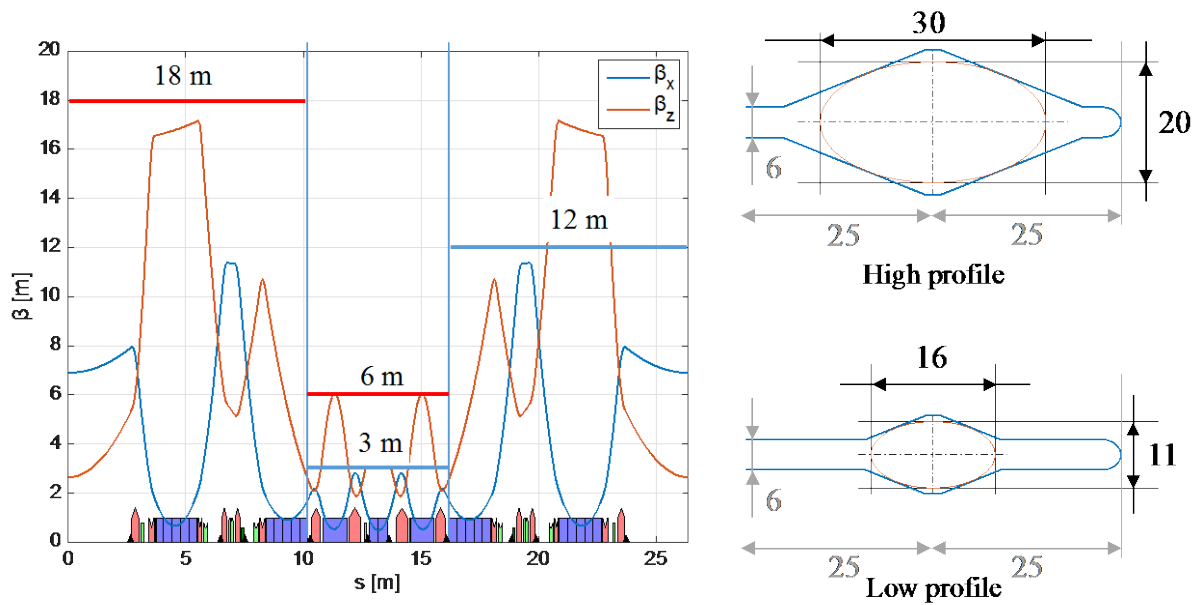
Figure 2: Beam stay-clear

5.5.5 Non-linear dynamics

The basic non-linear optimization involves 2 sextupole families (SF: focusing / SD: defocusing) per cell, located in the high-dispersion regions as in the standard DBA achromat. The phase advances between the high-dispersion regions at both ends of the cell are set to 3π in the horizontal plane and π in the vertical, giving a –I transform between the sextupoles. This property cancels most of the undesirable effects of the sextupoles and provides a very large dynamic acceptance without any need for additional sextupole families. However, it leads to very large tune shifts with amplitude. These are minimized by a combination of:

- a slight deviation from the exact π phase advance,
- the distribution of the defocusing sextupoles in two different families, and therefore 3 sextupole families in total (SF, SDA, SDB),
- the introduction of one family of octupoles.

The 3 sextupole families and the octupole family are finally tuned using a multi-objective genetic algorithm (NSGA II [4]). The optimization target is a combination of dynamic aperture and Touschek lifetime, computed on 10 different error seeds. Tune shifts for the nominal tunes 76.21 / 27.34 and for chromaticities of 6 / 4 are shown on Figures 3 and 4.
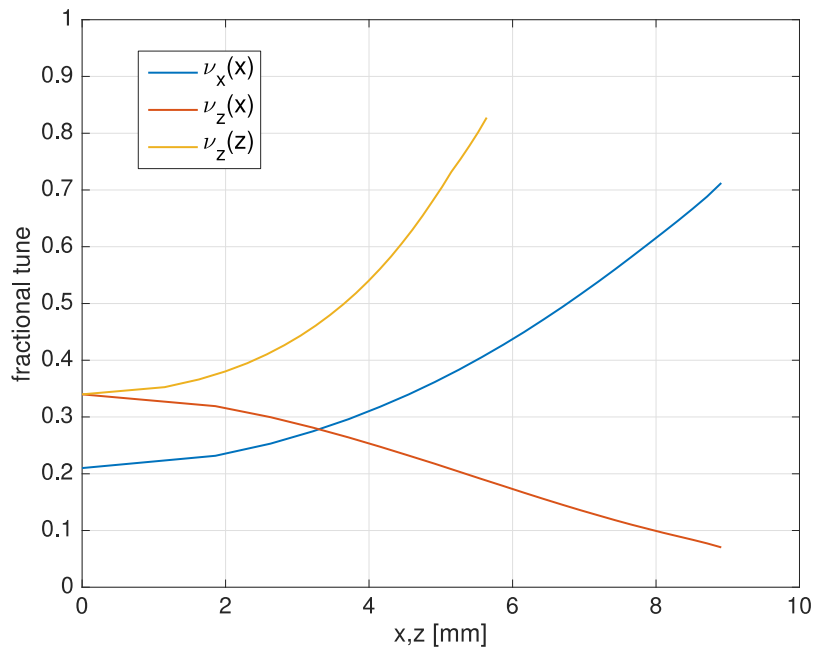
Figure 3: Tune shifts with amplitude
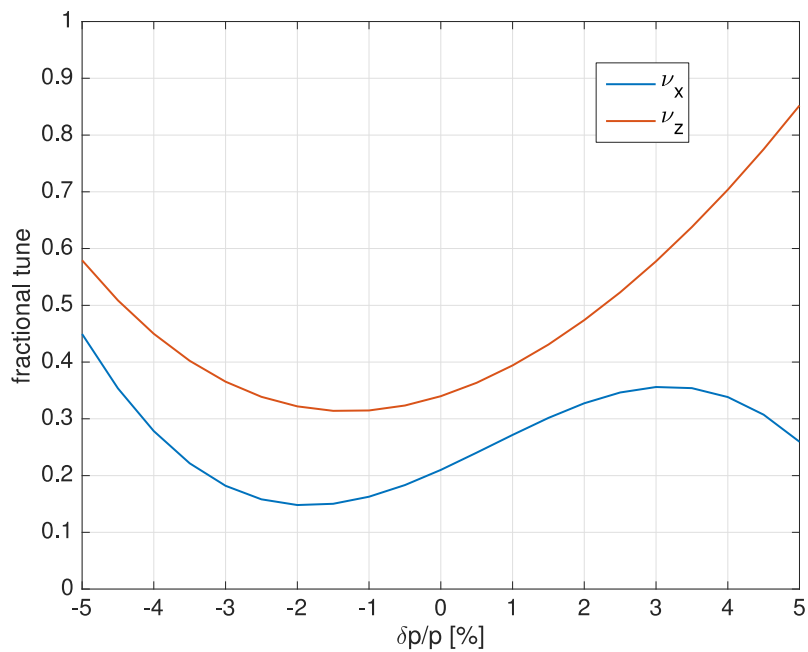
Figure 4: tune shift with momentum

5.5.6 Dynamic aperture

The dynamic aperture at the injection point (see Figs. 5 and 6) is computed in 3 different conditions: a perfect machine with no errors and no longitudinal motion, the

same machine with longitudinal motion (6-D tracking) and finally with all errors and corrections (10 samples). On the injection side (x<0), the aperture reaches -8.2 ± 0.4 mm. The acceptance reduction with longitudinal motion comes from the path lengthening appearing at large transverse amplitudes.
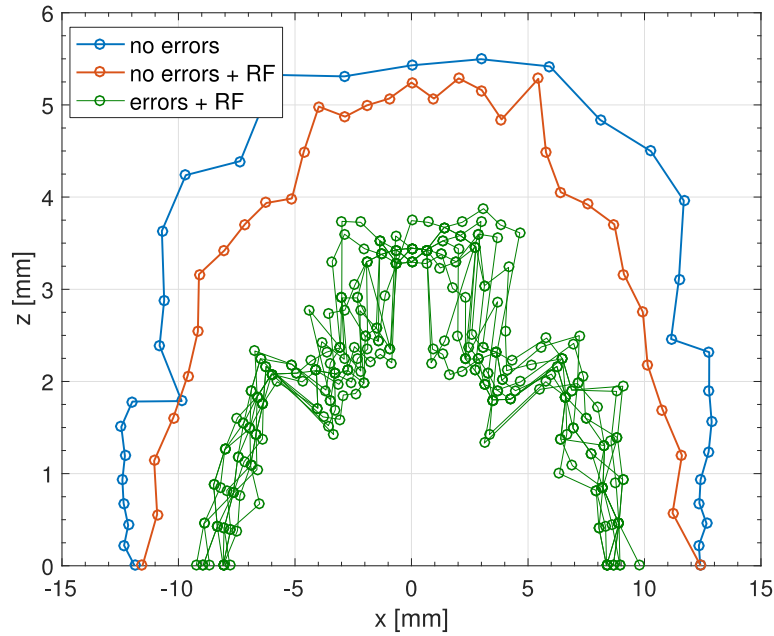
Figure 5: Dynamic aperture at the injection point (β_x = 18.64 m, β_z = 2.32 m)
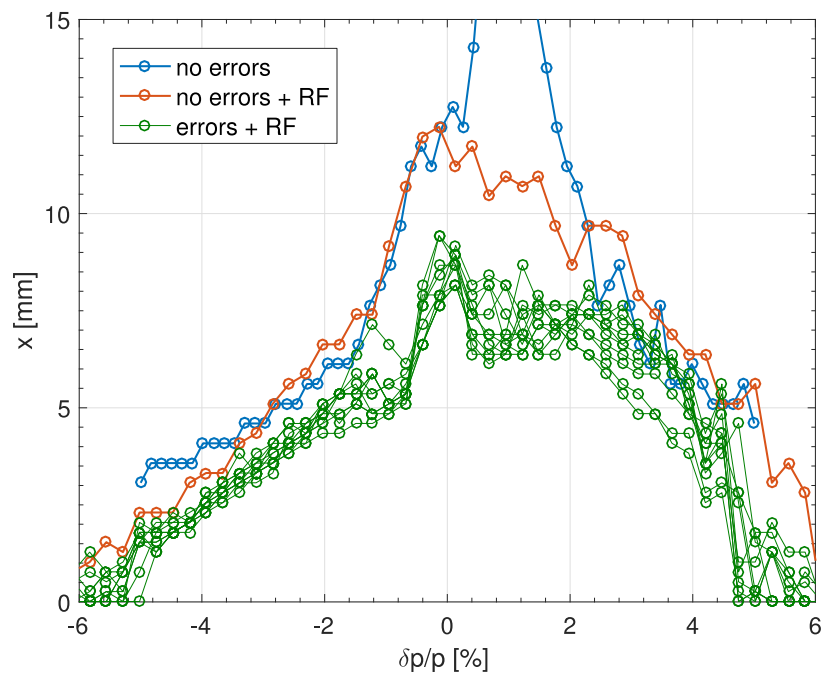
Figure 6: Momentum aperture at the injection point (β_x = 18.64 m)

5.5.7 Chromaticity tuning

The natural chromaticities are -109/-82 (horizontal/vertical). Chromaticities can be tuned between 0/0 and 15/15 or more. The latter may be necessary for the operation modes with a high bunch current and is obtained with a still reasonable sextupole gradient of

5.5.8 Path lengthening with amplitude

The path length at large horizontal amplitude is longer that nominal, as shown on Fig. 7. So a particle thrown on energy at large amplitude (injected beam, horizontal kick) will start a longitudinal oscillation. This explains the reduction of dynamic aperture with RF motion. This lengthening depends on the sextupole tuning and may explain that a better lifetime is obtained for positive chromaticity.
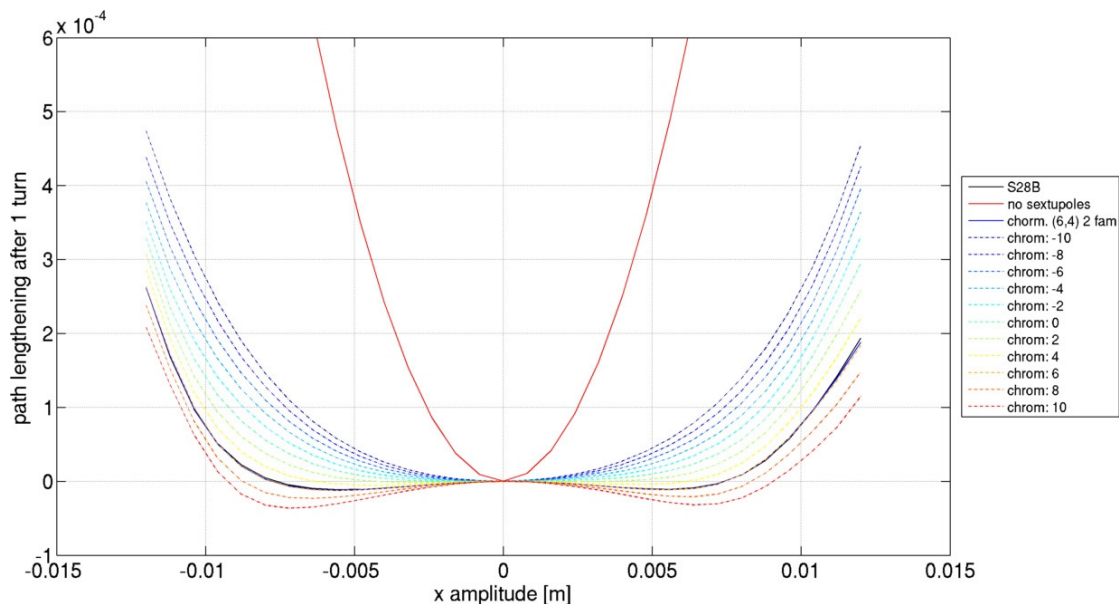
Figure 7: Path lengthening with amplitude for different horizontal chromaticities

5.5.9 Beam losses and collimation

The low emittance of the new ring will cause much stronger Touschek losses than presently. To avoid radioprotection issues, we will try and localize them in specially shielded regions with collimators. Two sets of horizontal collimators are located upstream the last DL dipole in cells 13 and 24. Their aperture is set on a compromise between re-localization of losses and lifetime reduction, resulting in 8.4 mm internal and 7.6 mm external. The distribution of the total losses along the cell (with all cells added up) is shown on Figure 8, with and without collimators (average over 10 error seeds). With the collimators closed, 78% of Touschek losses are located on the collimators and the lifetime is reduced by 5%.

Without collimator   with collimator
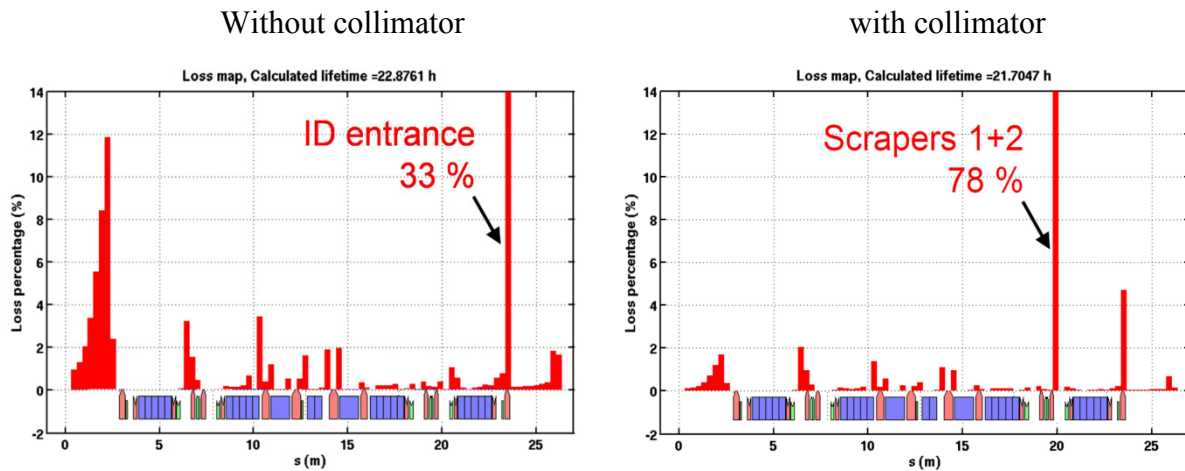
Figure 8: distribution of losses, 32 cells superimposed

5.5.10 **Errors and tolerances**

5.5.10.1 *Correction scheme*

The corrections scheme is based on a set of 10 beam position monitors (BPM) and 9 combined function correctors per cell. The 6 sextupoles of each cell are equipped with correction coils and can provide horizontal and vertical steering, and skew quadrupole correction. Three other dedicated magnets located inside the doublet at each end of the straight section and upstream the central bending magnet will provide similar corrections. Focusing errors and sextupole errors will be corrected using the main magnets, powered with individual power supplies. This setup is illustrated on Figure 9.

BPM: ◆   sextupole: ▮▮   Corrector: ▮
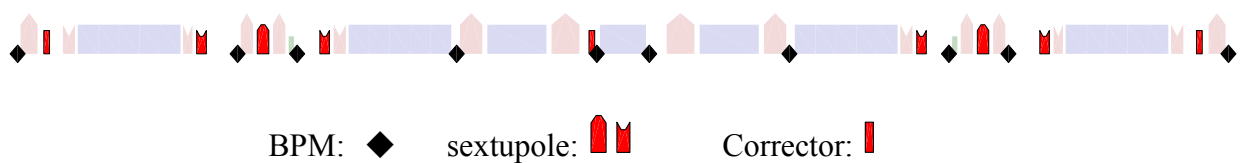
Figure 9: Schematic view of the correction equipment

The correction strategy is:

- 1st turn steering to get stored beam,
- Orbit correction using the theoretical response matrix,
- Measurement of the Orbit Response Matrix (ORM),
- Computation of an error model fitting the measured ORM,
- Simultaneous correction on the error model of resonant driving terms (RDT) and dispersions using quadrupoles and skew quadrupoles,
- Sextupole correction with a lifetime optimizer

- Iterate…

Fast orbit corrections will be performed up to 150 Hz with a subset consisting in the 3 dedicated corrector magnets and 6 among the 10 BPMs.

5.5.10.2 *Tolerances*

The tolerances have been defined by looking at the consequence on beam lifetime and dynamic aperture of applying the correction strategy on 10 sets of errors. Since we want the beam line source points located exactly as they are now, the machine will be aligned on a smooth trajectory differing from the ideal one by several millimetres. In the study, the girders are positioned according to sets of probable positions estimated by the alignment group. On top of that, the magnets are positioned on their girder with random errors shown in Table 3

Table 3: Tolerance specification (magnet alignment with respect to its girder)

	Δx [µm]	Δz [µm]	Δs [µm]	$\Delta \psi$ [µrad]	$\Delta L/L$
Long. Varying field dipoles	>100	>100	1000	500	10^{-3}
High gradient quadrupoles, Combined function dipoles	60	60	500	200	$5\ 10^{-4}$
Medium gradient quads	100	85	500	500	$5\ 10^{-4}$
Sextupoles	70	50	500	1000	$3.5\ 10^{-3}$
Octupoles	100	100	500	1000	$5\ 10^{-3}$

5.5.11 Injection cell

As the horizontal β-function in the standard straight section is only 6.9 m, a special injection section has to be designed. The symmetry breaking is limited by applying the following constraints: the phase advance in each plane is strictly identical to the one of a standard cell, and the optical functions are kept identical in most of the cell, especially at the sextupole locations. The only residual modification of the optics is the difference of local chromaticity generated by the quadrupoles of the injection region. This can be corrected by a slightly modified tuning of the sextupoles around the injection section. Figure 10 shows the optical functions of the injection cell. The horizontal β at injection reaches 18.64 m. As there is no sextupole within the injection kicker bump, there will be no perturbation of the circulating beam when powering the injection bump, ensuring a stable beam in top-up operation. A 2.8 m long free space is available in the middle of the straight section for the injection elements (septum magnets) and an additional quadrupole family is necessary.
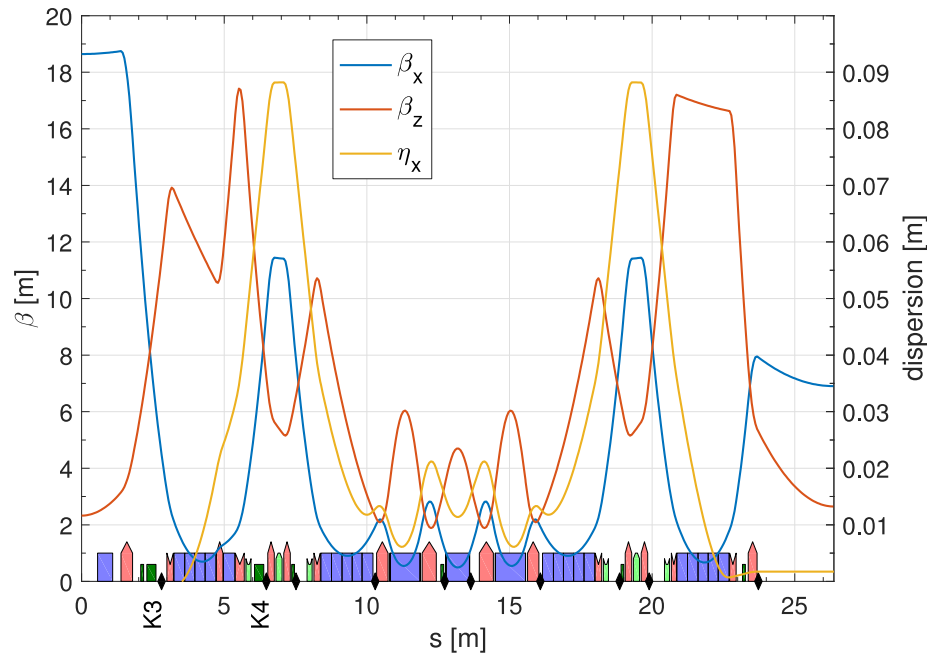
Figure 10: Optical functions of the injection cell

The injection efficiency depends on the Booster emittance and on the tuning of the collimators. Three different operating modes are being considered for the booster:

1) Present conditions,

2) Increase of the horizontal tune leading to a reduction of the equilibrium emittance and off-momentum operation giving a further reduction,

3) Same working point as before plus going to full H/V coupling at extraction

Table 4 summarizes the injection tuning for each booster configuration.

Table 4: injection efficiency

Booster setting	*Present configuration*	*Optimized optics, off-momentum*	**Full H/V coupling**
Booster emittances H/V [pm]	120/5	60/5	30/30
Efficiency without collimator	62%	84%	94%
Efficiency with collimator	46%	72%	90%

5.5.12 Impedance and collective effects

5.5.12.1 *Longitudinal impedance*

An estimate of the longitudinal impedance is given on Figure 11 and Table 5 (the contribution of scrapers and collimators is still not included):
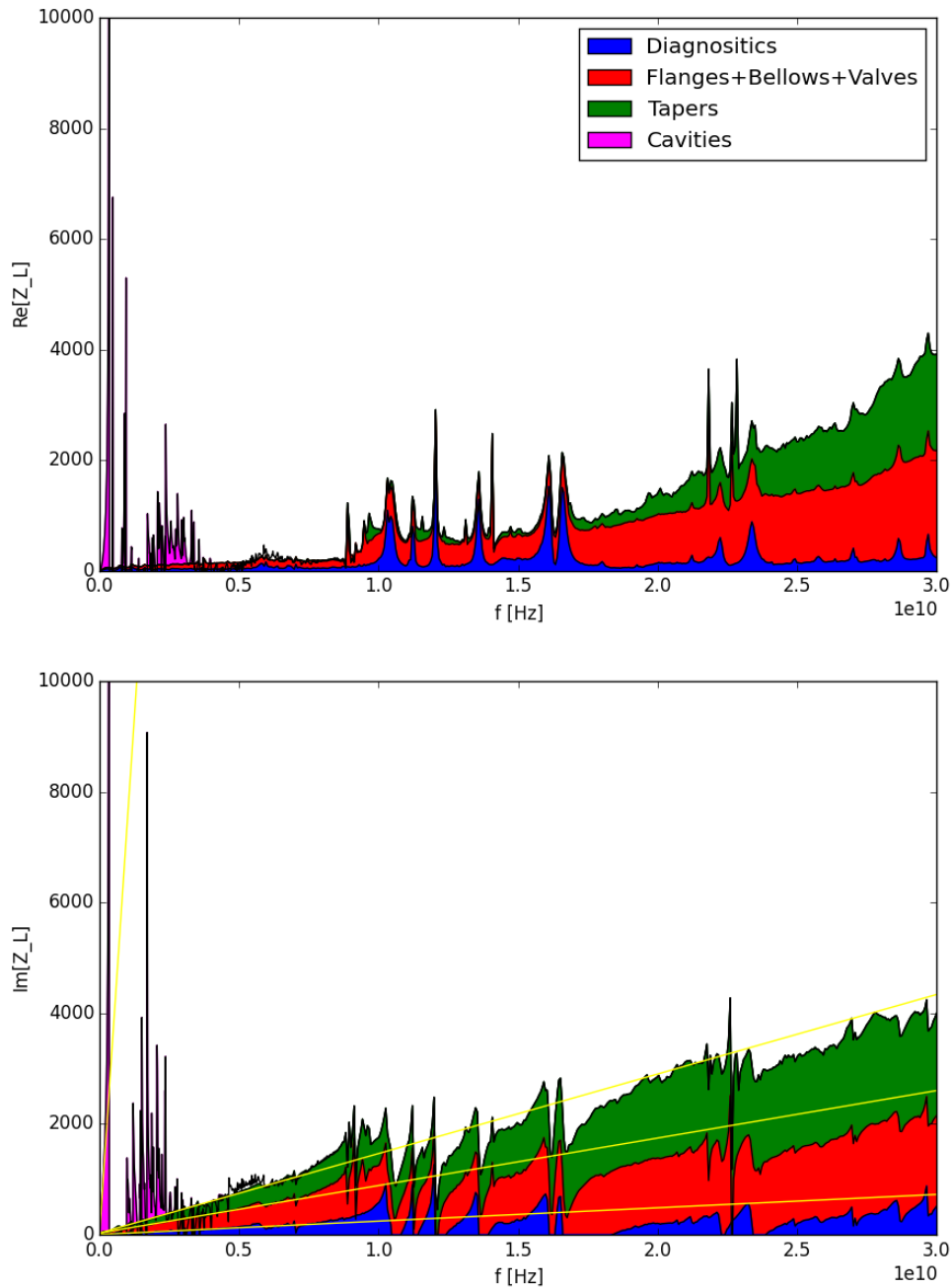
Figure 11: longitudinal impedance

Apart from the narrow-band contribution of RF cavities, the impedance is inductive up to 30 GHz. The effective impedance of 0.344 Ω is about half of the estimated value for the present storage ring.

Table 5: longitudinal impedance budget

	K_{loss} [V/pC]	Z/n_{eff} [Ω]
Diagnostics	4.02	$8.4\ 10^{-3}$
Flanges+bellows	9.27	$25\ 10^{-3}$
Scrapers	?	?
Tapers	3.2	$20\ 10^{-3}$
Cavities	6.66	$69\ 10^{-3}$
Resistive wall	38.7	0.222
Total	51.85	0.344

5.5.12.2 *Collective effects*

Intra-beam scattering: The effect of intra-beam scattering is an emittance growth of the order of 3% in multibunch, 19% in 16-bunch and 24% in 4-bunch modes.

Bunch lengthening: Figure 12 shows the bunch lengthening with bunch current for the present machine and the ESRF-EBS ring.
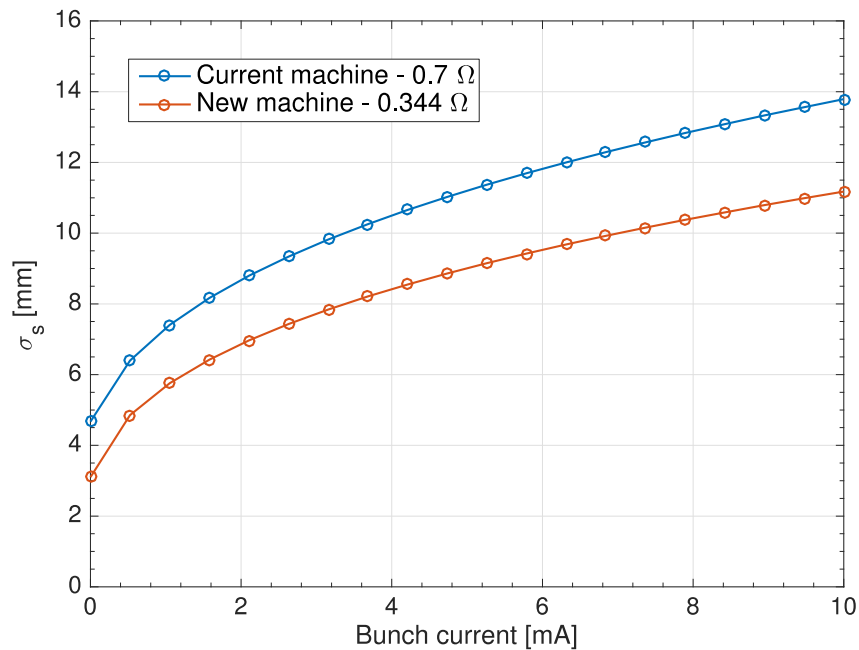
Figure 12: bunch lengthening with intensity

Multibunch instabilities: longitudinal coupled-bunch instabilities triggered by the Higher Order Modes (HOM) of the RF cavities are the present limitation. This should not be a concern in the new ring thanks to the new HOM-damped single-cell RF cavities. Transverse coupled-bunch instabilities have never been observed and we do not expect any new transverse narrow-band impedance. The transverse resistive-wall instability will be similar in the new ring and is cured by positive chromaticity.

Single bunch instabilities: assuming a product similar to the present one, the threshold of the transverse mode coupling instability will be lower because of the lower synchrotron frequency. Single bunch operation will therefore need a very high positive chromaticity.

5.5.13 Beam lifetime

Given the small emittances, the lifetime will be dominated in all operation modes by Touschek lifetime. It is computed taking into account the longitudinal motion, the intra-beam scattering and a bunch lengthening corresponding to the estimated longitudinal impedance. The scattering rate and momentum acceptance are computed at each point of the circumference and integrated over the ring. Table 6 summarizes the lifetime values for the main ESRF operation modes. Top-up operation is foreseen for all modes.

Table 6: Beam lifetime

	Multibunch	*16-bunch*	*4-bunch*
Intensity [mA]	200	90	40
Bunch current [mA]	0.23	5.62	10
V. emittance [pm]	5	60	60
Lifetime [h]	17	1.6	1.1

5.5.14 Influence of a 3rd harmonic RF cavity

For improving the Touschek lifetime, we looked at the effect of a 3rd harmonic cavity. The study was performed by tracking 100000 electrons over 10000 turns. Figure 13 shows the bunch length without harmonic cavity (solid lines) and with harmonic cavity (dashed lines) for different impedance values. For the estimated impedance of 0.35 Ω, the lengthening varies from a factor 4.1 (200 mA uniform filling) to 2.3 (4-bunch mode, 40 mA). The bunch profile is shown on Figure 14.
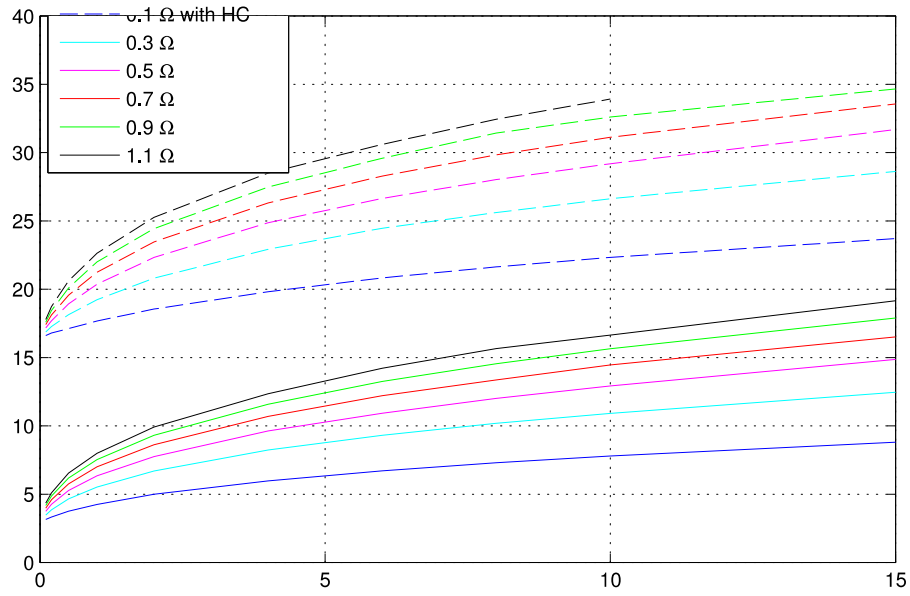
Figure 13: Bunch lengthening with intensity with and without harmonic cavity
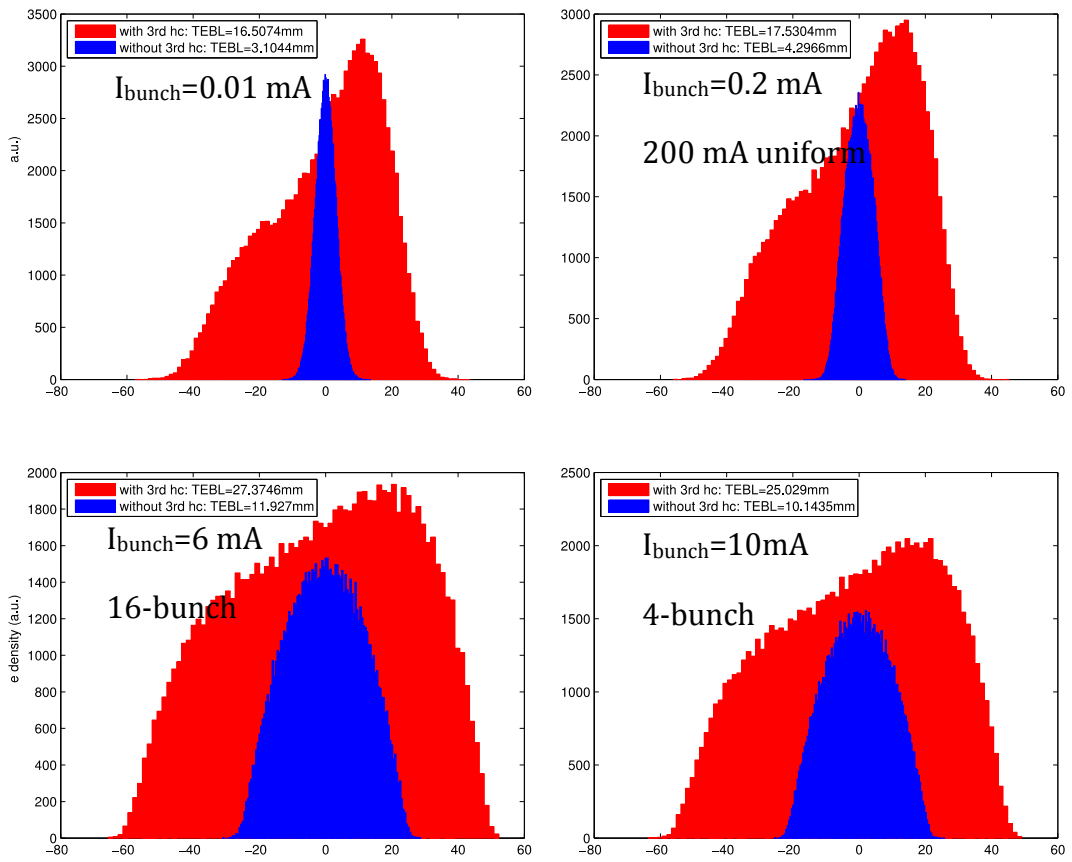
Figure 14: bunch profile

5.5.15 **Conclusion**

The start-up of the new ESRF-EBS storage ring is a major step in an ambitious upgrade programme initiated in 2009 and concerning both the beamlines and the accelerator. The main components of the new ring (magnets, vacuum chamber…) are now being constructed, the existing ring will be stopped at the end of 2018 and after one year of shutdown the commissioning of the new ring will start beginning of 2020. Together with the improvement of beamline performance, this fully renewed facility will be able to address the most challenging X-ray science questions for the subsequent 10-20 years.

5.5.16 Parameters

Table 7: Storage ring parameters

	ESRF	ESRF-EBS
Energy [GeV]	6.03	6
Circumference [m]	844.391	843.977
Beam current [mA]	200	200
Natural emittance [pm]	4000	132
Damping time (H/V/L) [ms]	7.1/7.0/3.5	8.8/13/9.1
Bunch length [mm]	4.28	2.91
Energy spread	$1.06 \cdot 10^{-3}$	$0.93 \cdot 10^{-3}$
E_{loss}/turn [MeV]	4.90	2.52
RF voltage [MV]	9	6
Synchrotron frequency [kHz]	2.10	1.30
Momentum compaction	$1.78 \cdot 10^{-4}$	$0.85 \cdot 10^{-4}$
Tunes (H/V)	36.44/13.39	76.21/27.34
Natural chromaticity (H/V)	-130/-58	-109/-82
Operation chromaticity (H/V)	10/10	6/4
Operation emittance (H/V) [pm]	4000/5	110/5
Multibunch lifetime [h]	40-60	17
16-bunch lifetime [h]	20	1.6
4-bunch lifetime [h]	8	1.1

Table 8: Insertion device source point parameters

		ESRF high-β	*ESRF low-β*	*ESRF-EBS*
H β	[m]	37.6	0.35	6.90
H η	[mm]	134	31	1.73
H beam size	[μm]	387.8	37.4	29.6
H beam divergence	[μrad]	10.3	106.9	4.28
V β	[m]	3	3	2.645
V beam size	[μm]	3.46	3.46	3.63
V beam divergence	[μrad]	1.15	1.15	1.37

Table 9: Bending magnet source point parameters

		ESRF high-β	*ESRF low-β*	*ESRF-EBS*
H β	[m]	1.06	1.61	1.42
H η	[mm]	51	75	16.6
H beam size	[μm]	77.9	112	20.5
H beam divergence	[μrad]	111	98.5	24
V β	[m]	42.0	32.2	3.00
V beam size	[μm]	12.9	11.3	3.9
V beam divergence	[μrad]	0.5	0.4	3.1

5.5.17 **References**

1. "ESRF Upgrade Programme Phase II (2015-2022) - Technical Design Study", http://www.esrf.fr/Apache_files/Upgrade/ESRF-orange-book.pdf, 2014

2. D. Einfeld, L. Schaper, M. Plesko, "A lattice Design to Reach the Theoretical Minimum Emittance for a Storage Ring", Proceedings EPAC 1996, Sitges 1996

3. "Detailed Design Report on the MAX IV Facility", https://www.maxlab.lu.de/node/1136, 2010

4. K. Deb, "A Fast and Elitist Multiobjective Genetic Algorithm: NSGA-II", IEEE transactions on evolutionary computation, vol. 6, no. 2, April 2002

5.6 Multi-objective Dynamic Aperture Optimization with Nonlinear Driving Terms for Storage Rings

Yongjun Li

Mail to: yli@bnl.gov

Brookhaven National Laboratory, Upton NY-11973, New York

5.6.1 **Introduction**

In designing ring-based X-ray light sources, accelerator physicists are pushed very hard to achieve low emittance pursuing bright photon beam. Low emittance means strong focusing quadrupoles, which requires strong sextupoles (installed at in dispersive region) to compensate chromatic aberrations. These strong sextupoles result in small dynamic aperture (DA), making it difficult to realize efficient off-axis injection, and maintain sufficient Touschek lifetime. Based on modern accelerator theory, improvement of DA can be realized by minimizing various nonlinear driving terms (NDT), which can be computed up to some certain orders [1]. But there are already several tens terms even we only compute them up to the 2nd order. In the meantime, the designers have to face the difficulty of specifying reasonable weights for numerous NDTs, if the conventional optimization method (single merit function) is used. So far, there is no systematic solution to address this difficulty. Designers need to choose these weights based on their own experience.

Recently people used a new method of simultaneously optimizing dynamic and momentum aperture [2], or beam lifetime [3, 4] with multi-objective genetic algorithm (MOGA). This method is very successful. The optimization heavily relies on a powerful and reliable tracking simulator to directly probe the dynamic and momentum apertures (or beam lifetime). Usually the optimization driven by the element-by-element symplectic-tracking simulator [5] is very time-consuming, especially when ring scale is big. This time-consuming objective function computation significantly degrades optimization efficiency although powerful parallel computers are available.

Based on previous genetic optimization experiences and results, we observed that: (1) the driving terms reduce automatically once DA was used as one of the objectives for optimization [3]; (2) the optimal candidates always have small driving terms, while small driving terms do not always imply a good DA [2]. In another word, having small driving terms is a necessary but insufficient condition for ensuring a good DA. This observation hints an efficient optimization method. First we can apply MOGA to optimize these driving terms simultaneously to avoid blindly assigning weights on them. Then a tracking simulation can be carried out as a final filter to select the best solutions among the last generation candidates. The reason of why this new strategy becomes more efficient is that the optimization driven by analytical formulae computation is much faster than direct tracking simulation. We can further extract the correlation between DA and driving terms from the raw data of simulation to identify which resonances dominate DA. The correlations can help us to better understand the nonlinearity from the view of beam dynamics.

5.6.2 Multi-Objective Genetic Algorithm

Multi-objective genetic (evolution) algorithm [6] has been widely adopted in storage ring lattice design in the last decade. Ring designer used it to find low emittance linear lattice for a given magnet layout [7, 8], or to optimize DA by varying sextupole configuration. The method we are using is an elitist multi-objective evolutionary algorithm proposed by K. Deb [6]. It is a population based evolution algorithm to find the Pareto optimum iteratively. Firstly, a fixed number of candidates are initialized as the first generation, and they are random chosen and uniformly distributed in their allowed ranges. Then one pair of them are randomly chosen as parents to cross over to generate two new children according to a certain probability density function. The process of crossover is repeated until the population is doubled. Next all children mutate randomly also with a certain probability density function. The objective functions and constraints are evaluated for each of these new children. The whole population, including the parents, is then sorted according to their dominance relations. Since parents are included into sorting, elitists are kept once they are found, which can speed up the performance of optimization significantly by preventing the loss of good solutions. Candidates not dominated by anyone are in the first rank. Only half of the better candidates are kept by dropping out the candidates with larger rank. Within same rank, candidates in a high population density region have lower priority to be selected. Up to this point, the population is kept the same but the overall qualities in terms of objective functions and constraints are evolved not worse than the previous population before crossover and mutation. The population is evolved generation by generation until it converges or the maximum number of iterations is reached.

5.6.3 Nonlinear Driving Terms

For storage rings, NDTs can be obtained by concatenating individual maps into one-turn-map via the similarity transformation and BCH formula in Lie algebra language [1]. C-X. Wang [9] explicitly derived all 2nd-order driving terms due to sextupoles and chromatic effects of quadrupoles. We combined them with 1st order driving terms as optimization objectives. Of course h_{11001} and h_{00111} are excluded to control linear chromaticity. In the meantime, h_{11110}, h_{22000}, and h_{00220} are imposed with some extra

constraints to reduce tune dependence on amplitude. In the next section, we demonstrate this method by applying it on NSLS-II storage ring dynamic aperture optimization.

5.6.4 Applications on NSLS-II ring

5.6.4.1 *NSLS-II ring layout*

NSLS-II [10] lattice has 30 double bend achromatic (DBA) cells. Two DBA cells with mirror symmetry have low- and high-beta functions at short and long straight sections. The linear optics for one cell is illustrated in FIG. 1. The whole bare lattice has 15-fold symmetry. Each DBA cell has nine sextupoles. Three of them are sitting in the dispersive region for chromaticity correction. The other six are geometric sextupoles.
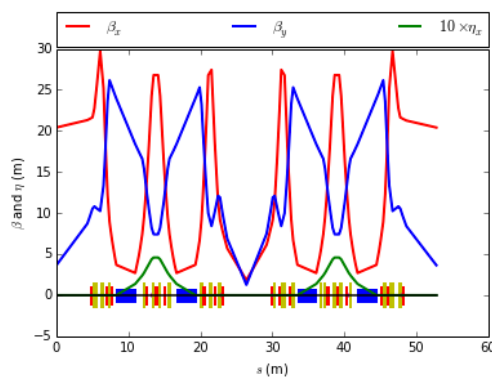
Figure 1: NSLS-II optics in one super-cell

5.6.4.2 *Chromaticity +7/+7 lattice*

To effectively suppress beam transverse instabilities at high beam current, high positive linear chromaticity is preferable. High positive linear chromaticity means stronger sextupoles, and then a smaller DA. The DA optimization is therefore more demanding than a low chromaticity configuration. In this case, the linear chromaticity is corrected to +7/+7 with three chromatic sextupoles (Fig. 2). Then the free parameter knobs left for DA optimization are 6 families geometric sextupoles located in non-dispersive straights. Our objective functions are ~ 30 low order NDTs totally. The searching spaces of free variables (i.e. sextupole strengths) are limited within the ranges limited by the engineering specification and power supply polarities. Three tune-dependency-on-amplitude terms were imposed with some extra constraints to boost the convergence of solutions. We use a population of 4000, and run for 100 generations. With 100 Xeon 2.33 GHz CPUs in a Sun Grid Engine cluster, it takes several hours to finish the optimization. Next we use a symplectic tracking code to check the DAs for all these 4000 candidates in the last generation. Base on tracking results, we can choose some of the best solutions among them.
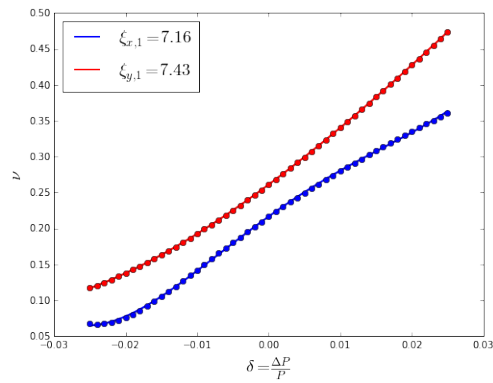
Figure 2: Tune vs. energy deviation for linear chromaticity +7/+7
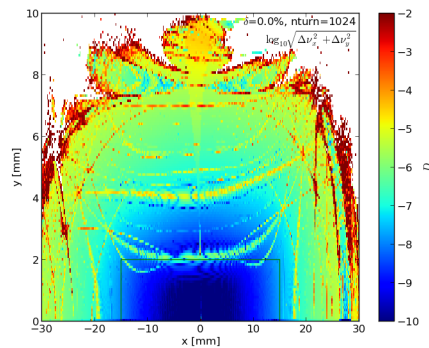
Figure 3: Dynamic aperture in x-y plane at the injection point
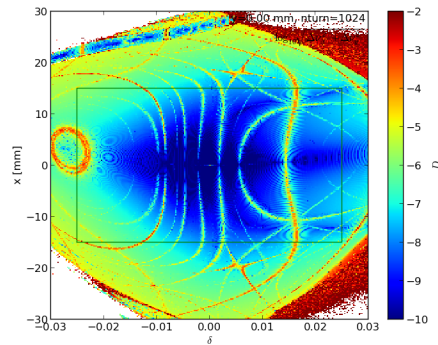
Figure 4: Energy acceptance in x-δ plane at the injection point

For one of best solutions, the chromaticity curve is illustrated in FIG. 2. The frequency map analysis was carried out as shown in FIG. 3 and 4. This sextupole configuration has been successfully tested at the NSLS-II ring. DA is proved to be sufficient for a decent injection efficient (>90%) and up to 18 hours lifetime was observed with 10mA stored beam in 100 bunches.

5.6.4.3 *Preliminary study for low-alpha lattice*

Our second application is optimizing a Low-alpha lattice. Such lattice has a short bunch longitudinal length, which can provide coherent synchrotron radiation in the THz range. This preliminary study focuses on the feasibility of low-alpha mode on the NSLS-II storage ring. The DA optimization is more difficult than the previous one, because we need to control linear chromaticity, DA and longitudinal stability simultaneously with sextupole configuration. There is no dispersion-free section, thus we can't separate chromaticity correction and DA optimization. Once the zero-th order momentum compactor is small enough, the higher order terms will play important roles in the longitudinal motion stability. And, we still need sufficient DA and energy acceptance to achieve decent injection efficiency and lifetime. All these optimization objectives need to be satisfied simultaneously. The preliminary results of linear optics, DA, energy acceptance and stable RF bucket are shown in FIG. 5-8, which are positive and promising.
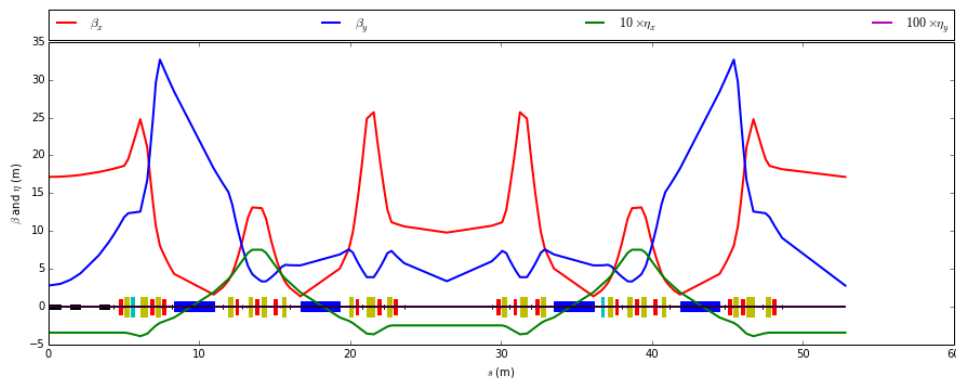
Figure 5: Linear optics for low-alpha configuration
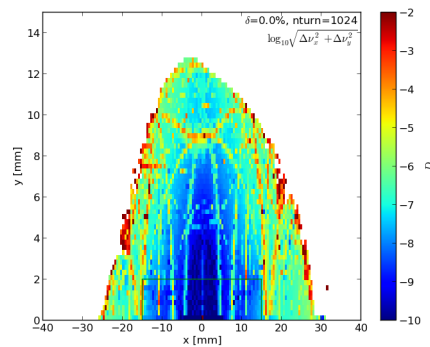
Figure 6: Dynamic aperture in x-y plane at the injection point
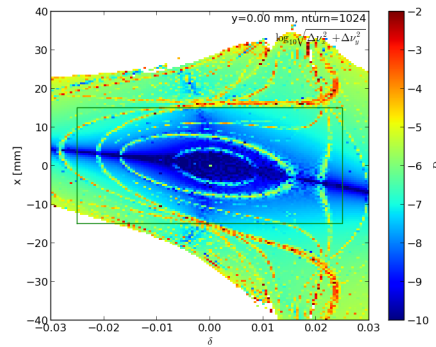
Figure 7: Energy acceptance in x-δ plane at the injection point
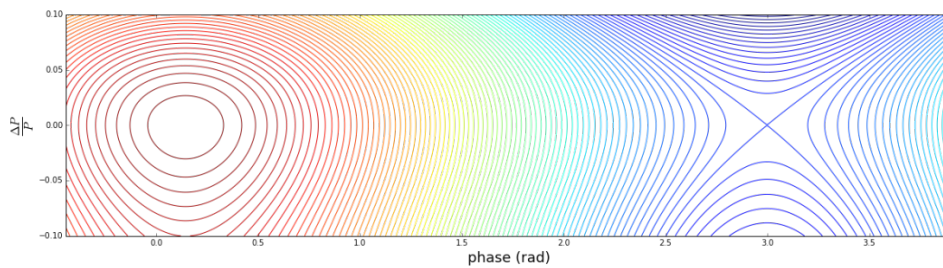
Figure 8: Stable bucket for low alpha configuration

5.6.5 Correlation between DA and NDTs

MOGA optimization can produce numerous raw data, which can be used to study the correlations between DA and NDTs. Usually, within the last generation, none of candidate in the same rank is dominated by any others. From the view of multi-objective optimization, they are equally good if only considering NDTs. But from the aspect of dynamic aperture, they are quite different. We use DA tracking simulator to compute their DAs for all 4000 candidates, and illustrate their correlation with the summation of NDTs in FIG. 9. By observing the correlation, we can conclude that having small low order NDTs is necessary but insufficient condition for having a good DA (as marked with red A). The necessity is demonstrated by observing that all candidates with large DAs must have small NDTS without exception.
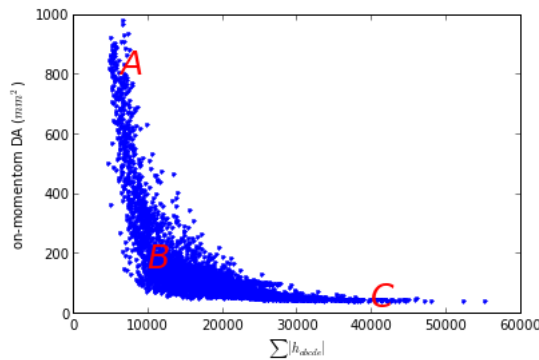
Figure 9: Correlation between DA and NDTs

5.6.6 Summary

An efficient approach of using MOGA driven by NDTs computation to optimize storage ring DA is discussed. The optimization produces numerous raw data, which can satisfy the necessary condition to have a good DA at the first step. Among them we can select some good solutions with the DA tracking code. Applying this approach on the NSLS-II bare lattice to achieve a high positive chromaticity was demonstrated experimentally. And a preliminary study on low-alpha lattice is quite positive also.

5.6.7 References

1. A. Dragt, AIP Conf.Proc. 87, 147 (1982).

2. L. Yang, Y. Li, and et al., Phys. Rev. ST, Accel. Beams 14, 054001 (2011).

3. M. Borland, L. Emery, V. Sajaev, and A. Xiao, Conf. Proc. C110328, 2354 (2011).

4. L. Wang, et al., Conf. Proc. C1205201, 1380 (2012).

5. H. Yoshida, Physics Letters A 150, 262 (1990).

6. K. Deb, Multi-Objective Optimization Using Evolutionary Algorithms (Wiley, 2001).

7. L. Yang, et al., NIM A 609, 50 (2009)

8. C. Sun, et al., Phys. Rev. ST Accel. Beams 15, 054001 (2012).

9. C. X. Wang, ANL/APS/LS-330 (unpublished) (2012).

10. BNL, "NSLS-II Conceptual Design Report (CDR)", (2013)

5.7 Emittance upgrade for the SPEAR3 storage ring

Xiaobiao Huang, Yuri Nosochkov, and James Safranek

Mail to: xiahuang@slac.stanford.edu

SLAC National Accelerator Laboratory, Menlo Park, CA, USA

5.7.1 Introduction

SPEAR3 is a third generation light source at the SLAC National Accelerator Laboratory. It was built on the footprint of its predecessors, SPEAR and SPEAR2, and was commissioned in 2004 [1]. With a circumference of 234 m, the 3-GeV storage ring

has an emittance of 10 nm. It operates with a beam current of 500 mA in top-off mode, with frequent refills at 5-minute interval.

Although SPEAR3 remains one of the best performing storage ring light sources, in recent years many new rings came online with lower emittance and higher photon beam brightness. This can be clearly seen in Figure 1, which shows the emittances of the newer medium-energy light sources currently in operation. It's worth noting that the emittance of the present SPEAR3 lattice is relatively low for the size and beam energy of the ring. Also shown in Figure 1 is the emittances of the storage rings normalized by a factor $\propto E^2/C^3$, where is beam energy and the ring circumference. By adopting a compact double-bend achromat (DBA) lattice design, SPEAR3 is one of the most efficient in achieving low emittance.
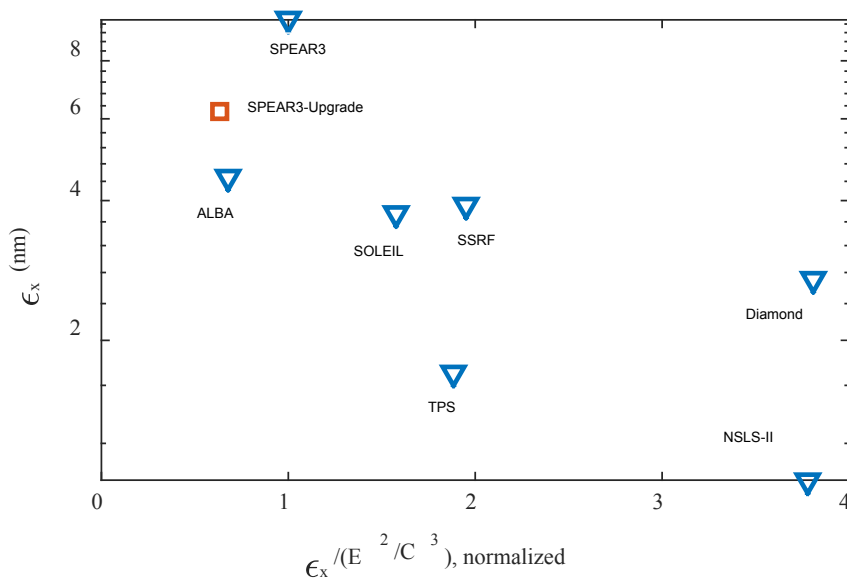
Figure 1: Horizontal emittances ϵ_x and $\epsilon_x/(E^2/C^3)$ for SPEAR3 and newer medium-energy light sources in operation. The $\epsilon_x/(E^2/C^3)$ factor is normalized by the SPEAR3 value.

Nonetheless, it would be desirable to push the SPEAR3 emittance further down to benefit users with higher brightness photon beams. The preferred approach is to reach lower emittance by changing the storage ring optics on the existing machine with minimum additional investment. In the last few years we studied the lattice upgrade options for SPEAR3 and identified a path to significantly reduce the emittance.

In this newsletter we report the accelerator physics work for the SPEAR3 emittance upgrade project. In section 2 we will discuss the potential of the SPEAR3 lattice. In section 3 we discuss the lattice upgrade options. In section 4 the optimization of the lattice performance in simulation is shown. In section 5 we discuss the required hardware upgrade and the experimental work in optimizing and characterizing the upgrade lattices. Section 6 gives a brief summary.

5.7.2 The SPEAR3 lattice layout and its potential

SPEAR3 has a race-track layout. The ring consists of 14 standard DBA cells and 4 matching DBA cells (see Figure 2). The two matching cells on each side enclose a long straight section. One of the long straight sections was modified to host two short straight sections with chicanes [2]. The bending angles of the matching cell dipoles are ¾ of the standard cell dipoles. The standard cell is composed of two dipoles, five quadrupoles, and four sextupoles over a cell length of 11.7 m.
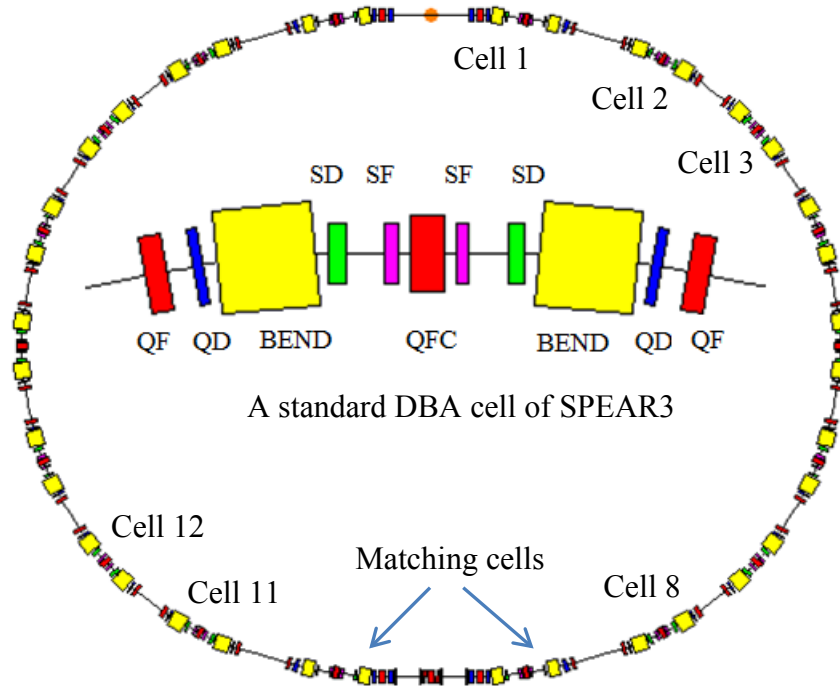
Figure 2: Layout of the SPEAR3 ring and a standard DBA cell (inlet).

Clearly the performance of the SPEAR3 lattice is mainly determined by its standard DBA cells. The potential of the DBA cell can be explored with the global scan technique [3]. Requiring reflection symmetry about the cell center, there are only three quadrupole variables in the cell, the strengths of the QFC, QF, and QD magnets. In the global scan the normalized gradients, $K_1 = \frac{1}{B\rho} \frac{\partial B_y}{\partial x}$, of all three magnets were varied between -2 m^{-2} and 2 m^{-2} with a step size of 0.02 m^{-2}. Only 4.4% of all scanned solutions are stable, almost all of which have positive QFC gradient (i.e., focusing in horizontal plane). Of these stable solutions, about 80% have horizontal emittance under 100 nm and $\beta_{x,y} < 100$ m at the ends of the cell (namely, at the center of the standard insertion device straight section). The distribution of these solutions in the quadrupole gradient parameter space is shown in Figure 3 with the color code indicating the horizontal emittance. The distribution of the solutions in the (ϵ_x, α_c) parameter space is

shown in Figure 4(a), where α_c is the momentum compaction factor. The potentially useful solutions are concentrated at the corner with small emittance and small momentum compaction factor. An expanded view of the solutions in this region is shown in Figure 4(b), where the horizontal dispersion D_x at the end of cell is indicated with color coding. Three existing lattice options for SPEAR3, the low alpha lattice [4], the achromat lattice, and the present 10-nm low emittance lattice are also shown. Each stripe of dots in Figure 4(b) corresponds to a QFC gradient value.
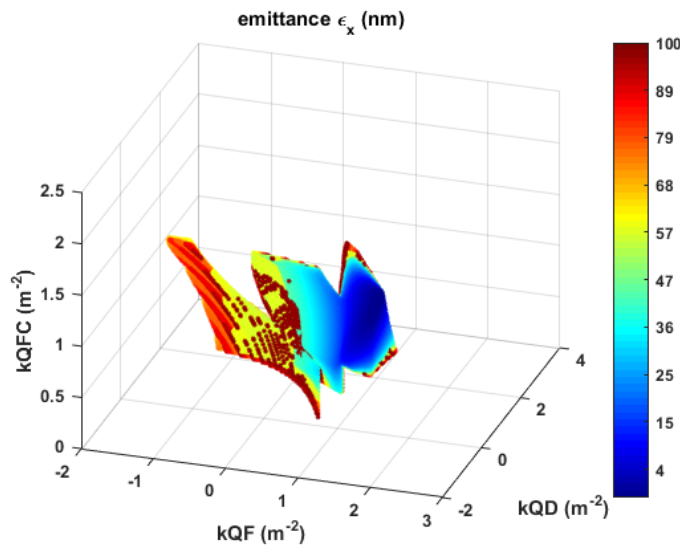
Figure 3: Distribution of all stable solutions with $\epsilon_x < 100$ nm and $\beta_{x,y} < 100$ m (at ends of the DBA cell). Color code indicates emittance.

(a) (b)
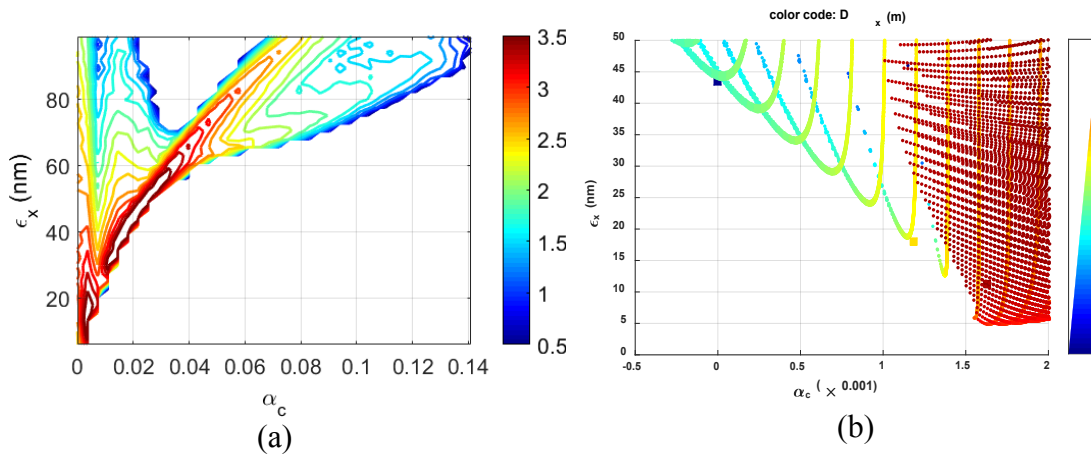
Figure 4: (a) Contour plot of stable solution distribution in the (ϵ_x, α_c) parameter space with color code indicating density of solutions in, where is the number of solutions on a uniform grid; (b) horizontal dispersion (at end of cell) vs. (ϵ_x, α_c) parameters for low emittance and low momentum compaction lattice solutions.

From the distribution of stable solutions we find that for the SPEAR3 standard DBA cell there is only one region in the quadrupole strength parameter space that contains lattice solutions with low emittance and this region is around the present operation lattice. Additional filters are applied to select the candidate solutions for a lower emittance upgrade. Requiring that $\epsilon_x < 12$ nm and that $\beta_x < 20$ m and $\beta_y < 10$ m at the end of the cell, only 0.16% of the scanned solutions qualify.

The low emittance lattices tend to have a positive dispersion function at the insertion device (ID) center [Figure 4(b)]. With a finite dispersion, the more relevant performance parameter is the effective emittance, defined as

$$\epsilon_{\text{eff}} = \epsilon_x \sqrt{1 + \frac{\mathcal{H}\sigma_E^2}{\epsilon_x}}, \tag{1}$$

where ϵ_x is the natural emittance, $\mathcal{H} = \frac{1}{\beta_x}[D_x^2 + (\alpha_x D_x + \beta_x D_x')^2]$ is the dispersion invariant, β_x is the horizontal beta function at the ID center, and σ_E is the energy spread of the beam. Figure 5 shows the effective emittance vs. horizontal phase advance and dispersion function at the ID center for all candidate solutions that meet the requirements set forth in the above.
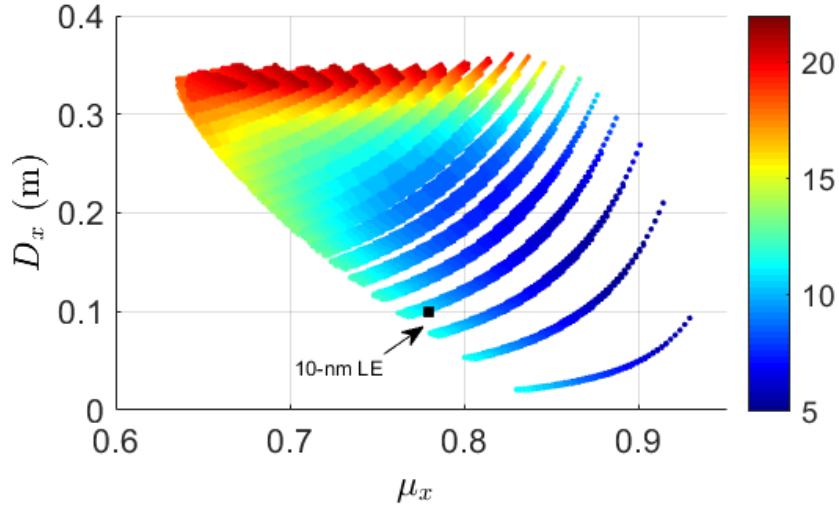
Figure 5: Effective emittance (color code) as a function of horizontal phase advance ($\psi_x = 2\pi\mu_x$) and dispersion at the end of cell.

Also shown in Figure 5 is the standard cell parameters for the present 10-nm lattice, which has horizontal phase advance of and $\mu_x = 0.78$ and dispersion $D_x = 0.1$m at the ID center. Figure 5 suggests that, starting from the present 10-nm lattice, the paths to lower effective emittance are to increase the horizontal tune and to increase the dispersion at the ID center.

Data from the global optics scan for the SPEAR3 standard DBA cell reveal several other interesting characteristics of the lattice. For example, the vertical beta function at

the ID center decreases with the vertical phase advance of the cell monotonically in a fashion almost independent of the horizontal phase advance. Increasing horizontal phase advance causes an increase of the magnitude of the horizontal natural chromaticity. Increasing the vertical phase advance, however, has a slight tendency to reduce the magnitude of the vertical natural chromaticity. For lattice solutions with lower emittances, the sextupole strengths required to correct chromaticities to 0 are not necessarily higher than the present lattice. Lower vertical phase advance is preferred for weaker sextupole strengths.

We also investigated the possibility of reducing the emittance by adding two symmetrically placed quadrupoles to the DBA cell, each between the SF and SD sextupole magnets. No improvement can be made with this approach.

5.7.3 Lattice options for lower emittance upgrade

To make full ring lattices the optics of periodic, DBA cells need to be matched to the racetrack sections with the matching cells. Matching setup and conditions for the east and west side section are not identical because the east side long straight hosts the double waist chicane. However, some requirements are the same for both sides. For example, the center of each 4.5-m long matching straight sections should be a waist and the vertical beta function needs to be $\beta_y = 2.5$ m at the waists to accommodate insertion device magnets with small vertical apertures. We try to make the phase advances on the east and west side racetrack sections equal to maintain the $N = 2$ super-periodicity.

Based on the results of the global scan of the SPEAR3 standard DBA cell, the horizontal tune of the ring needs to be increased in order to substantially reduce the emittance. To achieve a meaningful emittance reduction we decided to increase the horizontal tune by at least one unit, from $\nu_x = 14.13$ to above 15. Several full ring lattices were built in an initial study for which the horizontal tune were increased up to $\nu_x = 16.13$ while the vertical tune is kept around $\nu_y = 6.22$. The horizontal tunes and emittances for these lattices are shown in Table 1. The emittances shown in the table include radiation damping and quantum excitation effects of the existing SPEAR3 insertion devices.

Table 1: Emittance and amplitude dependent detuning coefficients dependence on horizontal tune for SPEAR3 lower emittance lattices.

Parameter	nominal	Lat 1	Lat 2	Lat 3	Lat 4
Horizontal tune, ν_x	14.13	15.127	15.31	15.54	16.13
Horizontal tune per cell, μ_x	0.780	0.832	0.844	0.850	0.896
Emittance, ϵ_x (nm), w/IDs	9.6	6.8	6.5	6.1	5.5
Detuning coefficient $\frac{1}{2}\frac{d\nu_x}{dJ_x}$, m^{-1}	1820	7660	8920	13480	24900
Detuning coefficient $\frac{1}{2}\frac{d\nu_x}{dJ_y}$, m^{-1}	2120	4980	5590	7810	7880
Detuning coefficient $\frac{1}{2}\frac{d\nu_y}{dJ_y}$, m^{-1}	2140	4410	4870	6040	4300

The lower emittance lattices in Table 1 have smaller dynamic apertures compared to the nominal lattice. It was found that the dynamic aperture reduction is closely related to the amplitude dependent detuning coefficients of these lattices, which are significantly higher than the nominal lattice. Table 1 shows the detuning coefficients, $\frac{1}{2}\frac{d\nu_x}{dJ_x}$, $\frac{1}{2}\frac{d\nu_x}{dJ_y}$, and $\frac{1}{2}\frac{d\nu_y}{dJ_y}$, where $J_{x,y}$ are the betatron action variables, e.g., $J_x = \frac{1}{2\beta_x}[x^2 + (\alpha_x x + \beta_x x')^2]$. Clearly, as the horizontal tune is increased, the detuning coefficients increase very quickly. Large detuning coefficients lead to a large tune footprint on the tune diagram for beams with varying oscillation amplitudes such as the injected beam. Because there is only a limited area on the tune diagram around the working point in which the beam can survive (without hitting resonance conditions and getting lost), large detuning coefficients typically lead to a smaller dynamic aperture. The detuning coefficients are the results of interactions between sextupoles. The rapid increase of detuning coefficients for the SPEAR3 lower emittance lattices is a consequence of deviations of the horizontal phase advances between the sextupoles from the nominal lattice setting.

As it was proven to be infeasible to substantially reduce the detuning coefficients with sextupole or octupole magnets for the SPEAR3 case (see next section), our lattice development effort was focused on the two areas around $\nu_x = 15.13$ and $\nu_x = 15.30$ (lattice options 1 and 2 in Table 1). The storage ring lattice design work was closely related to and impacted by the nonlinear dynamics optimization and the experimental work to be discussed in the next sections. After explorations of the working point and phase advances of the matching cells, two lower emittance lattices were developed as upgrade options. Selected parameters of the lattices are listed in Table 2, in comparison to the achromat lattice and the present operation lattice ("10-nm").

Table 2: Selected parameters of the SPEAR3 emittance upgrade target lattices. The momentum spread for all lattices is $\sigma_\delta = 0.97 \times 10^{-3}$.

Parameter	achromat	10-nm	7-nm	6-nm
tunes, ν_x, ν_y	14.13, 6.22	14.106, 6.177	15.10, 6.16	15.32, 6.18
Emittance, ϵ_x (nm), w/IDs	14.6	9.6	6.7	6.1
Effective emittance, $\epsilon_{x,\mathrm{eff}}$ (nm),	14.6	10.1	7.2	6.7
Horizontal beta, β_x (m), ID	10.22	8.85	8.96	9.46
Vertical beta, β_y (m), ID	4.92	4.86	5.29	5.24
Dispersion, D_x (m), ID	0	0.10	0.11	0.12

The two upgrade lattices are dubbed the 7-nm and 6-nm lattices. Their effective emittances are 7.2 nm and 6.7 nm, respectively. The 6-nm lattice is more challenging in terms of nonlinear beam dynamics. In simulation we demonstrated that its dynamics aperture and Touschek lifetime are adequate for operation. Nonetheless, we developed the 7-nm lattice as a fallback option. The 7-nm lattice is easier to implement and optimize with the existing septum magnet. It may serve as the initial operation lattice after the required hardware upgrade is complete before we transition to the 6-nm lattice through additional experimental development.

5.7.4 Nonlinear dynamics optimization in simulation

The reduced dynamic aperture of the lower emittance lattices is the biggest difficulty for operating with these lattices. Nonlinear dynamics optimization for the lower emittance lattices is essential. In the lattice development we have tried several approaches to improve the dynamic aperture and the Touschek lifetime.

Because the large amplitude dependent detuning is an important cause of dynamic aperture reduction, we tried to reduce the detuning coefficients by adding sextupoles or octupoles to the lattice. We considered modifying the corrector magnets between the QF and QD magnets in the standard cell to combined sextupole and corrector magnets as done for the ALS emittance upgrade [5]. Detuning coefficients were calculated for a wide range of sextupole strengths and various lattice options. It was found that the new sextupole family change $\frac{d\nu_x}{dJ_x}$ and $\frac{d\nu_y}{dJ_y}$ almost linearly in opposite

directions such that the sum of the two coefficients remain nearly constant. Tracking simulation done for lattices with reduced horizontal detuning and increased vertical tuning shows that there is no gain in dynamic aperture as the growth of vertical oscillation amplitude combined with small vertical physical aperture tends to limit the dynamic aperture.

Alternatively, we considered adding three families of octupole magnets to reduce the detuning coefficients (modifying six magnets). Varying the octupole strengths between $K_3 \equiv \frac{1}{6B\rho}\frac{\partial^3 B_y}{\partial x^3} = -200 \text{ m}^{-3}$ and 200 m^{-3} for all three families, we can't find a solution that substantially reduces all three detuning coefficients.

The approaches of adding sextupole or octupole magnets were not pursued further because of their ineffectiveness and high cost. Instead, we adopted a less expensive approach of regrouping the existing sextupoles to gain additional independent control and using the additional "knobs" to improve nonlinear dynamics performance. Originally for SPEAR3 the SF and SD magnets in the standard cells were powered in series, respectively. Combined with the two sextupole families in the matching cells, there were four sextupole families. We broke up the standard cell SF and SD magnets into four groups each, with mirror symmetry about the storage ring center lines for magnets in each group. For example, the SF magnets in cell 2, 8, 11, 17 are in one group that is powered in series. Six new power supplies and new cables were added, resulting in a total of 10 sextupole knobs. The sextupole power supply upgrade was completed in the 2014 summer shutdown.

Varying the sextupole knobs while keeping the chromaticities at fixed values, one could change the strengths of the detrimental nonlinear resonances to improve the nonlinear dynamics performance. This was first tested through nonlinear dynamics optimization studies in simulation. In the studies the dynamic aperture and momentum aperture are simultaneously optimized with multi-objective optimization algorithms. Particle tracking is used to evaluate the dynamic aperture and momentum aperture. It is necessary to track 5000 turns in order to determine the dynamic aperture reliably since some particles can get lost through resonances gradually over thousands of turns.

Initially we selected 6 sextupole families as free knobs and used the other 4 sextupole families (combined as two families) to compensate the chromaticity changes introduced by the free knobs. Two multi-objective optimization algorithms, the multi-objective genetic algorithm (MOGA) [6,7] and the multi-objective particle swarm optimization (MOPSO), were used for dynamic aperture and momentum aperture optimization. Details of the tracking and optimization setup, and a comparison of optimization performance for the two algorithms were reported in Ref. [8]. It was demonstrated that the MOPSO method has advantages over the MOGA method. First, MOPSO converges much faster than MOGA. Second, MOPSO does not need initial

seeding of good solutions while MOGA does. The 6-nm target lattice was used for the comparison study in Ref. [8].

Recently, following the online optimization of nonlinear dynamics described in Ref. [9], we updated the optimization study to use 8 free sextupole knobs, with each knob being a combination of all 10 sextupole families that does not change the chromaticities. The combination sextupole knobs are determined with the chromaticity response matrix (with a dimension of 2 by 10) by calculating its singular value decomposition. Each knob is a basis vector of the null space of the response matrix. The objective functions of the best solutions of MOPSO optimization for the 6-nm lattice for the 6-knob setup and the 8-knob setup are compared in Figure 6. The 8-knob solutions have much better momentum aperture than the 6-knob solutions.
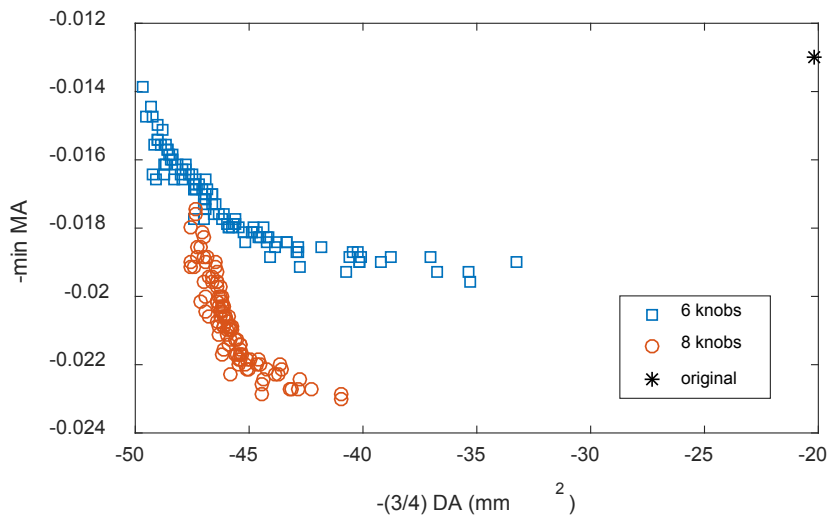
Figure 6: Objective functions of the final best solutions from MOPSO optimization for the 6-knob setup and the more recent 8-knob setup for the 6-nm lattice. "DA" for dynamic aperture and "MA" for momentum aperture.

Dynamic apertures for selected lattice solutions from the optimization results are checked by tracking with lattice errors. Systematic and random magnetic errors and perturbations from insertion devices (not including the new BL5 elliptically polarized undulator) are included. Lattices with 15 random error seeds are tracked. Linear optics are corrected to give a 1% beta beating for both transverse planes. Linear coupling is corrected to give a 0.2% coupling ratio (i.e., ϵ_y/ϵ_x). The vertical physical aperture at the injection septum is set to 3 mm to account for the small aperture IDs in the ring. The dynamic apertures at the injection septum for the 6-nm and 7-nm lattices with optimized sextupole solutions are shown in Figure 7. The average on-axis dynamic apertures on the injected beam side ($x < 0$) are 12 mm and 13.5 mm for the 6-nm and 7-nm lattices, respectively. The momentum aperture is also checked for both lattices. It is found that the Touschek lifetime at 500 mA beam current with a 0.1% coupling ratio is 5.9 hrs (6-

nm lattice) and 6.3 hrs (7-nm lattice), respectively for the optimized new lattices, which are comparable to the present 10-nm operation lattice.
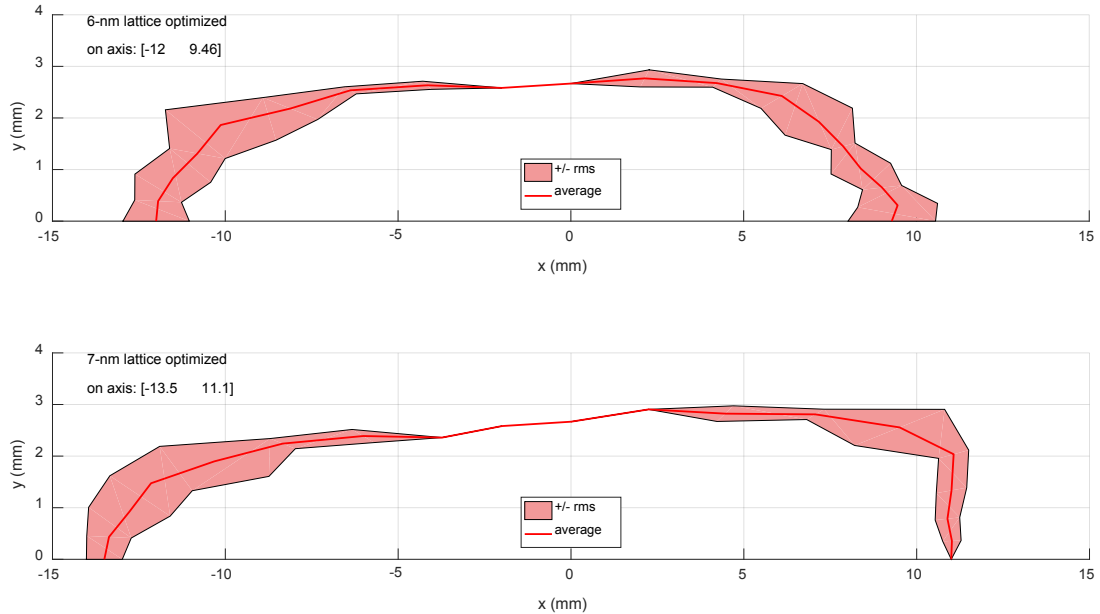
Figure 7: Dynamic aperture at the septum magnet for the 6-nm (top) and 7-nm (bottom) optimized lattices. Systematic and random magnet errors were included in tracking. Linear optics errors were corrected to 1% beta beat rms.Coupling is corrected to 0.2%. Average dynamic aperture and average $+/-$ rms of 15 random seeds are shown.

5.7.5 **Hardware requirements and experimental lattice study**

5.7.5.1 *Required hardware upgrade for operation*

The lower emittance lattices for SPEAR3 cannot be used for operation until some hardware upgrades are complete. The required hardware upgrades include the increase of kicker K2 pulser voltage, the addition of sextupole power supplies, and the injection septum magnet upgrade.

The SPEAR3 injection system includes three pulsed stripline kickers located in three adjacent straight sections. Kicker K2 is at the same straight section as the septum magnet and is shorter than the other two kickers because of space limitations. The three kickers make a horizontal closed orbit bump at the septum for less than one turn when the injected beam comes in. For previous SPEAR3 lattices the horizontal phase advance per standard cell is $0.78 \times 2\pi$ and hence the phase advance between kicker K1 and K3 is very close to 3π. Therefore, only a small kick from K2 is needed to form a closed orbit bump. As the horizontal tune is increased for the emittance upgrade lattices and the phase advance from K1 to K3 deviates from 3π, a stronger K2 is needed. For the 10-nm lattice, to make the 23-mm nominal kicker bump, the kick angles for K1, K2 and K3 are 2.2 mrad, -1.3 mrad, and 2.3 mrad, respectively. The kicker bump will be reduced to 13.5 mm for the upgrade lattices to alleviate the kicker strength requirements. The required kick angles are 1.3 mrad, -1.5 mrad, and 1.4 mrad for the 7-nm lattice

and 1.5 mrad, -2.0 mrad, and 1.6 mrad for the 6-nm, respectively. An upgrade to the K2 pulser to increase its peak voltage is necessary to deliver the required stronger kick. This upgrade was completed in 2014 summer shutdown.

The sextupole power supply upgrade was needed to obtain additional free knobs for nonlinear dynamics optimization. This was done by splitting the standard cell sextupole magnets into smaller groups as described in the last section. The sextupole power supply upgrade was completed in 2014 summer shutdown and the sextupole knobs have been used to achieve larger dynamic aperture on the machine [9].

The injection septum upgrade consists of two major changes. First, the septum magnet will be moved toward the stored beam to reduce the separation between the stored and injected beams. The distance of the septum wall to the unkicked stored beam will be reduced from the present value of 25 mm to 15 mm after the upgrade. This reduces the required kicker bump and the strength of the K2 kicker. The SPEAR end of the Booster-to-SPEAR (BTS) transport line needs to be realigned accordingly. Second, the septum wall thickness will be reduced from the present value of 5.4 mm to 2.5 mm. This is necessary because the upgrade lattices have smaller dynamic aperture than the 10-nm lattice. Reducing the septum wall thickness is equivalent to reducing dynamic aperture requirement. With the septum upgrade, the required dynamic aperture for full capture of the injected beam is estimated to be 10 mm, which includes the septum wall thickness (2.5 mm), 5σ half size of the stored beam (1.6 mm), 5σ full size of the injected beam (4.6 mm), and a 1.3 mm tolerance.

It is critical to have small magnetic field leakage on the stored beam side as such fields will perturb the stored beam during injection, causing transient oscillation and potentially reducing the dynamic aperture. The new injection septum magnet is expected to be installed in the 2017 summer shutdown.

5.7.5.2   *Experimental test and optimization of lattices*

Extensive experimental studies were done on SPEAR3 during the 2011-2013 runs to test and optimize the lower emittance upgrade lattices. With mis-matched kicker bumps, the 7-nm and 6-nm lattices achieved injection efficiency of ~50% and ~30%, respectively. A large DC orbit bump at the injection septum was needed for the 6-nm lattice. These experiments helped guide the design and simulation studies, for example, in choosing the working points and the distribution of phase advances between the matching and standard cells [8]. However, the vertical beta function at the matching straights for the lattices was $\beta_y = 3{\sim}4$ m, instead of the required value of 2.5 m. Lattices meeting the $\beta_y = 2.5$ m requirement have poorer dynamic aperture and are more difficult to implement without the injection septum upgrade, especially for the 6-nm lattice. During the 2015-2016 run we implemented the 7-nm lattice that meets all operation optics requirements.

After the sextupole power supply upgrade, during the 2014-2015 run, we developed and tested techniques to optimize nonlinear beam dynamics performance with the additional sextupoles knobs using online optimization algorithms. The test was done on the 10-nm operation lattice. In these experiments the injection efficiency was first lowered by reducing the injection kicker bump, then the online optimization algorithm

RCDS (robust conjugate direction search) [10] or the MOPSO algorithm were used to bring the injection efficiency up by turning the 8 combined sextupole knobs while keeping chromaticities fixed. Measurements showed that a significant increase of dynamic aperture, from 15.1 mm to 20.6 mm, was achieved [9]. The same techniques have been applied to the 7-nm lattice and a noticeable gain of dynamic aperture was obtained. However, because the kicker bump is not closed for the 7-nm lattice and the mismatch, which has a direct impact on the injection efficiency, is also affected by the sextupole knobs, the dynamic aperture improvement by online optimization is limited as compared to the 10-nm lattice case. We expect additional improvement after the septum upgrade.

An optimized sextupole solution from MOPSO in simulation for the 7-nm lattice has been dialed in on the machine in a test. After correcting the chromaticities to the nominal values of [3, 3], the dynamic aperture was measured. Results of dynamic aperture measurement for the dial-in sextupole solution and the online optimization solution are shown in Figure 8 left plot at two BL5 EPU gap values. In the measurements kicker K1 is fired with increasing strength until beam is lost. For both sextupole solutions the dynamic aperture is large enough to sustain the beam for kicker K1 voltage over 1.0 kV, which corresponds to 1.21 mrad. The measured dynamic aperture is at least 11.5 mm.

We also characterized the Touschek lifetime for the 7-nm lattice. In the experiment we filled 18 mA in 10 bunches so that the bunch current was the same as the 500 mA operation condition in which we fill 280 bunches. The coupling ratio was set to 0.12% and was verified with orbit response matrix measurement. The beam lifetime was measured at each step as the RF voltage was reduced (Figure 8 right plot). The Touschek lifetime was found to be 6 hrs at the nominal RF voltage.
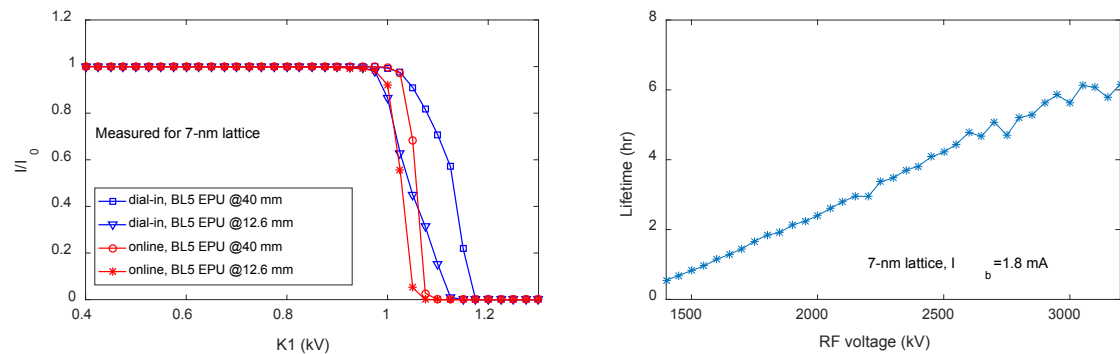
Figure 8: Dynamic aperture (left) and Touschek lifetime (right) measurements for the 7-nm lattice with optimized sextupole setting.

The dynamic aperture and Touschek lifetime measurements indicate that the 7-nm lattice is ready for operation as soon as the injection septum upgrade is complete. The 6-nm lattice will be implemented after additional experimental effort.

5.7.6 Summary

After a full exploration of the potential of the SPEAR3 standard DBA cell and several rounds of lattice design and optimization, we have designed two low emittance upgrade lattices for the SPEAR3 storage ring. The two lattices have effective emittances of 7.2 nm and 6.7 nm, respectively, as compared to the present value of 10.1 nm. Nonlinear beam dynamics optimization with multi-objective optimization algorithms in simulation made significant improvement for the dynamic aperture and Touschek lifetime of the upgrade lattices, using sextupole knobs as free variables. Simulation results show that both lattices meet operation requirements after a few relatively low cost hardware upgrades.

Two hardware upgrades have been completed already. One was to increase the kicker K2 pulser voltage. The other was to add 6 sextupole power supplies with new cables. The remaining upgrade is to replace the injection septum magnet in order to reduce the septum wall thickness and to reduce the separation between the stored beam and the injected beam. This is scheduled to complete in the 2017 summer shutdown.

The 7-nm lattice has been implemented on the machine. Its dynamic aperture has been partially optimized with online optimization. The optimized sextupole solution from simulation has also been verified on the machine. Beam based measurements showed that the dynamic aperture and the Touschek lifetime of the optimized solutions will meet the operation requirements when the injection septum upgrade is completed.

5.7.7 References

1. J. Safranek, et al, "SPEAR3 Commissioning", Proceedings of EPAC 2004, Lucerne, Switzerland (2004)

2. J. Corbett, et al, "Implementation of Double-Waist Chicane Optics in SPEAR3", Proceedings of EPAC 2006, Edinburgh, Scotland (2006)

3. David S Robin, Weishi Wan, Fernando Sannibale, and Victor P. Suller, "Global analysis of all linear stable settings of a storage ring lattice", Phys. Rev. ST Accel. Beams, 11, 024002, (2008)

4. X. Huang, J. Safranek, J. Corbett, Y. Nosochkov, J. Sebek, A. Terebilo, "Low alpha mode for SPEAR3", Proceedings of PAC07, 1308-1310 (2007)

5. C. Steier, et al, "Completion of the brightness upgrade of the ALS", Proceedings of IPAC2013, 261-263, (2013)

6. L. Yang, D. Robin, F. Sannibale, C. Steier, W. Wan, "Global optimization of an accelerator lattice using multiobjective genetic algorithms", Nucl. Instrum. Meth. A, 609 (2009) 50

7. M. Borland, V. Sajaev, L. Emery, A. Xiao, "Direct methods of optimization of storage ring dynamic and momentum aperture", Proceedings of PAC'09,

Vancouver, BC, Canada (2009)

8. X. Huang, J. Safranek, "Nonlinear dynamics optimization with particle swarm and genetic algorithms for SPEAR3 emittance upgrade", Nucl. Instrum. Meth. A, 757 (2014) 48-53

9. X. Huang, J. Safranek, "Online optimization of storage ring nonlinear beam dynamics", Phys. Rev. ST Accel. Beams, 18, 084001 (2015)

10. X. Huang, J. Corbett, J. Safranek, J. Wu, "An algorithm for online optimization of accelerators", Nucl. Instrum. Meth. A, 726 (2013) 77-83

5.8 Lattice Design and Optimization for the High Energy Photon Source

Yi Jiao, Gang Xu

Mail to: jiaoyi@ihep.ac.cn

Key Laboratory of Particle Acceleration Physics and Technology,
Institute of High Energy Physics, Beijing 100049, China

5.8.1 Introduction

Early in 2008, a kilometer-scale storage ring light source, originally with a beam energy of 5 GeV and called Beijing Advanced Photon Source and now with a beam energy of 6 GeV and named High Energy Photon Source (HEPS), was proposed to be built in Beijing [1]. Along with the progress in development of the accelerator hardware systems and progress in the ultralow-emittance storage ring beam dynamics studies, the basic lattice structure of the HEPS storage ring has been continuously evolved, from DBA, standard 7BA, TBA, standard 7BA with high-gradient quadrupoles to the 'hybrid' 7BA with high-gradient quadrupoles, while with the goal emittance decreased from about 1 nm.rad to a few tens of pm.rad, approaching the diffraction limit for the range of x-ray wavelengths of interest for scientific community (e.g. ~80 pm.rad for $\lambda = 1$ nm and ~8 pm.rad for $\lambda = 0.1$ nm, with λ being the wavelength). An overview of the worldwide efforts in designing diffraction-limited storage rings (DLSRs) can be found in [2]. Because of the extremely strong nonlinearities in ultralow-emittance lattices, it is a critical issue in the design of a DLSR to reach a good balance between the ultralow emittance and large enough ring acceptance. The former is closely related to the available maximum brightness of the light source, and is determined by only the parameters of the linear-field elements, including the drifts (no field), dipoles (constant magnetic field) and quadrupoles (constant magnetic gradient). While the latter is closely related to the available beam lifetime and injection efficiency and thus the availability and stability of the photon beams to user experiments, and is determined by both the linear optics and the settings of nonlinear elements, e.g., the locations and strengths of the sextupoles (to correct the linear chromaticity) and octupoles. In the following, we will briefly review the design and optimization of the HEPS lattices based on structures

of standard 7BAs with and without high-gradient quadrupoles and hybrid 7BAs with high-gradient quadrupoles, where we will especially introduce the analytical and numerical optimization methods that were used to improve the nonlinear performance of the HEPS designs.

5.8.2 Standard 7BA Lattices without High-Gradient Quadrupoles

The horizontal natural emittance ε_0 of a storage ring can be expressed as

$$\varepsilon_0 = C_q \gamma^2 \frac{F(type)}{J_x} \theta^3 \tag{1}$$

where $C_q = 3.83 * 10^{-13}$ m, γ is the Lorenz factor, J_x is the horizontal damping partition number, the value of $F(type)$ depends on the lattice type [e.g., the minimum F factor for a double-bend achromat (DBA) and a seven-bend achromat (7BA) are ~0.065 and ~0.034, respectively], and θ is the bending angle of the dipole.

Evidently, to reduce the emittance to a very small value, e.g., several tens of pm.rad, the most effective way is to decrease the bending angle of the dipole, or namely, to increase the number of the dipole N_d, which in turn implies a large circumference C ($\propto \sim N_d$) and hence a high budget. To control the budget to a reasonable level and meanwhile minimize the emittance as much as possible, multi-bend achromats with compact layout are necessary to reach a desirable DLSR design.

The first MBA lattice design (denoted by 'Version-I') for the HEPS [3] was based on standard 7BAs. To control the circumference and hence the total cost, several measures were adopted, such as using modified-TME unit cells [4] with horizontally defocusing gradient combined in the dipole (resulting in $J_x > 1$ for lower emittance), and utilizing small-aperture magnets and vacuum systems (with magnet bore radii of 12.5 mm, following MAX-IV design [5]) with multipole gradients of up to 47 T/m and 7700 T/m^2 (provided the available maximum pole face field is 0.6 Tesla). Finally a compact layout was reached with each unit cell of 3.8 m (see Fig. 1) and $C = 1263.4$ m. The natural emittance is 75 pm.rad at 5 GeV. The lattice has 16 superperiods, and each superperiod consists of two 7BAs. As shown in Fig. 2, in this design, high-beta 10-m and low-beta 6-m straight sections are alternatively distributed, for the sake of efficient injection and high-coherence flux emission from insertion devices (IDs), respectively. The main parameters of the ring are listed in Table 1.

Following the third-order achromat design philosophy proposed in [6], the linear optics was matched such that the phase advance of each superperiod is chosen to $\mu_x = 12\pi + \pi/4 + \delta\upsilon_x * \pi/8$ and $\mu_y = 4\pi + \pi/4 + \delta\upsilon_y * \pi/8$, where $\delta\upsilon_x$ and $\delta\upsilon_y$ are the expected decimal portions of the working point of the ring. In this way, every eight superperiods forms a quasi-3rd-order achromat, which helps to approximately cancel the 3rd- and most of the 4th- order resonances and hence facilitate the subsequent nonlinear optimization.

As a start of the optimization, and also for demonstration of the effect of quasi-3rd-order achromat, we first performed numerical tracking (with the AT program [7]) and frequency map analysis (FMA [8]) for the bare lattice with only two families of

chromatic sextupoles. The results are shown in Fig. 3. The on-momentum horizontal dynamic aperture (DA) is 7.5 mm, larger than the requirement ($\geq$ 5 mm) of off-axis injection with pulsed sextupoles [9]. The resonances have small driving terms due to approximate cancellation of the nonlinearities induced by sextupoles, and hence do not cause significant distortions in the frequency map (FM). In the absence of magnetic errors, the particles can pass through the integer resonances at x = 4.5 mm and y = 1.5 mm without loss. However, the rule of thumb is that the integer resonances are always dangerous in a realistic machine and can-not be passed. One can foresee that when the integer resonances are more excited due to magnetic field errors and misalignments, all the orbits beyond the integer resonances will become unstable, leading to a significant shrinkage in DA.

Further studies showed that the large detuning terms are responsible for particles quickly reaching the integer resonances. In order to minimize the detuning terms and meanwhile control the other nonlinear terms to an acceptable level, we used additional four families of chromatic sextupoles and six families of harmonic sextupoles and octupoles for nonlinear optimization. To understand the combined effects of multi-families of sextupoles and octupoles, we developed a theoretical analyzer based on Lie Algebra and Hamiltonian dynamics, from which one can obtain analytical expressions of the detuning (up to the 2nd order), chromatic (up to the 4th order) and resonance driving terms (up to the 6th order) with respect to the sextupole and octupole strengths (see [3] for details). It is worth mentioning here that the resonance driving terms obtained by the analyzer are somewhat different from those obtained with normal form method [10], which, however, does not affects the effectiveness of the analyzer in measuring the resonance strengths. We then made multi-objective genetic optimization with NSGA-II [11] by setting three objective functions f_1, f_2, and f_3 to characterize the detuning, chromatic and resonance driving terms, respectively. Fig. 4 presents the Pareto-optimal solutions obtained after 500 generations with NSGA-II. Note that the perturbation theory is based on the assumption of small particle offset and momentum deviation from the reference particle. The solutions from the analytical approach may fail to perform well for large transverse amplitudes and momentum deviation (especially for a DLSR with extremely large nonlinearities). It is necessary to verify the nonlinear performance of the lattice with these results by means of numerical tracking and FMA. Thus, among the obtained optimal solutions, we selected those providing good balance of three objectives and verify them with numerical tracking with the AT program and FMA. Finally, we obtained one optimal set of the sextupole and octupole strengths. The on-momentum DA and FM are shown in Fig. 5. In this case, particles reach the integer resonance at larger amplitudes, i.e., x = 6 mm and y = 2.6 mm, which basically satisfies the DA requirement for off-axis injection in the high-beta 10-m straight section. And the momentum acceptance (MA) δ_m is about 3%.

However, it was noted that in this design only half of the straight sections were designed with low beta functions for optimal matching of the electron and photon beam ($\beta \sim L_{ID}/\pi$ [12] or $L_{ID}/2\pi$ [6], with L_{ID} being the ID length). To provide as many ID sections with optimal beta functions as possible, a modified HEPS lattice (denoted by 'Version-II') composed of thirty six 7BAs with ε_0 = 51 pm.rad at 5 GeV and C = 1364.8 m was proposed [13]. The main parameters of this design are also listed in Table 1.

In this design, the length of each unit cell was further reduced to 3.6 m; every twelve 7BAs was designed to form a quasi-3rd-order achromat; and most importantly, among 36 straight sections, 34 of them were designed specifically for ID (see Fig. 6) while the other two were modified to have large beta functions and longer drift space (9.6 m vs. 7 m) to accommodate injection devices and RF cavities (see Fig. 7). To restore the periodicity, the phase advance of the high-beta section was tuned to be same as that of a normal section, or with a difference of $2n\pi$ (n is integer). After optimizing the nonlinear dynamics in the same way as for the 'Version-I' lattice, we were able to achieve a moderate integer resonance-clear acceptance ($\sim$ 7 mm in x plane and $\sim$ 5 mm in y plane), however, with a relatively small MA ($\delta_m \sim 1.5\%$). This is because that the difference in phase advance between two kinds of sections will deviate from $2n\pi$ as δ increases, and the periodicity will be destroyed. In the cases with nonzero momentum deviations, resonances will be more excited, leading to particle loss and MA reduction. Nevertheless, we will show next that this problem can be overcome, to a large extent, through careful tuning of the strengths of multi-families of sextupoles and octupoles.
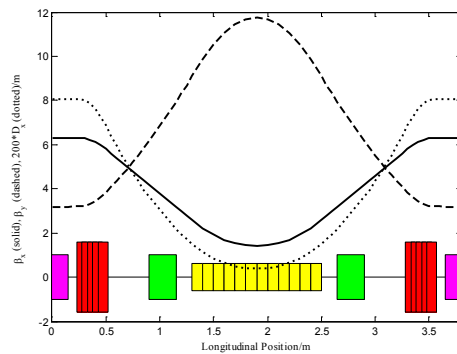
Figure 1: Layout and optical functions in a modified-TME unit cell.
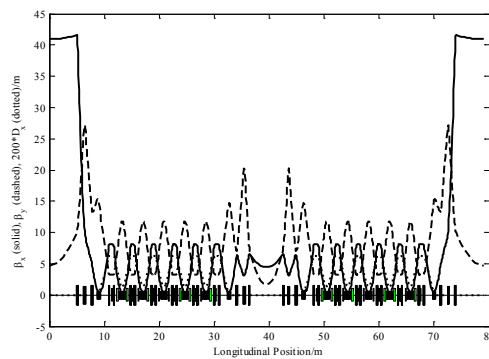
Figure 2: Optical functions in a superperiod consisting of two standard 7BAs.
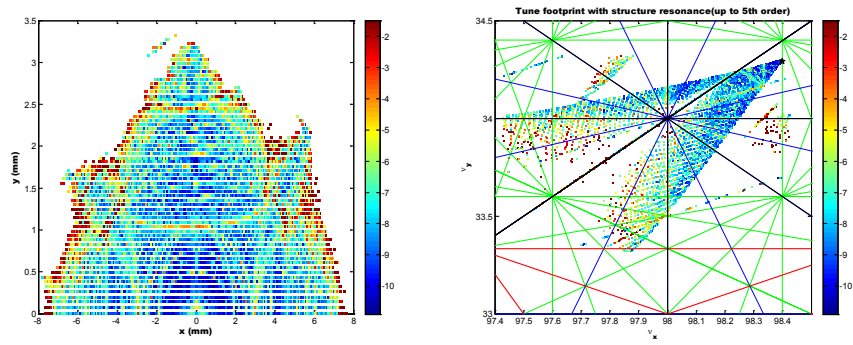
Figure 3: DA and FM obtained after tracking of 1024 turns for the BAPS 'Version-I' lattice with only two families of chromaticity-correction sextupoles. The colors, from blue to red, represent the stabilities of the particle motion, from stable to unstable.
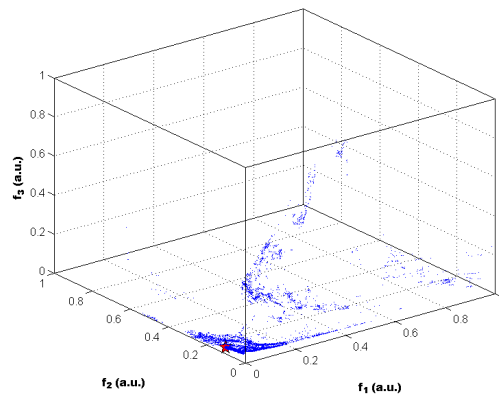
Figure 4: Pareto-optimal solutions obtained after 500 generations with NSGA-II. Three objectives are used, with f_1, f_2, and f_3 characterizing the detuning, chromatic and resonance driving terms, respectively. The star denotes the best solution found, which provides large dynamic aperture.
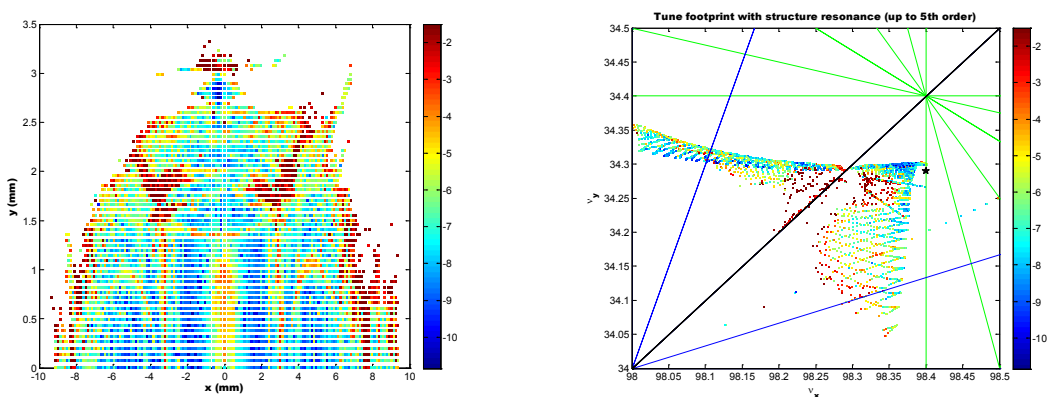
Figure 5: DA and FM obtained after tracking of 1024 turns for the BAPS 'Version-I' lattice by using 12 families of sextupoles and 6 families of octupoles with strengths obtained by NSGA-II. The colors, from blue to red, represent the stabilities of the particle motion, from stable to unstable.
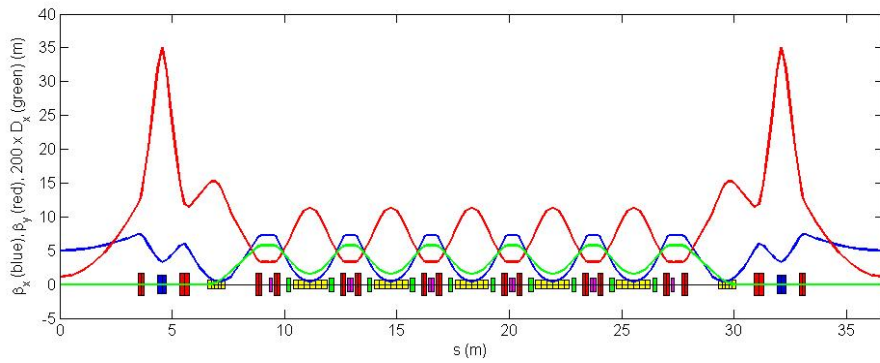
Figure 6: Layout and optical functions of a standard 7BA with a 7-m ID straight section for the HEPS 'Version-II' lattice.
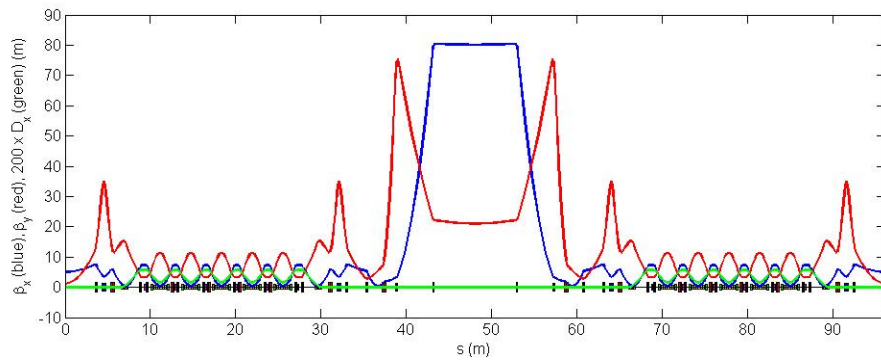
Figure 7: Layout and optical functions of two 7BAs with 9.6-m long straight section in between for the HEPS 'Version-II' lattice. The optics is matched so that the phase advance of the 9.6-m straight section is different from that of the normal 7-m straight section by $\mu_x = 2$ and $\mu_y = 0$.

5.8.3 Standard 7BA Lattice with High-Gradient Quadrupoles

In the ESRF-upgrade design [14], it was proposed to further enhance the quadrupole gradient to about ~100 T/m by using high-permeability pole material (e.g. vanadium permendur) or permanent magnet material near the poles to reduced saturation. This technique promises even shorter quadrupole/sextupoles and hence a more compact design. In addition, in 2014 it was decided that the HEPS lattice should be designed with a circumference around 1296 m (with +/−3 m varying range) to provide a harmonic number of 2160 (with ~500 MHz RF cavities), and the nominal beam energy was changed from 5 to 6 GeV. Based on the above, a new standard 7BA lattice with high-gradient quadrupole/multipoles [15] was proposed by using 44 normal 7BAs, with a circumference of $C = 1294.2$ m and a natural emittance of 90 pm·rad at 6 GeV (denoted by 'Version-III'). The main parameters of this design are also listed in Table 1.

In this design, due to the adoption of high-gradient quadrupole/sextupoles, more compact layout was reached than previously, with each unit cell of 3 m. Forty 7BAs were in standard design; the phase advance of each was chosen to be $\mu_x = 4\pi + \pi/4 + \delta\upsilon_x * \pi/20$ and $\mu_y = 2\pi + \pi/4 + \delta\upsilon_y * \pi/20$, such that every eight 7BAs constitutes a quasi-

3rd-order achromat. The other four 7BAs were designed to provide two 10-m straight sections, without any sextupole/octupoles therein (this is slightly different from the 'Version-II' lattice, see Fig. 8). The phase advance of these four 7BAs is set to $2n\pi$, which yields an identity linear transformation and hence restore the periodicity. However, this special design leads to great difficulty in MA optimization, a similar problem to that for the 'Version-II' lattice.

As mentioned, in this design, sextupoles and octupoles were located only in the standard 7BAs, where the sextupoles were grouped in eleven families (with 2 families of harmonic ones) and the octupoles were grouped in three families. With optimizations in the same way as for the 'Version-I' lattice, one solution promising large horizontal DA (larger than the physical aperture of 11 mm) and robust dynamics was obtained. The on-momentum DA and the corresponding FM are shown in Fig. 9. It was found that the half integer resonance $2\upsilon_x = 187$ and the integer resonance $\upsilon_x = 94$ are reached at a large x amplitude, i.e., -11.4 mm and -13 mm (or at even larger positive amplitudes); for the particle motion with $|x| < 11$ mm, no dangerous low-order resonance is crossed, and only two high-order resonances, $4\upsilon_x + 4\upsilon_y = 570$ and $7\upsilon_x = 652$, have weak impact on the dynamics. In addition, the tune shifts with amplitude and with δ calculated from numerical tracking and from theoretical analysis are plotted in Fig. 10. One can see that the analyzer succeeds to predict the tune shifts with amplitude for on-momentum particles, but fails to predict the tune shifts with δ at relatively large momentum deviation ($\delta \sim 1\%$). This is because that the nonlinear terms are derived by assuming the identity linear transformation of the injection section still holds as δ increases, which does not accord with the actual circumstances. It appears that this mode (denoted by mode 1) can be used for injection, while for storing the beam more efforts are needed to enlarge the MA.

To attain larger MA, we used directly the tune shifts with δ calculated numerically (this can be done in a short time) as the optimization goal, and search for the result promising a much less tune shift with δ and a fairly good on-momentum dynamics. Finally, we obtained another solution that promises MA of $\delta_m = 3\%$, while with certainly a price of smaller DA. The tune shifts with δ and the off-momentum DAs are presented in Fig. 11, and the on-momentum DA and the corresponding FM are shown in Fig. 12. It shows that for this mode (denoted by mode 2) the coupling resonance $\upsilon_x - \upsilon_y = 44$ and the integer resonance $\upsilon_x = 93$ dominate the beam dynamics in x and y planes, resulting in a smaller resonance-clear acceptance (~ 7 mm in x plane and ~ 5 mm in y plane). The acceptance is much smaller than that of the 'mode 1' design, but is still much larger than the equilibrium transverse size of the beam after injection. Further optimization was performed and it appeared scarcely possible to obtain a mode with both large DA (with similar size to mode 1) and MA (with similar δ_m to mode 2). As a compromise, we recommended using mode 1 during injection, and then switching to mode 2 (it may take a few seconds) for a long enough Touschek lifetime. Since the linear optics remains the same and only sextupole/octupole magnets need to be ramped, the dynamics will keep stable during the mode switching. The variation of the MA during the mode switching is shown in Fig. 13.
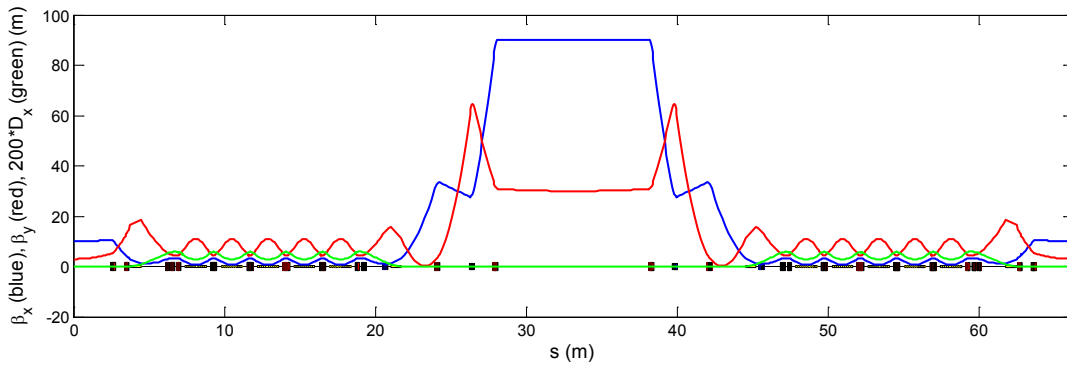
Figure 8: Layout and optical functions of two specially designed 7BAs with 10-m long straight section in between, for the HEPS 'Version-III' lattice. The phase advance of these two 7BAs is set to $\mu_x = 4\pi + \pi/4 + \delta\upsilon_x*\pi/20$ and $\mu_y = 2\pi + \pi/4 + \delta\upsilon_y*\pi/20$
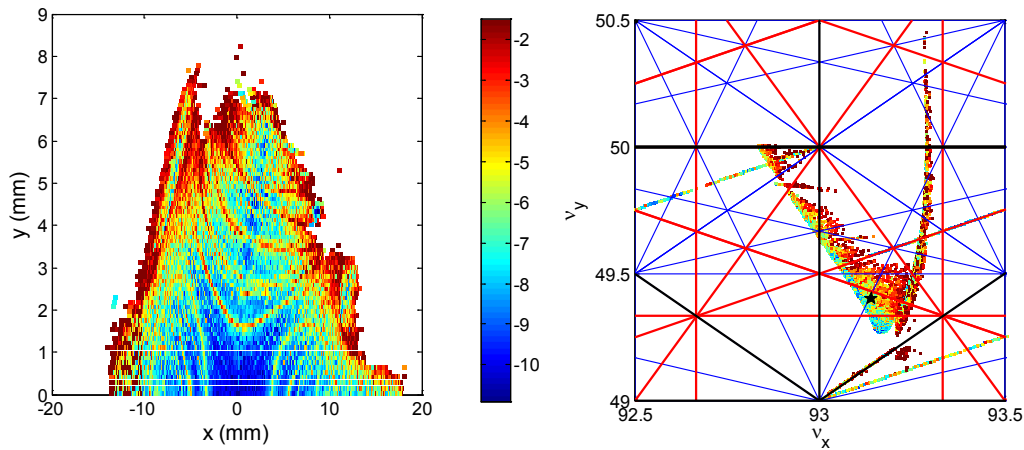
Figure 9: DA and FM obtained after over 1024 turns for the HEPS 'Version-III' lattice (mode 1). The colors, from blue to red, represent the stabilities of the particle motion, from stable to unstable.
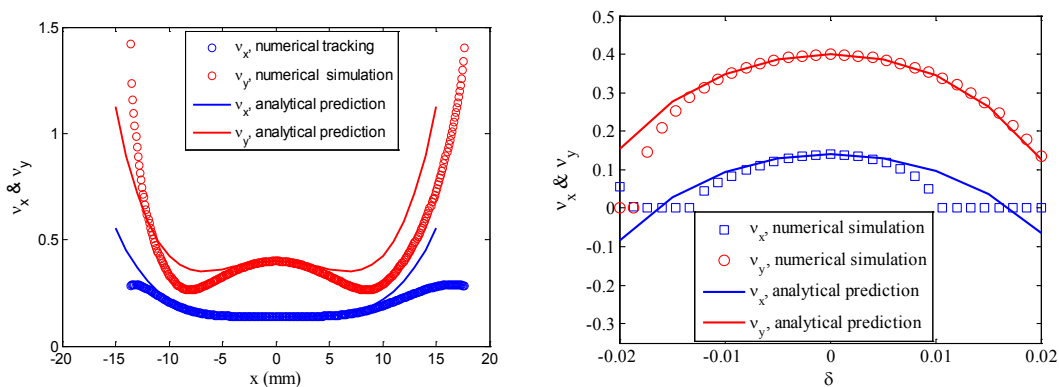
Figure 10: Tune shifts with horizontal amplitude (left) and with momentum deviation (right), extracted from the numerical tracking and theoretical analysis results, respectively, for HEPS 'Version-III' lattice (mode 1).
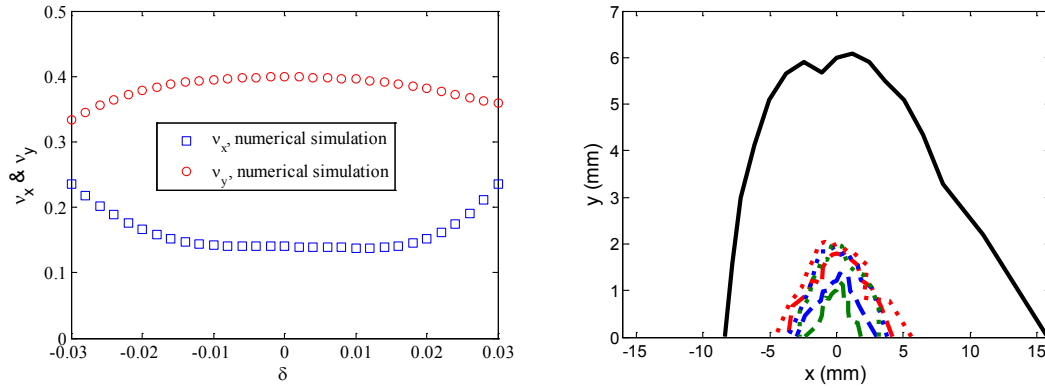
Figure 11: Simulation results of the tune shifts with δ (left) and of the off-momentum DAs for the HEPS 'Version-III' lattice (mode 2). In the right plot, with δ = 0 (black solid), δ = 1% (red dashed), δ = −1% (red dotted), δ = 2% (blue dashed), δ = −2% (blue dotted), δ = 3% (green dashed) and δ = −3% (green dotted).
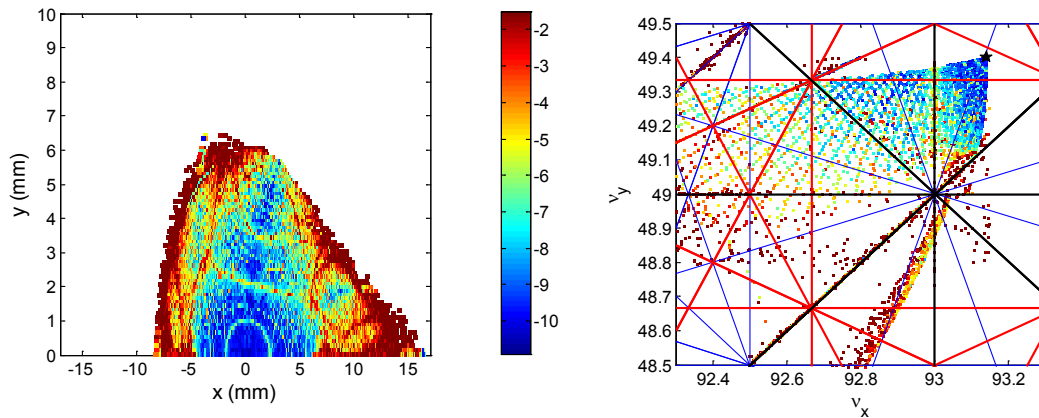
Figure 12: On-momentum DA and FM for the HEPS 'Version-III' lattice (mode 2). The colors, from blue to red, represent the stabilities of the particle motion, from stable to unstable.
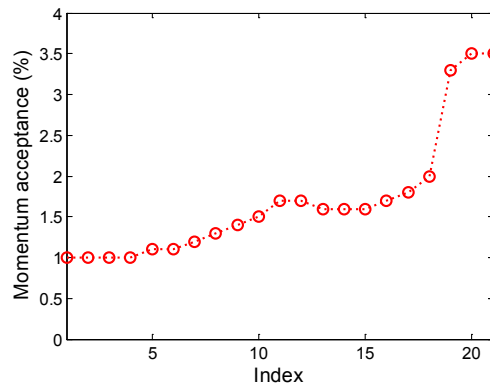
Figure 13: Simulation results of the MA variation during the mode switching (assuming the magnets are ramped in 21 steps) for the HEPS 'Version-III' lattice.

5.8.4 Hybrid 7BA Lattice with High-Gradient Quadrupoles

For the standard 7BA lattice with high-gradient quadrupoles, it was found very difficult to further push down the emittance; otherwise impractically high-gradient or thick sextupoles will be required to correct the increasing natural chromaticities. Following the so-called 'hybrid' MBA concept [14], we made a hybrid 7BA lattice design for the HEPS, with a lower emittance of 60.1 pm·rad at 6 GeV than that of the 'Version-III' lattice, while with a similar circumference ([16]). In addition, the sextupole strengths can be controlled to an achievable level with conventional magnet technologies.

In the design of a hybrid-7BA, several key demands should be satisfied. First, for the central three unit cells, quadrupoles with strong horizontal focusing and dipoles combined with vertical focusing gradients are required to minimize the emittance and the cell length. Second, it needs to create two symmetric dispersion bumps in the gaps between the outer dipoles (with as large a dispersion as possible between the first and the second, and between the sixth and the seventh dipoles) with all the sextupoles located therein to correct the linear chromaticity. Third, the phase advance between each pair of sextupoles in a hybrid-7BA should be at or close to odd integer times of π, thus eliminating most of the undesirable effects of sextupoles. Fourth, it needs to introduce longitudinal gradient into the outer dipoles (with stronger bending field at the part with greater distance from the dispersion bump), to increase the dispersion at the sextupole and to further decrease the emittance.

Based on the above, the hybrid-7BA for HEPS was designed in two steps. First, the case without longitudinal gradient combined in the outer dipoles was considered. The linear optics was matched such that the first three demands mentioned above are satisfied. To make a practical design, as many constraints on the magnets and drift spaces as possible were included in the optics matching. For instances, it was required that the maximum focusing gradient is 80 T/m for the quadrupoles in the central three unit cells, and 50 T/m for the others (the corresponding pole face fields are 1 T and 0.625 T, respectively, with bore radius of 12.5 mm); for the central three combined-function dipoles, the bending radii should be larger than 40 m and the gradients should

be smaller than 48 T/m, with pole face gap of 38 mm; the length of the long straight section for insertion devices (IDs) or injection is fixed to 6 m; enough drift spaces are preserved for sextupoles, octupoles, diagnostics, correctors, and for fast feedback kickers (in the drift between the first and the second quadrupoles and that on mirror side, more than 0.3 m) and a 3-pole wiggler (in the drift next to the third or the fifth dipole, more than 0.35 m) as well. In addition, the lengths of quadrupoles were minimized, while keeping the required gradients well below their upper limits. Finally, a hybrid-7BA of 26.992 m was reached, with the layout and the optical functions presented in Fig. 14 (solid curves).

In the second step, longitudinal gradient was introduced into the outer dipoles and the emittance was further minimized. Each of the outer dipoles was split into five slices, which were considered to have different bending radii. Moreover, the bending angles were redistributed among the seven dipoles. Keeping the other parameters unchanged, the analytical expression of the emittance was derived following Ref. [17] and then minimized. As a result, the emittance was decreased from 100 pm·rad to 60.1 pm·rad. Since rectangular dipoles were used in the lattice and their lengths were unchanged, the Courant-Snyder parameters remain the same. The variations in the bending radii of dipoles cause only a small change in dispersion functions, with the dispersion increasing slightly from 5.7 cm to 5.85 cm near the center of the dispersion bump (see the dashed curve in Fig. 14).

Three families of sextupoles (one family with horizontal focusing, SF, and the other two with vertical focusing, SD1 and SD2) were used for chromatic correction and were all located in the dispersion bumps, where the large dispersion helps to control the gradient and length of sextupoles to a reasonable level, i.e., below 6000 T/m^2 (the corresponding pole face field is 0.47 T with bore radius of 12.5 mm) and ~0.3 m, respectively. Except for the three families of sextupoles, only one family of octupoles (Oct) was used to correct the high-order aberrations, especially the vertical detune terms.

Since two sextupole families were for chromatic correction, and only two free knobs were left for DA and MA optimization. This, however, enabled us to globally scan the multipole strengths in a reasonable computing time, based on numerical tracking with the AT program and FMA. Unfortunately, it was found difficult to simultaneously optimize the effective DA and MA. Note that here we used the 'effective' DA and MA of the bare lattice as indicators of the nonlinear performance. Within the effective DA or MA, it is required not only the motion remains stable after tracking over a few thousand turns, but also the tune footprint is bounded by the integer and half integer resonances nearest to the working point. The reasoning behind this definition is that in a DLSR the linear optics is generally pushed to its extreme and the nonlinearities are extremely large, the resonances near the nominal tunes are usually reached for small betatron amplitudes or momentum deviations. The higher order resonances are generally weak for small amplitudes and just weakly impact the beam dynamics; while the IRs or HIRs have strong effects on the dynamics (their effects do not depend on amplitudes), and become the major sources limiting the available ring acceptance of a DLSR. A compromise solution predicts an effective DA of 2.5 (or 2.2) mm in the x (or y) plane and an effective MA of 2.4%.

To resolve the difficulty for injection due to the small DA, we proposed a novel on-axis longitudinal injection scheme enabled by phase manipulation of a double-frequency RF system [18]. Compared with that with a single-frequency RF system [19], this scheme can greatly reduce the requirement of the MA to about 3%. We believe that it is possible, although challenging, to reach such a target on MA.

To improve the nonlinear dynamics, genetic optimization of the linear optics (while with the same layout, or namely, only varying the quadrupole strengths) was performed, so as to find all the possible solutions which promise weaker chromatic sextupoles and hence weaker nonlinearities, while keeping the emittance at the same level as the original design. From a tune space scan based on the obtained solutions, we were able to increase the effective MA to ~3% and the effective DA to ~2.5 (or 3.5) mm in x (or y) plane [20], while keeping the emittance at the same level, 59.4 pm.rad. Hereafter this design will be denoted by 'Version-IV' lattice, with the main parameters also listed in Table 1. And the effective on-momentum DA and FM are shown in Fig. 15.

Although this design basically satisfies the DA and MA requirement of on-axis longitudinal injection, it is necessary and important to globally scan all the tunable element parameters (while keeping the circumference basically unchanged, i.e., varied in +/− 1 m) to explore the ultimate performance of such a hybrid 7BA design. The performance parameters include the achievable minimum natural emittance, and the maximum ring acceptance at a specific natural emittance.

For a hybrid 7BA, there are more than 20 tunable element parameters. A global grid scan may take too long a time to exhaust all the possibilities. In contrast, a more efficient way is to use stochastic optimization algorithms, e.g., the multi-objective genetic algorithm (MOGA) and multi-objective particle swarm optimization (MOPSO). The MOGA methods mimic the process of natural selection and evolution of species, and have been widely applied to many accelerator optimization problems [21-25]. While MOPSO emulates the self-organizing behavior of social animal living in group, and has been recently used to optimize the linac operation and ring dynamics [26-28].

It has been demonstrated that both algorithms are powerful and effective in solving the problems with piecewise continuous and highly nonlinear objectives and many local optima. Nevertheless, a recent study [28] showed that MOPSO converges faster than MOGA, and is not as dependent on the distribution of initial population as MOGA. By comparing the performance of these two algorithms by applying them to a problem whose answer had been known, we found that [29] each algorithm has its own unique advantage, and implementing them in a successive and iterative way will be more effective than using either of them alone in approaching the true global optima for an explorative multi-objective problem.

The ID section length of the 'Version-IV' lattice is L_{ID} = 6 m (hereafter L_{ID} represents the ID section length). It is known that if with a shorter L_{ID}, the variables for the position and length of magnets will have larger adjustment space, and it will be feasible to achieve designs with better performance. We tested the effectiveness of the MOGA and MOPSO in solving this problem.

In the optimization, two objective functions, weighted natural emittance and weighted chromatic sextupole strengths, were defined. For ease of comparison of the

sextupole strengths between different solutions, the sextupoles were grouped in just two families (SD, SF) with identical lengths of 0.2 m, such that for specific corrected chromaticities ([0.5, 0.5] in this study) there is a unique solution of the sextupole strengths (K_{sd}, K_{sf}), which were then represented with a nominal strength,

$$K_s = \sqrt{(K_{sf}^2 + K_{sd}^2)/2} \tag{2}$$

We first obtained the optimal results for the case with fixed ID section length ($L_{ID} \equiv$ 6 m). Based on these solutions, we initialized the population for the cases with variable ID section length, where the initial values of L_{ID} were drawn from a normal distribution with an average of 6 m and the standard deviation of a small value (0.1 m), with the aim to ensure that most of the individuals in the initial population have stable optics. However, the available tune range for the L_{ID} values was set to a larger range, i.e., [5, 7] m.

The solutions obtained with MOGA and MOPSO after evolution of 800 generations are shown in Fig. 16. It shows that both MOGA and MOPSO predict solutions with better performance (e.g., with smaller K_s at a specific ε_0). However, the difference in the performance of these two algorithms is also obvious. For MOGA, the L_{ID} values of the final population do not exceed the L_{ID} covering range of the initial population, with a minimum of about 5.75 m. While for MOPSO, a majority of solutions have L_{ID} values close to 5 m and with better performance, indicating MOPSO has the ability of breeding diversity during the evolution of population.

Then the MOPSO solutions were further evolved with MOGA and MOPSO for 500 more generations, with the results shown in Fig. 17. At this time, MOGA reached a better convergence than MOPSO, having solutions with all L_{ID} values close to 5 m and with superior performance over those optimized for $L_{ID} \equiv 6$ m in the whole emittance range of interest.

From the above comparison one can learn that MOGA depends significantly on the distribution of initial population. If without enough diversity in the initial population, MOGA may converge to local optima rather than the true global optima. Worse still, the MOGA itself cannot give a measure of the diversity of a population. Consequently, if applying MOGA to a typical exploratory multi-objective problem with many optimizing variables and local optima, and without another effective algorithm (e.g., MOPSO in this study) for comparison, one cannot know for sure whether the final solutions reveal optimal trade-offs between the different objectives. In short, to make an effective MOGA optimization, it is critical, and also challenging, to seed the initial population with high enough diversity. Fortunately, as demonstrated above, this difficulty can be overcome with the MOPSO, which has an intrinsic ability of breeding more diversity in the evolution of population. And once the diversity of solutions is ensured, MOGA can reach a better convergence than MOPSO to the true global optima. Therefore, evolving the population with a rational combination of MOPSO and MOGA would be more effective than using either of these two algorithms alone.

We then performed a successive and iterative implementation of the MOPSO and MOGA in the optimization of the HEPS hybrid 7BA lattice, with objectives of weighted natural emittance and ring acceptance. It was empirically found essential to evolve the

population with MOPSO over enough generations (1000 generations in our study), so as to generate solutions with diverse optical parameters. Otherwise, the subsequent MOGA will quickly converge to specific local optima, with solutions gathered in a few small distinct regions in the objective function space.

In spite of limited tuning ranges of the optimizing variables and various constraints in the optimization, after several iterations of MOPSO and MOGA, nearly continuously distributed solutions in the objective function space were obtained, showing almost a monotonous variation of the scaled ring acceptance with the natural emittance. Fig. 18 shows the evolution of the population at the last iteration of MOPSO and MOGA. From the final population of MOGA, one can see a turning point around ε_0 = 50 pm.rad. The available ring acceptance decreases rapidly with the emittance for ε_0 below 50 pm.rad, while decreases at a much smaller slope for ε_0 above 50 pm.rad. This suggests that for the HEPS hybrid 7BA design, it is best to keep the natural emittance above 50 pm.rad to achieve a robust nonlinear performance, i.e., with a high tolerance to small deviations in the linear optical parameters.

From post analysis of the obtained solutions, we found designs with better performance than the 'Version-IV' lattice. They promise lower natural emittance and larger effective DA and MA, while using weaker sextupoles and octupoles. For more details one can see Ref. [29].
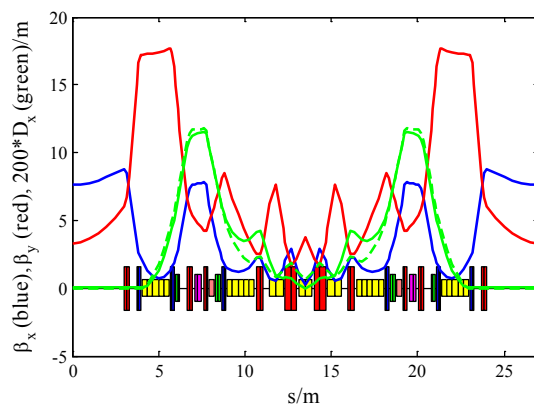
Figure 14: Layout and optical functions of the hybrid-7BA designed for HEPS, without (solid curves) and with (dashed curves) longitudinal gradient combined in the outer dipoles.
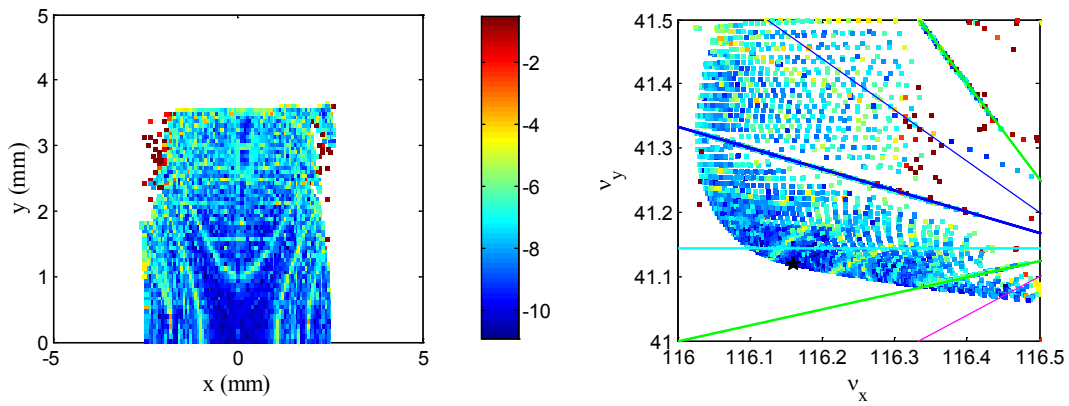
Figure 15: The effective DA and the corresponding FM for the HEPS 'Version-IV' lattice consisting of hybrid 7BAs. The colors, from blue to red, represent the stabilities of the particle motion, from stable to unstable.
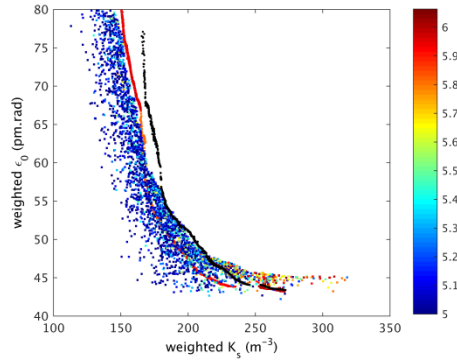
Figure 16: MOGA solutions for fixed ID section length, $L_{ID} \equiv 6$ m (black curve), and the solutions with MOPSO (sparsely distributed dots) and MOGA (narrowly distributed dots) for a variable L_{ID}, with the colors representing the L_{ID} values (in unit of m).
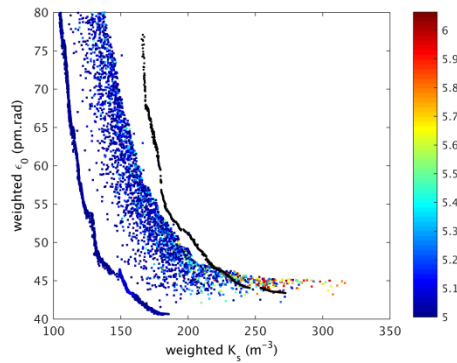
Figure 17: MOGA solutions for fixed ID section length, $L_{ID} \equiv 6$ m (black curve), and the solutions for variable L_{ID} after evolution of 500 more generations with MOPSO (sparsely distributed dots) and MOGA (narrowly distributed dots) for a variable L_{ID}, with the colors representing the L_{ID} values (in unit of m).
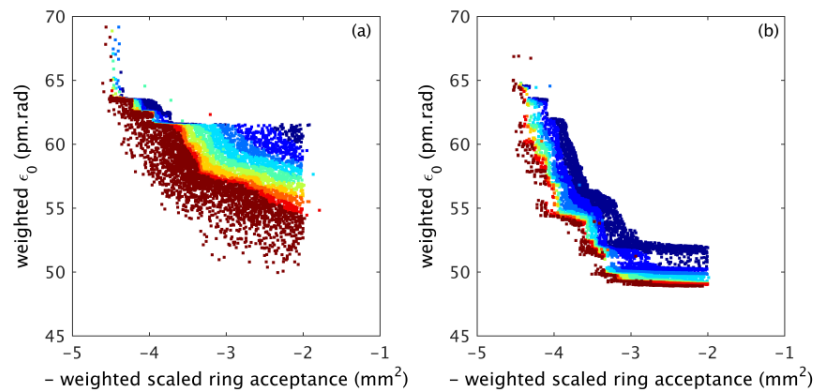
Figure 18: Solutions of the last iteration of MOPSO (a) and MOGA (b) in the objective function space. The population is plotted at every 100 generation and marked with different colors (from blue to red).

5.8.5 Conclusion

In this paper we present a brief review of the evolution of the lattice design for the HEPS as well as the optimization of the nonlinear dynamics. From comparison of different linear optics designs, with the hybrid MBA lattice one can reach lower natural emittance than with standard MBA lattice. For the presented HEPS hybrid 7BA design, the DA is not sufficient for off-axis injection. Thus an on-axis injection is considered. It is worthy to note that we are also making candidate hybrid 7BA designs that promise off-axis injection, by inserting a high-beta function section in the lattice.

Another important issue in a DLSR design is to attain large enough ring acceptance when squeezing the emittance. We used a theoretical analyzer to derive the chromatic, detuning and resonance driving terms as functions of multipole strengths. Combining this analyzer and genetic methods one can quickly found settings of multipole strengths promising good balance in minimizing different nonlinear terms. Nevertheless, the analytical approach applies well to the cases with small deviation of the amplitude or momentum, but might fail to accurately predict the tunes for a large amplitude or momentum deviation that is close to the boundary of the dynamic aperture or momentum acceptance. Thus, the optimization based on analytical approach was found not very effective in optimizing the nonlinear performance of the HEPS lattices, especially for those with high-beta function sections.

A more effective approach is to optimize the nonlinear performance with stochastic optimization methods based on time-consuming but more precise numerical tracking. In this approach one can globally vary all tunable parameters of both the linear and nonlinear elements to find solutions showing optimal trade-offs between different performance parameters, e.g., the emittance and ring acceptance of a DLSR. In addition, through comparisons we found that the MOGA method which is usually used in accelerator community may fail in reaching the global optimum for an explorative optimization problem with various stringent constraints and many variables with limited

tuning ranges. To solve this problem, we recommend using an iterative and successive implementation of the MOGA and MOPSO algorithms, rather than either of them alone, in the global optimization of a DLSR design. Besides, for this numerical approach, it is necessary to optimize the computing speed. We proposed the so-called 'effective' DA and MA of the bare lattice, which can give a quick and reasonable evaluation of the realistic ring acceptance in the presence of practical errors, which can greatly facilitate the optimizations based on numerical tracking. We hope the experience of design and optimization of the HEPS lattice presented here can provide useful reference for scientists who are designing or will design ultralow-emittance storage rings.

Table 1: Main parameters of different HEPS designs.

Parameter	Version-I	Version-II	Version-III	Version-IV
nominal beam energy (GeV)	5	5	6	6
circumference (m)	1263.4	1364.8	1294.2	1295.6
natural emittance (pm.rad)	75	51	88	59.4
working point (H/V)	98.40/34.30	113.39/39.30	93.14/49.40	116.16/41.12
natural chromaticities (H/V)	-189/-113	-184/-181	-112/-107	-214/-133
number of 7BAs	32	36	44	48
no/length (m) of high-beta sections	16/10	2/9.6	2/10	0/-
no/length (m) of low-beta sections	16/6	34/7	42/5	48/6
beta functions (m) in low-beta sections (H/V)	4.5/1.7	5/1.11	10/3	9/3.2
rms energy spread (zero current)	8×10^{-4}	7×10^{-4}	1×10^{-3}	7.9×10^{-4}
momentum compaction	3.86×10^{-5}	4.0×10^{-5}	5.9×10^{-5}	3.74×10^{-5}

5.8.6 References

1. X.M. Jiang *et al.*, BAPS preliminary design report, internal report. Beijing: Institute of High Energy Physics, CAS, 2012 (in Chinese).

2. R. Hettel, J. Synchrotron Radiat. **21**, 843-855 (2014).

3. G. Xu, Y. Jiao, Chin. Phys. C, **37**(5): 057003(2013).

4. Y. Jiao, Y. Cai, and A.W. Chao, Phys. Rev. ST Accel. Beams **14,** 054002 (2011).

5. P.F. Tavares *et al.*, J. Synchrotron Radiat. **21**, 862-877 (2014).

6. Y. Cai *et al.*, Phys. Rev. ST Accel. Beams **15,** 054002 (2012).

7. A. Terebilo, SLAC-PUB-8732, 2001.

8. L. Nadolski and J. Laskar, Phys. Rev. ST Accel. Beams **6**, 114801 (2003).

9. H. Takaki *et al.*, Phys. Rev. ST Accel. Beams **13**, 020705(2010).

10. A.J. Dragt and J.M. Finn, Journal of Mathematical Physcis, 1979, 20(12):2649.

11. K. Deb, IEEE Trans. Evol. Comput. 6, 182 (2002).

12. M. Borland *et al.*, J. Synchrotron Radiat. **21**, 912-936 (2014).

13. G. Xu, BAPS lattice design, In: the Workshop on Accelerator R&D for Ultimate Storage Rings, Beijing, 2012

14. L. Farvacque *et al.*, in Proceeding of IPAC2013, Shanghai, China, 2013, pp. 79-81.

15. Y. Jiao, G. Xu, Chin. Phys. C, **39**(6): 067004(2015)

16. G. Xu, Y. Jiao, and Y.M. Peng, Chin. Phys. C **40**, 027001 (2016).

17. G. Xu, Y.M. Peng, Nucl. Instrum. Methods Phys. Res., Sec. A, **654**: 24-28(2011)

18. G. Xu *et al.*, in Proceeding of IPAC2016, Busan, Korea, 2016, WEOAA02.

19. M. Aiba *et al.*, Phys. Rev. ST Accel. Beams **18,** 020701 (2015).

20. Y. Jiao, Chin. Phys. C **40**, 077002 (2016).

21. I.V. Bazarov and C.K. Sinclair, Phys. Rev. ST Accel. Beams **8,** 034202 (2005).

22. L. Yang *et al.*, Nucl. Instrum. Methods Phys. Res., Sect. A **609**, 50-57 (2009).

23. M. Borland *et al.*, in Proceeding of PAC'09, Vancouver, Canada, 2009, pp. 3850-3852.

24. L. Yang, Y. Li, W. Guo, and S. Krinsky, Phys. Rev. ST Accel. Beams **14,** 054001 (2011).

25. W. Gao, L. Wang, and W. Li, Phys. Rev. ST Accel. Beams **14,** 094001 (2011).

26. Z. Bai, L. Wang, and W. Li, *in Proceeding of IPAC2011, San Sebastián, Spain, 2011*, pp. 2271-2273.

27. X. Pang and L.J. Rybarcyk, Nucl. Instrum. Methods Phys. Res., Sect. A **741**, 124-129 (2014).

28. X. Huang and J. Safranek, Nucl. Instrum. Methods Phys. Res., Sect. A **757**, 48-53 (2014).

29. Y. Jiao, G. Xu, Optimizing the lattice design for a diffraction-limited storage ring with a rational combination of particle swarm and genetic algorithms. arXiv:1605.05021 (2016), submitted to Phys. Rev. Accel. Beams.

6 Workshop and Conference Reports

6.1 Report from IPAC'17

Gianluigi Arduini

Mail to: Gianluigi.Arduini@cern.ch

CERN, Geneva, Switzerland

The 8th International Particle Accelerator Conference (IPAC) took place in Copenhagen, Denmark, on 14-19 May and was attended by more than 1550 people from 34 different countries. Hosted by the European Spallation Source (ESS), and organized under the auspices of the European Physical Society Accelerator Group and the International Union of Pure and Applied Physics, the event was also supported by the MAXIV facility and Aarhus University.

As noted in the opening addresses by the Danish minister for higher education and science and the Swedish State Secretary to the Minister for Higher Education and Research accelerators were initially developed to understand the infinitesimal constituents of matter. However, they soon evolved into sophisticated instruments for a wide range of fundamental and applied research, and today particle accelerators serve society in numerous ways ranging from medicine and energy to the arts and security.

MAX-IV and the ESS are two of the most powerful instruments available to life and materials scientists, and are respectively operating and under construction. Meanwhile, the most brilliant source of ultra-short flashes of X-rays, the European X-XFEL at DESY, has recently achieved first lasing and will soon be open to users. Advanced light sources represent a continuously increasing fraction of global accelerators, following the steady improvement in their performance in terms of brilliance and temporal characteristics. Another X-ray free-electron laser, the SwissFEL at PSI, has just produced laser radiation in the soft X-ray regime and is aiming to achieve smaller wavelengths by the end of the year. New synchrotron light sources have come to operation like the Polish synchrotron radiation facility SOLARIS in Krakow and upgrades based on new concepts like the Hybrid Multi Bend Achromat for the European Synchrotron Radiation Facility (ESRF) in Grenoble are planned. This concept has earned Pantaleo Raimondi from ESRF the EPS-AG IPAC'17 Gersh Budker Prize, for "a recent significant, original contribution to the accelerator field, with no age limit".

Particle physics remains one of the main drivers for new accelerator projects and for R&D in IPAC's many fields. In 2016 CERN's LHC exceeded nominal luminosity by almost 50% thanks to operations with more tightly spaced bunches (25 ns) and due to the higher brightness of the beams delivered by the LHC injectors. Mastering the effects of electron clouds and carrying out progressive "scrubbing" of the surfaces of the LHC beam screens have been key to this performance. The achievement of the nominal luminosity in the LHC has marked the ideal completion of one of the most ambitious science projects, testifying Lyndon Evans' leadership abilities and experience which

motivated the award of the EPS-AG IPAC'17 Rolf Wideröe Prize for "outstanding work in the accelerator field without age limit" to him.

On the lepton machine front, the Super KEKB electron—positron collider at KEK in Tsukuba, Japan, was successfully commissioned with beam in 2016. The installation of the superconducting quadrupoles and correctors of the final focussing system and the BELLE detector are being installed and the commissioning with beam is due to be completed in 2018 when first data are also expected. Concerning the quest for higher energy circular and linear electron-positron colliders, the main accelerator technology choices for the Compact Linear Collider (CLIC) have recently been validated at CERN's test facility (CTF3) and the gradient of CLIC's two-beam acceleration principle has been established beyond 100 MV/m. There has also been impressive progress in the design of a very large high-luminosity circular electron-positron collider in the frame of the Future Circular Collider (FCC) design study, in addition corresponding studies for a future hadron-hadron collider at CERN and similar studies are underway in China.

Advances on the high-intensity, high-energy frontiers demand for continuous advances in accelerator technology. Superconductivity is playing a key role both in the design of high field magnets and of high gradient superconducting RF cavities for CW operation. A significant breakthrough has been made by the winner of the Frank Sacherer Prize, Anna Grassellino from Fermilab. She first contributed to the improvement of the quality factor of superconducting cavities by discovering the technique of nitrogen-doping, and more recently showed how the method of nitrogen infusion has the potential to improve not only the quality factor but also the accelerating gradient.

Normal conducting RF structures operated at high frequency are also achieving new performance records, demonstrating accelerating gradients up to 120 MV/m, and this technology is attracting the attention of several laboratories keen to build compact FEL-based photon sources.

In the field of novel accelerator concepts, a new scheme to produce very low emittance muon beams based on the interaction between a 45GeV positron beam and a thin target has been devised by researchers at INFN Frascati. Finally, with increasing attention to the energy efficiency of accelerators, major steps are being made in the domain of high efficiency RF sources where efficiencies of up to 85% were reported.

The Copenhagen conference also saw 115 companies from 16 countries present their products as part of an industrial exhibition, which was complemented by lively panel discussions on industrial careers, intellectual property and other relevant issues.

A special student poster session took place during registration, the day before the conference opened. Prizes awarded by the European Physical Society's Accelerator Group (EPS-AG) for the best student posters were presented later in the week during a special awards session. The prizes went to Annalisa Romano (CERN, Geneva) and Daniel Leslie Hall (Cornell University-CLASSE, Ithaca, New York). An additional Industrial Committee Student Poster Award was to be given to three students whose work, presented in the special session for students, most incorporates criteria relative or applicable to industry. The winners were Jean-Michel Antoine Bereder (The University

of Tokyo), Yumi Lee (Korea University Sejong Campus) and Hiroaki Takeuchi (The University of Tokyo). In addition Fabrizio Giuseppe Bisesto (INFN/LNF) received the EPS-AG IPAC'17 Bruno Touschek prize for his contributions to the plasma related activities underway at SPARC-LAB, exploiting the high-power laser FLAME. In particular, for his experimental work on the single shot diagnostics systems, including Electro Optical Sampling (EOS) for temporal measurement and Optical Transition Radiation (OTR) measurements for an innovative, one-shot emittance measurement.

In total there were 45 invited and 51 contributed oral presentations and approximately 1400 posters. The final version of the proceedings of IPAC'17 was published at the JACoW site (www.jacow.org) just three weeks after the conference thanks to the excellent work of the JACoW Editorial Team.

The ninth IPAC will take place in Vancouver, Canada on 29 April - 4 May 2018.

6.2 Advanced and Novel Accelerator for High Energy Physics Roadmap workshop 2017

Brigitte Cros, CNRS, LPGP Université Paris Sud, Orsay, France

Patric Muggli, MPP, Germany and CERN, Switzerland

Mail to: brigitte.cros@u-psud.fr

The ANAR2017 workshop was held from April 25 to 28, 2017 at CERN. Organized at the initiative of the ICFA panel for Advanced and Novel Accelerators (http://www.lpgp.u-psud.fr/icfaana), the ANAR2017 workshop brought together about 80 participants to discuss the issues to be addressed in the near future to be in a position to identify promising technologies for future advanced accelerators.

Figure 1: Participants of the ANAR2017 workshop

The workshop was organized around the four Advanced and Novel Accelerators (ANAs) concepts that have already reached, or hold the promise to reach an accelerating gradient larger than 1 GeV/m: the laser wakefield accelerator (LWFA), in which an intense laser pulse drives a plasma wake; the plasma wakefield accelerator (PWFA), in which a particle bunch drives a plasma wake; the structure wakefield accelerator (SWA), in which a particle bunch drives wakefields in a dielectric tube; and the dielectric laser accelerator (DLA), in which a laser pulse drives wakefields in a periodic dielectric structure. The program of the workshop is available at https://indico.cern.ch/event/569406/.

After a summary introductory talk for each ANA, four working groups (WG) were formed and worked to identify the main advantages and challenges of each ANA concept; the results of the working groups were then shared with the entire workshop attendance in short summary talks followed by a 90 minutes global discussion of the scientific aspects to be used as input to a roadmap. The second part of the workshop was dedicated to discussions of the strategy to push forward the development of advanced accelerators in the context of the next international project at the TeV scale (e^-/e^+ or e^-/p^+ collider).

The main conclusions of the workshop discussions can be summarized as follows:

- Advanced and novel accelerators have achieved electron energy gains in the multi-GeV range, relevant for high-energy physics applications. Several remaining scientific challenges have been identified and need to be addressed in order to deliver by 2035 a design for an advanced linear collider. This goal requires larger facilities and projects than those of today, and broader coordination.
- A preliminary scientific roadmap towards the design of an advanced linear collider is proposed as the outcome of the ANAR2017 workshop, as described in a detailed report of the workshop discussions and conclusions (released in September 2017, available on the ICFA ANA and workshop websites).
- It was decided to constitute a study group towards Advanced Linear Colliders, named ALEGRO for Advanced LinEar collider study GROup. ALEGRO's general charge will be to coordinate the preparation of a proposal for an advanced linear collider in the multi-TeV energy range. In the short term, the first objective of ALEGRO will be to provide input towards the update of the European strategy for particle physics.

This workshop will be followed by other workshops addressing more specific issues related to an Advanced Linear Collider, the first one tentatively scheduled for March 2018 in Oxford, organized by the John Adams Institute.

6.3   The Future Circular Collider Week 2017

Panos Charitos and Frank Zimmermann

Mail to: panagiotis.charitos@cern.ch or frank.zimmermann@cern.ch

CERN, 1211 Geneva 23, Switzerland

The Future Circular Collider (FCC) Week 2017 (https://fccw2017.web.cern.ch/) was held in Berlin, Germany, from 29 May to 2 June 2017. It was organized jointly by CERN, DESY, and the German Physical Society (DPG), with support from the European Commission and from the IEEE Council of Superconductivity. This fourth annual meeting of the FCC collaboration followed the FCC kick-off in Geneva (2014), and two earlier FCC Weeks in Washington (2015) and Rome (2016). The FCC Week 2017 brought together more than 500 leading minds in engineering and science from 147 institutes to discuss the study progress and to lay the foundations for FCC design report. The steadily increasing participation numbers of both individuals and institutes testify to the attractiveness of the project and to the diversity of the scientific challenges offered by the various FCC scenarios and topics.

Namely, the FCC study is developing the accelerator design, the technologies, the detectors, and the physics program for an energy-frontier hadron collider (FCC-hh) and for a high-energy luminosity-frontier lepton collider (FCC-ee). In addition, a hadron-lepton collider (FCC-he), complementing the FCC-hh, would enhance the diverse scientific programs of the proposed future large-scale research infrastructure. The FCC study is also designing an energy upgrade of the LHC (HE-LHC), based on the FCC-hh magnet technology. The various colliders designed under the umbrella of the FCC study would surely test the Standard Model to its limits and shed light on the dark contents of the universe.

The 2017 FCC Week reviewed the progress in all study areas, ranging from accelerators to detectors and experiments, including the technological R&D and infrastructure developments. In Berlin, Michael Benedikt, the FCC Study Leader, underlined that "Over the past years we have studied, in depth, the parameters of future colliders pushing the energy and intensity frontiers. By now we have obtained an excellent understanding of all the key parameters and of the dependencies that affect the building and operation of these machines along with the associated physics motivation." The CERN Director for Accelerators and Technology, Frédérick Bordry, remarked that "Designing and building a post-LHC accelerator should be based on the use of breakthrough technologies to afford the beam energy, intensity and brightness which are required for a future discovery machine. The ongoing FCC R&D program is a natural extension of the High-Luminosity LHC activities and ensures an efficient use of past investments".

Building and operating large-scale research infrastructure like the FCC's in an efficient and reliable way poses a number of exciting challenges for scientists working in several different fields. Since the launch of the FCC study, significant advances in superconducting magnets, in SRF technologies, RF power sources and other key

technologies were accomplished, as was evidenced by the almost 300 oral presentations and about 50 topical posters. The design of cost-effective 16 Tesla accelerator magnets remains one of the challenges of a future hadron-hadron collider along with the associated development of a high-quality superconducting Nb_3Sn wire. This FCC wire needs to be qualitatively different from the one produced for the international fusion reactor, ITER. It should also be 50% better, in terms of current density, than the wire used to construct the Nb_3Sn magnets for the LHC luminosity upgrade (HL-LHC), which will be installed around 2025. Since, for the FCC, the target performance of the Nb_3Sn wire exceeds the present state of the art, over the past two years worldwide development programs for the magnet superconductor have been set up with competent partners in Europe, the US, Japan, Korea, and Russia.

Another critical element of FCC-hh is the cryogenic beam vacuum system, which has to cope with an unprecedented amount of synchrotron radiation, whose heat should be extracted efficiently from inside the cold magnets, while also providing an ultrahigh vacuum and suppressing electron-cloud build up. Since early June 2017, a prototype of the FCC-hh beam screen is undergoing first radiation tests at the ANKA synchrotron light source in Germany, signalling a major milestone in the development of the FCC technology.

The Berlin meeting saw new reference designs for future experiments both in future proton-proton and lepton-lepton circular colliders. Consensus was reached that the next generation of detectors will have to surpass the performance limits of the LHC experiments and must be able to handle higher event pile up, higher luminosity values, shorter bunch spacing, and enhanced radiation levels. This is not a trivial task, but, learning from the LHC experiments, including their HL-LHC upgrades, incorporating other detector concepts plus exploiting recent technological advancements, scientists made significant progress, which they showcased in Berlin.

Along with progress on the accelerator and detector designs, also substantial developments on the civil engineering plans were reported in Berlin. The new layout of the FCC defines an overall tunnel length of 97.75 km, compatible with the existing CERN accelerator complex, allowing the use of the existing LHC or SPS as injectors, and optimized for the geographical conditions in the Lake Geneva basin.

Similar to the previous FCC meetings, special emphasis was placed on public engagement and outreach activities. For example, "Small particles, big machines" was the theme of the public hands-on exhibition run in parallel to the FCC Week 2017. The aim of the exhibition was to bring the public closer to the science and technology of particle physics and particle accelerators. In addition, the annual FCC innovation awards were presented to two young scientists, recognizing some of the most exciting technological and scientific developments in the collaboration.

Next year's FCC Week 2018 will take place in Amsterdam, from 9 to 13 April 2018. The Amsterdam FCC Week will be the key meeting to prepare and finalize the FCC Conceptual Design Report, which should be published before the end of 2018, in time for the next Update of the European Strategy for Particle Physics.

Figure 1: FCC Week 2017 Poster (Image credit: CERN/FCC).

Figure 2: Participants of the 2017 FCC Week (Image credit: CERN).

6.4 The 57th ICFA Advanced Beam Dynamics Workshop on Energy Recovery Linacs, ERL17

Erk Jensen, CERN

Mail to: Erk.Jensen@cern.ch

The 57th Advanced Beam Dynamics Workshop on Energy Recovery Linacs (ERL17, www.cern.ch/ERL17), was the seventh in the series of International Workshops on ERLs. It was held at CERN from the 18th to the 23rd of June 2017.

The workshop organization was shared between the International Organizing Committee, this time chaired by E. Jensen, the Scientific Program Committee, chaired by O. Brüning and the Local Organizing Committee, chaired by L. Hemery. For best productivity and to encourage active participation by the whole community, the workshop was organized to have plenary sessions only with enough time allotted to discussions, which was well received by the participants. Another feature was to have the posters on display during the entire workshop in CERN's "salle pas perdu" right in front of the Council Chamber, which allowed stimulating and detailed discussions during the coffee breaks. A total of 90 participants, 60 plenary talks and 20 posters clearly document the continued interest of the community in Energy Recovery Linacs and the usefulness of this successful series of workshops.

Figure 1: ERL17 Workshop Poster

The workshop was structured in 5 working groups; WG1 on ERL Injectors was convened by K. Aulenbacher (JGU Mainz) and E. Wang (BNL), WG2 on Optics, Beam Dynamics and Instrumentation by D. Schulte (CERN) and A. Bogacz (JLAB), WG3 on Test Facilities by G Hoffstaetter (Cornell) and A. Stocchi (LAL), WG4 on Superconducting RF by I. Ben Zvi (BNL) and F. Gerigk (CERN) and WG5 on Applications by I. Konoplev (JAI) and Peter MacIntosh (STFC).

An important outcome of the workshop is a tabular overview of (tentatively) all ERL facilities world-wide, with their main characteristics, their status, and their targeted applications. This overview is of course a living document with presently 27 facilities listed – its present version is available from the workshop web site. It clearly emerges from this table that rich experience is available from presently and formerly operating facilities (cERL, Alice, JLAB's demo ERL, BNL's test ERL and the BINP ERL), which provides guidance with the design of future facilities. Concerning the injectors, the maturity of DC injectors employing high QE alkali-antimonide photocathodes was confirmed, and substantial recent progress was reported with SRF guns (both at BNL and HZDR), operating stably in CW. Semiconductor cathodes start to demonstrate acceptable QE with remarkable lifetimes of the order of months. New facilities, including those in planning, construction and commissioning very clearly are the first generation of ERLS to reach the multi-MW range for the "virtual beam power", i.e. the product beam current × top energy/e (MESA: 1 MW, bERLinPro: 5 MW, CBETA: 6 MW, PERLE: 8 MW). Also, most of these new facilities feature multiple recirculations.

Figure 2: Participants of ERL17 at CERN in June 2017

Progress in the specific optimization of superconducting RF cavities and cryomodules for ERLs was remarkable – the specific needs include the operation in CW with large beam currents and consequently the need for effective damping of HOMs (while fundamental beam loading is naturally small). Recent progress in SRF R&D in general, in particular the significant increase in reachable Q using nitrogen doping, opens new opportunities for ERLs. Since due to the energy recovery principle only minimal RF power is required to accelerate the beam, the relative importance of cavity stability, bandwidth and microphonics is of course largely increased, an area of R&D presently in the centre of attention. A special cavity geometry presented at ERL17 is the

dual-axis superconducting cavity – it could potentially allow for very compact ERLs for special applications.

Thanks to their potential large "virtual beam power" at moderate power consumption, ERLs allow interesting applications, and one could observe at ERL17 a large interest in photonics applications, including THz radiation sources, IR and EUV FELs as well as γ-ray sources using Laser Compton scattering.

The ERL series of workshops is part of the Advanced Beam Dynamics Workshop series and the organizers very much appreciate the support by the ICFA Beam Dynamics Panel. The proceedings are in preparation and will be published via JACOW.

6.5 The 18th International Conference on RF Superconductivity, SRF 2017

Jens Knobloch, Helmholtz-Zentrum Berlin and Universität Siegen
Mail to: knobloch@helmholtz-berlin.de

Superconducting RF (SRF) systems are essential for many new accelerator projects. Not surprisingly, the world-wide SRF community continues to grow rapidly as exemplified by the success of the recent International SRF Conference, hosted by the Institute of Modern Physics (IMP) and the Institute of High Energy Physics (IHEP). Details can be found at http://srf2017.csp.escience.cn.

The conference was the 18th in a series that dates all the way back to 1980. Yuan He from IMP was the Conference and Program Committee Chairman while Shenghu Zhang headed the Local Organizing Committee. Nearly 400 delegates, including 85 industrial exhibitors, from 31 countries attended the conference, which was held from July 17 through 21, 2017 in downtown Lanzhou at the University Conference Center. 65 talks were presented over five days of plenary sessions, with three poster sessions to provide ample time for in-depth discussions. A pre-press release of the proceedings is given at http://vrws.de/srf2017/ with the final proceedings to be published on the JACOW website.

The conference opened with a session on SRF-based accelerators in the construction or commissioning phase, including many large facilities such as XFEL, LCLS-II, FRIB, ESS, PIP-II and projects that support the development of ADS. Nearly two days were dedicated to fundamental SRF research, in particular issues related to RF losses in niobium and the development of new superconductors—essential aspects for future CW SRF accelerators. Two full sessions then focused on SRF technology such as new cavity and cryomodule designs as well as diagnostics and treatment techniques. The scientific program was rounded out by "Hot Topic Sessions" with lively discussions by the delegates, moderated by experts in the fields. These three one-hour sessions focused on how to maintain good SRF performance in operating accelerators, flux trapping in niobium and the resultant RF losses, and finally the exploration of the performance-limit of niobium.

For students and other newcomers to the field of SRF, the conference provided a comprehensive overview during three days of tutorials (July 13 – 15). Ten lectures covered the basic principles of RF Superconductivity, cavity design, cavity testing, couplers, cryogenics and cryomodules, cavity processing as well as the current status of niobium and other materials. Remarkably, SRF 2017 was able to sponsor a total of 40 students by covering the conference fee and the costs for accommodation. Prizes for young scientists were awarded for the best posters (Douglas Storey, TRIUMF / Julia Marie Köszegi, HZB) and the best presentations (Weiming Yue, IMP / Hernan Furci, CERN / Sam Posen, FNAL).

SRF 2019 will continue the bi-annual conference series. It will be hosted by the Forschungszentrum-Dresden Rossendorf in Germany.

SRF 2017 participants

SRF 2017 conference poster

7 Recent Doctorial Theses

7.1 Study on the Key Physics Problems of SPPC/CEPC Accelerator Design

Feng SU

Mail to: Principal.Author@myplace.org

Graduation date: May 2017

Institutions: Institute of High Energy Physics (IHEP), CAS, China

Supervisors: Prof. Jie Gao (IHEP)

Abstract

The development and history of particle physics is a magnificent poetry of the verification of Standard Model. With the discovery of the Higgs boson at LHC, people found all the particles predicted by Standard Model in laboratory. But due to some imperfection of theory, the physicists believe that Standard Model is just the low energy part of a larger basic theory. To explore the new physics beyond Standard Model will be the key point of the whole physics world. This is also the goal to design a new collider. The particle accelerators have been widely used for fundamental physics

research for more than 60 years. Many important discoveries of particle physics were based on the development of accelerator. After the discovery of Higgs boson at LHC in 2012, the world high energy physics community is investigating the feasibility of a Higgs Factory as a complement to the LHC for studying the Higgs and pushing the high energy frontier. CERN physicists are busy planning the LHC upgrade program, including HL-LHC and HE-LHC. They also plan a more inspiring program called FCC, including FCC-ee and FCC-hh, aiming to explore the high energy frontier and expecting to find new physics. Chinese accelerator physicists also came up an idea to build an ambitious machine called CEPC-SPPC (Circular Electron Positron Collider-Super Proton Proton Collider)

during a workshop in Beijing on September 13, 2012. The CEPC-SPPC program contains two stages. The first stage is an electron-positron collider with centerof-mass energy 240 GeV to study the Higgs properties carefully. The second stage is a proton-proton collider at center-of-mass energy of more than 70 TeV. This thesis focuses on key physics problems of SPPC/CEPC accelerator design. The first part is about the parameter choice, lattice design and the beam dynamic studies of SPPC. The second part is about the lattice design of CEPC, including partial double ring scheme, advanced partial double ring scheme and double ring scheme. We developed a systematic method of how to make an appropriate parameter choice for a circular proton-proton collider by using an analytical expression of beam-beam tune shift limit, starting from the required luminosity goal, beam energy, physical constraints at the interaction point (IP) and

some technical limitations. We calculated and designed a set of SPPC parameter list including 61 km-70 TeV, 100 km-100 TeV, 100 km-130 TeV, 100 km-70 TeV and 82 km- 100 TeV. Then we start the lattice design according to the parameter choice and focused on the 61 km-70 TeV and 100 km-100 TeV scheme. We designed the first version lattice and showed the result of the dynamic aperture. For CEPC design, there were several schemes developed after the publication of the Preliminary Conceptual Design Report(Pre-CDR) of CEPC-SPPC in March 2015, including single ring scheme with pretzel, partial double ring scheme, advanced partial double ring scheme and double ring scheme. For CEPC partial double ring scheme, we gave the layout according to SPPC layout and the possibility of installation in the same tunnel and running at the same time. Then we designed lattice of the partial double ring part according the appropriate parameter choice for the electro-static separators. We also studied the dynamic aperture of this scheme. For CEPC advanced partial double ring scheme and double ring scheme, we also gave the layout, designed the lattice and studied the beam dynamics.

8 Forthcoming Beam Dynamics Events

8.1 Space Charge 2017

The workshop "Space Charge 2017" is scheduled on 4-6th October 2017 at Darmstadt, Germany. Following the success of Space Charge 2013 (CERN), of Space Charge 2015 (Oxford UK), and based on a community demand, GSI and Technische Universitaet Darmstadt organise the 2017 edition of the workshop. The workshop will address current topics boiling in the accelerator community, and provide a forum for discussions between experts, complementary to the well-established HB workshops series. Space Charge 2017 is organised under the auspices of ICFA and is an event of APEC/ARIES, the successor of XRING/XBEAM/EuCARD2, which jointly with TU Darmstadt and the DPG AccelencE Reasearch Training Group covers the majority of the cost for the workshop.

All details of the workshop are available on the web page

https://indico.gsi.de/event/5600/

which will be regularly updated.

Oliver Boine-Frankenheim, Giuliano Franchetti, Chairs

8.2 ICFA Mini-Workshop on Dynamic Apertures of Circular Accelerators

Nowadays for all future circular accelerators, such as lepton colliders, hadron colliders, lepton-hadron and lepton-heavy ion colliders, advanced light sources, boosters, damping rings, etc. dynamic apertures are becoming key limiting factors for the corresponding required machine performances. In the last years, many theories, methods, codes, and optimization experinces have been accumulated in different circular accelerator communities.

The main purposes of this ICFA Beam Dynamics Panel Mini Workshop on this important beam dynamics issue are to promote further studies on this subject for different circular accelerators and to make the established knowledges and on-going studies to be well communicated among circular accelerator physcists in different communities.
This ICFA Mini Workshop will be held in Institute of High Energy Physics (IHEP), during Nov 1-3, 2017 in Beijing, China, prior to International Workshop on High Energy Circular Electron Positron Collider 2017, IHEP, Nov. 6-8, 2017 (http://cepcws17.ihep.ac.cn/index.html). The workshop website

http://indico.ihep.ac.cn/event/7021/

will be regularly updated to include the latest information as it becomes available.

Jie Gao, Workshop Chair

8.3   2017 Slow Extraction Workshop

A dedicated Workshop on Slow Extraction will take place from November 9 to 11th, 2017 at CERN, Geneva Switzerland.

The event follows on from the success of the inaugural 2016 Slow Extraction Workshop, held in GSI, Germany. The program will address topical issues associated with Slow Extraction, as well as providing a forum for discussion between experts in this specialised domain. The Workshop aims to review slow extraction spill performance and bottlenecks in terms of losses and spill quality, both for past and present facilities, in addition to new requirements from different communities. Topics ranging from beam dynamics and feedback systems to hardware innovations will be discussed. Ideas to improve performance will be a focus.

The Workshop will be held at CERN, on the outskirts of the city of Geneva that boasts many attractions as a cultural, humanitarian and scientific center. Thanks to its central location in the very heart of Europe, it is easy to reach by plane or train, and boasts a first-class infrastructure and public transportation. There will be the opportunity to visit some of CERN's facilities as part of an organised tour.

Young researchers are particularly encouraged to attend and to present their work. The workshop website

https://indico.cern.ch/event/639766/

will be regularly updated to include the latest information as it becomes available.

Brennan Goddard, IOC Chair, Slow Extraction 2017

8.4   International Workshop on Beam-Beam Effects in Circular Colliders

The 5th workshop on Beam-Beam Effects in Circular Colliders will take place from February 5-7, 2018 at the Lawrence Berkeley National Laboratory, Berkeley, USA. This workshop is a successor and follows up to similar workshops held at CERN in April 1999, at Fermilab in June 2001, in Montauk 2003, and at CERN in March 2013.

A lot of progress has been made since the last workshop at CERN in the study of the beam-beam effects in colliders such as the LHC. Meanwhile, there are also beam-beam challenges in future colliders such as the next generation nuclear physics electron ion collider (EIC). The purpose of this workshop is to bring experts in this field to review progress in beam-beam studies of the current and past colliders and to discuss potential beam-beam issues and solutions in the future colliders. The workshop website:

https://indico.physics.lbl.gov/indico/event/431/

will be regularly updated to include the latest information as it becomes available.

Ji Qiang and Jean-Luc Vay, IOC Chairs BeamBeam2018.

8.5   A Summary of Upcoming Workshops and Conferences

FFAG'17	**2017 International Workshop on FFAG Accelerators, September 6-12, 2017, at Cornell University, USA.** **https://www.bnl.gov/ffag17/**
	ICFA Mini-Workshop on Impedances and Beam Instabilities in Particle Accelerators, September 19-22, 2017 in Benevento, Italy. http://prewww.unisannio.it/workshopwakefields2017/
	ICFA Mini-Workshop on Non-linear Dynamics and Collective Effects, September 19-22, 2017 in Arcidosso, Italy. **https://www.elettra.eu/Conferences/2017/NOCE/**
Space Charge 2017	**ICFA Mini-Workshop, "Space Charge 2017", October 4-6, 2017, at TU Darmstadt, Germany.** **https://indico.gsi.de/conferenceDisplay.py?confId=5600**
ICALEPCS2017	**International Conference on Accelerators and Large Experimental Physics Control Systems, October 8-13, 2017 at the Palau de Congressos de Catalunya in Barcelona, Spain.** **http://icalepcs2017.org**
	ICFA Mini-Workshop on Dynamic Apertures of Circular Accelerators, November 1-3, 2017, at IHEP, China. **http://indico.ihep.ac.cn/event/7021/**
	ICFA Mini-Workshop on Slow Extraction 2017, November 9-11, 2017, at CERN. https://indico.cern.ch/event/639766/
	ICFA Mini-Workshop on Beam-Beam Effects in Circular Colliders, February 5-7, 2018 in Berkeley, CA, USA. **https://indico.physics.lbl.gov/indico/event/431/**
FLS2018	**60th ICFA Advanced Beam Dynamics Workshop on Future Light Sources, March 4-9, 2018, at SINAP, China.**
HB2018	**61st ICFA Advanced Beam Dynamics Workshop on High-Intensity and High- Brightness Hadron Beams, June 17-22, 2018, in Daejeon, Korea.**
	ICFA Mini-Workshop on Slow Extraction, November 2018, at FNAL, USA.

9 Announcements of the Beam Dynamics Panel

9.1 ICFA Beam Dynamics Newsletter

9.1.1 Aim of the Newsletter

The ICFA Beam Dynamics Newsletter is intended as a channel for describing unsolved problems and highlighting important ongoing works, and not as a substitute for journal articles and conference proceedings that usually describe completed work. It is published by the ICFA Beam Dynamics Panel, one of whose missions is to encourage international collaboration in beam dynamics.

Normally it is published every April, August and December. The deadlines are 15 March, 15 July and 15 November, respectively.

9.1.2 Categories of Articles

The categories of articles in the newsletter are the following:

1. Announcements from the panel.
2. Reports of beam dynamics activity of a group.
3. Reports on workshops, meetings and other events related to beam dynamics.
4. Announcements of future beam dynamics-related international workshops and meetings.
5. Those who want to use newsletter to announce their workshops are welcome to do so. Articles should typically fit within half a page and include descriptions of the subject, date, place, Web site and other contact information.
6. Review of beam dynamics problems: This is a place to bring attention to unsolved problems and should not be used to report completed work. Clear and short highlights on the problem are encouraged.
7. Letters to the editor: a forum open to everyone. Anybody can express his/her opinion on the beam dynamics and related activities, by sending it to one of the editors. The editors reserve the right to reject contributions they judge to be inappropriate, although they have rarely had cause to do so.

The editors may request an article following a recommendation by panel members. However anyone who wishes to submit an article is strongly encouraged to contact any Beam Dynamics Panel member before starting to write.

9.1.3 How to Prepare a Manuscript

Before starting to write, authors should download the template in Microsoft Word format from the Beam Dynamics Panel web site:

http://icfa-bd.kek.jp/icfabd/news.html

It will be much easier to guarantee acceptance of the article if the template is used and the instructions included in it are respected. The template and instructions are expected to evolve with time so please make sure always to use the latest versions.

The final Microsoft Word file should be sent to one of the editors, preferably the issue editor, by email.

The editors regret that LaTeX files can no longer be accepted: a majority of contributors now prefer Word and we simply do not have the resources to make the conversions that would be needed. Contributions received in LaTeX will now be returned to the authors for re-formatting.

In cases where an article is composed entirely of straightforward prose (no equations, figures, tables, special symbols, etc.) contributions received in the form of plain text files may be accepted at the discretion of the issue editor.

Each article should include the title, authors' names, affiliations and e-mail addresses.

9.1.4 Distribution

A complete archive of issues of this newsletter from 1995 to the latest issue is available at

http://icfa-usa.jlab.org/archive/newsletter.shtml.

Readers are encouraged to sign-up for electronic mailing list to ensure that they will hear immediately when a new issue is published.

The Panel's Web site provides access to the Newsletters, information about future and past workshops, and other information useful to accelerator physicists. There are links to pages of information of local interest for each of the three ICFA areas.

Printed copies of the ICFA Beam Dynamics Newsletters are also distributed (generally some time after the Web edition appears) through the following distributors:

John Byrd	jmbyrd@lbl.gov	North and South Americas
Rainer Wanzenberg	rainer.wanzenberg@desy.de	Europe++ and Africa
Toshiyuki Okugi	toshiyuki.okugi@kek.jp	Asia**and Pacific

++　Including former Soviet Union.

**　For Mainland China, Jiu-Qing Wang (wangjq@mail.ihep.ac.cn) takes care of the distribution with Ms. Su Ping, Secretariat of PASC, P.O. Box 918, Beijing 100039, China.

To keep costs down (remember that the Panel has no budget of its own) readers are encouraged to use the Web as much as possible. In particular, if you receive a paper copy that you no longer require, please inform the appropriate distributor.

9.1.5   **Regular Correspondents**

The Beam Dynamics Newsletter particularly encourages contributions from smaller institutions and countries where the accelerator physics community is small. Since it is impossible for the editors and panel members to survey all beam dynamics activity worldwide, we have some Regular Correspondents. They are expected to find interesting activities and appropriate persons to report them and/or report them by themselves. We hope that we will have a "compact and complete" list covering all over the world eventually. The present Regular Correspondents are as follows:

Liu Lin   *Liu@ns.lnls.br*   *LNLS Brazil*

Sameen Ahmed Khan   Rohelakan@yahoo.com   SCOT, Middle East and Africa

We are calling for more volunteers as Regular Correspondents.

9.2 ICFA Beam Dynamics Panel Members

Name	eMail	Institution
Rick Baartman	baartman@lin12.triumf.ca	TRIUMF, 4004 Wesbrook Mall, Vancouver, BC, V6T 2A3, Canada
Marica Biagini	marica.biagini@lnf.infn.it	INFN-LNF, Via E. Fermi 40, C.P. 13, Frascati, Italy
John Byrd	jmbyrd@lbl.gov	Center for Beam Physics, LBL, 1 Cyclotron Road, Berkeley, CA 94720-8211, U.S.A.
Yunhai Cai	yunhai@slac.stanford.edu	SLAC, 2575 Sand Hill Road, MS 26 Menlo Park, CA 94025, U.S.A.
Swapan Chattopadhyay	swapan@fnal.gov	Northern Illinois University, Dept. of Physics, DeKalb, Illinois, 60115, U.S.A.
Yong Ho Chin	yongho.chin@kek.jp	KEK, 1-1 Oho, Tsukuba-shi, Ibaraki-ken, 305-0801, Japan
Jie Gao	gaoj@ihep.ac.cn	Institute for High Energy Physics, P.O. Box 918, Beijing 100049, China
Ajay Ghodke	ghodke@cat.ernet.in	RRCAT, ADL Bldg. Indore, Madhya Pradesh, 452 013, India
Eliana Gianfelice-Wendt	eliana@fnal.gov	Fermilab, Mail Station 312, PO Box 500, Batavia IL 60510-5011, U.S.A.
Ingo Hofmann	i.hofmann@gsi.de	High Current Beam Physics, GSI Darmstadt, Planckstr. 1, 64291 Darmstadt, Germany
Sergei Ivanov	sergey.ivanov@ihep.ru	Institute for High Energy Physics, Protvino, Moscow Region, 142281 Russia
In Soo Ko	isko@postech.ac.kr	Pohang Accelerator Lab, San 31, Hyoja-Dong, Pohang 790-784, South Korea
Elias Metral	elias.metral@cern.ch	CERN, CH-1211, Geneva 23, Switzerland
Toshiyuki Okugi	toshiyuki.okugi@kek.jp	KEK, 1-1 Oho, Tsukuba-shi, Ibaraki-ken, 305-0801, Japan
Peter Ostroumov	Ostroumov@frib.msu.edu	FRIB, National Superconducting Cyclotron Laboratory, Michigan State University, 640 S. Shaw Lane East Lansing, Michigan 48824, U.S.A.
Mark Palmer	mpalmer@bnl.gov	Brookhaven National Lab, Upton, NY 11973, U.S.A.
Chris Prior	chris.prior@stfc.ac.uk	ASTeC Intense Beams Group, STFC RAL, Chilton, Didcot, Oxon OX11 0QX, U.K.

Yuri Shatunov	Yu.M.Shatunov@inp.nsk.su	Acad. Lavrentiev, Prospect 11, 630090 Novosibirsk, Russia
Jiu-Qing Wang	wangjq@ihep.ac.cn	Institute for High Energy Physics, P.O. Box 918, 9-1, Beijing 100039, China
Rainer Wanzenberg	rainer.wanzenberg@desy.de	DESY, Notkestrasse 85, 22603 Hamburg, Germany
Zhentang Zhao	zhaozhentang@sinap.ac.cn	SINAP, Jiading campus: 2019 Jia Luo Road, Jiading district, Shanghai 201800, P. R. China Zhangjiang campus: 239 Zhang Heng Road, Pudong New District, Shanghai 201203, P. R. China

The views expressed in this newsletter do not necessarily coincide with those of the editors.
The individual authors are responsible for their text.